



FERROUS METALLURGY
MONTANUNIVERSITAET

Influence of alkalis on the process behavior of iron carriers in different ironmaking reactors

Dissertation

by

Anton Pichler, MSc.

handed in at the Montanuniversitaet Leoben/ Chair of Ferrous Metallurgy for attaining the degree of a Doctor of Metallurgical and Mining Science

under the direction of

Univ.-Prof. Dipl.-Ing. Dr. tech. Johannes L. Schenk
(Chair of Ferrous Metallurgy, Montanuniversitaet Leoben)

Peer-reviewed by

Univ.-Prof. Dipl.-Ing. Dr.-Ing. Dieter Senk
(Department of Ferrous Metallurgy/ RWTH Aachen)



Chair of Ferrous Metallurgy/ Montanuniversitaet Leoben
Franz-Josef-Straße 18 – 8700 Leoben, Austria

Preface

I wish to thank everyone who has supported me, both financially and personally, during my time working at the Chair of Ferrous Metallurgy. Thank you for making this work possible.

Special thanks go out to my colleagues and the entire staff of the Chair of Ferrous Metallurgy for their contribution to this work. In addition, thanks to all colleagues and friends who made this time so special and memorable.

This work was performed within the K1-MET metallurgical competence centre. It was financially supported by BMVIT, BMW_F, and the provinces of Upper Austria, Styria, and Tyrol. My sincere thanks also to the industrial partners Primetals Technologies Austria GmbH, voestalpine Stahl GmbH, and voestalpine Stahl Donawitz GmbH for their excellent collaboration throughout the project. Furthermore, thanks to POSCO for their financial support during the project.

Last, but most importantly, I thank my family for their complete and unconditional support.

Affidavit

I declare, in lieu of oath, that I wrote this thesis and performed the associated research work myself, using only the literature cited in this paper.

Anton Pichler

November 15th, 2016

Abstract

During ironmaking processes, iron is not the only element to be charged in the reactor. Unwanted and harmful elements like alkali metals are also present during iron ore reduction and smelting. For instance, a higher load of sodium (Na) and potassium (K) leads to an increase in emissions (dust, cyanides, etc.) and causes malfunctions in the process performance. So, it is in the interest of operators to gather knowledge about the interaction of K and Na during iron ore reduction—specifically their effect on reactivity and mechanical properties, softening and melting behaviour, and circulation within the reactor. This thesis sought to determine two important aspects of alkalis during ironmaking: the macroscopic behaviour of enrichment and circulation, and the microscopic effects on ferrous burden materials during reduction.

An alkali model for ironmaking reactors was developed to demonstrate the behaviour and distribution of alkali compounds in the blast furnace and during smelting reduction processes. Based on empirical models and thermochemical calculations, it is possible to define the amount and the composition of alkali compounds for different reactor areas. The results were compared with industrial data and they show certain analogies. By modifying the process parameters (temperature profile, gas volumes, etc.), the effect on the distribution, flow, and load of alkalis is determinable.

To investigate the key aspects of alkalis microscopically, experimental simulations derived from industrial-scale ironmaking processes were performed. After an aqueous K/Na treatment of ferrous burden materials, the assimilation behaviour of different morphological phases was evaluated. Thereafter, reduction and tumbling tests were carried out to define the reactivity and mechanical properties of the iron carriers. To complete the interaction of iron carriers and alkali metals, softening and melting tests were performed. It was shown that the morphological structure is a main factor in the resistance against alkali influence. Lumpy iron ores were less affected than artificial materials like pellets and sinter. Pellets, in particular, showed a lower mechanical stability and an increase in reactivity during reduction. With regard to their melting behaviour, both pellets and sinter demonstrated significantly lower temperatures during phase transformations on the addition of alkali metals.

Kurzfassung

Bei der Herstellung von Eisen können durch die Verwendung von natürlichen Einsatzmaterialien (Erz, Kohle, Zuschlagsstoffe) unerwünschte Elemente in den Reaktor eingetragen werden. Ein Typus solcher schädlichen Substanzen sind Alkalimetalle wie Kalium und Natrium. Beide führen zu erhöhten Emissionen (z.B. Staub, Zyanide, etc. im Gichtgas) und können den Betrieb signifikant stören. Daher ist es im Interesse des Betreibers, über die Wechselwirkungen von Alkali-Elementen mit diversen Prozessparametern der Eisenerzverhüttung Bescheid zu wissen. Dies sind im Spezifischen die Reduzierbarkeit/Reaktivität, Einfluss auf mechanische Eigenschaften, Effekte auf Erweichungs- und Aufschmelzverhalten bzw. die Zirkulation und Anreicherung im Reaktor. Daraus entwickelten sich zwei wesentliche Aspekte dieser Arbeit: die makroskopische Betrachtung von Alkalien in Reaktoren der Eisenverhüttung und die mikroskopische Beurteilung des Einflusses von Alkalien auf diverse Eisenträger (Sinter, Pellets, Stückerze).

Ein Alkalien-Modell für Reaktoren der Eisenverhüttung wurde entwickelt, um das Verhalten und die Verteilung unterschiedlicher Alkaliverbindungen im Hochofen und in Schmelzreduktionsprozessen abbilden zu können. Durch Verbindung eines auf Empirik basierenden Modells mit thermochemischen Kalkulationen ist es gelungen, die stabilen Alkaliverbindungen für bestimmte Reaktorregionen zu bestimmen. Die Validierung des Modells erfolgte durch Vergleich mit industriellen Daten und deren Übereinstimmungen. Mittels Variation von Prozessparameter (Temperaturprofil, Gasvolumina, etc.) können Einflüsse auf die Alkalien-Verteilungen und -Flüsse bestimmt werden.

Die Untersuchung der mikroskopischen Zusammenhänge wurde durch experimentelle Simulation von Verhüttungsprozessen durchgeführt. Die Eisenträger wurden zuerst mittels wässrigen Alkali-Lösungen behandelt (Bestimmung der K/Na-Assimilation durch verschiedene morphologische Phasen) und danach Reduktions- und Trommelversuchen zugeführt. Diese dienten zur Bestimmung von mechanischen Kennwerten und der Reaktivität. Zusätzliche Erweichungs- und Schmelzversuche evaluierten das Aufschmelzverhalten. Es wurde dabei gezeigt, dass die morphologische Struktur das Verhalten gegenüber Alkalien prägt. Stückerze wurden weniger beeinflusst als Agglomerate. Vor allem Pellets zeigten bei den Reduktionstests signifikant höhere Reaktivitäten und niedrigere mechanische Festigkeiten. Die Sinterproben zeigten während der Schmelzversuche durch die Alkalienzugabe eine wesentliche Verschiebung der Phasenumwandlungstemperaturen zu niedrigeren Werten.

Table of Contents

Preface	i
Affidavit	ii
Abstract	iii
Kurzfassung	iv
Table of Contents	v
1 Introduction and Objectives	1
1.1 Iron and Steel in a Modern Society	2
1.2 Research Objectives	4
2 Ironmaking: Background and Fundamentals	5
2.1 Ironmaking Processes	5
2.1.1 Historical Background of Iron Production	5
2.1.2 Overview: Routes of Steel Production	6
2.1.3 Blast Furnace Process	8
2.1.4 Direct and Smelting Reduction Processes	12
2.1.5 Alternative Routes of Ironmaking	16
2.2 Fundamentals of Ironmaking	17
2.2.1 Thermodynamics of Reduction Processes	17

2.2.1.1	Direct and Indirect Reduction of Iron Ores	21
2.2.2	Kinetics of Iron Ore Reduction	24
2.2.3	Softening and Melting	29
3	Alkalis and Ironmaking Processes	32
3.1	Alkalis in Ferrous Burden Materials: Geological Origin and Mineral Processing	34
3.2	Thermodynamics of Alkalis and Behaviour in Ironmaking Processes	36
3.2.1	Alkali Flow in the Blast Furnace	42
3.2.2	Alkali Flow in Direct and Smelting Reduction Processes	47
3.3	Effect of Alkalis on Reduction and Melting Behaviour of Ferrous Burden Materials	49
3.4	Previous Problems and Approach of Work	52
4	Macroscopic Effect of Alkalis: Modelling of Ironmaking Reactors	53
4.1	Layout of the Alkali Model for Ironmaking Reactors	53
4.2	Alkali Model for the Blast Furnace Process	55
4.2.1	Data Input and Profiles of the Standard Blast Furnace Model	55
4.2.2	Slag Model	57
4.2.3	Multi-stage Shaft Reactor Model	60
4.2.4	Results and Alkali Distribution in the Standard Model	62
4.2.5	Validation of Standard Model	65
4.2.6	Parameter Analysis with Focus on Slag Properties	69
4.3	Alkali Model for Smelting Reduction	73
4.3.1	Fundamental Layout of the Alkali Model for the COREX® or FINEX® Process	73
4.3.2	Data Input and Outline of the Melter Gasifier	74
4.3.3	Results of the Standard Melter Gasifier	76
4.4	Discussion about Alkali Model	79
4.4.1	Background of the Standard Blast Furnace Model	79
4.4.2	Comparison between Blast Furnace and Melter Gasifier	79
4.5	Results of Alkali Model: Future Potentials	82

5	Microscopic Effect of Alkalis on Reduction, Disintegration and Melting.....	83
5.1	Methodology for Investigations of the Samples of Ferrous Burden Material	84
5.2	Alkali Assimilation of Ferrous Burden Material.....	85
5.3	Influence of Alkalis on Reduction Reactions and Mechanical Stability	89
5.3.1	Testing Equipment and Programs for Reducibility and Mechanical Stability.....	89
5.3.2	Results of the Reduction Tests	91
5.3.3	Influence of Alkalis on Mechanical Stability during Reduction	96
5.3.4	Morphological Investigation of Reduced Samples	99
5.3.5	Comparison with Literature and Discussion of Results	100
5.4	Effects of Alkalis on Softening and Melting Behaviour	105
5.4.1	Preparation of Material and Methodology	105
5.4.2	Methods of Testing (Softening and Melting Temperature)	106
5.4.3	Influence of Alkalis on Melting and Softening Behaviour: Test Results	108
5.4.4	Influence of Alkalis on Melting and Softening Behaviour: A Comparison with Literature and Data Evaluation	112
5.4.4.1	Evaluation of Testing Results and Comparison of Different Methods	112
5.4.4.2	Discussion of the Melting Tests and Conclusion	115
6	Summary, Conclusion, and Outlook	123
6.1	Macroscopic Correlations between Process Parameters and Alkali Behaviour.....	123
6.2	Microscopic Correlation between Iron Ore Reduction and Alkalis	124
6.3	Outlook and Future Potentials	127
7	References	129
	Appendix	I
A-1	Reduction curves of ferrous burden materials under different process conditions and alkali contents.....	I
A-2	Observations by HT-LSCM (partially reduced iron carrier)	IV
A-3	Ternary systems for the evaluation of alkali addition.....	VI
A-4	Profiles of elements in experimental blast furnace	VII

B-1	List of Figures.....	VIII
B-2	List of Tables.....	XIV
B-3	Acronyms.....	XVI
B-4	Publications	XVII
B-5	Curriculum Vitae.....	XIX

1 Introduction and Objectives

There are many arts and sciences of which a miner should not be ignorant. First there is Philosophy, that he may discern the origin, cause, and nature of subterranean things; for then he will be able to dig out the veins easily and advantageously, and to obtain more abundant results from his mining.

Georgius Agricola, De Re Metallica

The production of iron and steel has always played a major role in the development of humankind. Since ancient times, iron has been used to manufacture tools and weapons. It has influenced inventions and progress in fields such as agriculture, industry, and trade. Developments in metallurgical processing and material science have led to the evolution of cultures, both internally (improvement of life quality) and externally (advantages over other cultures). The Hittites (2nd millennium BC), Indians (3rd century BC), Romans (1st century BC), Arabs (8/9th century BC), British (18th century), Germans (19th century), and Americans (20th century) are outstanding examples of their respective times. Furthermore, developments in metallurgy radiate into the study of scientific fundamentals (physical chemistry), social economics and politics (unions and cooperative organizations), and even literature (Mime in the Germanic tale of the Nibelungs; dwarfs as the masters of blacksmiths). Ironmaking has always been a developing field of technology and this is true even today. Aspects like economic feasibility (e.g. cost-effectiveness, stakeholder value), ecological sustainability (e.g. recycling, zero waste, and emission production), and technological progress (e.g. modelling, automatization, and digitalization) are driving forces in the field of ironmaking. The engineer, in particular, has the key function of solving problems and reaching targets in this field. Economically speaking, the lowering of costs is achieved through a lower input of raw materials and energy. Higher value is placed on new products that satisfy the requirements of consumers. Intelligent use of manpower and the connection of production with society—including social welfare—are also economic aspects. Ironmaking has a huge global impact ecologically as well. The use of non-renewable sources of energy (especially coal) and, consequently, the emission of carbon dioxide (CO₂) have to be avoided. Hydrogen technology and electric power from renewable sources of energy may be a way forward. There is also zero-waste production, which means the recycling of, for example, dust, and the transformation of waste into useable products

(e.g. the topic of alkalis in the top gas treatment of the blast furnace [BF] will be discussed in this thesis). In fact, the iron and steel industry in Europe is an exemplar in the area of recycling (high scrap ratio, internal recycling of dust, smart gas-heat power grids). Furthermore, technological circumstances are leading to higher use of computer-aided methods. Digitalization, smart production, and modelling are key areas in an increasingly globalized world (e.g. this thesis discusses the process modelling for iron production based on computer-aided calculations).

1.1 Iron and Steel in a Modern Society

Although a considerable section of society considers steel to be a backward and dirty material,² modern civilization cannot exist without it. The global gross domestic product (GDP) is closely linked to the global steel production³ (see Figure 1-1 for national economies). Steel is present in infrastructure, construction, machinery, automotives, and consumer goods. The average person in western industrial countries consumes 200–600 kg steel/capita (usage in fields of Figure 1-2) and has a personal steel stock of 4.4–12 tons/capita.^{4–6} According to the World Steel Association⁷ and internal studies,^{4,5} 500±100 kg steel/capita for consumption and 10±2 tons/capita as stock are seen as a sign of stability in a modern society.

Given the annual production of 1.6 billion tons of crude steel (2015)^{6,8}, steel is the leading metal globally (compared to 52.29 million tons [mio.t.] of primary aluminium [Al] and 21 mio.t. of copper [Cu] in 2014⁸). Especially since the industrial revolution in the 18th century, the demand for and supply of iron and steel has risen nearly continuously—from 4.25 mio.t. in 1850, 28.1 mio.t. in 1900,⁹ and 189.1 mio.t. in 1950¹⁰ to 849 mio.t. in the year 2000.⁹ Steel offers several advantages, which will be discussed in the following. But there are some disadvantages as well.

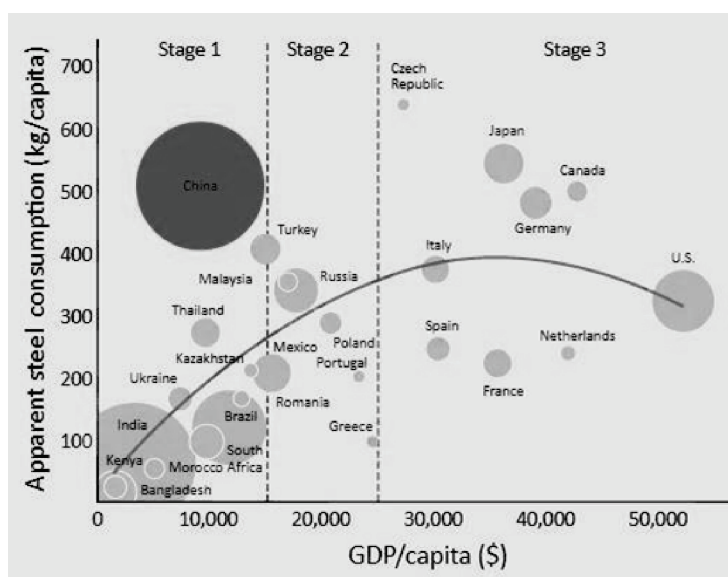


Figure 1-1: Steel consumption in relation to the GDP/capita [US\$], including the population (circle size)¹



Figure 1-2: Steel usage in modern civilizations

The recyclability of steel is unlimited. Leaving aside problems relating to trace elements (copper [Cu], tin [Sn], lead [Pb], chromium [Cr], nickel [Ni], molybdenum [Mo]) for specific steel grades,¹³ iron and steel can be remelted without loss of quality. A global return of 585 mio.t.

scrap⁸ and a scrap ratio of 56%, such as for the European crude steel production (2012)⁵, show the opportunities for steel in a future blue economy¹⁴.

The Earth's crust contains ~5.6 wt-% iron,¹⁵ which makes iron a frequent and globally spread element. This results in the low price of iron-bearing raw materials (approximately US\$40/dry metric ton in January 2016) compared to other metals.¹¹ Taking into account the production costs, a hot rolled coil (HRC) cost ~US\$300 in March 2016¹⁶ on the world market. This makes iron a cost-effective construction material (e.g. the cost is five times more for Al and 17 times more for Cu).¹⁷

Moreover, its combination of properties is a key factor in the use of steel. To visualize some of these links, Ashby¹² developed correlation diagrams (see Figure 1-3 for an example). These Ashby diagrams show the fields of application in correlation with strength, density, elongation, heat transfer coefficient, maximum service temperature, price, energy input, impact toughness, and so on. The diagrams present the advantages of steel in detail, especially in terms of strength, service temperature, and price.

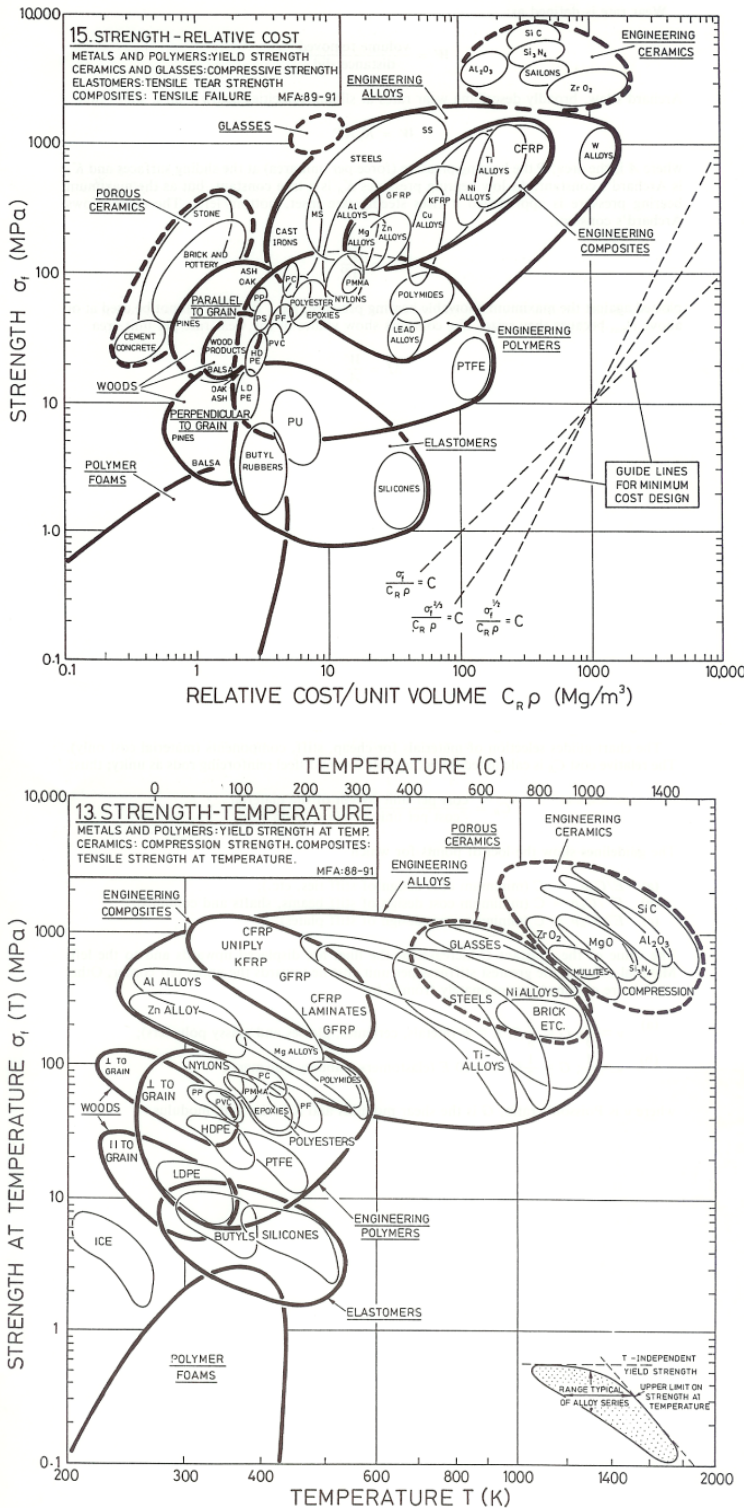


Figure 1-3: Ashby diagrams for strength-density and strength-service temperature^{11,12}

The main disadvantage of steel is that its production is based on carbon (C): Coke is used as fuel in the BF. This accounts for 7% of the global consumption of energy and 5% of the global emission of CO₂.¹⁸ In addition, chemical substances like HCl, SO₂, NO_x, PCDD/F (organic, cyclic compounds with halogens), and dust particles of different sizes are emitted by the BF or by supporting processes like the coking and sinter plant. Waste gas treatment—technologically at the state of the art in most cases¹⁹—is minimizing the relative emissions per ton of steel. However, the absolute impact on the environment is still too high for sustainable steelmaking.

Another disadvantage, which is linked to carbon, is the multi-step process for hot metal and crude steel production.^{9,20} In the BF, the liquid metal is saturated with carbon (4.3% C). It then has to be decarbonized by a second step (in the basic oxygen furnace [BOF]) to produce crude steel (<300 ppm C).²⁰ A big target of metallurgists, therefore, is developing a single-step process for the future. Further information about the routes of ironmaking and steelmaking are summarized in Chapter 2.1.2.

1.2 Research Objectives

This thesis aims to examine the influence of alkali metals (specifically potassium and sodium) on ironmaking processes. The list of harmful effects is quite long:

- Increased dust formation
- Formation of scaffolds
- Refractory consumption
- Change in softening and melting performance of iron carriers
- Sticking, swelling, and change in mechanical properties
- Cyanides in waste gas treatment
- Higher coke and carbon consumption

Macroscopic and microscopic aspects have to be considered to get a full understanding of the effects and interactions.

The work is separated into two main parts:

In the first part, the alkali flows in different ironmaking reactors had to be evaluated. This was achieved by creating an alkali model. After fundamental considerations relating to the mass flows and influencing parameters, a model was developed that combines empirical models, thermochemical calculations, and industrial data. The results show the alkali distribution in different reactors (see Chapter 4).

The second part focused on the microscopic aspects of alkalis. Based on earlier work at the Chair of Ferrous Metallurgy (Montanuniversitaet Leoben), reduction tests and melting tests were performed. In addition, a new method to determine alkali assimilation by different burden materials was developed. All results will be presented in Chapter 5.

2 Ironmaking: Background and Fundamentals

Secondly there is Medicine, that he may be able to look after his diggers and other workmen. Thirdly follows astronomy, that he may know the divisions of the heavens and from them judge the directions of the veins.

Georgius Agricola, De Re Metallica

The main step for the production of steel is the earlier smelting of iron. This usually involves a reduction of iron oxides and melting the iron to a liquid metal. The hot metal is a common product of the BF and an important input material for steel production. The following chapter provides an overview of common ironmaking routes and the fundamentals of iron ore smelting.

2.1 Ironmaking Processes

The following chapter studies the link between historical development, actual routes of ironmaking, and further progress in the field of ironmaking (reduction and melting).

2.1.1 Historical Background of Iron Production

Geologically speaking, iron occurs as an oxide or a minor sulphide. Only in special cases does metallic iron form naturally (e.g. metal in meteors from space; in very rare cases, through the combination of an iron-bearing ore layer with a carbon-bearing coal layer, including energy supply by vulcanism). From a historical point of view, this is the reason for the late usage of iron compared to precious metals like silver and gold (before 5000 BC), which appear as metals under atmospheric conditions. The stability of the oxide combined with the melting temperature of the metal are the boundary conditions for further development of metallurgy. After the precious metals, metals with low melting points were smelted—for example, mercury (-39°C), tin (232°C), lead (327°C), zinc (420°C), arsenic (615°C), and copper (1083°C). To achieve higher temperatures, clay-based furnaces were used. These were fired by charcoal and natural wind.

Technical progress led to hotter furnaces that operated at temperatures of nearly 1100°C. They were able to smelt iron the first time; presumably 1200 BC as solid iron sponge, which was forged to the final products. The subsequent 3000-year history of ironmaking has led to the development of a huge number of ironmaking reactors. Starting from the early batch-working clay furnaces and smelting pits, improvements in gas generation (blasts from bellows, medieval hydropower), furnace design (higher layouts that led to higher temperatures at the bottom, right up to the melting temperature of highly carbonized iron), and energy supply (coke from coal instead of wood or charcoal as fuel) ended in the BF process. In particular, economic aspects like the scarcity of timber led to disruptive innovations like the use of the coke BF (18th century). Given continuous technological progress, the BF still represents the main process in ironmaking. The availability of electric power since the beginning of the 20th century forced a development towards submerged arc furnaces (SAFs) and electric blast furnaces (EBFs).⁹ Moreover, modern direct reduction processes also have their historical background in the early furnaces, which produced sponge iron for forging. For further information on technological innovations, see Gudenau et al.;^{9,21} for the mythological and cultural aspects of metals in history, see Paschen et al.^{22,23}

2.1.2 Overview: Routes of Steel Production

Nowadays, there are several different routes for the production of iron and steel. The most effective route depends on local energy supply (cheap natural gas, cheap electricity, or quality of coal—e.g. thermal or coking coal) and the product itself. For instance, reinforcing steel is often limited to a small consumer area, plus fewer requirements of the product (only strength and elongation allow the input of unclean scrap). This leads to the scrap electric arc furnace (EAF) route being the favoured way. Other examples are the production of rails and wire using the integrated route (high requirements for trace elements), iron production in South Africa and India via the COREX[®] process or rotary kilns (thermal coal instead of coking coal), and direct reduction in Iran using the MIDREX[®] SAF route based on cheap natural gas and electricity.²⁴ Four main routes^{20,21,25–32} for the production of crude steel are prevalent (see Figure 2-1, including further treatment of the liquid crude steel by secondary metallurgy, casting, and processing to the semi-finished product). For stainless and special steels, see Bernhard et al.³³

The globally dominant way is the integrated route. The main steps here are the reduction and melting of hot metal by the BF and the steelmaking step using a BOF. The BF is charged with lumpy ferrous materials like sinter, pellets, and lump ore. The energy is supplied by coke and substitute reducing agents (coal, natural gas, plastics). For the slag formation, fluxes like lime, dolomite, and olivine are added. Hot metal is the main product. Slag is processed into lump or granulated slag for construction, and the top gas is used for heating and power production. For further information about the BF, see Chapter 2.1.3. The hot metal contains a high amount of sulfur, which is removed during hot metal desulphurization, and carbon and phosphorous, which have to be removed by processing in an oxygen converter (BOF).

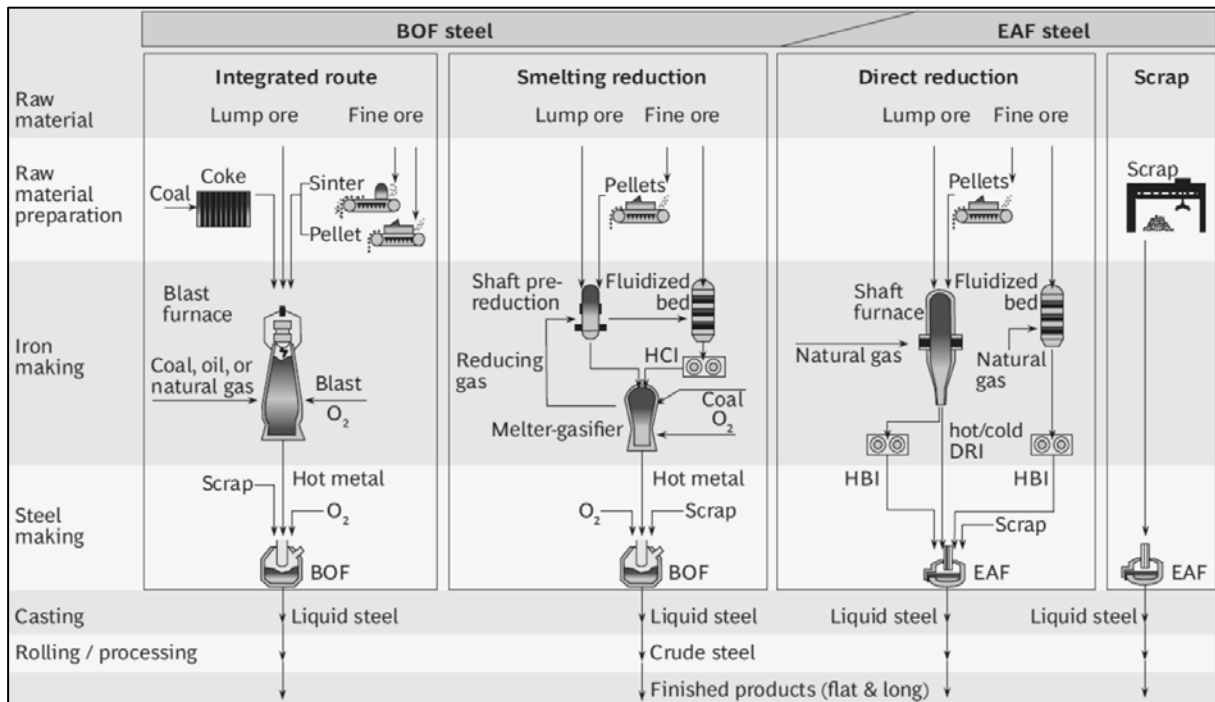


Figure 2-1: Actual routes of steel production³⁴

The second important method of crude steel production is using the EAF. In general, the input is only scrap (modified furnaces also deal with a specific ratio of hot briquetted iron [HBI] or liquid metal). The energy is mainly supplied by electrical power. Due to the higher scrap rates, the EAF route is becoming more common for developed countries. The products are a FeO-containing slag and crude steel. The off-gas is energetically used.

Direct reduction is an alternative route for the production of metallized HBI, which can subsequently be melted and refined to form steel in an EAF. Similar to the direct reduction processes, smelting reduction produces direct-reduced iron (DRI) or hot compacted iron (HCI) in reduction aggregates without coke and at low temperatures (<1100°C). However, an additional step of melting is included in these processes. The melter gasifier melts the DRI or HCI to liquid hot metal (similar to hot metal from a BF) and provides the reducing gas for the previous reduction steps by combustion of thermal coal. More details and an overview of different direct and smelting reduction processes are summarized in Chapter 2.1.4.

In this thesis, ironmaking processes are at the forefront; therefore, direct and smelting reduction, and the BF process are discussed in detail.

2.1.3 Blast Furnace Process

In the field of ironmaking, more than 92% (1.15 bn t in 2016⁶) of primary iron is produced by the BF process, which is globally the most common route of iron production.^{21,25,27,28,38,39} Its main characteristic is its layout as a shaft furnace based on the principle of counter current flow. The solids and liquids descend in the furnace, while the gaseous compounds ascend with the exchange of heat and mass (especially oxygen from the iron oxides). This thesis provides only an overview of the BF process, including important aspects for thermochemical and experimental modelling (see Chapters 4 and 5). For detailed information, see Biswas,²⁸ Geerdes,³⁵ Senk,⁴⁰ and Gudenau.²¹

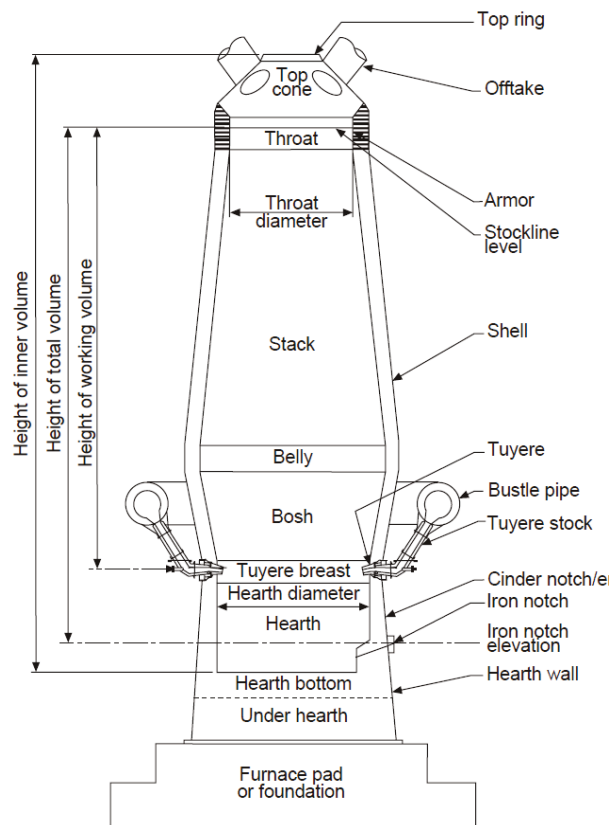


Figure 2-2 (left) shows the technological layout of a modern BF. The reactor is a shaft furnace with a refractory-lined steel shell. The tuyeres for the firing are located at the bottom. Below the tuyeres are the tapping holes for the iron or slag discharge. Due to the high carbon activity and the high temperatures, the hearth is lined with carbon bricks. The top consists of a charging system for the burden and the waste gas pipes for the top gas. The treatment of the top gas is shown in Figure 2-2 (right). The top gas enters a dust catcher first, where the coarse particles are segregated by cyclones. Afterwards, the gas stream enters a scrubber unit that removes particles by the addition of circulating water.

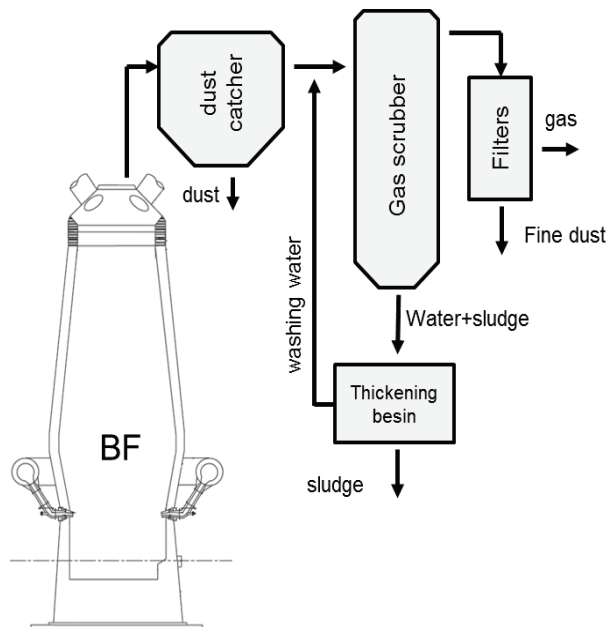


Figure 2-2: Layout of a modern blast furnace (top)³⁵ and a schematic picture of the top gas treatment system (bottom)^{36,37}

The water transports the particles into a thickening basin, where the sludge is separated and the washing water is recycled into the scrubber. Here, especially harmful trace elements, such as chlorides and cyanides, are removed from the waste gas. Finally, the gas flow passes electrostatic filters for the finest dust fraction.

An important aspect of the shaft reactor is the classification of the reaction zones. The multi-zone layout for the BF process is depicted in Figure 2-3 (left), including the chemical reactions. Coke, ferrous burden material, and fluxes are charged from the top as layers in the furnace. In the top region (heating zone), the solids are heated up by the ascending gas (top gas temperature of approximately 150–200°C). The material is dried, the limonites ($\text{Fe}_2\text{O}_3 \cdot \text{H}_2\text{O}$) are dehydrated, and carbonates from burden materials and fluxes like MgCO_3 , CaCO_3 , and FeCO_3 are calcined. Usually, the gas in the upper stack region can reduce hematite to magnetite and, further, to wuestite. This reducing power of the process gas increases from the top to the bosh region (thermodynamic relations will be discussed in Chapter 2.2.1). According to Figure 2-3 (right), the process gas contains oxidizing gases (CO_2 and H_2O) and reducing gases (CO and H_2), which shifts the thermochemical stability of iron oxides to magnetite and wuestite. With the increase of reducing components in the middle shaft region (soaking zone), even reduction to solid metallic iron is possible. Below the soaking zone, the Boudouard equilibrium leads to the generation of CO from solid carbon and CO_2 (the CO_2 content in the process gas drops in the Boudouard zone). The water gas shift equilibrium (interaction between CO/CO_2 and $\text{H}_2/\text{H}_2\text{O}$) is another reaction between the compounds of the process gas, which influences the gas composition and energy balance. The temperature increases down the shaft to the melting temperature of the ferrous burden material. This area in the bosh region is called the melting or cohesive zone. This zone has a major influence on the pressure balance, and, consequently, on the gas flow and process performance. The effects of the burden material on this zone will be discussed in Chapters 3.3 and 5.4). Below this zone, coke acts as the only remaining solid. Oxides and metals occur in their liquid phases (slag and hot metal). In the metallurgical zone (bosh or hearth), the high temperature ($>1400^\circ\text{C}$) and carbon activity or a CO partial pressure leads to a final reduction of the iron oxide and the partial reduction of SiO_2 , MnO , and P_2O_5 . The final metal quality depends on these relations. Given the sulfur content, the low oxygen potential and the CaO in the lime lead to the bonding of sulfur in the slag and a high desulphurization capacity, which is expressed by the ratio $(\text{S})/[\text{S}] > 10$.^{28,41,42}

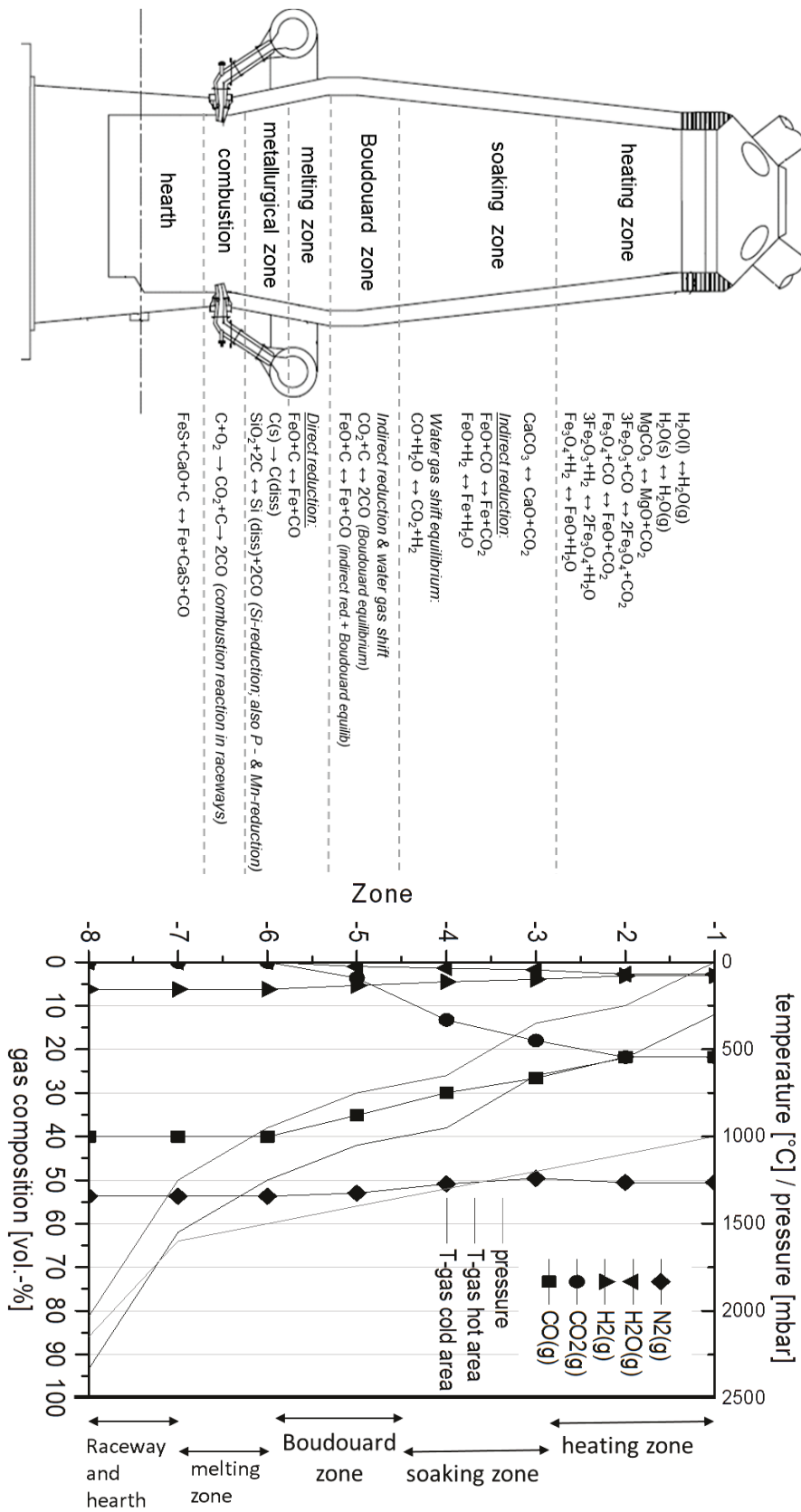


Figure 2-3: Multi-zone model of the blast furnace (top)³⁷ and the gas, temperature, and pressure profile for an exemplary furnace derived from literature^{28,35,43} (bottom)

The charged burden materials are dependent on the geographical region and the operation time. For instance, the average burden distribution of German BFs changed from 1965 (60% sinter, 40% lump ore) to 2010 (60% sinter, 10% lump ore, 30% pellets) mainly by substituting lump ores with iron ore pellets. Geographically, European BFs are mainly sinter-based furnaces. Moreover, in Brazil, Japan, and Korea, BFs operate with a high sinter ratio (70% sinter, 10% pellets, 20% lump ore). In North American (NA) countries, the process is pellets-based with a pellets ratio >80 % (10% sinter, 10% lump ore). The data is average data taken from the literature.^{34,44-47}

For modelling the BF and carrying out the related calculations, several parameters have to be defined (see Table 2-1). The input materials are ferrous burden materials (mainly sinter with 900–1000 kg/per t hot metal [tHM], as well as minor pellets and lump ore) and fuels (mainly coke and additionally pulverized coal, oil, natural gas, or other substitute reduction agents). The pressure is measured at the bottom (blast from tuyeres) and at the top. According to the gas balance, the main parameters are the temperature and the composition of the hot blast and the top gas.

Table 2-1: Typical process condition of the BF derived from literature: The basis for the standard BF model^{35,40}

Ore consumption (sinter, pellets and lump ore)	1500–1600 kg/tHM	Coal rate	0–200 kg/tHM
Fuel rate	450–600 kg/tHM	Coke rate	300–600 kg/tHM
Slag basicity	0.9-1.25	Melting rate	50–200 tHM/h
Tapping temperature	1420–1450 °C	Slag volume	220–300 kg/tHM
Blast temperature	1100–1250 °C	Top gas temperature	110–150°C
Blast pressure	2.1 bar absolute	Top gas	21–35% CO, 20–25% CO ₂ , 3–6% H ₂ , >35% N ₂
Tuyere oxygen volume	1000–1500 m ³ /tHM	Top gas pressure	1 bar (absolute)

2.1.4 Direct and Smelting Reduction Processes

Direct and smelting reduction processes are alternatives to the BF. Both have advantages as they substitute the expensive coke by other fuels like natural gas or thermal coal. Figure 2-4 gives an overview of different processes, including the sources for iron and energy.

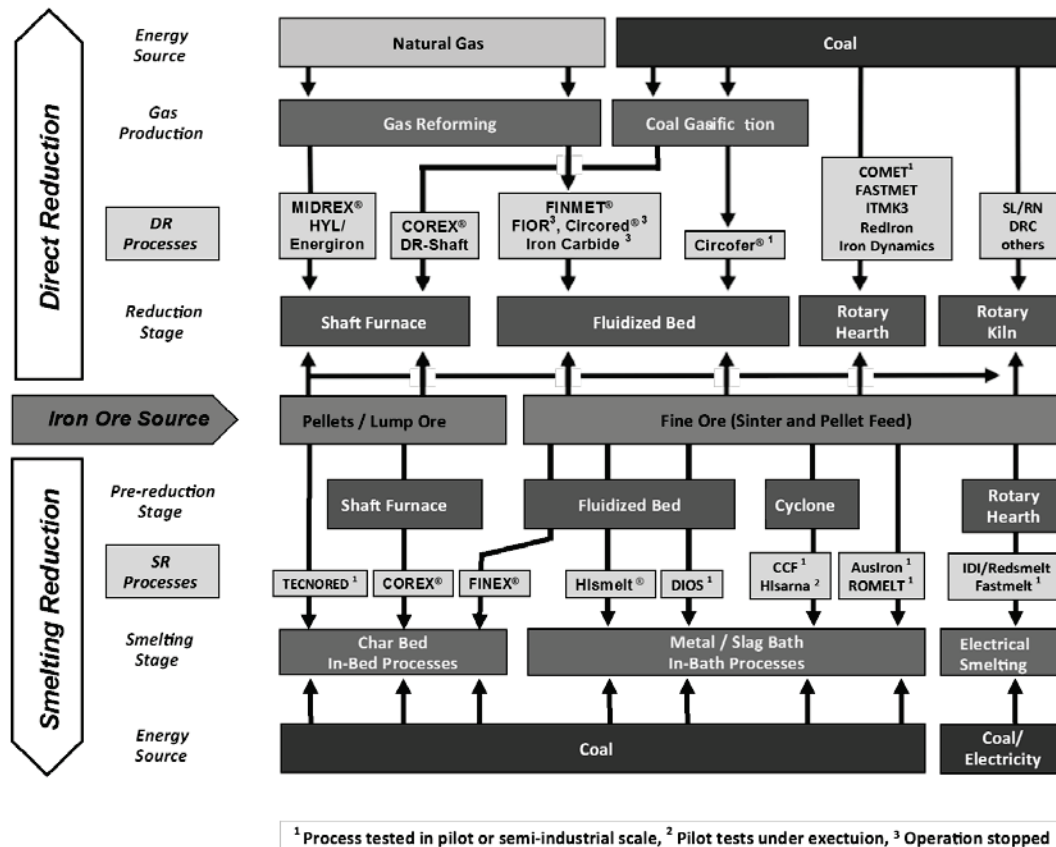


Figure 2-4: Flow sheet for direct and smelting reduction processes, including energy and iron ore sources⁴⁸

In general, a direct reduction process describes the transformation of iron oxides into metallic iron by means of indirect reduction and no molten phases. This implies process temperatures below 1100°C, and a solid state reduction with gaseous mixtures of H₂ and CO,⁴⁹ which flow into the shaft furnace or fluidized bed reactors. The MIDREX[®] and the FINMET[®] process are two examples of this procedure. Some direct reduction processes, like rotary kilns and rotary hearth reactors, combine the production of the reducing gas (mainly based on coal) with the reduction of the ore in one reactor. This is performed by direct reduction reactions and by indirect reduction mechanisms with the partial combustion of carbon (see Equations 2-11 to 2-16 and 2-21). As iron carriers, lumpy materials like pellets and lump ore can be charged in shaft furnaces and rotary kilns. Fine iron ores can be processed in fluidized bed reactors and rotary kilns. The product is DRI (also called sponge iron) for all processes, which has to be briquetted to HBI due to its high surface area and reactivity (especially in the case of earlier fine ore reduction by a fluidized bed). This HBI is globally traded (70 mio.t. in 2010³⁴), and has become a major scrap

substitute for inputs in EAF and BOF. The combination of energy source and iron source led to different process layouts of direct reduction (see Figure 2-4). With 78.6% usage (2013),⁵⁰ shaft furnace-based processes like MIDREX® and HYL are the leading direct reduction processes.

Smelting reduction means the production of liquid hot metal without the use of coke. In general, the process is divided into two aggregates: a reduction facility and a melting furnace. The reduction step is similar to the direct reduction processes. In a solid-gaseous reaction, iron carriers are reduced to solid metallic iron (iron sponge). The layout of the reduction facility depends on the input material (lumpy or fine). For better processing, an interim product is formed to charge into the melter gasifier (e.g. additives like lime and the reduced iron are pressed into HCl during the FINEX® process). The reduction degree of this interim product varies between >90% for the COREX® or FINEX® process to <20% for Hismelt®, where the main parts of the reduction are also carried out by the melting facility. As the energy source, thermal coal is charged into the melting furnace. It generates heat for the melting and provides the reducing gas for the previous reduction reactors. The layout of the melting reactor also defines the slag and hot metal quality. In-bed reactors form a char bed similar to the lower BF areas. So, the process conditions are comparable between melter gasifier hearth and BF hearth, which leads to similar hot metal quality and slag properties. The FeO content is low, which leads to good desulphurization, but there is also high C and P content in the metal. The melter gasifier of the COREX® or FINEX® process is an example of an in-bed reactor. In contrast, an in-bath reactor forms a metal-slag bath similar to the BOF. The slag contains FeO due to a higher oxygen potential in the reactor. This consequently leads to good decarbonization and dephosphorization of the metal, but the ability for desulphurization of the slag is low. However, smelting reduction is still a niche technology. Metal production by smelting reduction processes amounted to ~6 mio.t. in 2014 (<1% of global ironmaking),⁵¹ whereas COREX® and FINEX® were the predominant process schemata with a globally installed capacity of ~12 mio. T. HM.

COREX® and FINEX® processes: These smelting reduction processes consist of two main aggregates: a direct reduction step in a reduction shaft (COREX®) or fluidized bed reactors (FINEX®) and a melting step in a melter gasifier (same for both processes). This is visualized in Figure 2-5.

The function of the reduction step is the heating, calcination (CO₂ and H₂O removal) and, partially, reduction (up to 94% metallization). The generator gas from the melter gasifier is used as the reductant (gas mixtures of CO, CO₂, H₂, H₂O, CH₄, and N₂). The COREX® process has a single reduction shaft, which is charged with a lumpy iron carrier like lump ore and pellets (from average statistical data,⁴⁴⁻⁴⁷ nearly 50/50%) with a grain size of 8–16 mm⁵² from the top. The reduction shaft is operated at the reduction gas inlet with a temperature of 800°C and the top gas temperature is about 250–300°C⁵³ (gas oxidation degree [GOD] ~50%). In contrast, the FINEX® process consists of several fluidized bed reactors for pre-reduction. Charged by fine iron ores (sinter feed grade of up to 6.3 mm), the material is reduced stepwise from hematite or limonite to magnetite (first stage), to wuestite (second stage), and finally to metallic iron (third stage). The fine DRI is briquetted afterwards together with the calcined additives (lime) to HCl and charged into the melter gasifier. The temperature increases with each step (480, 750, 760°C); meanwhile, the GOD decreases (0.42, 0.39, 0.29 at the reactor's exit).⁵⁴

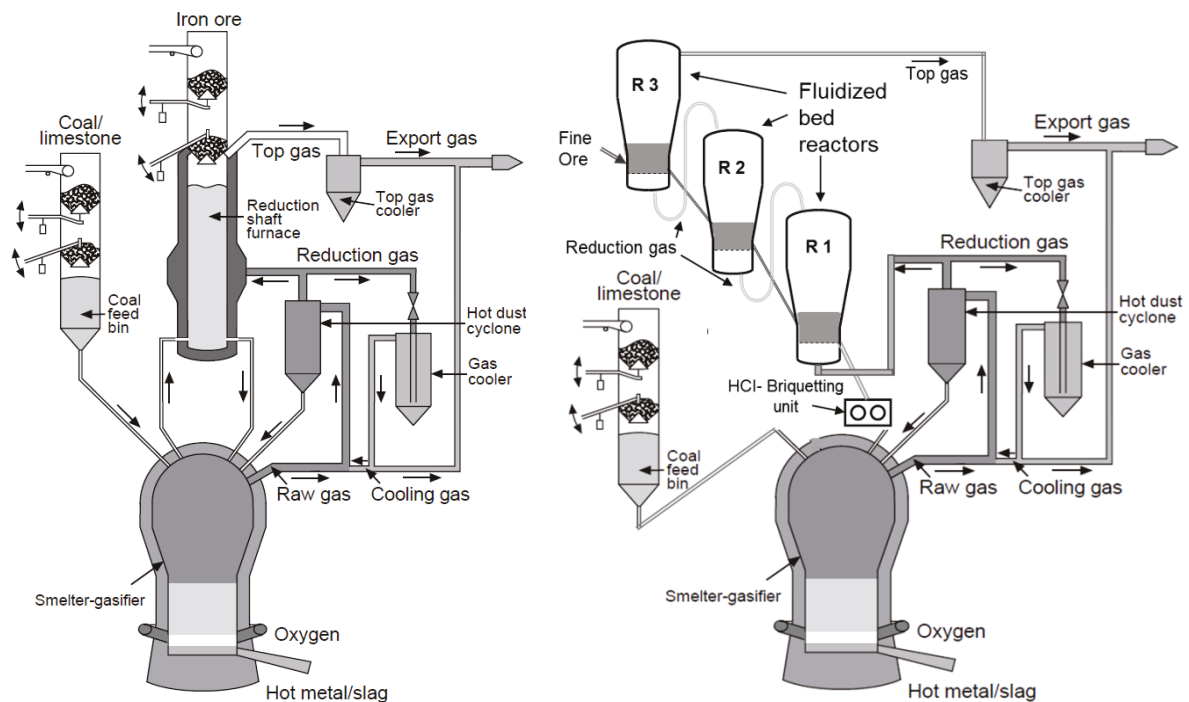


Figure 2-5: Schematic pictures of the COREX® process (left)⁹ and the FINEX® process (right)

The melter gasifier (MG) operates in both processes following the same principle. It melts the partially reduced material (HCl) and produces hot metal by final reduction of the remaining oxides and carbonization of the liquid metal. The energy is generated by gasification of coal (and a small ratio of coke) with oxygen, which also supplies the reduction gas for the pre-reduction stages. The different zones in the reactor are shown in Figure 2-6. Oxygen (99.5% purity) enters at the tuyeres. It gasifies the carbon carriers in the raceway area similarly to the BF. The generated hot gas ascends through the char bed into the dome area and exits as generator gas (1050°C, GOD ~20%). The solids are charged from the top (except fines charged by the feed ducts closely above the char bed and pulverized coal injection [PCI] from tuyeres). The HCl and coal briquettes are centrally charged, which leads to the formation of a hotter edge zone and a cooler centre. The coal is pyrolysed in the upper char bed, and volatiles and tar crack due to the high dome temperature (>1000°C). The ferrous material and additives melt first; liquid slag and metal phases lead to a cohesive zone similar to that seen in the BF. In the hearth, the final slag is formed (high Al₂O₃ and MgO content, low FeO content) and the hot metal is carbonized to its final properties. The products are tapped periodically.

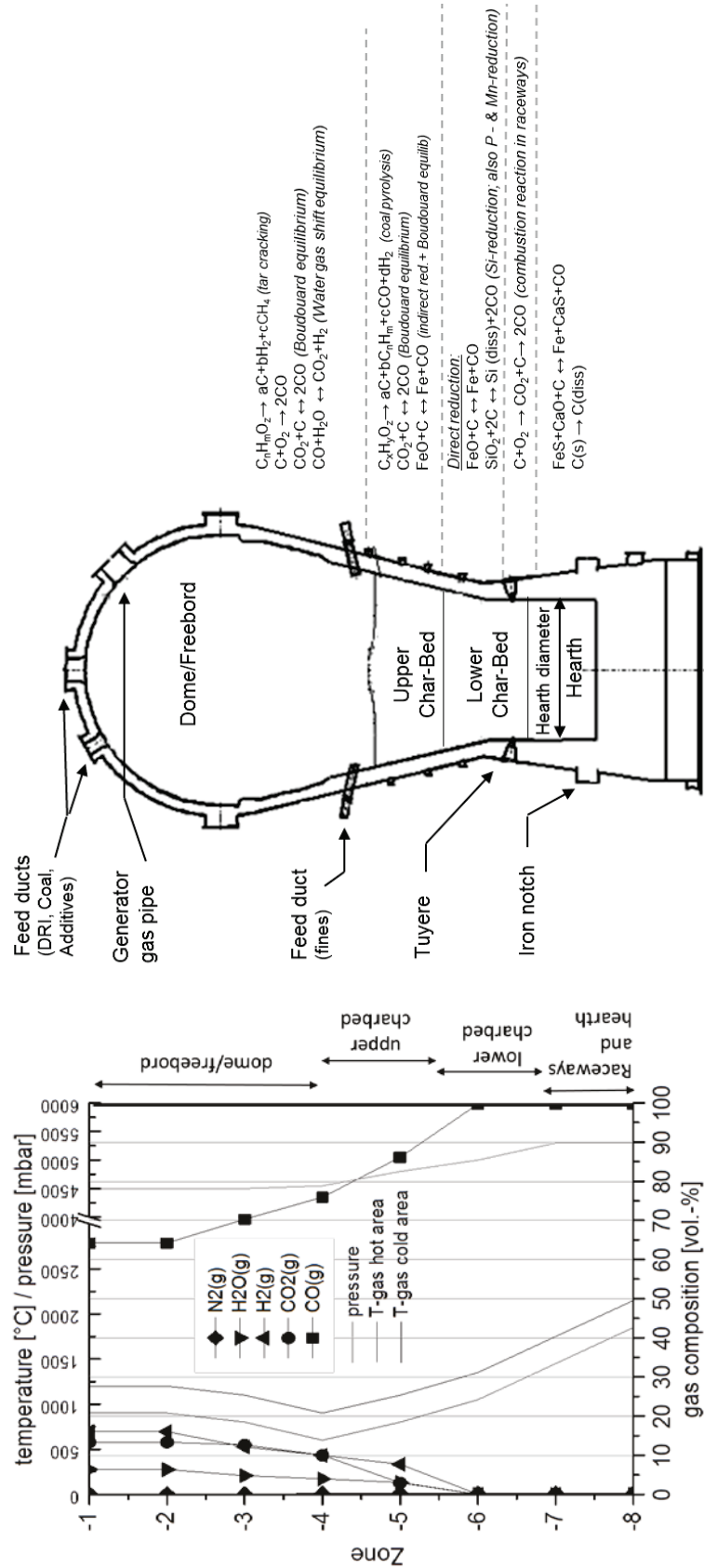


Figure 2-6: Layout of the melter gasifier, including the chemical reactions (top) and process parameters like temperature, pressure and gas profile for each zone (bottom) ⁵⁵

In Figure 2-6 (right) and Table 2-2, the process parameters are shown. These are also the basics for the development and calculation of the standard model for the melter gasifier. For additional information regarding mass and energy balance and the technological layout of the COREX® and FINEX® processes, see the literature^{30,46,55–58} and the calculations in Chapter 4.3. Actually, seven COREX® (RSA, IND, CN) and three FINEX® plants (KOR) are in operation, with annual outputs ranging from 0.8–2 mio.t.

Table 2-2: Typical process condition of melter gasifier derived from literature: A basis for the standard melter gasifier model^{53,59}

Ore consumption	1300–1650 kg/tHM	Coal rate	700–1200 kg/tHM
Fuel rate	500–1500 kg/tHM	Coke rate	0–100 kg/tHM
Slag basicity	1–1.4	Melting rate	80–160 tHM/h
Tuyere oxygen volume	36000–60000 m ³ /h approx. 1700 m ³ /tHM	Generator gas	64–70% CO, 2–9% CO ₂ , 19–23% H ₂ , 4–5% H ₂ O, 0– 3% CH ₄
Slag volume	315 kg/tHM		

OxiCup® process: This process was developed as an internal recycling process to recycle ferrous and carbon-bearing dust (e.g. top gas sludge, dust from sinter and steel plant, top gas dust, etc.). The dust is agglomerated with carbon to form a self-reducing briquette. These briquettes are charged concurrently with another lumpy iron carrier (e.g. steel plant buttons, broken slags, etc.) in a shaft furnace. Like in the BF, a hot blast is blown into the reactor by the tuyeres. As products, hot metal and slag are tapped. From the metallurgical point of view, the working of the OxiCup® process is somewhere between a melting reactor (cupola furnace) and a reduction and melting reactor (BF). For further information concerning technological details, see Senk et al.⁴⁰ At present, four plants with a daily output of 500–2000 tHM/day are in operation.

Other processes of smelting reduction either are in development (Hisarna,⁶⁰ etc.) or have been shut down (e.g. Hismelt® with an annual production of 0.8 mio.t until 2006⁶¹).

2.1.5 Alternative Routes of Ironmaking

The focus on carbon-free ironmaking has led to disruptive new concepts for ironmaking reactors in the last few decades. Electrolysis and H₂-plasma reduction are only two examples.

Metal production by electrolysis is a well-known technology in metallurgy. However, it has not had its breakthrough for iron production yet. Electrolysing facilities based on alkali solutions or liquid slag have been developed. The dissolved iron ions are reduced by electrical current. Although electrolysis seems to be an elegant method of iron production, actual investigations have pointed out the problems of this technology with regard to high energy consumption, low efficiency, and fluid dynamics.^{62–64}

Finally, the production of iron and steel by H₂-plasma shall be highlighted. Research work has already been performed successfully using thermal plasma, which creates ionic H⁺ or atomic H from molecular H₂ for the reduction and supplies the heat for the melting. Liquid iron or steel can be produced with low carbon content. Low-temperature plasma by microwaves also presents an opportunity for the reduction to sponge iron. Although the concepts are possible for lab-scale reactors, a scaling up to a pilot plant has not been done yet.^{65,66}

2.2 Fundamentals of Ironmaking

Ironmaking involves two steps to achieve the metal stage. First, the iron compounds (e.g. oxides, hydroxides, carbonates, etc.) have to be reduced to the metal form. In general, this can be achieved by a reaction with carbon or hydrogen. Second, the non-metallic compounds need to be separated from the metal. Nowadays, this is achieved by melting. In most cases, two liquid phases will form. This enables separation of the liquid metal from the slag phase as a result of the differing densities. Subsequently, the basics of ironmaking reactions are discussed, followed by the production of metallic iron.

2.2.1 Thermodynamics of Reduction Processes

The laws of thermodynamics are the main fundamentals of modern physical chemistry. They also form the basis of metallurgy. These axioms help to interpret and connect such discrete terms as heat, temperature, and energy. They also constitute the boundary conditions for reactions in a closed system. The following section, in connection with additional literature, provides an introduction to the fundamentals of thermodynamics.^{67,68}

Zeroth law of thermodynamics:

*If two systems are both in thermal equilibrium with a third, then they are in thermal equilibrium with each other.*⁶⁹

The zeroth law of thermodynamics leads to the existence of a state variable that describes an axiom and an independent (path-independent) parameter in thermodynamics, the temperature T . In practice, it will lead to the thermic balance (same temperature) of two or more independent systems, if they get connected. The zeroth law was added to the other three laws as a fundamental idea.⁶⁹

First law of thermodynamics:

*Law of Conservation of Energy: Energy cannot be created and destroyed in chemical reactions.
(Mayer, Joule)*

The first law of thermodynamics describes the equivalence of energy and heat. The sum of energy in an isolated system is constant. It can only be changed by outer influences. In simple terms, it can be expressed by Equation 2-1:

$$\Delta U = \Delta Q + \Delta W \quad 2-1$$

The change of inner energy ΔU can be enlarged by $\Delta Q = m c_{p/v} \Delta T$ as an expression of the thermic energy flow and $\Delta W \approx \delta W = \delta p \cdot \delta V$ as an expression of the added mechanic energy (see Boyle's law of gases⁷⁰). For metallurgical reactions, it defines the parameters pressure, volume, temperature, and specific heat capacity as interacting variables (although the heat capacity is mainly known as material constant, it varies depending on the temperature in isotherm or isobar systems).^{69,70} Derived from the first law, the energy consumption or release of a chemical reaction can be calculated. The enthalpy H defines the sum of energy as a state function ($U+p \cdot V$) and as path-independent (the enthalpy depends only on the start and final conditions of a

system, not on the process, as per Hess's law). To sum up, the enthalpy defines the energy of a phase and of chemical reactions by Equation 2-2.

$$\Delta H = \sum H_{End} - \sum H_{Start} \quad 2-2$$

Second law of thermodynamics:

The entropy of an isolated system always increases. (Clausius, Thomson, Plank)

The second law of thermodynamics describes the irreversibility of natural processes and contributes information in addition to the first law. To define the direction of a chemical reaction, a variable has to be added—the entropy S. Mathematically, the entropy S is defined by Equation 2-3:

$$\Delta S = \frac{\Delta q}{T} \quad 2-3$$

This equation shows the heat flow Δq in an isolated system at a certain temperature T based on the statistical thermal movement of particles ($S=k \cdot \ln(W)$).⁷⁰ This movement contributes the basic idea of the second law that $\Delta S \geq 0$.

Third law of thermodynamics:

The entropy approaches zero at $T = 0$ K. (Berthelot, van Hoff, Nernst)

The third law of thermodynamics states that all substances have a positive value for the entropy at temperatures above 0 K (mathematically, $\lim_{T \rightarrow 0} S = 0$). The entropy at absolute zero is zero for a perfect crystal structure; every phase transformation is characterized by $\Delta S > 0$.

Based on the law of thermodynamics, the change in chemical compositions, reactions, and equilibria can be derived. Therefore, a connection between enthalpy H and entropy S was defined, called the free enthalpy G, which gives the thermodynamic potential of a system. It is the driving force that causes a reaction. Mathematically, it is defined for isotherm systems by Equation 2-4 (Gibbs equation).^{69,70}

$$\Delta G = \Delta H - T \cdot \Delta S \quad 2-4$$

Natural processes always try to minimize this ΔG ; depending on $\Delta G > 0$ or $\Delta G < 0$, reactions are endergonic or exergonic.⁷⁰ The Gibbs energy G for a chemical reaction is the thermochemical basis for all metallurgical reactions.

The Gibbs energy (or free enthalpy), as the ultimate force for chemical reactions, is linked by the equilibrium constant K to the following important factors of thermodynamics: the partial pressure p and the activity a (both expressions for the chemically active concentration of a reaction participant). The partial pressure is equal with the activity of an ideal gas. First, K is defined by Equation 2-6, wherein a_A and a_B are the activities of the reactants and a_C and a_D are the activities from the products. The reaction partners are shown in Equation 2-5 with A and B as reactands and C and D as products. A,B,C,D are the chemical symbols and a,b,c,d are the corresponding stoichiometric coefficients.



$$K = \frac{a_C^c \cdot a_D^d}{a_A^a \cdot a_B^b} \quad 2-6$$

Independent of the state of the reactants and products, the equilibrium constant k is the quotient of the activities for gaseous, liquid and solid matters. For a system at equilibrium, the Gibbs energy for the reaction is defined as

$$\Delta G_r = -R \cdot T \cdot \ln K_{equ} \quad 2-7$$

For further information according to thermodynamic fundamentals, see Froberg,⁶⁹ Bodgandy,^{71,72} and Eucken.⁷³

To describe the reduction reaction to iron, the fundamental equations focus on the interaction between the oxide and metal phases. Due to the natural origin of metals as oxides (only rarely as sulphides, chlorides, etc.), the main reduction reaction is given in Equation 2-8.



Due to the impact of the gaseous oxygen, the pressure (especially the partial pressure p^* of O_2) plays a major role during the production of metals. By enlarging the correlation of Equation 2-6 with the partial pressure, the equilibrium constant will transform into

$$K = \frac{a_{Me_xO_y}}{a_{Me}^x \times \left(\frac{p_{O_2}}{p_{tot}}\right)^{\frac{y}{2}}} \quad 2-9$$

Assuming that the matter consists of standard conditions (pure substances; activity of metal and oxide compound is one; p_{tot} of the system is 1 bar), the equation can be simplified to Equation 2-10 (followed by the connection of K with the Gibbs formula).

$$\Delta G^0 = -R \cdot T \cdot \ln \frac{1}{p_{O_2}} = R \cdot T \cdot \ln p_{O_2} \quad \text{with} \quad K = \frac{1}{p_{O_2}} \quad 2-10$$

This ΔG^0 is known as the oxygen potential (also see sulfur potential [$R \cdot T \cdot \ln p_{S_2}$] and nitrogen potential [$R \cdot T \cdot \ln p_{N_2}$]).⁷⁴ For chemical reactions, it is found that low values for the enthalpy of the reaction lead to stable products. In particular, metals with a very negative oxygen potential form very stable oxides. The different elements (e.g. metals and their corresponding oxides) can be combined with the oxygen potential at different temperatures in a Richardson-Ellingham diagram. Noble metals (gold, copper, nickel) are characterized by high oxygen potentials. They are found in the upper part of the diagram and form oxides of low stability. Reactive metals like calcium and magnesium are located at the lower part of the diagram. They form very stable oxides and have a low oxygen potential. Generally, the Richardson-Ellingham diagram gives fundamental information about physical chemistry.

- The y-axis shows the free energy of the reactions for elements with one mol O_2 to corresponding oxides.
- The gradient of the curves gives information about the entropy (in general, entropy decreases for all reactions except $2C + O_2 \leftrightarrow 2CO$).
- The transformation temperatures (melting, boiling, and sublimation) are connected with a change in the gradient.
- The partial pressure of oxygen and, consequently, the ratios for H_2/H_2O and CO/CO_2 can be changed (see axis in Figure 2-7 on the right). This leads to other values for the free enthalpy and changes the stability areas in the diagram.
- It has to be considered that the diagram is standardized for 1 mol O_2 , and that the activity of metals and oxides is 1.

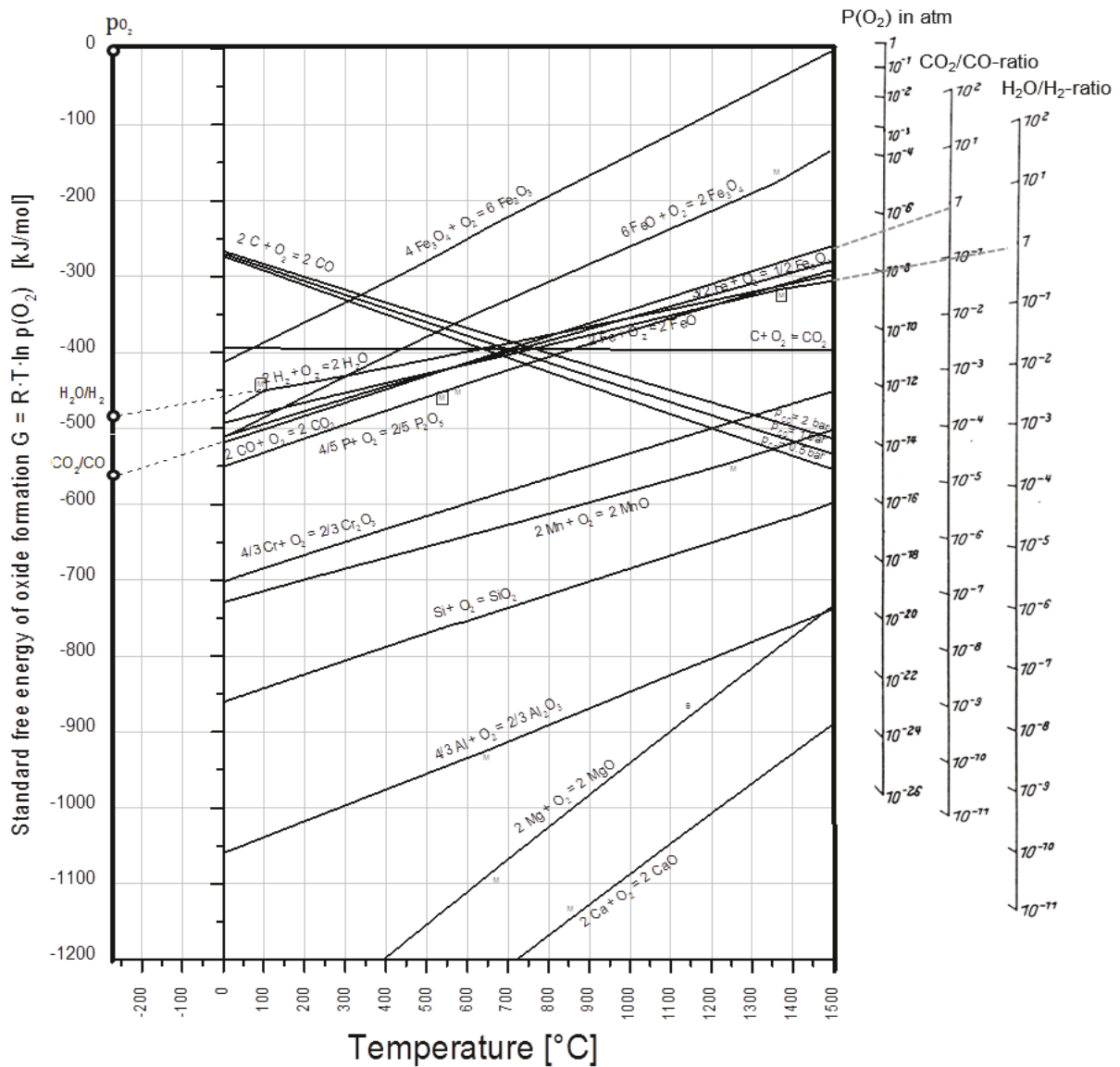


Figure 2-7: Richardson-Ellingham diagram for the most important metals, oxides, and gases in ironmaking reactors (data from Factsage 7.0⁷⁵)

Figure 2-7 shows the Richardson-Ellingham diagram, including the most important elements for ironmaking reactions. The axes show the temperature and the standard free energy of oxide formation in kJ/mol O₂ (also called the oxygen potential). The ordinate also shows the formation energy for H₂O(g) and CO₂(g) for a temperature of -273.15°C. The intersection of axes also points (0/0) to the origin for the oxygen partial pressure identification. Starting with these three points, for each temperature and reaction, the equilibrium composition of CO₂/CO and H₂O/H₂ as well as the oxygen partial pressure p(O₂) can be determined (see axes on the right side of the diagram). The equilibrium lines for the formation reaction of the four main slag-forming compounds (Ca, Si, Al, Mg) are located in the lower part. In the upper part, the formation equilibrium lines for the iron oxides are shown, as well as the reactions of hydrogen, carbon, and carbon monoxide with oxygen. From the crossings of the Fe-FeO with the Fe-Fe₃O₄ the wuestite point (also see Figure 2-9) can be derived. Moreover, the Boudouard equilibrium (see Equation 2-21) can be determined at the crossing of C-CO, C-CO₂, and CO-CO₂. The dependency of this

reaction on the pressure can be seen for the different partial pressures of CO in the equilibrium line C-CO (higher pressure leads to less ΔG). The melting (M) and boiling (B) temperatures are included in the diagram (framed for oxide). The change in state also leads to other specific values for entropy, and, therefore, to different free energies and gradients in the Richardson-Ellingham diagram (see H₂/H₂O line for 100°C). Summing up, the diagram shows the reduction of iron oxides by carbon and hydrogen at temperatures >800°C as well as the stability of Si-, Ca-, Al-, and Mg-oxides up to 1500°C.

2.2.1.1 Direct and Indirect Reduction of Iron Ores

Due to the important role of the oxygen partial pressure in ironmaking reactions, the interaction between iron and oxygen has to be considered. Therefore, the binary system Fe-O (Figure 2-8) illustrates the stability of different phases at different oxygen contents. Iron occurs in several oxidation stages, mostly as Fe³⁺, Fe²⁺, and Fe⁰ (rarely Fe⁶⁺).³⁷ Derived from these levels of oxidation, different compounds are formed by decreasing oxygen contents as Fe₂³⁺O₃²⁻ (hematite), Fe₂³⁺O₃²⁻ · Fe²⁺O²⁻ (magnetite), Fe²⁺O²⁻ (wuestite), and, finally, metallic iron Fe_{met}⁰.

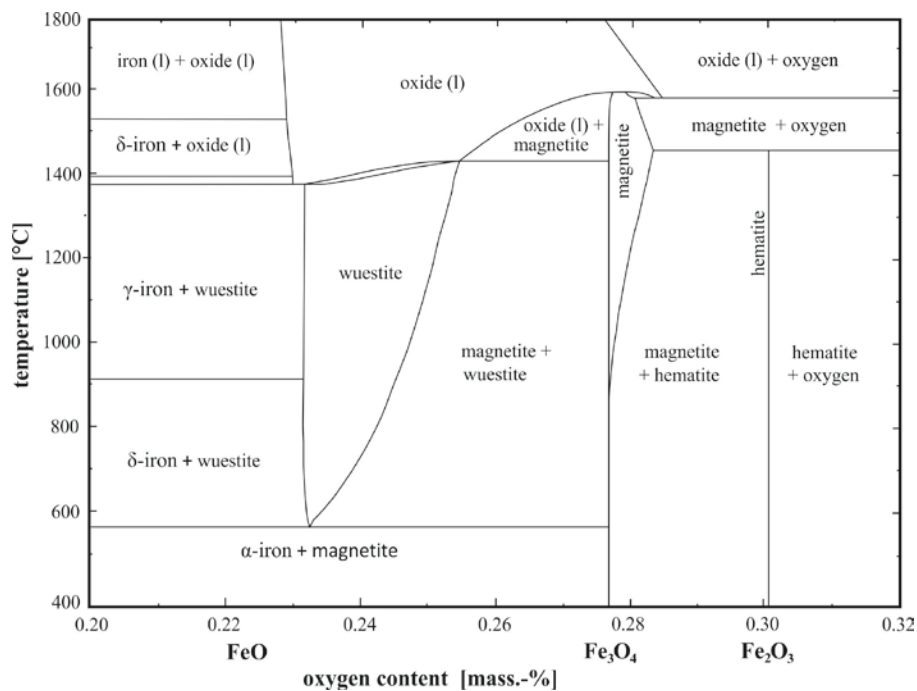
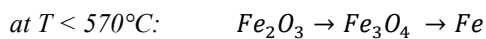
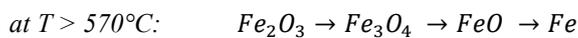
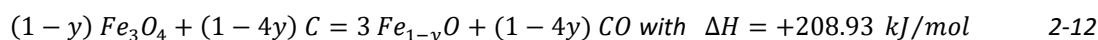
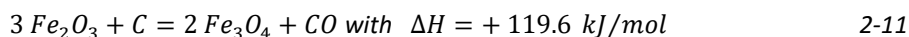


Figure 2-8: Phase diagram iron and oxygen⁷⁶

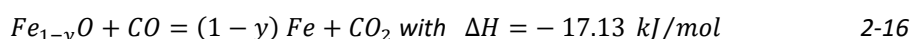
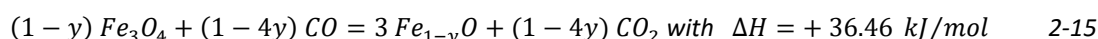
The increase in oxygen content has a great influence on the reduction path. So, the reduction of iron ore is defined as the oxygen removal of an iron oxide to its subordinated oxidation state by a more oxygen-affine reducing agent. For industrial applications, the take-out by carbon or hydrogen is the most economical way, and it is performed according to the Fe-O binary system:



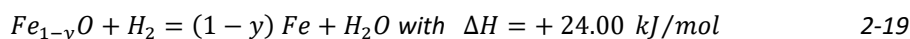
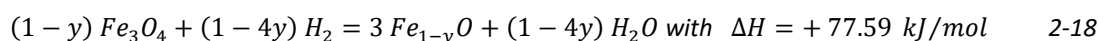
Depending on the state, reduction is grouped into direct and indirect reduction. Direct reduction is carried out by solid or dissolved carbon. The product gaseous CO is formed. The reduction of hematite to metallic iron (>570°C) is given by Equations 2-11 to 2-13.³⁷ For the reactions with wuestite (FeO), the formula is adapted to its non-stoichiometric bond of Fe and O.⁷⁷



Direct reduction is characterized as a highly endothermic reaction. Furthermore, the reaction rate between solid carbon and oxide is kinetically inhibited due to the small reaction surface. In contrast, indirect reduction is energetically and kinetically favoured. Given the gaseous state of CO and CO₂, the reduction is accelerated and the reaction enthalpy is lowered. Equations 2-14 to 2-19 show the way in which hematite transforms to metallic iron by the indirect reduction with carbon monoxide and hydrogen. In addition, the differences in reaction enthalpy between CO and H₂ are mentioned. In general, all these indirect reduction reactions are reversible and depend on the temperature.^{71,72} In a CO atmosphere, the reduction reactions are:



Similarly, the reduction with H₂ is achieved by:

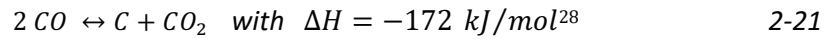


Caused by a constant gas volume (no volume change between gaseous reactant and product), the total pressure has no influence on the reaction process and the gas ratios can be set in relation easily. However, the dependence on pressure for iron oxide reduction is a matter of debate among several authors.^{78,79} One method of depicting the interaction of the reducing and oxidizing gases is the Baur-Glaessner diagram. It shows the stability regions for certain iron oxides in relation to the temperature and the gas composition (GOD). The GOD indicates the reduction force of the gas and it can be calculated by Equation 2-10.

$$GOD = \left(\frac{x_{H_2O} + x_{CO_2}}{x_{H_2} + x_{H_2O} + x_{CO} + x_{CO_2}} \right) \text{ with } x_i \text{ being the molar ratio of the gas component } i \quad 2-20$$

The Baur-Glaessner diagram (see Figure 2-9) shows the equilibrium lines for the reactions with H₂ (grey) and CO (black). For gas mixtures, the equilibrium line is between a pure H₂/H₂O atmosphere (left for T <800°C, right for T >800°C) and a pure CO/CO₂ atmosphere (right for T <800°C, left for T >800°C). At a temperature of 800°C, the reduction forces of hydrogen and carbon monoxide are equal.¹⁹ On the left side, with a low GOD (high reduction potential), metallic iron will form as a stable phase. On the right, magnetite will be formed at a higher GOD. The highest oxidation stage of iron (hematite) is seen as the line phase at GOD=1. In the middle, wuestite is the most stable phase for T >570°C. An additional important relation considered in the Baur-Glaessner diagram is the Boudouard reaction (see Equation 2-21). This adds the

stability of C, CO, or CO₂ according to the CO/CO₂ ration and the pressure (caused by different molar volumes of CO and CO₂ in the reaction). For a total pressure of 1 bar, the equilibrium is shown in Figure 2-9 as a dashed line. For higher pressure, this relation shifts to higher temperatures; for lower pressure, it moves to lower temperatures. For practical use, this means that, for example, at low temperatures and low GOD, the formation of carbon and CO₂ out of CO is favoured, and the gas composition moves to a higher GOD automatically.²⁸



In that context, the reduction degree (RD) and the metallization degree (MD) specify the progress in reduction and metallization from the oxide to the metal according to Equations 2-22 and 2-23:

$$\text{RD} = \left(1 - \frac{X}{1.5}\right) \cdot 100 \quad \text{with } X = \frac{O}{\text{Fe}_{\text{tot}}} \quad (\text{in } \%) \quad 2-22$$

$$\text{MD} = \frac{\text{Fe}_{\text{met}}}{\text{Fe}_{\text{tot}}} \cdot 100 \quad (\text{in } \%) \quad 2-23$$

To get a better understanding of these settings, the following outcomes can be determined: For hematite, both the RD and the MD are zero (GOD=100%); for the pure metal, the reduction and MDs are 100% (GOD=0%). The interim steps, which are reached continuously, form magnetite (RD=11%, MD=0%) and wuestite (RD=33%, MD=0%). The reduction and MDs are directly linked to the mass loss, which is depicted in Figure 2-10.

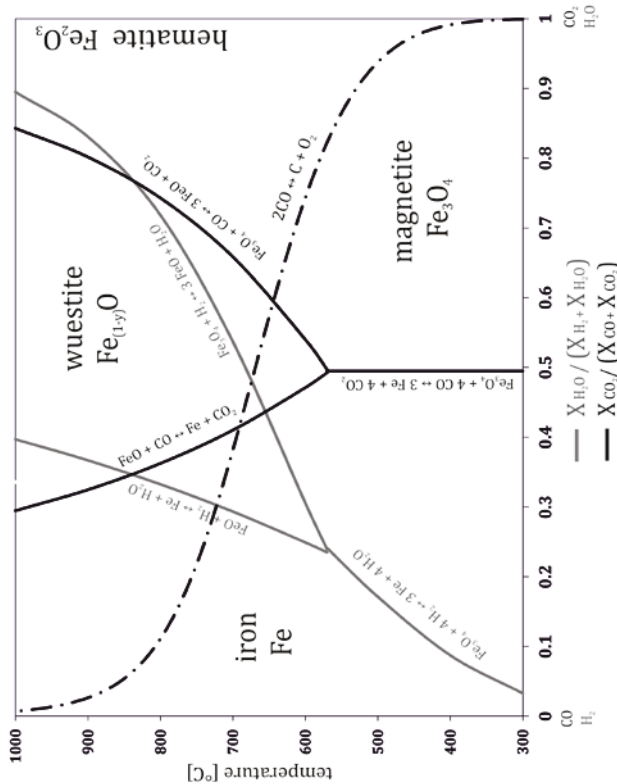


Figure 2-9: Baur-Glaessner diagram for CO/CO₂ and H₂/H₂O mixtures⁸⁰

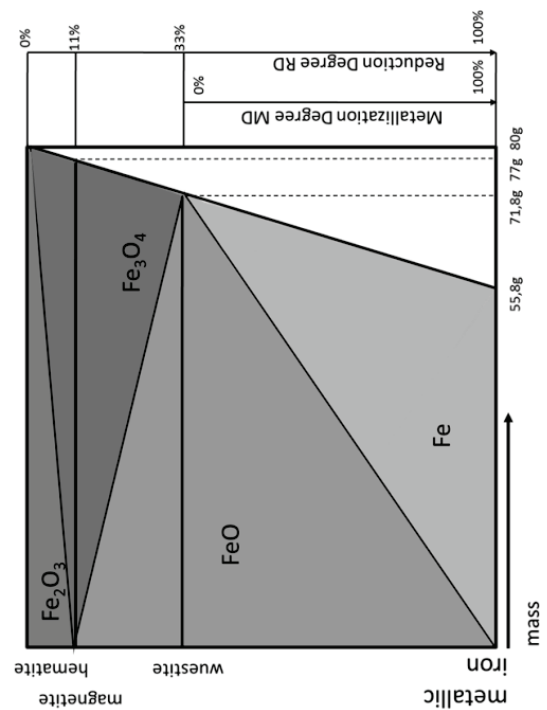


Figure 2-10: Mass loss for iron and iron oxides during reduction in relation to RD and MD⁸¹

2.2.2 Kinetics of Iron Ore Reduction

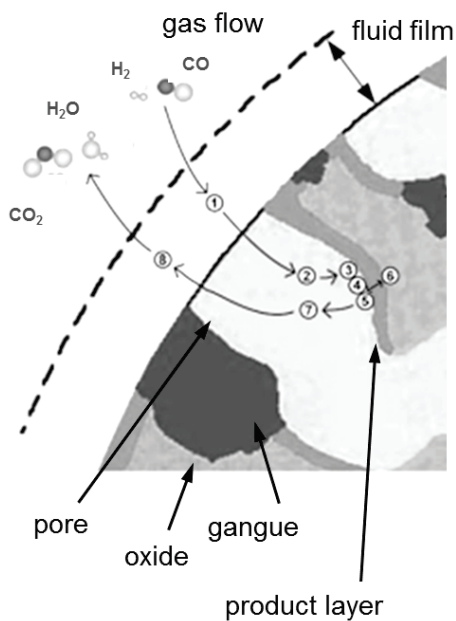
In addition to the laws of thermodynamics, which define if a reaction will take place, kinetics delivers information about the reaction rate. Mechanisms like mass transport by diffusion, specific surface area, and so on, are linked to the total reaction process. These key factors are linked to equilibria that try to describe these important kinetic aspects. The most important values are the mass flow in general (see Fick's first law in Equation 2-24) and the mass transfer through an interface or boundary layer (see diffusion flow with the mass transfer coefficient β in Equation 2-25):^{82,83}

$$j = -D \cdot \frac{\Delta c}{\Delta x} \quad 2-24$$

$$j_{interface} = \beta \cdot (c_i^g - c_i^p) \quad 2-25$$

Here, the mass flow is defined as j [mol/(m²·s)] and the mass flow through an interface as $j_{interface}$ [mol/(m²·s)]. The diffusion coefficient (diffusivity) D [m²/s] is a function of temperature, activation energy, and a standard diffusivity. It can be seen as a material characteristic property. The mass transfer coefficient β is derived from the diffusivity and it describes the conditions for interface transfers. For Equation 2-24, the variables are Δc , which describes the difference in concentration between c_1 and c_2 [mol/m³], and Δx , which represents the diffusion length between point 1 and point 2 [m]. For the interface diffusion, c_i^g shows the concentration in the gas phase and c_i^p the concentration at the particle's surface [mol/m³]. Derived from these general considerations, the characteristics of dense and porous particles will be examined in specific.

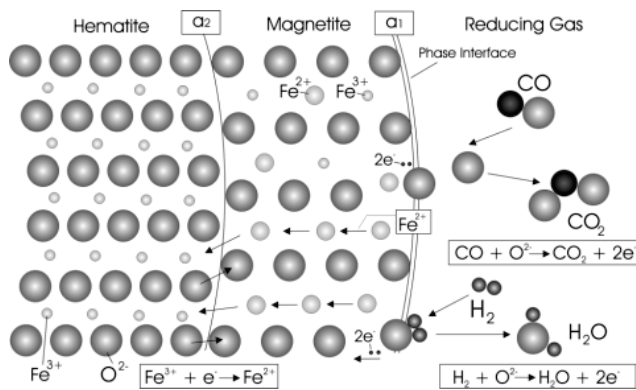
Porous and dense particles: The indirect reduction of iron ores is a typical example of a solid-gaseous reaction, where the solid iron-bearing fraction is separated from the gas phase by a boundary layer. The gas phase transports the reducing gas (CO, H₂) as well as the gaseous products (H₂O, CO₂). With regard to the gaseous-solid reaction, the following have to be mentioned if the particle has a porous or dense structure.



1. Transport of the reducing gas (CO, H_2) by convection and diffusion from the free gas phase and through the laminar layer (fluid film) to the interface
2. Transport of the reducing gas through macropores and micropores to the inner surface
3. Adsorption of the gas molecule
4. Chemical reaction and removal of oxygen from the crystal lattice (for further information see Hofbauer⁸³)
5. Desorption of gaseous product ($\text{H}_2\text{O}, \text{CO}_2$)
6. Solid phase diffusion of the solid reaction products to the nuclei, including nucleation and growth of product layer
7. Diffusion of the gaseous reduction product through micropores and macropores
8. Transport through the laminar layer to the gas stream

Figure 2-11: Kinetic mechanisms of iron ore reduction for porous particles^{71,72}

In general, porous particles show a reaction through the total particle. Gas diffusion and chemical reaction at the inner surface area, which can be reached easily by the reducing gas, are closely linked. However, the total kinetic reaction is divided into several steps (see Figure 2-11); the part with the highest resistance is called the limiting step.^{82,84-87}



1. Transport of the reducing gas by convection and diffusion from the free gas phase to the reaction area
2. Phase interface reaction of the reducing gas
 $\text{H}_2 + \text{O}^{2-} \rightarrow \text{H}_2\text{O} + 2\text{e}^-$
 $\text{CO} + \text{O}^{2-} \rightarrow \text{CO}_2 + 2\text{e}^-$
3. Diffusion of the iron cations and the electrons caused by different iron activities (α_1 and α_2)
4. Reaction at the internal phase interface
 $4\text{Fe}_2\text{O}_3 + \text{Fe}^{2+} + 2\text{e}^- \rightarrow 3\text{Fe}_3\text{O}_4$
 $\text{Fe}^{3+} + \text{e}^- \rightarrow \text{Fe}^{2+}$
5. Gaseous products (CO_2 and H_2O) migrate back to the emulsion phase

Figure 2-12: Kinetic mechanisms of iron ore reduction for dense particles⁸⁸

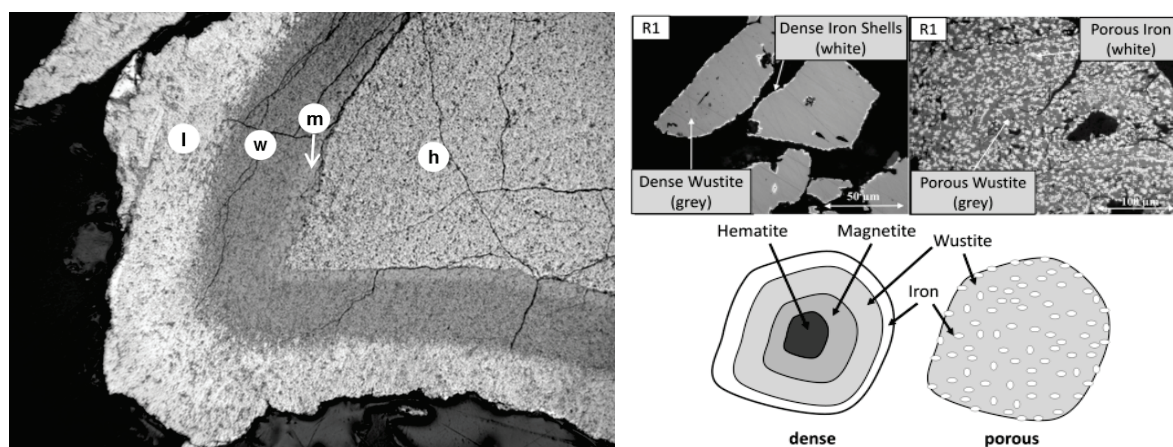


Figure 2-13: Exemplary pictures of a dense hematite particle, including the defined interface areas (left) and a comparison between dense and porous particles after reduction^{80,84,89}

According to the kinetics, dense particles show a different picture of the reduction mechanism. There, the reduction gas is unable to permeate through the dense structures. Instead, electrons and ions (oxygen, iron) move from inside to the reaction location at the phase interface (see Figure 2-12). In general, the reaction takes place in defined interfaces between two different phase layers. Consequently, the oxidic and metallic layers grow into the grain. Exemplary pictures can be seen in Figure 2-13. The left picture shows a dense hematite lump ore after CO reduction with the defined interfaces between metallic iron (light outer layer), wustite (medium grey), magnetite (light grey), and the still hematite core. The right side shows a comparison between a dense particle (formerly magnetite) and a porous particle (formerly limonite) after reduction under fluidizing bed conditions. The contrast is similar to the theoretical models that are described in the literature (see the schematic pictures on the right from Chatterjee⁸⁴).

Kinetic models (shrinking core and progressive conversion): Depending on the specific effect of the single steps on the total kinetic reaction, several models were developed to describe the total mechanisms and, specifically, to determine the limiting step. In the field of iron ore reduction, the kinetic model of the shrinking core is favoured (rather than the model of progressive conversion). It is characterized by the reaction of the reduction gas at the particle surface, which leads to the formation of an ash layer. The ash or product layer is mostly porous and it allows a fast mass transport of the reaction gases. The core is still original, non-reacted material. The product layer grows towards the centre of the particle and the core shrinks. However, this model simplifies the complex kinetic mechanisms (for further information, see Szekely and Evans⁹⁰).

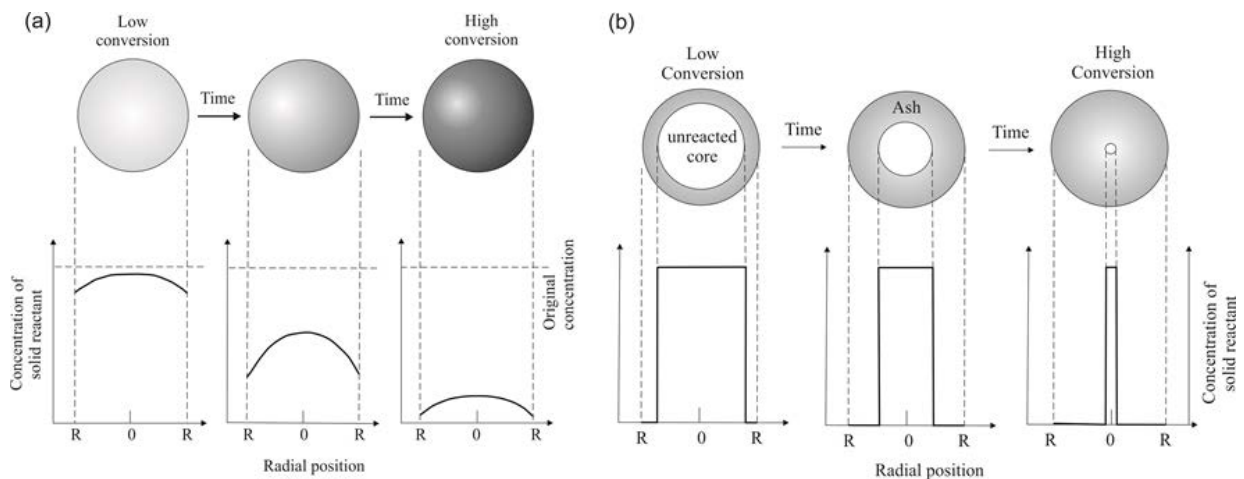


Figure 2-14: Kinetic models of progressive conversion (a) and shrinking core (b), including the concentration profiles of the solid reactant^{80,91}

The model of progressive conversion pictures particles that do not change their size during reduction and that often have dense outer layers of the product. For more precise information according to the shape and concentration profile of the gas phase during reaction, see Figure 2-14. It shows the slow diffusion in Model (a) and a higher gradient over the particle diameter. Model (b) is characterized by fast diffusion and a big gradient on the phase boundary of the reacted and unreacted layers. The particle diameter is named R . Both models are useful for the determination of the limiting step, which controls the total reaction speed (limitation by diffusion, boundary layer or chemical reaction).

Diffusion-limited: A diffusion-limited process is characterized by a concentration gradient of the reacting gas between the outer gas film and the reaction area at the inner surface. A schematic description is shown in Figure 2-15 for both dense and porous particles. It depicts the concentration of the gaseous compound (e.g. CO) over the particle diameter. The exchange between core (C_{Ac}) and gas stream (C_{Ag}) is inhibited. A gradient is formed. In that case, the diffusion in the gas film is seen as higher than through the ash layer; the concentration of the compound is equal between the gas phase and the particle surface ($C_{Ag}=C_{As}$). If the reaction is inhibited by diffusion, an increase in the pressure, concentration gradient, or temperature can accelerate the total process.

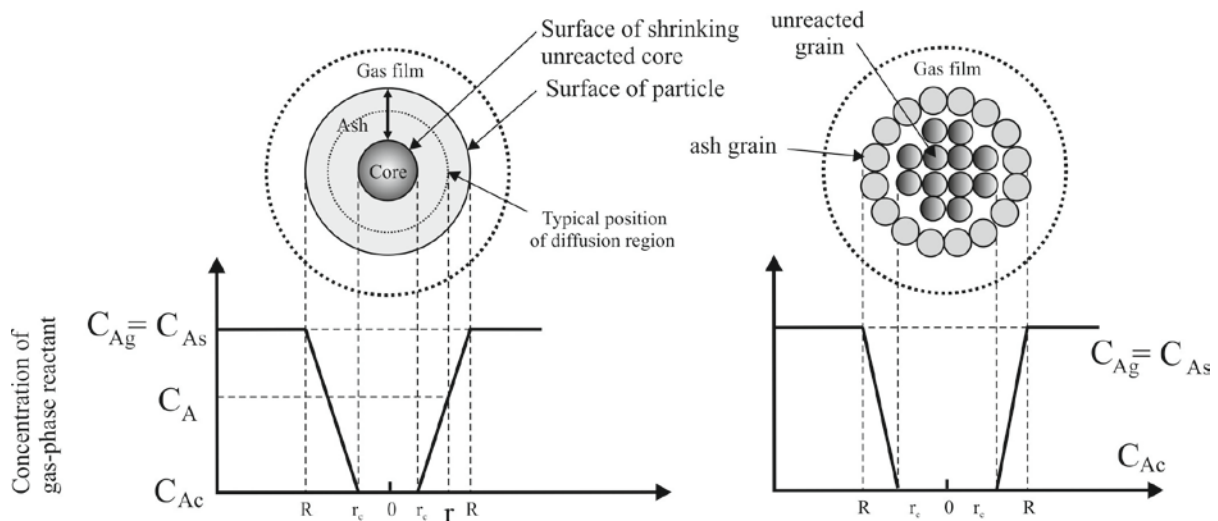


Figure 2-15: Schematic picture of the solid particles and the gas-concentration profiles for diffusion-limited processes for a dense (left) and a porous (right) particle⁸⁰

Chemical reaction-limited: For chemical-limited processes, the reaction has no concentration gradient from the gas flow to the reaction area. The mass transport through the boundary layers is fast and the limiting step is the chemical reaction itself. The total process can be faster if the chemical reaction is accelerated (e.g. by temperature increase—see Arrhenius and Equation 4-3). A schematic figure of the particles, including the gas profile, is presented in Figure 2-16. The exchange of gas compounds between the gas stream (C_{Ag}) and the core surface (C_{Ac}) is faster than the reaction at the phase boundary of the ash layer and the core. This fast exchange leads to the same composition of the gas phase over the particle diameter.

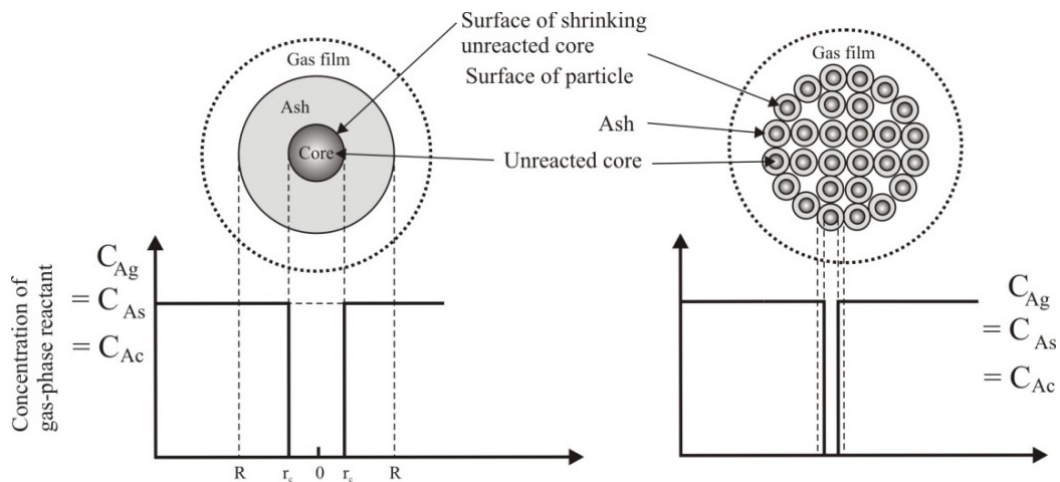


Figure 2-16: Schematic representation of the solid particles and the gas-concentration profiles for reaction-limited processes for a dense (left) and a porous (right) particle⁸⁰

For additional information on the kinetics in iron ore reduction, see Oeters.⁸²

2.2.3 Softening and Melting

In addition to thermodynamics and kinetics, the physical processes of softening and melting play a major role in ironmaking reactors. The hot metal and slag formation affects the pressure and gas performance of the whole process, particularly in the cohesive zone. Both metal and slag are first formed by the ferrous burden materials. So, their composition and properties have an influence on the formation of the first liquid phases—the so-called primary slag. The basicity is often acid, due to the natural composition of gangue phases (high SiO_2 and Al_2O_3 content) and it has a higher content of FeO . The first liquid phase forms in the upper cohesive layers. In the lower layers of the cohesive zone, artificial material like sinter and additional fluxes (lime, dolomite) get dissolved in this acid primary slag. The slag basicity rises and the bosh slag is formed. Here, the FeO content is already low because of the further reduction to Fe_{met} . The basicity is higher than for the final slag. The final slag is created in the BF hearth by the dissolution of the remaining acid slag compounds (ash from PCI coal and coke) and the removal of FeO , MnO , and P_2O_5 from the slag phase by direct reduction. A comparison of materials with different basicity and composition is provided in Table 5-1 and Table 5-10.³⁵

A detailed view on the ferrous burden materials shows that the first melt forms from the phase with the lowest T_m . This point is often linked to a higher concentration of SiO_2 and FeO , in general, and alkalis, in particular. In most cases, the first melt is formed by 40% FeO and 60% gangue at a temperature of 1100°C . Of

course, these compositions depend on the burden charging (e.g. BF with higher sinter rates or fluxed pellets). The investigations for this research on the influence of alkalis on the softening or melting behaviour confirm this temperature and deliver additional information (see Chapter 5.4). After the first melt is formed, the bed collapses intermediately. Simultaneously, the permeability and pressure drops. Between temperatures of $1200\text{--}1350^\circ\text{C}$, the permeability decreases significantly (for temperature and pressure drop in the cohesive zone, see Figure 2-17). In this context, hydrogen has to be mentioned. It diffuses easily into compact structures and can continue reduction, even though the CO reduction has slowed down. Permeability is an

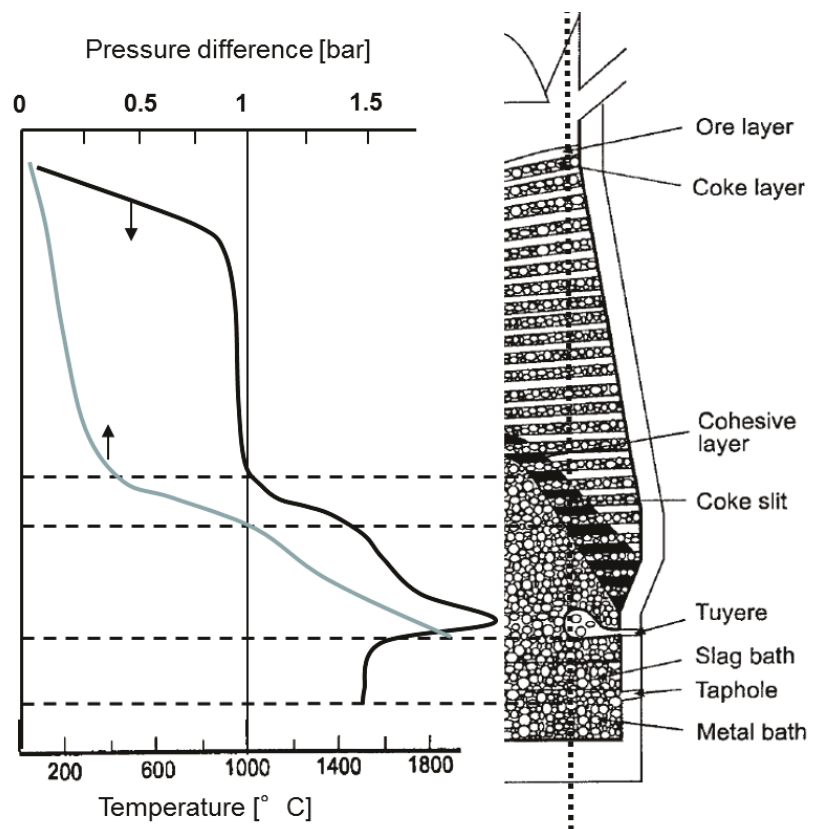


Figure 2-17: Layout of the blast furnace, including the correlation between temperature/pressure profile and softening/melting areas in the cohesive zone^{21,35,92}

important aspect for productivity. Fines from burden as well as low-melting phases can lead to disruptions in productivity. Prevention is possible through good screening work before charging and the lowering of degradation during the process (e.g. by less alkali load in the reactor and better mechanical prosperities of burden material, especially against low-temperature degradation reduction degradation index [RDI]).^{35,92} The formation of liquid iron becomes more complex in the melting process. Carbonization and reduction are major driving forces for the formation of hot metal. Both lower the melting point of the metal phase to approximately 1450°C. Carbonization in the hearth finally leads to a carbon content of 4.2–4.7% in the hot metal and, finally, tapping temperatures of ~1400–1450°C. In terms of melting behaviour, the usage of ternary systems is essential, especially if a look at oxidic systems is taken (see also Chapter 5.4). Ternary systems can visualize the stable compounds at a certain temperature (isothermal section) or demonstrate the melting points for certain compositions. For instance, Figure 2-18 shows an isothermal section at 1600°C and 1 bar for a CaO-SiO₂-Al₂O₃ system [CSA]. The corners are defined by the pure substances. Especially the high melting temperatures of CaO, SiO₂, and Al₂O₃ are clearly visible. For each mixture (axis show the wt-%), the stable compounds are mentioned. The areas of pure liquid (slag in the middle of the diagram) are shown as well as two phase areas. A second type of ternary system is depicted in Figure 2-19, where the liquidus lines for several different temperatures are visualized. In the special case of a CSF diagram, the lowest melting area is near the FeO corner. Starting with a small liquid area at 1200°C, the zone expands with increasing temperature.⁹³ The melting behaviour of oxides (CaO, SiO₂, Al₂O₃, FeO, and MgO, including all types of mixtures) in the cohesive zone and the effect of alkali oxides can be evaluated with such ternary systems (see Chapter 3.3).

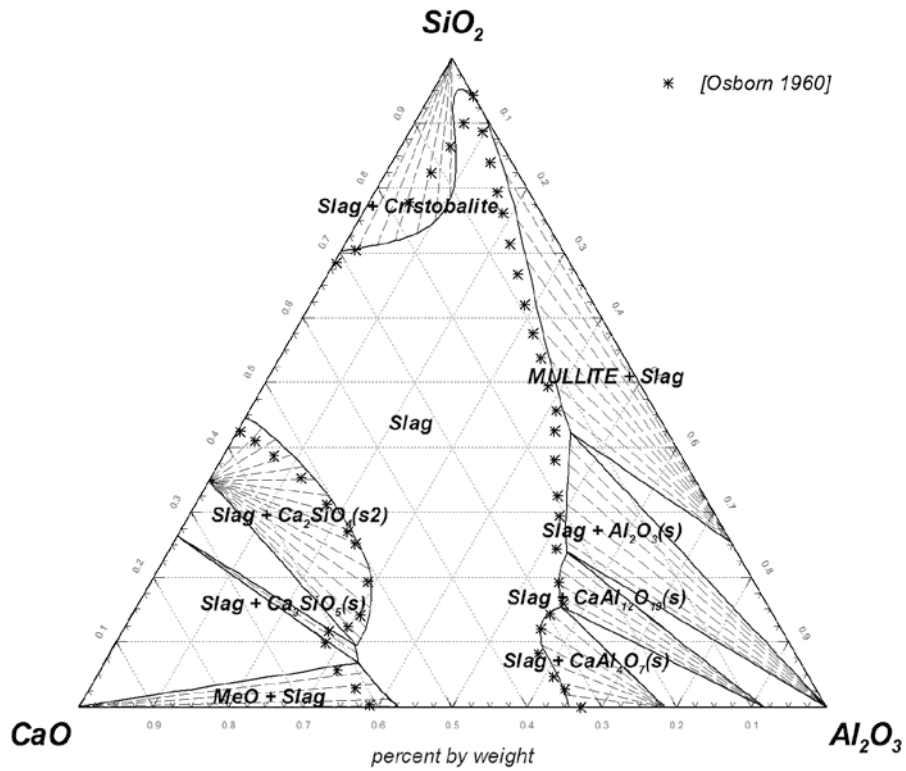


Figure 2-18: Ternary system CaO-SiO₂-Al₂O₃ (CSA) calculated by Factsage™ and compared with data from literature (isothermal section at 1600°C and 1 bar)⁹³

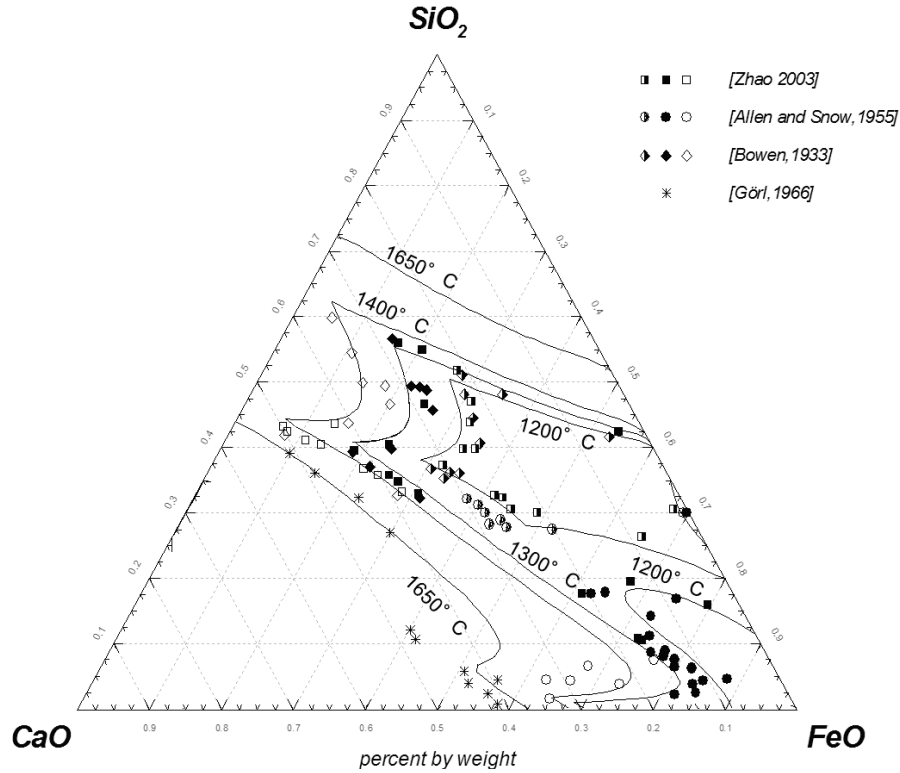


Figure 2-19: Ternary system CaO-SiO₂-FeO (CSF) calculated by Factsage™ and compared with data from literature (liquidus lines for 1200, 1300, 1400, and 1650°C, and 1 bar)⁹³

3 Alkalis and Ironmaking Processes

Fourthly, there is the science of Surveying that he may be able to estimate how deep a shaft should be sunk. Fifthly, his knowledge of Arithmetical Science should be such that he may calculate the cost to be incurred in the machinery and the working of the mine.

Georgius Agricola, De Re Metallica

Alkali is a synonym for alkali metal elements like lithium (Li), sodium (Na), potassium (K), rubidium (Rb), caesium (Cs), and francium (Fr). In metallurgical processes (e.g. in ironmaking) only Na and K play a significant role. The name 'alkali' is likely derived from the Arabic word 'al-qaliy-', which means potash. Potash is an important salt that is mainly used as fertilizer.⁹⁴⁻⁹⁶ In general, all alkali metals have similar physical and chemical properties:

- Alkalis have a valency of 1+ (one outermost electron in the s-orbital); due to low ionization energy, they easily release their other electron and occur as positive ions (cations like Na¹⁺ and K¹⁺). As metals, they have shiny and soft properties. The colour is silver-grey. The crystal lattice of pure alkalis is cubic body-centred.⁹⁷
- The electronegativity is low compared to other elements (Na: 1, K: 0.9). This leads to the favoured combination with electronegative elements, like halogenides (F,Cl) and chalcogens (O). The formation of salts is a typical reaction for alkalis as well as the highly exothermic reaction with water (formation of highly basic hydroxides, such as KOH and NaOH). This reactivity to non-metals will be considered in the following aspects.
- The melting temperature is low for all alkalis (from Li at 181°C to Fr at 27°C). A reason is the big atom size, which does not allow a dense package.⁹⁸ A summary of the melting and boiling temperatures of alkalis and their main compounds is presented in Table 3-1.

Na and K were described in 1807 for the first time by Davy. Identification of the others continued until 1939 (Fr).

Table 3-1: Melting and boiling temperatures of alkali compounds (left value from Factsage™⁷⁵, right from Gudenau²¹)

Alkali compound	Melting temperature [°C]	Boiling temperature [°C]	Alkali compound	Melting temperature [°C]	Boiling temperature [°C]
Na	98	883/880	K	63	759
NaCl	800	1465	KCl	771	1477
Na₂O	1132/920	-	K₂O	878	881
NaOH	323	1388	KOH	406	1323
Na₂CO₃	858/851	-	K₂CO₃	901/891	-
NaCN	562/564	1530/1467	KCN	622/635	1625/1350
Na₂SiO₃	1089	-	K₂SiO₃	976/974	-

In nature, alkali metals occur as compositions. A stable and common form is the binding with halogens. K is bounded in carobbiite (KF) or sylvite (KCl), Na in villiaumite (NaF) or halite (NaCl). For ironmaking processes, the halogens play a minor role: first, because of the low Cl/F content in the processes and, second, because the ratio of alkali halogens in natural iron ores is negligible compared to other alkali components.

Another favoured binding is the placing into alumina silicates. Common minerals are leucite (KAlSi₂O₆) and feldspar (KAlSi₃O₈). However, due to the ionic replacement in alumina silicates, K can set a position in biotites and muscovites—both being the main formers of rocks. Na is bounded in silicates as albite (NaAlSi₃O₈) or as pyroxene. A common form to visualize these complex, petrographic correlations between alumina silicates and alkali metals is a ternary system. Figure 3-1

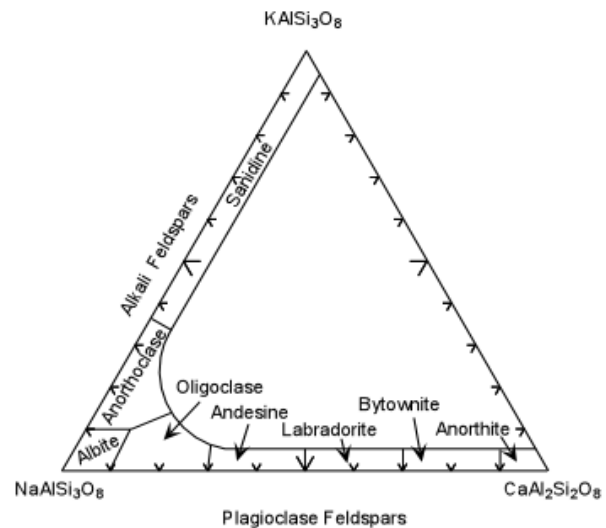


Figure 3-1: Interaction of alumina silicates with K, Na, and Ca in a ternary system, including minerals⁹⁵

shows minerals of the geological classes of alkali feldspars and plagioclase feldspars. The exchange of K, Na, and Ca cations leads to continuous change between the single minerals from their stoichiometric composition (KAlSi₃O₈-NaAlSi₃O₈-CaAl₂Si₂O₈).

Although the bindings with silicates and alumina silicates are the geologically most important correlations, even in basic or mafic rocks and ores high amounts of K/Na minerals can be found (see Erzberg ore in the next chapter).^{15,95,99}

3.1 Alkalis in Ferrous Burden Materials: Geological Origin and Mineral Processing

Apart from artificial iron sources (scrap, dust, mill scale, sludge), natural iron ores are the most important iron carriers for ironmaking processes. Depending on the deposit, each iron ore blend has its specific characteristics (mineralogy, chemistry, grain size distribution, tumbling, and disintegration index). Nowadays, most of the iron ore is mined in countries outside of Europe.⁸ In general, oxidic iron ores can be classified into several types based on the dominant iron component—such as hematite, limonitic, magnetite, and siderite ores (see Chapter 2.2.1.1). Sulphide iron ores have minor importance for ironmaking. For evaluation of the alkali content in the ferrous raw material for further processing, chemical analysis is necessary. Normally, only the K_2O and Na_2O content are measured. Unfortunately, this gives no information about the alkali compounds (especially carbonates and silicates). This information is important with regard to the alkali balance in the reactor. In the following sections, the iron sources will be discussed with reference to K and Na.

Hematite ores are the most important iron ores and they consist of high amounts of hematite (Fe_2O_3). The high iron content ($>65\% Fe_{tot}$) makes it a favoured iron source. The mineralogical structures vary according to the geological origin (dense and clearly shaped by the oxidation of magnetite, layers from banded iron formations¹⁵). The main source for alkalis is the gangue phase. As an example, hematite iron ore from the Sishen mine in South Africa (see Table 5-1 and Figure 3-2) will be examined. The Fe-rich (dark) and the quartzite-rich (light) layers both have a dense structure (see mineralogical view via optical microscopy in Figure 3-2 [left and middle]). The acid gangue layer is based on acid compounds like SiO_2 and Al_2O_3 . Especially SiO_2 is a collecting basin for K (see scanning electron microscopy [SEM] picture in Figure 3-2 [right]). How the banded structure was generated is not clear; nevertheless, fluctuations in hydrothermal activity would have led to alternate sedimentation of silicates and iron oxides. The K content in the final ore is $>0.1\% K$ and $>0.02\% Na$.¹⁰⁰ For global trading this can be problematic. In general, consumers in the field of ironmaking prefer contents $<0.1\% K$ and $<0.02\% Na$ to prevent reactor problems.¹⁰¹

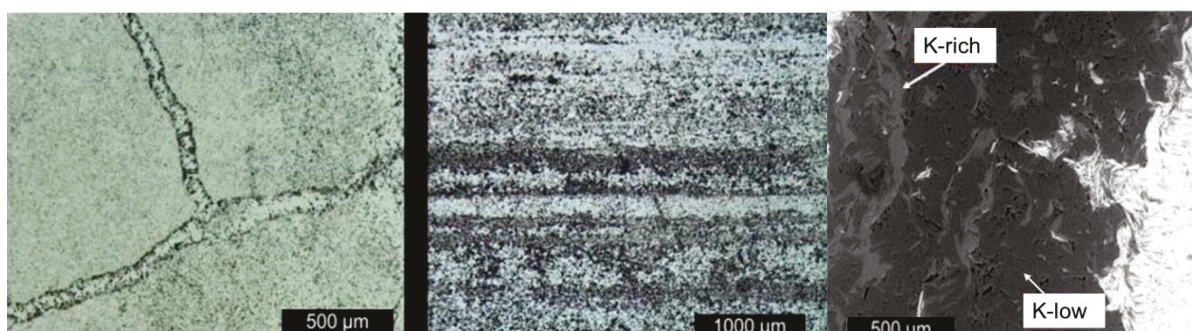


Figure 3-2: Geological structure of hematite iron ore from banded iron formations (left and middle: optical microscopy; right: SEM)¹⁰²

Magnetite iron ores are dominated by Fe_3O_4 . The ore is mostly characterized by high density and high Fe_{tot} content $>65\%$.⁸¹ However, the amount of magnetite used globally for iron production

is low. With regard to alkali elements, the content varies from 0.02–0.2% K (or 0.02–0.1% Na).¹⁰⁰ An example of a magnetite deposit is the mine of Kiruna in Sweden, which is geologically an intrusive deposit.¹⁰³ The alkali content of the raw iron ore can reach up to 0.33% K. This high content is minimized by mineral processing.¹⁰⁰

Limonitic ores are based on FeOOH minerals (limonite or modifications like goethite and lepidocrocite¹⁰⁴). Limonite develops during the weathering of former iron oxides like hematite (such as $\text{Fe}_2\text{O}_3 + \text{H}_2\text{O} \rightleftharpoons 2 \text{FeOOH}$). From the limonitic structure, the geological origin can be derived easily (e.g. ooidic oxides from ballast beds, shaped structures from former magnetite, leaf-shaped structures from former organic material).⁸¹ The iron content is high (>60% Fe_{tot} after dehydration), which makes limonite a main source for iron production. In terms of alkali metals, limonites have in common that the alteration has led to the washing out of alkali compounds and, consequently, to low content of K and Na (0.023% for Robe River in Australia, 0.009% for CVRD in Brazil; see Table 5-1).^{81,100}

Although siderite iron ores are hardly used for ironmaking, siderite (FeCO_3) has to be considered because of the nearby Erzberg mine in Austria. The low content of Fe ($\text{Fe}_{\text{tot}} < 40\%$) and the emission of additional CO_2 during processing (e.g. sintering) make it an unfavourable iron source. However, the positive aspects are a very good reducibility and, in case of the Erzberg, a favourable basic gangue.⁸¹ The alkali content for siderite ores is quite high (0.15–0.3% K, 0.03% Na). This is caused by the geological origin. The mine is a metasomatic deposit, which means the formation of siderite occurs through the exchange of Ca^{2+} in lime by Fe^{2+} ($\text{CaCO}_3 \rightarrow \text{FeCO}_3$)¹⁵. In addition to the exchange of the cations, even the replacement by Mg^{2+} , K^+ and Na^+ is common, and it leads to higher content of these elements in alkali and earth alkali metals.

For further information about hematite, limonitic, magnetite, and siderite ores, and their origin and interaction with Na or K minerals, see the literature.^{15,81,95,99,103,105}

As extracted material is difficult to process in metallurgical reactors directly from the mining, beneficiation and mineral processing are essential (crushing, grinding, screening, concentrating, blending, agglomeration). These stages lead to homogeneous material with a higher value component (Fe content). In general, sinter feed (100 μm –8 mm) and pellets feed (<100 μm) are the important grades of iron ore fines.^{9,28} For use in shaft furnaces, an agglomeration is also needed by sintering or pelletizing. With regard to alkalis, mineral processing can cause a higher load in the burden material. Often, Fe-bearing dust with a higher amount of alkalis (e.g. from the top gas treatment) is recycled in the sinter process. The alkalis are bounded in the sinter and are emitted again in the BF (and again in the dust fraction of the top gas treatment). This circulation outside of the reactor is also called an external alkali cycle. In terms of pellets, the binders are mainly based on different types of alumina silicates. They can lead to the input of mainly Na (by bentonite) or minor K (by feldspar).

3.2 Thermodynamics of Alkalis and Behaviour in Ironmaking Processes

In general, K and Na have oxygen-affine characteristics. Under atmospheric conditions with oxygen pressure of 0.21 bar, metallic K/Na reacts to K_2O/Na_2O . However, ironmaking reactors are characterized by a reducing gas atmosphere, with a reduction force depending on the reaction area, and its temperature and gas composition (CO , CO_2 , H_2 , and H_2O content). Furthermore, even silicate and carbonate compounds have higher stability at temperatures $<1000^\circ C$ than do metallic K/Na. To sum up, the stability of metallic K/Na rises with higher temperatures and a lower oxygen potential (correlating with the sinking layer in BF). Figure 3-4 shows stability lines for different alkali compounds. To show the stable compounds in different ironmaking reactors, the oxygen potentials in the melter gasifier and the BF are included, respectively. The path for the BF (long-dashed line) starts at the bosh area with $1500^\circ C$ and ~ 2.2 bar absolute pressure (see point A), and follows the lines for the carbon and carbon monoxide oxidation down to $<200^\circ C$ (see point B). The path of the melter gasifier (dotted lines) is characterized by a higher pressure (~ 4.5 bar absolute). The oxygen potential moves from the lower reactor regions (see point C at $1500^\circ C$) to the reactor top at $1000^\circ C$ (see point D).

Due to the change in temperature and gas composition over the reactor, the stability areas vary for all alkali compositions. In the higher areas, carbonates and oxides are stable; in the lower area, metals and cyanides are common. The free enthalpy of the compounds (Figure 3-4) and the low melting and boiling temperatures (see Table 3-1) lead to a specific behaviour in ironmaking reactors. Their common process conditions lead to oxidation, reduction, and several phase transformations (melting, solidification, boiling, condensing) over the reactor's height. The combination of these effects leads to circulation inside the reactor and an internal alkali cycle is formed. Na follows the same reaction as K for the equations in this chapter.

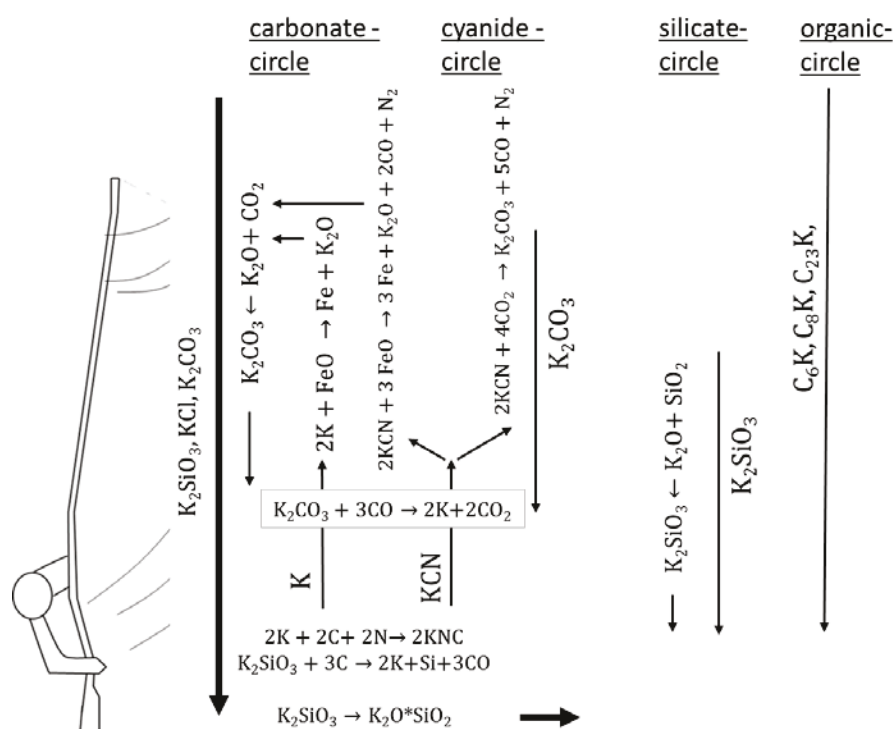


Figure 3-3: Internal alkali cycles for potassium in a blast furnace²¹

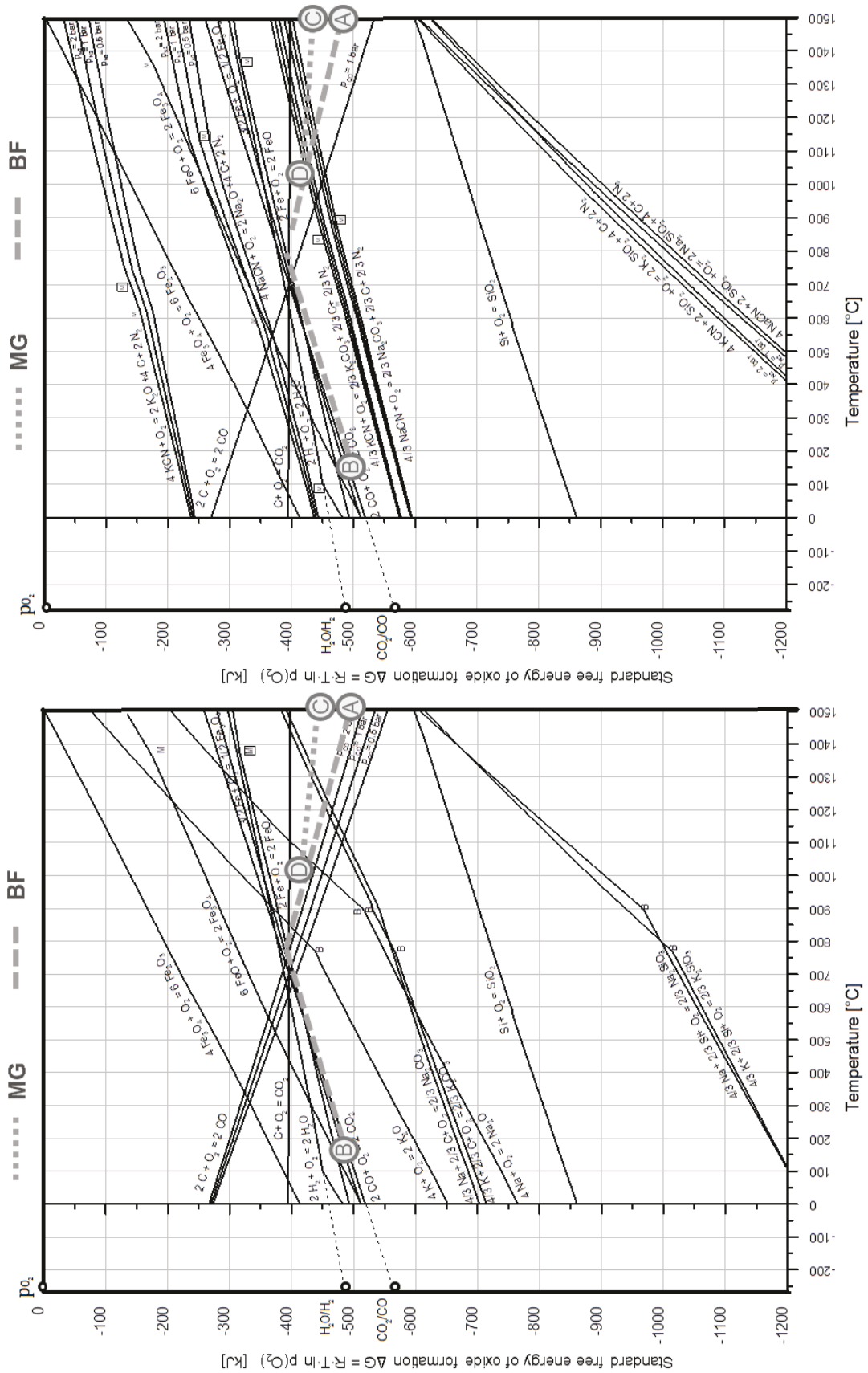
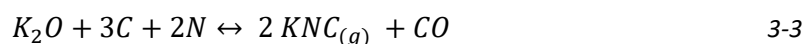
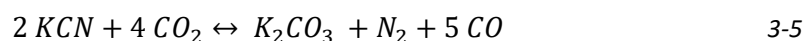


Figure 3-4: Richardson-Ellingham diagrams for alkali compounds (left: metals and oxides; right: cyanides), including the process conditions for BF and MG^{75,106}

According to literature¹⁰⁷ and industrial data, the alkalis are mainly charged into the furnace as silicates, and partially also as halides and carbonates (see Figure 3-3). Primarily, alkali silicates in the ash and gangue phases descend in the furnace, hardly affected by the process gas due to their thermochemical stability.^{75,106} In the cohesive zone, alkali-containing phases start to melt and mix with the slag phases and the liquid metal. The alkali silicate decomposes into K_2O/Na_2O and SiO_2 (see Equation 3-1) and gets dissolved in the liquid phases (more precisely, into ions according to the ion-slag theory²⁵). A certain amount of alkalis is discharged by the slag. Small amounts are reduced by carbon, following Equations 3-2 and 3-3, and evaporated by the high temperature of the metal or slag phase (1400–1500°C).



Gaseous metals and cyanides rise to higher regions of the reactor. In connection with lower temperatures and higher amounts of oxidizing gases (CO_2), the alkali gases react to carbonates. The oxidation reactions are summarized in Equations 3-4 and 3-5.



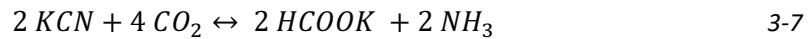
The carbonates occur as liquid phases. This leads to the condensation of liquid particles out of the gas flow and, moreover, to the transport to lower regions by the descending burden. This again leads to the reduction of the carbonates due to the higher CO content and to the evaporation of the metallic K/Na by the higher temperatures (see Equations 3-6).



Alkali oxides like K_2O and Na_2O (which, for example, are often mentioned in chemical analyses) are not stable in common ironmaking processes (reduction and decomposing on the one hand, further oxidation to carbonates on the other).

Alkali circulation: Equations 3-2 to 3-6 lead to circulation inside the reactor and, consequently, to an enrichment of alkalis. Only a small ratio of the total circulating load finally leaves the furnace from the top. Specifically, cyanide and carbonate compounds can be found in the dust, sludge, and washing water of the waste gas treatment. In addition, Altpeter⁹⁶ points out the formation of four separated types of alkali cycles (see Figure 3-3):

The cyanide cycle is based on the formation of cyanides at high temperatures ($>1625^\circ C$). Especially the area near the raceways is characterized by high carbon and nitrogen activity, both favouring the formation of cyanides. In this context, a new approach for the oxidation of cyanides in the upper regions of the reactor should be mentioned. Based on the formation of ammonia gas in the BF top, a theory was developed that follows Equations 3-7 to 3-9.



The silicate cycle is formed between the cohesive and slag zones. In the cohesive zone, gaseous alkalis react with silicates and form very stable alkali silicates, which are reduced in the BF hearth. This cycle can improve the discharge of alkalis via the slag phase.

In the BF shaft, alkali carbonates are formed from gaseous compounds. They condense and descend in the reactor, where the carbonates are reduced or transformed into silicates. This leads to the formation of a carbonate cycle.

The fourth type is linked to coke, where alkalis can impregnate the carbon structure and form C_6K , C_8K , or C_{24}K . In the lower areas, the carbon is oxidized and the alkalis rise with the process gas to higher areas.

Input and output—general aspects:

Coal, coke, and burden materials are the main sources for alkali input. From the chemical point of view, the alkalis are charged as silicates, carbonates, and oxides.¹⁰⁸ The load ranges from <2 kg/tHM (modern BFs with imported raw materials) to 12 kg/tHM (usage of domestic ore—e.g. in East Europe and Russia⁹⁶). The mass ratio K/Na is 2/1 for most cases.

The discharge of the alkalis is mainly done by the slag. The rest is emitted by the top gas, including a significant dust fraction.¹⁰⁹ Small amounts are adsorbed by the refractory material (~1% of total load^{28,82}). The alkali steams infiltrate the lining through the open porosity. There, the K can react with the refractory material and oxidates to kaliophilite ($\text{K}_2\text{O}\cdot\text{Al}_2\text{O}_3\cdot 2\text{SiO}_2$) and leucite ($\text{K}_2\text{O}\cdot\text{Al}_2\text{O}_3\cdot 4\text{SiO}_2$). Mechanical destruction by volume-induced stress formation lowers the stability of the refractory material. Furthermore, low-melting alkali compositions are formed.¹¹⁰

The operation parameters of the furnace can change the alkali distribution in particular. This will be discussed in Chapter 4. In general, the slag/top gas ratio of K is higher than for Na.¹⁰⁹ Also, own investigations (see output data in Figure 4-16) and other authors²⁸ confirm that the discharge by the slag is more effective for K than for Na. Figure 3-5 presents a summary of the discharged alkalis for both K and Na.

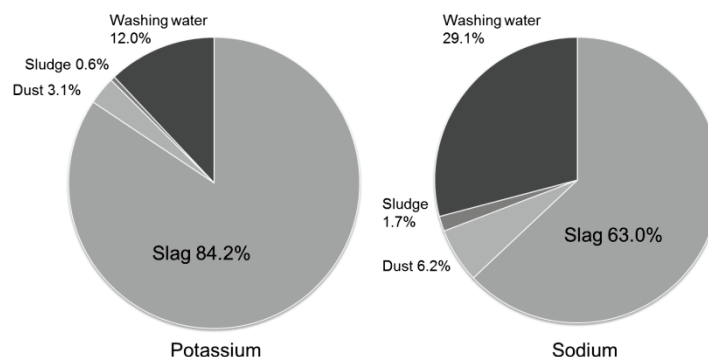


Figure 3-5: Exemplary amounts of the alkali output of European BFs¹⁰⁹

Process behaviour: Alkali enrichment leads to scaffolds and attacks the refractory materials.²⁸ Scaffolds are mainly formed in interaction with carbon and zinc.⁹⁶ The shaft and belly regions are the most important areas here. Scaffolds up to 1.5 metres can decrease the furnace section by up to several metres. The scabs show a multi-layer structure of burden material, carbon, and fines (see Figure 3-6). Consequently, the material sticks, gas flow changes, and the dust ratio at the top increases. Taken together, this leads to a drop in productivity.

Second, the alkali can attack the refractory as a gas compound or dissolved in the slag phase. Normally, the BF refractory is based on acid compounds like corundum, chromium-corundum, and alumina silicates. Such oxides are easily impregnated by Na and K, which leads to new low-melting compositions. Experimental data confirms the increase in alkali content, depending on the infiltration area (an example of the chemical composition of bricks after the operation is shown in Figure 3-7). In addition, a change in volume and thermal expansion leads to stress and blistering of the refractory's surface.¹⁰⁹ Moreover, hydration of impregnated alkali compounds can lead to hydrate formation and attrition.¹⁰⁸ In case of carbon bricks, alkalis can weaken the refractory as liquids, vapours, and metals; solid alkali compounds show no influence on the destruction of bricks. The literature¹¹¹ defines the formation of carbon-alkali interface phases and, consequently, local stress and cracks as the main factors causing the mechanical weakening. With regard to the fuels, the coal or coke rate increases because of a catalytic effect on the reaction of carbon carriers with CO₂. Moreover, the equilibrium of the Boudouard reaction (see Equation 2-21) shifts to lower temperatures; consequently, the range of direct reduction increases and leads to higher coke consumption.

From the energy point of view, the accumulation of alkalis leads to a change in the energy balance. The reduction and oxidation reactions and the boiling and condensing mechanisms lead to the transfer of energy from the lower to the upper regions. This is unwanted and harmful for the total process performance.¹⁰⁸

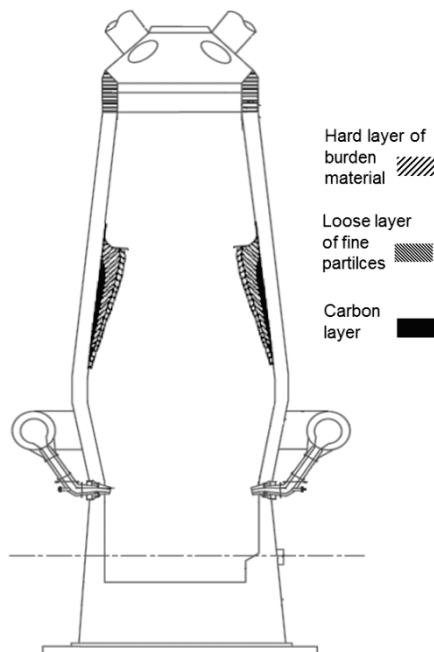


Figure 3-6: Model of the formation of scaffolds in the blast furnace shaft⁹⁶

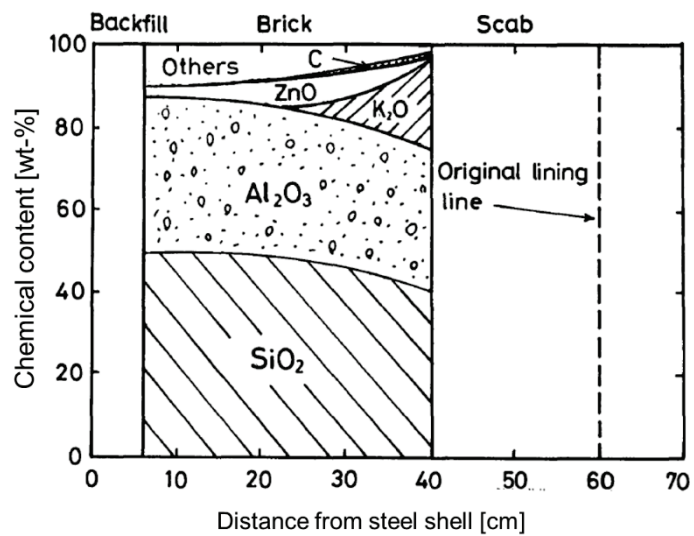


Figure 3-7: Alkali infiltration into the refractory of the middle part of the shaft (including the consumption of material during operation)¹¹⁰

According to the alkali load, 1 kg alkalis/tHM leads to a decrease in productivity of 3–8% and an increase in coke consumption of 3–8%. So, there are several opportunities to lower the impact on the process performance.^{28,96,112}

- Use of input material with low alkali content (e.g. the standard for globally traded iron ores is <math><0.1\% \text{ K}</math>;¹⁰¹ oil and natural gas as reductant instead of coal and coke with alkali-bearing ash¹⁰⁸)
- No recycling of alkali-bearing dust and slag by the sinter plant (no formation of external alkali cycle)
- Change in basicity for BF slag and sinter mixture; only a short time because S content will increase
- Increase in slag mass and change in flux charging (e.g. more MgO up to 9.5%, more Al_2O_3 ¹⁰⁹)
- Change in process conditions, like decrease of tapping temperature, higher process pressure (higher p_{CO} to oppose alkali gasification reaction by oxygen enrichment or high top pressure²⁸), lower nitrogen partial pressure in raceways, lower flame temperature,²⁸ etc.
- Centred process flow in reactor—higher gas velocities transport droplets and dust out, higher temperature in the centre leads to less condensing¹⁰⁸
- De-alkalization of input materials (by chlorination)⁹⁶
- Charging of CaCl_2 if the furnace is in deep trouble; the fundamental mechanisms are not clear yet (washing out of the alkali vapours by gaseous CaCl_2 , breakdown of scaffolds by weakening of their structure)¹¹³

These opportunities are always connected with a worsening in other aspects (e.g. sulfur versus alkali capacity of slags¹⁰⁹).

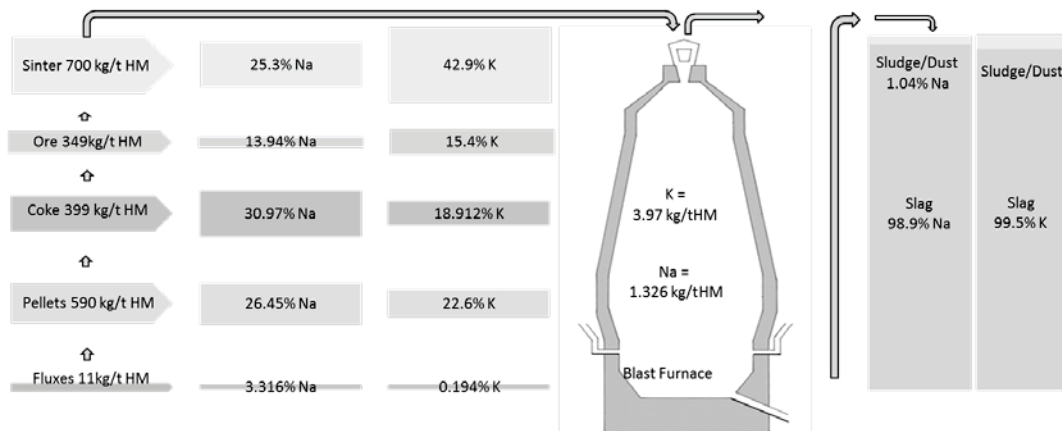
3.2.1 Alkali Flow in the Blast Furnace

In this chapter, aspects of alkali balance and accumulation in the BF are considered. Data from industrial plants should help to get an understanding of the input and output flows. An overview of different ironmaking reactors and important information concerning their alkali balance gives Table 3-2. In addition, three different European BFs are evaluated in particular (see Figure 3-8). This also supplies important information on evaluation of the results of the alkali model in Chapter 4.

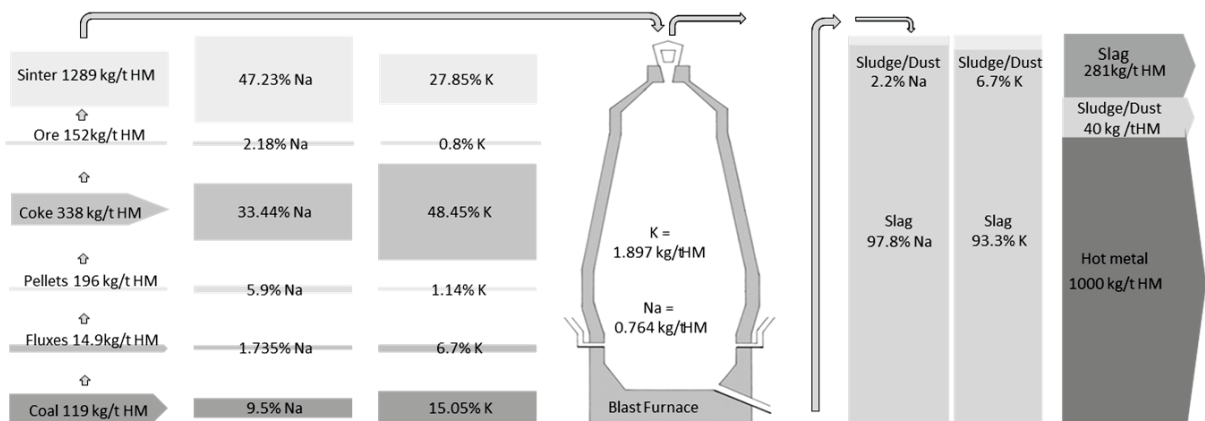
Table 3-2: Summary of the alkali balances of different blast furnace operators (European Union [EU], Eastern Europe and Russia [EaEu], Japan [Jpn], North America [NA])

Blast Furnace (BF)	(K+Na) [kg/tHM]	Details Input/Output (% of total input/output)	Slag Properties
BF-EU1 ¹¹⁴	8.0	burden: 83%, coke: 14%, coal: 3% slag: 99.3%, top gas: 0.7%	B ₃ =1.05
BF-EU2 ³⁶	5.3	See Figure 3-8	B ₂ =0.95 ~2% K+Na
BF-EU3 ³⁶	2.55–2.79	coke: 48–59%, sinter: 21–28%, coal: 10–17%, pellets+ore: 6–13% slag: 82%	B ₂ =1.1 0.42% K/0.30% Na
BF-EU4 ³⁶	2.7	coke: 49%, sinter: 31%, pellets: 18%	
BF-EU5 ³⁶	2.66	See Figure 3-8	0.53% K, 0.20% Na
BF-EU6 ³⁶	1.4 kg K 0.52 kg Na	K: slag: 82%, dust: 4%, sludge: 4%, washing water: 9% Na: slag: 93%, dust: 2%, sludge: 1%, washing water: 4%	B ₂ =1.1–1.2 0.25–0.35% K
BF-EU7 ¹¹⁵	2.84	See Figure 3-8	
BF-EU8 ¹¹⁶	1.4–1.55 kg K	Output: slag: 90% K, top gas: 9% K	B ₂ =1.1–1.25 ~0.25–0.42% K
BF-EU9 ¹¹⁷	5	Enrichment to 30 kg alkalis/tHM	
BF-EU10 ¹¹⁸	7.5		B ₄ =1.05–1.2 1.3–2.8% K+Na
BF-EaEu1 ¹⁰⁹	8.2		B ₂ =1.2
BF-EaEu2 ¹⁰⁹	5.5–8		B ₂ =1.2–1.3
BF-Jpn1 ^{119,117}	4.43	Enrichment to 17–18 kg alkalis/tHM	B ₂ =1.25
BF-Jpn2 ^{110,117}	2.14	Enrichment to 22–23 kg alkalis/tHM	
BF-Jpn3 ¹¹⁷	2.29	Enrichment to 13.1 kg alkalis/tHM	
BF-NA1 ¹¹⁸	2.8		B ₄ =1.0–1.1 0.6–1.8% K+Na
BF-NA2 ¹¹⁸	3		B ₄ =1.0–1.2 0.8–1.5% K+Na
BF-NA3 ¹¹⁸	5		
BF-NA4 ¹¹⁸	5.5		
Smelting Reduction (SR)	(K+Na) [kg/tHM]	Details Input/Output	Slag Properties
SR1 ¹²⁰	2.99 kg K		0.75%K
SR2 ^{55,121}	2.415 kg K 0.54 kg Na	See Figure 3-11 and Figure 4-16	B ₂ =1.2; 0.3–0.9% K, 0.15–0.25% Na

Alkali balance of BF with high alkali load, oil injection, low basicity ($B_2=0.95$), and high pellets rate (BF-EU2)³⁶



Alkali balance of BF with low alkali load and PCI (BF-EU5)³⁶



Alkali balance of BF with low alkali load and high slag ratio (BF-EU7)¹¹⁵

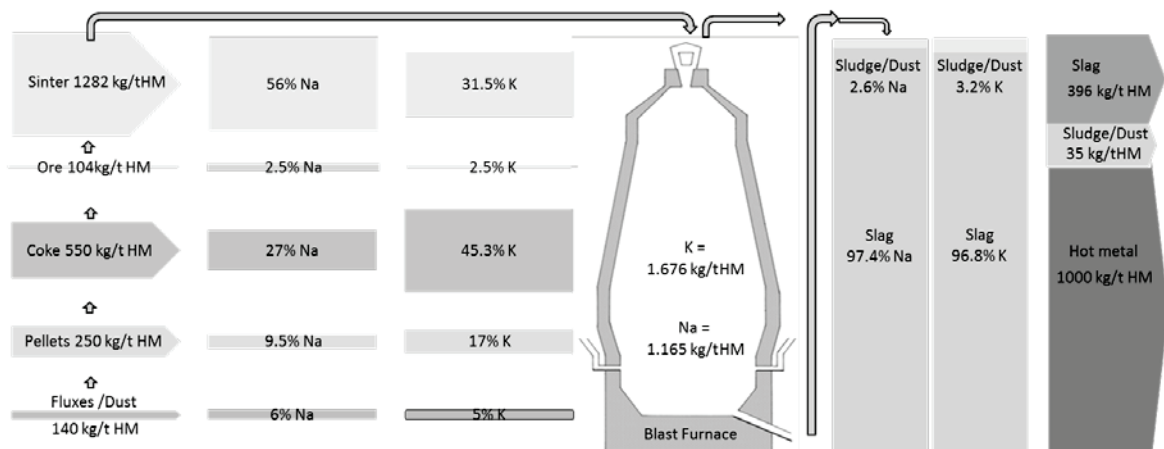


Figure 3-8: Comparison of different BFs according to their alkali balance (left: input masses and the ratio of K or Na in the specific phase compared to the total K or Na load; centre: alkali load; right: output ratio of Na and K and masses)

Input: Modern BFs are operated with alkali loads up to 5 kg/tHM.⁹⁶ However, in several plants with special input material, alkali input up to 12 kg/tHM is possible. For instance, in Eastern Europe, BFs are charged with local high-K/Na-bearing-ore or Fe-containing material from the production of ferro alloys.¹⁰⁹ According to the accumulation, these high loads lead to enrichments in the shaft of up to seven to 15 times. Some of the literature determines an increase in the sinter samples of the furnace of five to 10 times and, in the dust, 2.6–16.6% of alkali oxides can be found (alkali load of 8.2 kg K+Na/tHM).¹⁰⁹

Operators try to prevent problems during the process by the careful selection of low-alkali-bearing input materials. Table 3-2 gives details of the alkali load, which varies from 1.4 to 8.2 kg of K+Na. The data is calculated originally from K₂O and Na₂O analyses of the elementary content. The distribution of the alkalis in the input materials was considered for the European BFs. They illustrate a high deviation of the K/Na ratios in the charged materials connected to local conditions. For the Japanese BFs (BFJpn1 to 3), the enrichment of alkalis in the reactor is also mentioned, whereas peaks in the alkali load of more than 10 times of the input mass was measured.

Supporting and more precise information about the alkali balance in European BFs is provided in Figure 3-8. Three different operation conditions are linked to the input and output materials. According to the input, the masses and the K/Na ratios of the single material classes are included. BF-EU2 is a blast furnace with a high alkali load (especially K by the sinter). Although oil injection and the usage of high-quality coke (low K content) lower the total alkali load a bit. BF-EU5 and BF-EU7 are furnaces with a lower alkali load. However, two methods of operation are compared. BF-EU5 is operated with PCI. This leads to an additional alkali source (coal ash). Compared to BF-EU7, the alkali load by PCI can be neglected because of the total decrease in reducing agents (coke and coal). So, the minimization of the coke or coal rate brings economical benefits as well as a lower alkali load. A discussion on the output streams and the connection with the slag properties will follow. To sum up, the main alkali sources are coke and sinter, which are related to the high input masses. Moreover, here a diversity of the K/Na ratio is visible: The ratio of K charged by the sinter is between 28 and 43 wt-%; for coke it ranges from 19–48 wt-%. Coke is generally a bigger source of K than sinter. The reason is the amount of K₂O-containing ash. For the Na load, the ratio in the input materials is less spread out. For coke, the value varies from 27–33 wt-%. By the sinter, 25–56 wt-% of the total Na load is charged.

Output: For the analysis of the alkali output, the main products will be evaluated: the hot metal, the slag, and the top gas. Depending on the slag properties, the main discharge occurs in the slag phase (>90%). Only a small fraction exits the reactor via the top gas (<7%). These findings will now be discussed more precisely.

In the metal phase (hot metal), no alkalis are detectable. This is due to the high temperature and the low solubility of Na/K in iron.⁷⁵

The most important alkali discharge is carried out by the slag. The performance of the slag in relation to K/Na depends on several parameters like basicity, temperature, and alkali capacity (for further information, see Ivanov¹⁰⁹). Especially the data of Table 3-2 shows the close connection between slag properties like basicity with the final K/Na content in the slag and, consequently, the total alkali output. In general, the K+Na content in the final slag is <1%.

However, a high alkali input (>5 kg K+Na/tHM) and a low basicity ($B_2 < 1.1$) can lead to an alkali capacity of the slag of over 2% K+Na.

In addition, Figure 3-8 shows details of the alkali output for three different operation modi of European BFs. BF-EU2 is characterized by a high alkali load and a very low slag basicity ($B_2 < 0.95$). Both lead to a high alkali capacity of the slag and to a high alkali discharge by the slag phase ($>99\%$ of alkalis). The two furnaces with a lower alkali load (BF-EU5 and BF-EU7) have a lower discharge by the slag (between 93–98%). The main difference is the higher slag volume for BF-EU7. A higher slag volume has negative aspects according to the energy balance, but more slag can dissolve and discharge more alkalis. Consequently, even the alkali load of the top gas (including sludge and dust) is lower if the slag volume is higher.

A specific view on slag properties like basicity and temperature is given in Chapter 4.2.2 for the slag model of the alkali model. In addition, Figure 3-9 sums up the operation modi of several European BF operators with respect to alkali load [kg/tHM] and the slag basicity. The picture shows the split into three areas: For a K_2O load < 1.8 kg/tHM, the operator selects the slag basicity independent from the alkali load and does not lower the slag basicity with regard to better desulphurization abilities; in a transition from 1.8–2.6 kg/tHM, the slag basicity shows high variations between $0.85 < B_2 < 1.2$. The dramatic drop in basicity is important with regard to the prevention of alkali accumulation.¹²² The third area is characterized by BF operators with a high alkali load > 2.6 kg/tHM. Here, low basicities are used to handle the alkali emission by the slag; further lowering of $B_2 < 0.8$ is limited by desulphurization constraints and the melting temperature of the slag. To sum up, a load of 1.8 kg/tHM seems to be the transition point for the operator to change from an alkali-independent to an alkali-dependent operation mode reactor.

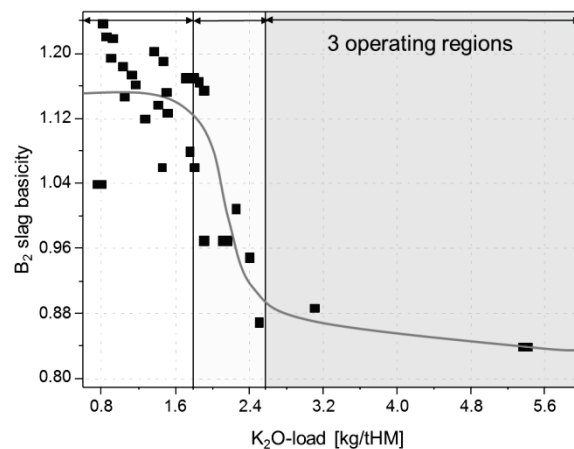


Figure 3-9: Alkali handling of European BF operators: Correlation of alkali load [kg/tHM] and B_2 -basicity¹⁰¹

Table 3-3: Overview of the chemical analysis of dust or gas samples over the BF: A horizontal profile³⁶

Alkali compound	Hot area (centre)			Cold area (wall)			Hot area (centre)			Cold area (wall)		
	Dust in [wt-%]			Dust in [wt-%]			Condensate in [mg/l]			Condensate in [mg/l]		
K (min)	3.5	0.6	0.2	0.1	0.1	0.2	384	23	4	1	0	10
K (max)	29	24	3.1	2.1	1.8	4.5	1628	1240	439	360	907	2,433
Na (min)	0.4	0.3	0	0.1	0	0	63	4	1	0	0	2
Na (max)	4.9	3.9	1.6	1.6	1.6	1.3	434	322	65	41	133	360

The rest of the alkali compounds are emitted from the slag phase into the reactor and discharged by the top gas. Here, the distribution and composition of the dust fraction has to be mentioned. Higher values of K and Na (analysed as oxides with X-ray fluorescence analysis [XRF]) are present in the dust fraction, compared to the burden material. Table 3-3 shows the analysis of dust and gas samples in a BF taken by a horizontal probe in the upper layers (dust) and an inclined probe above the stockline (gas sampling).³⁶ The values are listed from the centre (left) to the wall (right), including the minimum and maximum values from the testing campaigns. These results assume that especially the centre shows a higher load of alkalis (for Na, the increase is less than for K).

This also leads to the attachment of a dust factor in the alkali model. Derived from the chemical analysis of dust samples, a summary of stability areas can be seen in Figure 3-10, whereas the left columns show the ratio of K/Na in the dust (up to 15 wt-%) and the right column visualizes the measured compounds analysed by XRF.³⁶ Moreover, the total amount of dust rises by a higher alkali load in the reactor. Specifically, the dust load after the electrostatic precipitator (ESP) can rise from 30–80 mg/Nm³ (2–3 kg alkalis/tHM) to 100–230 mg/Nm³ (4–4.8 kg alkalis/tHM).¹⁰⁹ The alkali fraction of the dust inside and outside the reactor mainly consists of carbonates and KCl/NaCl. Cyanide droplets are found in the dust samples at the centre of the upper stack region and the edge of the lower stack region. In addition, complex alkali compounds were analysed by XRF, like (K,Na)HCO₃, KZn(CN)₃, (Na_xK_yZn_z)CO₃, etc.³⁶

Finally, the top gas treatment gives three separated materials with higher alkali content: dust, sludge, and the washing water (see Figure 2-2). The separation of K and Na compounds into these different output materials is due to the thermochemical properties (oxygen potential, melting temperature, etc.). Some general considerations may take into account the separation of the top gas material into single compounds (dust, sludge, washing water). The separation degree of dust between the cyclone and the ESP is ~90/10%, whereat the coarse fraction is separated by the cyclone (>40 μm, ~10 kg/tHM). The sludge fraction is ~2 kg/tHM. All these considered aspects of the alkali balance are mentioned in the alkali model. The data delivers information about dust ratios, contents of alkalis in the dust, distribution over the reactor height, and much more, which is important for the modification and validation of the BF model.

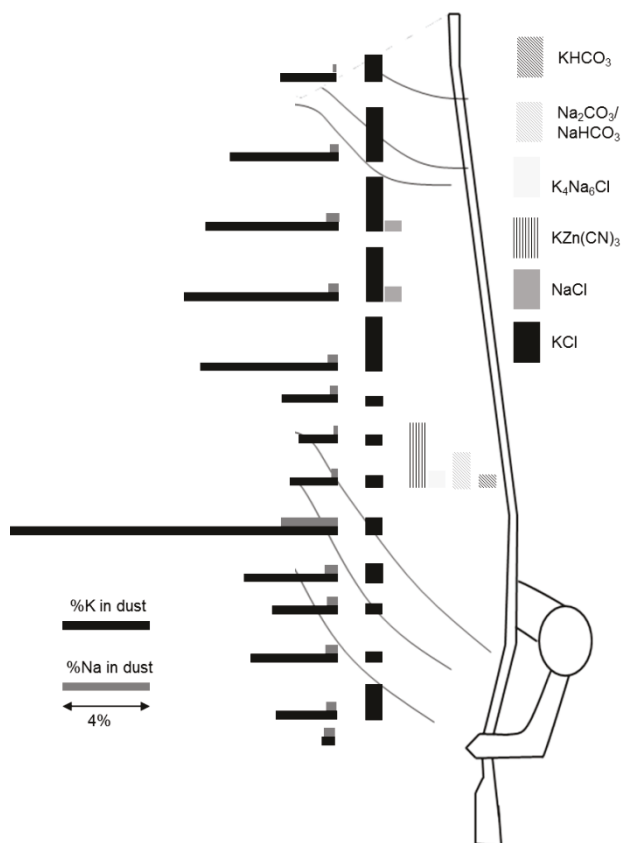


Figure 3-10: Alkali distribution in the dust over the BF height (left: total content of K/Na; right: compounds measured by XRF analysis); data derived from Lin³⁶

3.2.2 Alkali Flow in Direct and Smelting Reduction Processes

In terms of direct and smelting reduction processes, a clear separation is necessary with regard to alkalis.

Direct reduction processes are not significantly affected by alkalis. Since the alkali metals are mainly charged as K/Na silicates, the process temperatures are too low (<1100°C) for reduction to metals or formation of cyanides. Moreover, the absence of liquid phases does not favour alkali generation. This statement can also be confirmed by own investigations with high-K-bearing iron ores.¹²³ The lump ores were reduced by laboratory-scale rotary kilns ($T_{\text{Process}}=1100^{\circ}\text{C}$, direct reduction by coal with a high CO-containing atmosphere); no change in alkali load before and after the testing was observed. Derived from that, no significant effect of alkalis on the process performance can be determined.

For smelting reduction processes, the situation is similar to the BF. The formation of a liquid product (metal and slag) is linked to high temperatures and highly reducing conditions, which favours the reduction of K/Na silicates and carbonates. In the following, the COREX[®] and FINEX[®] processes will be examined. With regard to the higher specific fuel rate compared to the BF, the alkali load from fuels is suggested to be higher. Most coals show an alkali content between 0.5-5% in the ash phase. If the ash content varies, this can lead to an increase in alkali input of up to three times compared to the BF.¹²⁰ A second main difference is the discharge by three different possibilities: the slag, the cooling gas, and the off-gas. In addition, several properties lead to different alkali flows in the smelting reduction processes: higher dust generation (approximately 40 kg/tHM instead of 20 kg/tHM), lower alkali and dust absorption of the bulk, filter effect of coke is missing, higher gas velocities, higher slag volumes, and higher pressure.¹²⁰ According to the slag, which has the most powerful impact on the alkali discharge, a higher alkali content is suggested for the melter gasifier (MG). This is caused by the high ratio of non-stoichiometric reactions in smelting reduction processes (some alkali silicates leave the furnace unreacted by the slag). Furthermore, the gas properties above the slag (high process pressure) influence the maximum alkali content of the slag. In the generator gas, the alkalis are suggested to occur as metal and carbonate. Although the amount of K_{met} and Na_{met} is high after the melter gasifier, the rising CO_2 content leads to a further carbonizing of the carbonates. A full transformation of metals to carbonates takes place after the hot gas cyclone. The alkali content of the sludge after the cooling gas-cleaning unit is high; however, a small ratio is recycled and it gets into the hot gas cyclone again via the cooling gas. In the off-gas, the alkali content is higher than in the BF. This is caused by the smaller adsorption properties via the coke-less bulk (reduction shaft in COREX[®] process) and the high gas velocities (fluidized bed reactor in the FINEX[®] process). Based on the formation of cyanides, smaller amounts will occur due to the use of technical pure oxygen as hot blast (N_2 content <1 vol-%). Further information about cyanides will follow in Chapter 4.3). Summing up all possibilities of alkali discharge, the balance between input and output is better for smelting reduction processes than for the BF process.¹²⁰

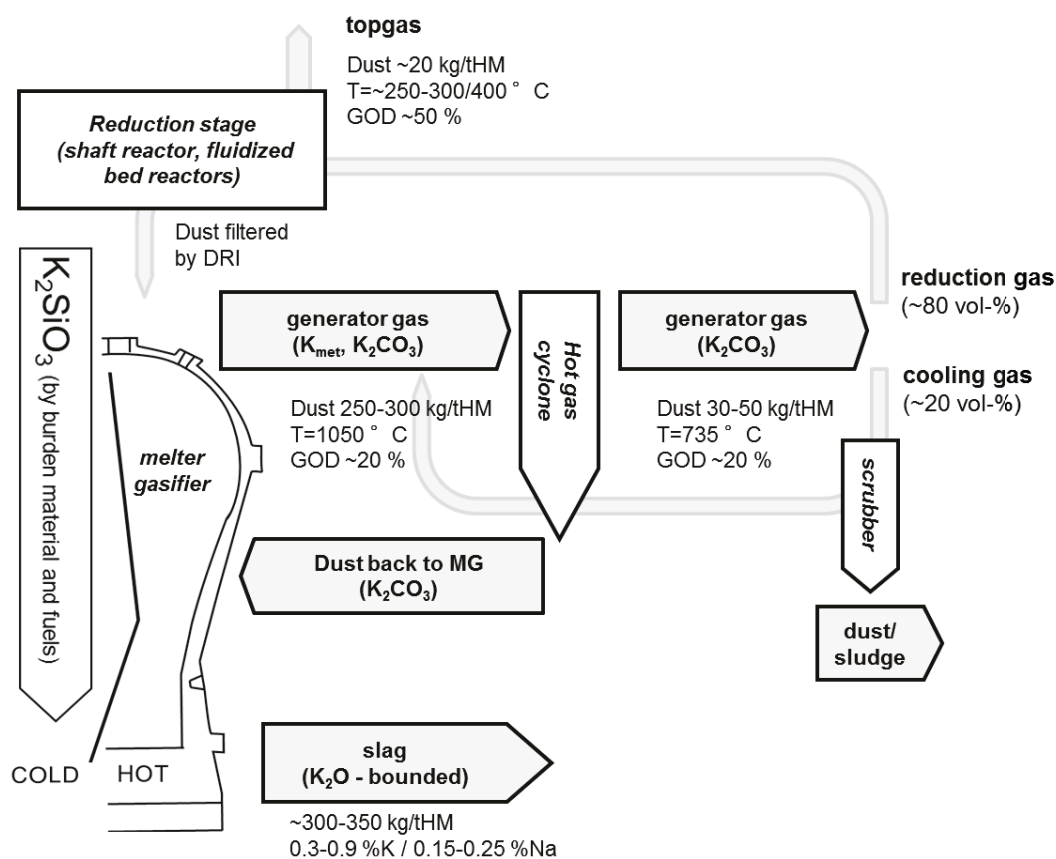


Figure 3-11: Alkali flow for potassium in the COREX® and FINEX® process, including the stable phases and complex gas treatment system^{120,121}

The complex gas flows of the COREX® and FINEX® processes are summarized in Figure 3-11. Based on data from earlier research work^{120,121} and considerations from the alkali model (see Chapter 4.3), a schematic figure of the alkali cycle for the COREX® and FINEX® processes can be illustrated. Like in the BF, the main discharge is done with the slag. The K leaves the reactor bounded in the glassy slag phase as K_2O . The rest gets into the generator gas. There, the temperature is high and the oxygen potential is low. K_{met} and K_2CO_3 are formed. In the hot gas cyclone, the temperature drops and K_2CO_3 gets the most stable phase. Especially the hot gas cyclone has a high impact on the alkali accumulation and the total alkali balance. A higher separation rate leads to a higher accumulation because of dust recycling (see Chapter 4.3). The cleaned generator gas is separated into the reduction gas and the cooling gas. The cooling gas is cleaned in a scrubber, where all alkalis are removed into a dust or sludge phase. In the cleaned cooling gas, no alkalis are left. The reduction gas gets into the reduction stage, where alkalis can further react with the input materials or get deposited on the solids. From there, a repeated charging into the melter gasifier is possible (outer alkali cycle).

Industrial investigations show that the K_2O content in the dust before the fluidized bed reactor R1 in FINEX® correlates with the K_2O content in the slag. Specifically, 10 wt-% K_2O can be found in the dust if 0.9% K_2O is in the slag; 5 wt-% is found in the dust if 0.5% K_2O is in the slag.¹²¹

In general, it can be assumed that the internal and external alkali flows in direct and smelting reduction processes are less researched than that of the BF.

3.3 Effect of Alkalis on Reduction and Melting Behaviour of Ferrous Burden Materials

Apart from operative aspects, the microscopic interaction between burden materials and alkalis has to be considered to get a full understanding. The following chapter summarizes investigations by other authors into the effect of K/Na on reducibility, as well as on mechanical and melting properties. In general, ferrous burden materials are always affected negatively by higher alkali content. For instance, swelling, disintegration, abrasion, and sticking occur, as well as an increase in the melting range. A positive aspect of K/Na is the increase in reactivity, which leads to faster reduction. A bigger surface or reaction area and an effect on nucleation and grain growth of Fe_{met} are named as reasons for this.¹¹⁸ The microscopic effects are important for both the BF and smelting reduction process. This thesis describes and interprets these effects in a precise way and compares results from literature with those from its own investigations (see Chapter 5.3.4).

Alkalis and reducibility: The influence of alkalis on reducibility is well researched and significant. The influence on the reaction rate is correlated with the ionic radius of alkali metals. Figure 3-12 shows this correlation for alkali and earth alkali elements in their ionic states. Here, a difference between K and Na in terms of reducibility is identified. K is expected to show a higher increase in reducibility than Na due to a bigger atomic diameter of the ion. Bahgat¹²⁴ shows that a maximum reducibility is reached at a total content of 1–3 % K_2O in the sample. With higher addition, the reduction velocity decreases again. However, for temperatures $>1000^\circ\text{C}$ no change in reducibility by alkalis was measurable. In line with the work of Davies,¹¹⁸ the increase in reducibility starts at 0.4 wt-% K_2O and rises linearly up to 1.2 wt-% K_2O (reducibility doubles from 0.4 to 1.2 wt-%). Other authors also point out the influence of K/Na on reduction and define alkali metals as activators for iron ore reduction (hematite to iron¹²⁵ as well as wuestite to iron,¹²⁶ whereat the step from wuestite to metal is affected more). In particular, pellets are a key point of interest in this research because the relations between alkali input on pellet stability and furnace permeability were observed¹²⁷ (see also alkalis and swelling). Concurrently, investigations on mechanical values as well as reducibility were conducted. These show the increase in reducibility by small amounts of K/Na. The results will be discussed in comparison with the analysis of this research in Chapter 5.3.4, in correlation with thermodynamics (activation energy) and kinetics (chemical/diffusion controlled). However, investigations on reducibility in the mentioned literature have been carried out on natural and artificial materials—for example, $(\text{K,Na})_2\text{SiO}_3$, $(\text{K,Na})\text{Cl}$, or $(\text{K,Na})_2\text{CO}_3$ impregnation before or during sintering. For the testing procedure of the present thesis, these considerations were evaluated and included.

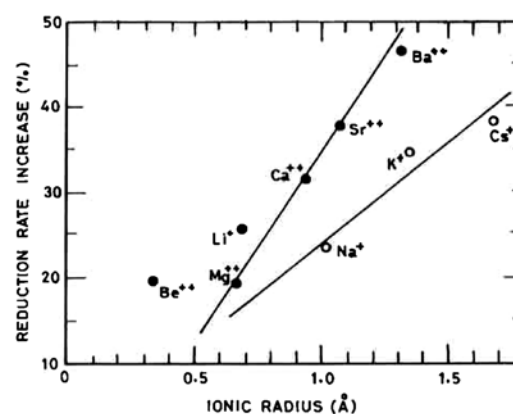


Figure 3-12: Increase in reaction rate of iron oxide in correlation with the ionic radius of alkali and earth alkali elements²⁸

Alkalis and mechanical properties: In general, alkalis increase the loss of strength of ferrous burden materials.²⁸ Low temperature breakdown (LTB) tests show that alkalis lead to a detrimental effect on the stability of pellets and sinter. Clear reasons have not been found yet, but relations with higher reducibility are obvious.²⁸ Davies¹¹⁸ describes the surface reduction from hematite to magnetite as the main cause for higher stress and, consequently, of weakening. Fluxed pellets have not shown these significant effects due to more slag bonding inside these pellets. Sinter with medium basicity showed adverse properties after LTB (high disintegration). Iljana gives examples of the influence of additives on mechanical behaviour.^{128,129} He assumes that K leads to cracks in pellets (olivine bounded). The reason is the migration of K inside the particle and the formation of fibrous iron at the cracking boundary. In total, a significant increase in the abrasion index after reduction was observed for magnetite pellet grades. The investigations for this research focus on degradation, abrasion, and the swelling or sticking of lump ore, pellets, and sinter (see Chapter 5.3.4).

Alkalis and swelling: Swelling is the abnormal growth of particle geometry during reduction of more than 400%. At high temperatures (~1000°C), alkali metals lead to extreme swelling of pellets. Consequently, porosity increases and strength drops. The gas flow is affected by compacted, broken pellets and the higher amount of dust.²⁸ During stepwise reduction of iron ore pellets (magnetite-wuestite metal) under CO/CO₂ atmospheres at 1000°C, a volume change was observed for alkali-treated and untreated materials. The volume increases the most from hematite to magnetite, leading to brittle, magnetite interim products. The formation of metallic iron normally leads to restabilization. The comparison of K-dotted with non-dotted samples showed different types of iron nucleation.¹³⁰ Ende et al.¹²⁷ separate the total swelling into normal and anomalous swelling. Normal swelling is caused by the volume of change during phase transformation (especially from hematite to magnetite, a lower effect from magnetite to wuestite, and no effects from wuestite to iron). This type of swelling is also observed in alkali-free materials during reduction. Anomalous swelling is linked to the placing of K/Na into the crystallographic structure. This makes the anomalous swelling independent of the phase transformation and the oxidation degree. The swelling can be controlled by additives or slag formers. Acidic compounds bind the alkalis, whereas basic additives shift the alkalis to the iron-bearing phases, leading to higher swelling rates.

Alkalis and melting: For ironmaking reactors, the influence of K_2O and Na_2O on oxidic systems is significant. Due to the low melting temperature of alkali oxides, even compounds with CaO , SiO_2 , and Al_2O_3 show lower transition temperatures than the pure substances (e.g. T_m of SiO_2 decreases from $1713^\circ C$ to $1089^\circ C$ for Na_2SiO_3 ; see Figure 5-33). In that context, Figure 3-13 shows the influence of K_2O addition to the CaO - SiO_2 system.

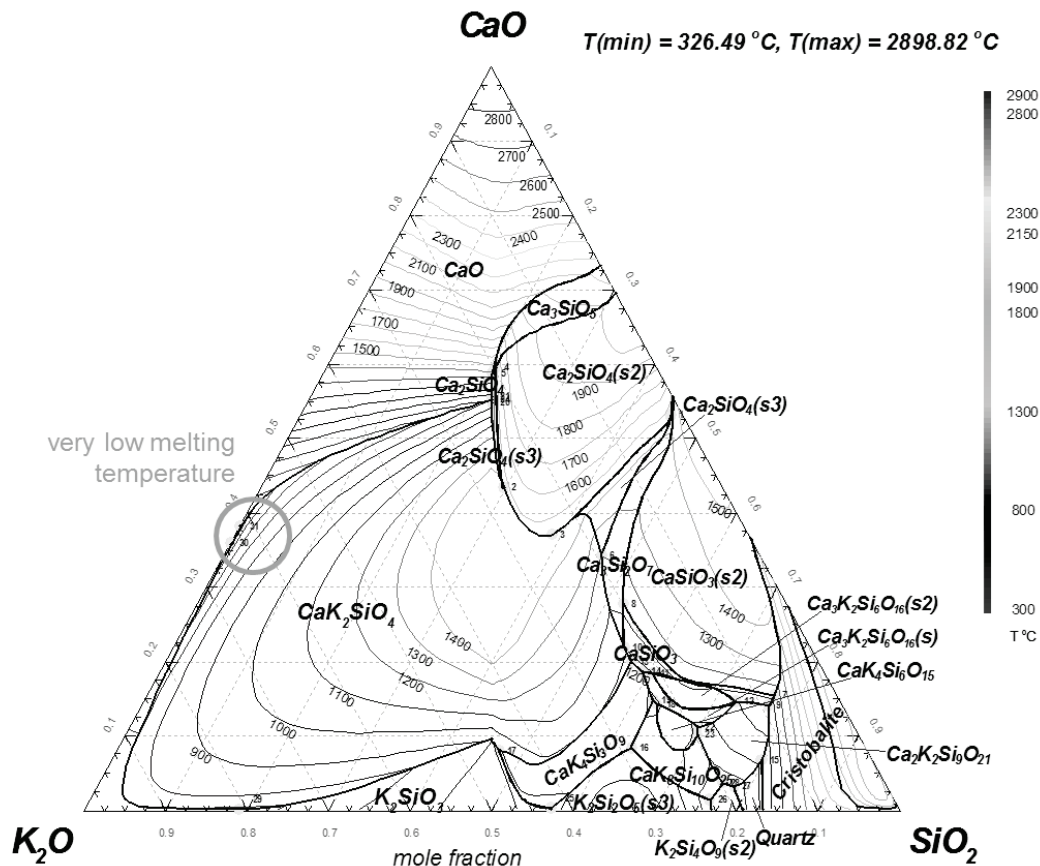


Figure 3-13: Ternary system for CaO - SiO_2 and K_2O projection, including the isothermal lines for T_m for different compositions (pressure = 1 atm)⁹³

The melting temperature can drop to $<500^\circ C$ (see grey area in Figure 3-13 with the minimum at $326^\circ C$, caused by a low-melting eutectic of CaO and K_2O at 62 mol-% K_2O), which has effects on the burden materials stability and melting range of the cohesive zone, and, consequently, on permeability and pressure drop. Although investigations on the softening or melting behaviour of burden materials with varying contents of FeO and alkali oxide have been performed in earlier research,³⁶ the effects are not clear yet. The addition of Na_2O showed a decrease in solidus temperature, especially for pellets and the corresponding slag compositions (high SiO_2 content). For CaO/Al_2O_3 -rich slags, the decrease in the melting temperature was not high and, in some cases, not even measurable. Especially for industrially used materials (reduced pellets and sinter), the effect of FeO_{liquid} formation is larger than the addition of alkali oxides. Moreover, in terms of viscosity, the effect of FeO is higher than the added content of alkali oxides. These considerations are the basis for the investigations of this research on the melting range of alkali-treated and -reduced burden materials (see results and discussion in Chapter 5.4).

3.4 Previous Problems and Approach of Work

As described in the previous chapter, alkalis mainly occur as harmful elements during ironmaking. Based on these considerations, this work took a closer look at the interaction between burden material and alkali compounds. The approach by the microscopic analysis of influenced materials was derived from former research work in the field of iron ore reduction.^{54,131} Investigations have been done in the field of iron ore reducibility and characterization of reduction mechanisms for lumpy and fine iron carriers. Based on these, a closer look at the process behaviour of ferrous materials had to be taken under a higher load of alkalis in the reactor. Higher amounts of dust and enlargement of the cohesive zone are two aspects that needed to be linked to fundamental mechanisms of ironmaking. Therefore, an approach was considered that simulates the whole ironmaking reactor from the top to the bosh region. The total path of the iron carrier was separated into alkali assimilation (upper shaft), reduction, and mechanical stress (lower shaft), as well as softening and melting (cohesive zone). Each zone of the reactor was linked to a certain methodology, which will be described together with the testing results and the evaluation in Chapter 5.

Another point of view is the total alkali balance of ironmaking processes (BF and direct/smelting reduction processes). The literature review shows that a clear determination of the alkali flows in a reactor is difficult due to the enrichment inside the reactor. Furthermore, even the mapping of alkali compounds (cyanides, carbonates, etc.) is a necessary tool for the evaluation of alkali flows. In addition, the literature shows the difficulties in the balancing of alkalis. Therefore, a new type of model was developed to illustrate the alkali balance of an ironmaking reactor. To reach a successful result, this model is based on thermochemical fundamentals to depict the chemical reactions and on a new model layout to implement data from the mass balance. In particular, the modelling of smelting reduction processes in correlation with alkali metals is a new topic. Further information about the layout, results, and validation of the model is contributed in Chapter 4.

4 Macroscopic Effect of Alkalis: Modelling of Ironmaking Reactors

Sixthly, his learning must comprise Architecture, that he himself may construct the various machines and timber work required underground.

Georgius Agricola, De Re Metallica

To gain a full understanding of ironmaking processes, thermochemical modelling has become essential over the last few decades. Moreover, in the field of alkalis, calculation using thermochemical programs is especially helpful. An alkali model for ironmaking processes was developed within the frame of this work. Based on a multi-reaction-area model, a standard BF model was defined and the alkali flow inside the reactor was calculated. Several variations of parameters were used to evaluate their influence on the alkali distribution. In addition, other ironmaking processes like the COREX[®] and FINEX[®] processes were investigated in this work.

4.1 Layout of the Alkali Model for Ironmaking Reactors

The alkali model consists of an input file that is operated by the user and the thermochemical calculation file. The user document is based on a multi-zone model created with Microsoft Excel,¹³² the thermochemical calculations are performed by the program Factsage[™]. The user inserts the needed parameters in two data sheets. The sheets contain the input masses, chemical analysis, and the most important process parameters (for an example, see Table 4-2). Furthermore, the profiles for gas composition, temperature, and pressure are defined by these data sheets. This makes a connection with other calculation models (for instance, a raceway model or an alternative slag model.) possible. The necessary data for the input will be described in Chapter 4.2.1.

The initial point of the model is the slag phase. The discharge of alkalis by the slag phase and the generation of alkalis in the BF take place there. The alkali distribution between the gas phase

and the slag phase in relation to the temperature, pressure, and basicity is calculated by an empirical model. The slag model is only calculated by Excel. Chapter 4.2.2 will discuss the outline of the slag model.

Next, 14 separated zones are fed with information about gas composition, temperature, pressure, and alkali flow from the input sheets and the slag model. These reaction zones will be described in Chapter 4.2.3. Each zone gives information to the program Factsage™,⁷⁵ which calculates the thermochemical equilibria automatically (linked to Excel by a macro code). The results (stable alkali compounds) are sent back to the Excel file. This is done for each zone. Because of the melting and vaporizing temperatures of alkali compounds (mainly from 100–1000°C), a high ratio condenses or solidifies within the reactor. Gaseous compounds and dust enter the higher zones, while solid and liquid compounds descend into the lower zones of the reactor. The alkali cycle starts to build up. After an iterative calculation, the result simulates the alkali distribution of a steady-state ironmaking process. The base for the multi-stage model is the interaction of the alkalis with the gas phase (in kmol per hour). This was chosen due to the high impact of gaseous reactions on the alkali cycle. The size of the reaction areas is defined by the gas profile (T, p, GOD) over the reactor height. The edge of the reaction area is defined by isotherms (more details in chapter 4.2.3).

In general one step for the iteration is equal with one hour of operation. The slag phase emits a constant amount of alkalis into the reactor and the calculated alkali flow starts to converge. After 200-300 steps (depending on the process conditions) the material flow reaches a steady state. The abort criterion is reached if the evaporated amount of alkalis from the slag is equal with the amount of alkalis in the top gas.

The fundamental layout is similar for the BF and smelting reduction processes.

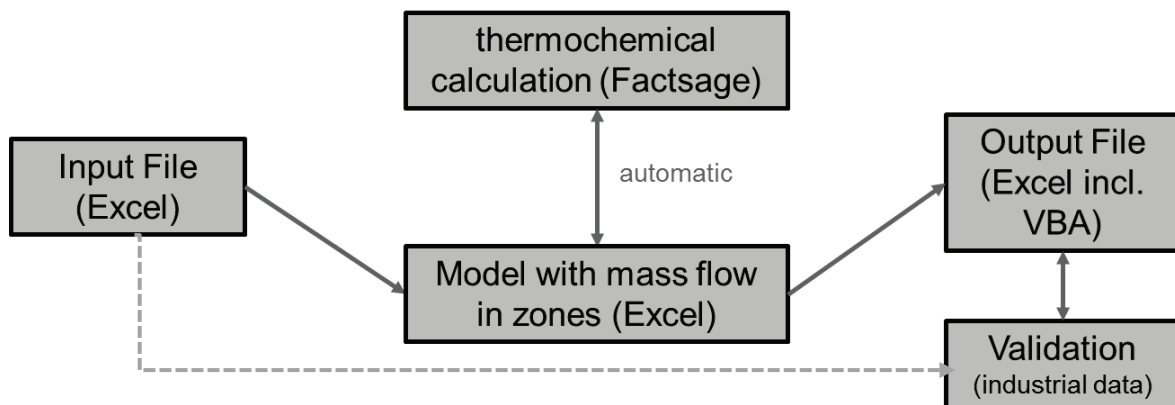


Figure 4-1: Connection between single elements of the model¹³²

Finally, the calculated data is post-processed and can be compared with data from industrial plants. This output sheet also provides information for the validation of the model. The approach involved a deviation analysis between calculated and measured values for the products.

Figure 4-1 gives an overview of the single process steps and their connections. Further information about the outline (including the program codes) and the handling can be taken from the User Manual.¹³²

4.2 Alkali Model for the Blast Furnace Process

The alkali model for BF ironmaking is based on a multi-stage model with a slag zone and seven independent reaction zones. To describe the input parameters, the outline, and the results, a standard BF was defined. Later, variations of chosen process parameters were used to evaluate their influence on the alkali flows within the reactor.

4.2.1 Data Input and Profiles of the Standard Blast Furnace Model

Before the calculation begins, the following important parameters have to be added into the file: Analysis and input masses: The input materials such as ferrous burden materials and fuels are inserted into the model in terms of their masses per ton of hot metal (tHM) and their chemical analysis (K and Na content in wt-%). For further calculations, all charged alkalis are seen as alkali silicates, which means that the total alkali load will descend in a stable manner to the slag phase. The input and output analysis for the standard BF are derived from industrial charged materials and products.^{19,115,133} These are summarized in Table 4-1.

Table 4-1: Exemplary data of potassium and sodium in input and output materials derived from literature for standard BF model^{19,36,115,133}

Charged materials	Input masses [kg/tHM]	Chemical analysis	Input alkali metals [kg/tHM]
Sinter	1000	0.17% K/0.06% Na	1.66 kg K/0.59 kg Na
Pellets	300	0.04% K/0.04% Na	0.12 kg K/0.11 kg Na
Lump Ore	300	0.08% K/0.03% Na	0.25 kg K/0.09 kg Na
Coke	400	0.21% K/0.07% Na	0.83 kg K/0.30 kg Na
Coal (PCI)	100	0.05% K/0.05% Na	0.05 kg K/0.05 kg Na
Total Input			2.91 kg K/1.14 kg Na
Product	Output masses [kg/tHM]	Chemical analysis	Output alkali metals [kg/tHM]
Hot Metal	1000	<0.003% K+Na	0
Slag	230	1.08% K/0.37% Na	2.484 kg K/0.851 kg Na
Dust (top gas)	10	0.21% K/0.19% Na	0.021 kg K/0.019 kg Na
Sludge (top gas)	3	0.50% K/0.10% Na	0.015 kg K/0.003 kg Na
Washing water			0.031 kg K/0.029 kg Na
Total Output			2.551 kg K/0.902 kg Na
Discrepancy			0.35 kg K/0.02 kg Na

The data of the products is needed for the comparison with the calculated results, but they have no further impact on the calculations. The difference between input and output is based on industrial data. The discrepancy is normal. It is caused by deviations during measurement and the increase of the alkali stock in the reactor.

Temperature, pressure, and gas composition: Temperature, pressure, and gas profiles are derived for all reaction zones from top gas and hot blast parameters. Table 4-2 shows the process parameters for the standard BF model. By multiplying the oxygen content with the gas volume, calculation of the total oxygen in the blast [kmol/h] is possible. The further reactions with carbon to CO (raceway reactions) give the total CO amount [kmol/h] in the lowest zone. On

the other side, the specific gas streams in the top gas are received by multiplying the vol-% of the gas with the total gas volume [kmol/h]. The results give the gas flows in the highest reaction zone. For the other zones, the gas volume is a combination of the described boundary areas (top-highest and raceway-lowest) with gas profiles from the literature³⁵ (see Figure 2-3).

Moreover, for the temperature and pressure profile, the boundary conditions (top and raceway areas) are inserted by the top gas and hot blast properties (see Table 4-2). Based on top gas temperature and flame temperature and top pressure and blast pressure, the profile for the total reactor height is calculated according to empirical profiles from the literature³⁵ (see Figure 2-3). The pressure is always mentioned as the total pressure (pressure absolute). The temperature of the model describes the gas temperature, not the temperature of the solid material. For the implementation of a horizontal temperature profile, a temperature range can be added to simulate the cold edge and hot centre zones ($\pm 150^\circ\text{C}$ for the standard BF). Further details in line with the single reaction zones will be described with the outline of the multi-stage reactor in Chapter 4.2.3.

Table 4-2: Process parameters for the outline of the reactor profiles and the following thermochemical calculations for the standard blast furnace model

Top gas properties		Hot blast properties	
Top gas temperature	150	Temperature [$^\circ\text{C}$]	1150
CO [vol-%]	21	Blast pressure abs. [bar]	2.15
CO ₂ [vol-%]	21	Blast humidity [%]	4
H ₂ [vol-%]	3	Gas volume [m ³ /tHM]	1000
Top pressure abs. [bar]	1	O ₂ content [vol-%]	23
Gas volume [m ³ /tHM]	1500	Flame temperature [$^\circ\text{C}$]	2200
Hot metal/ Slag		Slag composition	
Temperature [$^\circ\text{C}$]	1420	CaO [%]	50
Slag basicity (B ₃)	1000	SiO ₂ [%]	50
Productivity [tHM/h]	50	Al ₂ O ₃ [%]	0
Slag volume [kg/h]	13500	MgO [%]	0
		Rest (K ₂ O, MnO, S, TiO ₂ , Fe ₂ O ₃ , Na ₂ O)	0

For the slag reaction zone, the slag temperature, the productivity, and the slag composition are mentioned. These values are directly linked to the activity $a_{\text{K}_2\text{O}}$ in the slag phase.

Dust ratio: For the construction of the alkali model and, in particular, the formation of a circulation, a kinetic factor called dust ratio was included. It gives the ratio of an ascending dust fraction compared to the dust, which is deposited and descends in the reactor. The dust factor has to be inserted as an input parameter. Based on literature and own calculations, the dust factor for a successful modelling is between 30–40 mol-%. More details will be presented in the multi-stage model description of Chapter 4.2.3.

4.2.2 Slag Model

The evaporation of alkali-based gases (K_{met} , KCN, Na_{met} , NaCN) mainly occurs in the slag zone of the ironmaking reactors.^{96,107,109,113} Moreover, in the alkali model, the initial point for the alkali flow inside the reactor is based on the produced slag. Therefore, all alkalis of the input material first enter the slag phase as silica-bounded K_2SiO_3/Na_2SiO_3 . There the silicate decomposes into K_2O/Na_2O and SiO_2 (see Equation 3-1 for K). The silica and the alkalis dissolve in the slag and leave the reactor by the slag phase. Only a specific ratio of alkalis reacts with the dissolved carbon and nitrogen of the liquid phases (according to Equations 3-2 and 3-3). To model this complex interaction, the main parameters were determined according to Figure 4-2. To simplify the total reaction, a homogeneous liquid slag phase and a gaseous phase interact in the hearth of the BF.

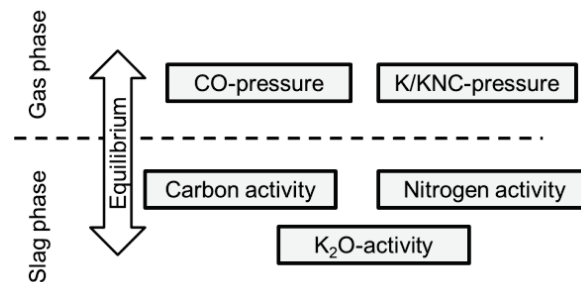


Figure 4-2: Simplified equilibrium conditions for the reduction and evaporation of alkalis in the slag phase

Based on Equations 3-1 to 3-6, the molar ratio of K and KCN (similarly for Na and NaCN) in the gas phase for the equilibrium reactions is determined.

$$x_K = \sqrt{\frac{k \times a_{K_2O} \times a_C}{x_{CO} \times p_{ges}^3}} \quad 4-1$$

$$x_{KCN} = \sqrt{\frac{k \times a_{K_2O} \times a_C^3 \times a_N^2}{x_{CO} \times p_{ges}^3}} \quad 4-2$$

The following parameters are involved in the reaction:

The molar ratios x_K and x_{KCN} of the gas phase are the results of Equations 4-1 and 4-2, and they give the equilibrium composition between slag and gas phase. Further calculations in the bottom zone lead to the amount of gaseous $K_{(g)}$ and $KCN_{(g)}$ per ton hot metal. To picture the equilibrium composition, the equilibrium constant k has to be considered. It is calculated from the free reaction enthalpy ΔG of each reaction through Equation 4-3.

$$k = e^{-\frac{\Delta G}{R \times T}} \quad \text{with} \quad \Delta G = \Delta H - T \times \Delta S \quad 4-3$$

The CO of the gas phase is the product of the K_2O reduction by carbon and it affects the equilibrium in terms of CO partial pressure. It is calculated by the mol-% of CO in the gas phase above the slag (CO generated by full combustion of the hot blast oxygen) and the total gas pressure in the hearth.

The carbon activity in the liquid phase affects the reduction of the dissolved K_2O . An increase in carbon activity leads to higher amounts of K and KCN evaporation. Derived from the low oxygen potential in the hearth zone of the BF (no FeO in the blast furnace slag, carbon saturation of the hot metal), the carbon activity of the liquid phases can be determined as $a_C=1$.⁷⁴

The nitrogen activity in the melt is calculated based on Equation 4-4. It combines the interaction parameter, the equilibrium constant, and the partial pressure of N_2 in the gaseous phase. The

interaction parameter f_N combines the reactions of N with other elements like C, O, etc. For defined conditions in the BF hearth (1600°C, C-saturated hot metal), it has the constant value 3.606. The equilibrium constant k_N between dissolved nitrogen and gaseous N_2 depends on the slag temperature and follows for the liquid phase an empirical equation of Turkdogan.⁷⁴ Equation 4-4 combines the interaction parameter and the equilibrium constant with the partial pressure of N_2 in the gas (law of Sievert). The nitrogen activity directly influences the KCN evaporation according to Equation 4-2.

$$a_N = f_N \cdot k_N \cdot \sqrt{p_{N_2}} \tag{4-4}$$

with $f_N = 10^{(0,557)} = 3.606$ for liquid phases (1600°C) and $k_N = 10^{\left(\frac{-188}{T_{slag}} + 2.76\right)}$

The most complex parameter of Equations 4-1 and 4-2 is the activity of the alkali oxide. The main parameters for a_{K_2O} are the slag temperature and the slag composition. According to Ivanov¹⁰⁹ and Abraham,¹⁰⁶ higher temperatures lead to more evaporation as well as to a higher basicity. In order to include these connections in the model, a specific slag model was developed, which combines empirical data with thermochemical equations and kinetics. Due to the importance of the basicity for the activity of the alkalis in the slag, the optical basicity Λ is included. Each single slag compound (CaO, SiO₂, Al₂O₃, MgO, MnO, K₂O, etc.) is connected with a specific, theoretical optical basicity Λ_{th} .¹⁰⁹ The sum is calculated by Equation 4-5 and it gives the total optical basicity of the mixture. Meanwhile, x gives the molar ratio of a compound in the slag and n is the number of oxygen atoms of each compound (e.g. n=2 for SiO₂, n=3 for Al₂O₃).

$$\Lambda = \frac{\sum x_i n_i \Lambda_{thi}}{\sum x_i n_i} \tag{4-5}$$

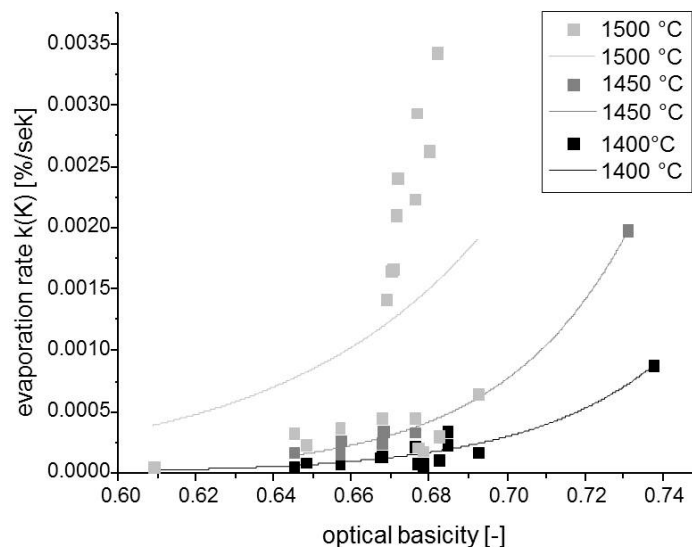


Figure 4-3: Evaporation rate for K (empirical) in connection with the optical basicity of blast furnace near-slag compositions and different temperatures (curves mathematically fitted to results and points from literature^{109,122,134–136})

According to Ivanov,¹⁰⁹ an increase in the optical basicity leads to higher activity and, furthermore, to higher evaporation rates k of metallic potassium. Tests have been carried out for optical basicity levels between 0.6 and 0.75 (this equates to a B_2 basicity of approximately 0.9–1.4). The temperature was varied from 1400 to 1500°C. The determined empirical evaporation rates are summarized in Figure 4-3 (with points from literature^{109,122,134–136} and the mathematically fitted curves at special temperature).

In addition, the increase in slag temperature (light grey for 1500°C) leads to higher K evaporation. Equations 4-6 and 4-7 are derived from the empirical data. They attempt to correlate the basicity and the temperature with $k(K)$. The mathematical approach was performed using different types of exponential regression. This model is limited to an optical basicity between 0.6 and 0.7 ($B_2=0.9–1.2$) and a temperature range of 1350–1500°C. For a higher basicity, the alkali capacity of the slag leads to lower evaporation rates $k(K)$ for industrial applications.

$$k_{K_2O} = \frac{a_1}{a_1 - a_2} \times (e^{(-a_2 \times \Lambda)} - e^{(-a_1 \times \Lambda)}) \text{ with } a_1, a_2 \text{ as mathematical coefficients} \quad 4-6$$

$$k_{K_2O} = m \times e^{(b \times T)} \quad \text{with } m, b \text{ as mathematical coefficients} \quad 4-7$$

Ivanov¹⁰⁹ also points out the direct correlation between evaporation rate $k(K)$ and the activity a_{K_2O} in the slag phase. This correlation was implemented in the model by an upscaling term, which is based on investigations by Fukutake,¹³⁴ Friedrichs,¹³⁵ Meimeth,¹²² Choi,¹³⁶ and Ivanov.¹⁰⁹ The upscaling term is necessary to reach industrial near conditions in the BF (experimental investigations were done under Ar flow, with small sample masses and under batch mode conditions). The determined K and KCN flow from the slag phase into the gas phase connects the slag model with the following multi-stage shaft model.

Other approaches have not led to the suggested mass transport from the slag phase into the reactor. For instance, models from literature¹⁰⁹ lead to excessively high evaporation rates; meanwhile, the calculation by thermochemical programs⁷⁵ delivers values that are too small. However, the slag model has to be developed according to alkali capacity. Therefore, empirical equations (see Equation 4-8)¹⁰⁶ can be included to illustrate the relation between K_2O capacity and activity.

$$\% K_2O \text{ in slag} = (1.44 \times \frac{\%CaO + \%MgO}{\%SiO_2 + \%Al_2O_3})^{(-7.47)} \quad 4-8$$

In addition, Biswas²⁸ names an activity of the alkali silicate of 0.02–0.06. The equilibrium pressure of K and Na above the slag phase is 0.025 and 0.015 atm.²⁸ In the standard BF model, an equilibrium pressure of approximately 0.002 atm is reached for the evaporation of realistic values, which shows the discrepancies between the modelling and measured data.

4.2.3 Multi-stage Shaft Reactor Model

The results of the slag model for the metal and cyanide flow into the reactor are the initial points for the calculation with the thermochemical program Factsage™ (version 7.0; FactPS database).⁷⁵ The gas flow from the slag area (also named zone 8) is separated into a hot and a cold column. In each column, the gas flow ascends from zone 7 to zone 1. Zone 7 represents the lowest zone (comparable with the bosh area). The gaseous and dust product of zone 1 (comparable with the furnace top) exits the reactor by the top gas. Each reaction zone acts as an ideal stirred reactor, where the alkali compounds have enough time to react with the process gas to their most stable composition. The main constituents of the gas mixture are CO, CO₂, N₂, CH₄, H₂, and H₂O in different ratios depending on the reaction area. The gaseous fraction fully rises into the next reaction area. The liquid and solid compounds are separated into an ascending and a descending dust fraction,³⁶ which flow into both higher and lower areas. The movement of liquid or solid particles into lower and higher zones is mainly caused by the rise of droplets and dust particles by the process gas flow. Biswas²⁸ also highlighted the separation of fine carbonates into the ascending gas and the descending burden column.

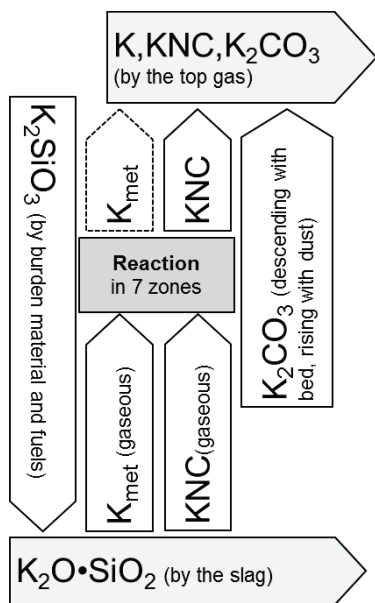


Figure 4-4: Simplified alkali flow in the reactor for the reaction model⁴³

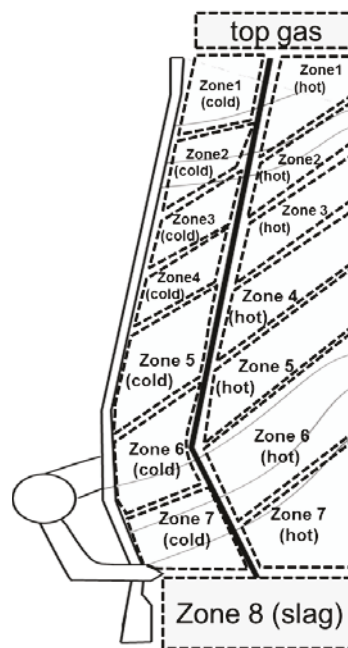


Figure 4-5: Reaction areas of the multi-stage model and the separation into cold and hot zones

Based on industrial investigations,³⁶ this factor is between 30–40% (35% for the basic model) of the total liquid and solid mass fraction. The rising and descending of the alkali compounds lead to the formation of a circulation similar to the observed alkali cycle in the BF. This circulation between zone 7 and zone 1 is an iterative process that leads to an output above zone 1 (top gas). Besides the vertical temperature profile, it is necessary to define a horizontal temperature profile. This is done by the separation of the BF into a colder and a hotter column (see Figure 4-5). The gas flow and the alkali flow from the slag phase for the standard BF is separated 50/50 mass-% into two independent systems. The circulation of the alkali compounds leads to a steady-state mode after a certain number of iterations. Then the ratio of alkali compounds in the top gas as well as the enrichment in the specific reaction zones can be determined.

Table 4-3: Reaction zones of the standard blast furnace, including temperature, pressure (absolute), and gas composition derived from industrial data^{21,28}

Reaction Area	Blast furnace zone	Temperature (hot/cold area)	Pressure (abs.)	Gas composition[mol-%]
Top gas	Top	160°C	1.0 bar	22% CO, 23% CO ₂ , 3% H ₂ , 4% H ₂ O, 48% N ₂
Zone 1	Top	300/50°C	1.0 bar	22% CO, 23% CO ₂ , 3% H ₂ , 4% H ₂ O, 48% N ₂
Zone 2	Heating zone	550/250°C	1.1 bar	22% CO, 23% CO ₂ , 3% H ₂ , 4% H ₂ O, 48% N ₂
Zone 3	Heating zone	650/350°C	1.1 bar	27% CO, 19% CO ₂ , 4% H ₂ , 2% H ₂ O, 48% N ₂
Zone 4	Heating/soaking zone	950/650°C	1.2 bar	31% CO, 14% CO ₂ , 5% H ₂ , 1% H ₂ O, 49% N ₂
Zone 5	Soaking zone	1050/750°C	1.3 bar	37% CO, 4% CO ₂ , 6% H ₂ , 1% H ₂ O, 52% N ₂
Zone 6	Boudouard zone	1250/950°C	1.4 bar	42% CO, 7% H ₂ , 52% N ₂
Zone 7	Melting zone	1550/1250°C	1.5 bar	42% CO, 7% H ₂ , 52% N ₂
Slag zone	Metallurgical zone /hearth	1420°C	2.15 bar	42% CO, 7% H ₂ , 52% N ₂

To simplify the model, a selection of the most important gas compounds and alkali compositions was performed (see schematic alkali flow of Figure 4-4). The following compositions are considered in the standard model:

Gaseous: H₂, CH₄, N₂, O₂, H₂O, CO, CO₂, K, KCN, Na, NaCN;

Liquid: H₂O, Na, NaCN, K, KCN, K₂O, Na₂O, K₂CO₃, Na₂CO₃;

Solid: C, H₂O, Na, NaCN, K, KCN, K₂O, Na₂O, K₂CO₃, Na₂CO₃;

Halides, silicates, and further alkali compounds play a minor role for the circulation and are neglected by the calculations of the multi-stage model. For the slag model (Chapter 4.2.2), the input by silicates and the interaction of K/Na with all slag compounds is mentioned.

Table 4-3 shows the gas and temperature profile of the standard BF. The lower regions near the bustles are characterized by high temperatures (>1000°C) and higher contents of H₂ (2–6%) and CO (up to 35%) in the process gas. This leads to a gas mixture with a high reduction potential, as it is necessary for the reduction of iron ores to metallic iron. In higher regions of the BF, the reduction potential decreases as a result of the increasing amount of CO₂ up to 24%. Moreover, the temperature decreases to 150–200°C at the top. The pressure mainly depends on the hot blast pressure in the tuyeres, which is derived from the burden distribution of the charging program and the melting behaviour of the ferrous burden material and the additives.

4.2.4 Results and Alkali Distribution in the Standard Model

The main outputs of the calculations carried out by the alkali model for the BF are summarized in this chapter.

The basis for the evaluations is a 50 tHM/h-standard BF. The results for the calculation are summarized in Figure 4-6. The main result is the calculated amount of different alkali compounds over the BF height. The zones are based on the multi-stage model of the previous chapter. The process conditions and input parameters belong to the standard BF, with parameters described by Table 4-1, Table 4-2 and Table 4-3. The total input of alkalis is 2.9 kg K and 1.14 kg Na (see Table 4-1).

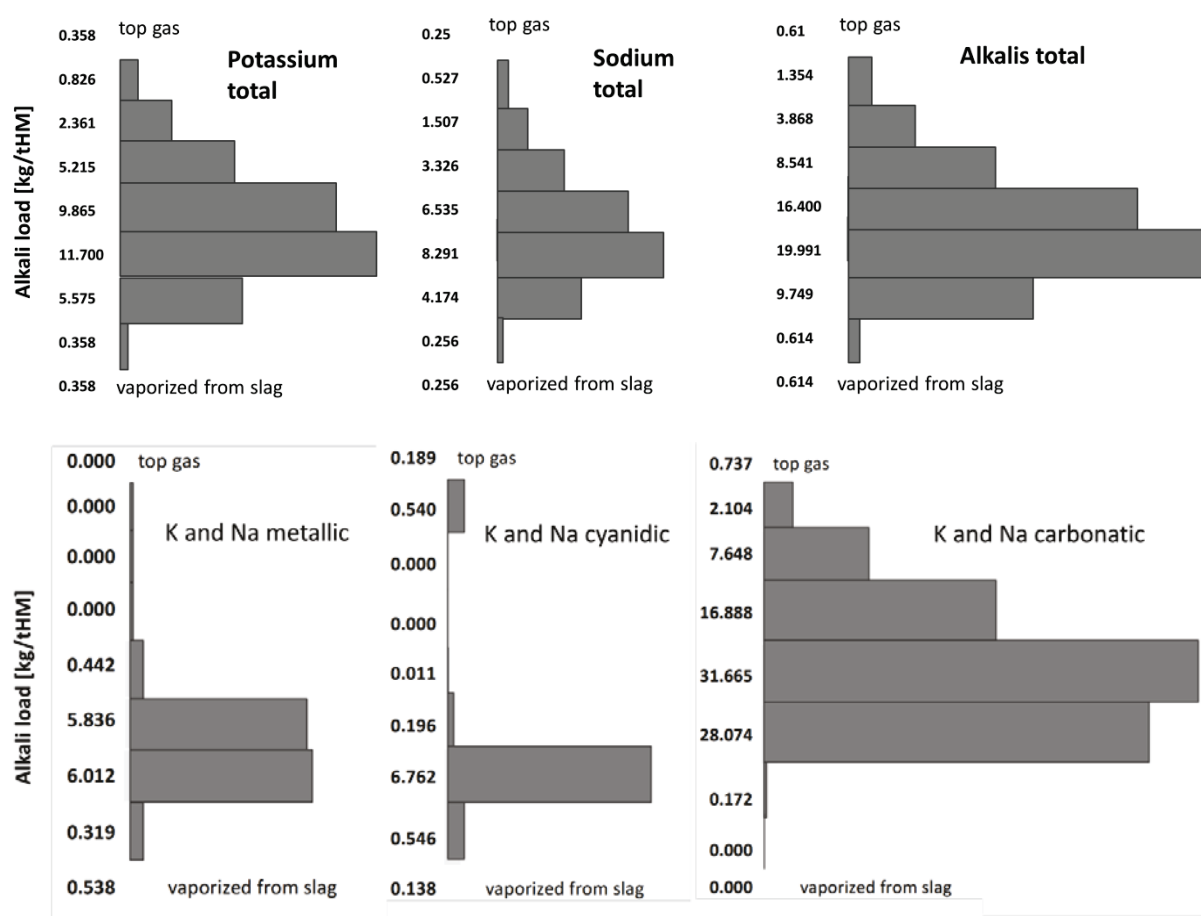


Figure 4-6: Distribution of alkali compounds for the standard blast furnace over the furnace height⁴³

The calculated capacity of the slag is 3.44 kg K+Na/tHM, which is approximately 85% of the total alkali load. The evaporation of alkalis by the slag reaches 0.614 kg/tHM (15% of the total load), whereas 0.358 kg is K and its compounds, while 0.256 kg is based on Na. Data from the literature³⁶ shows similar values. Approximately 50% of the alkalis are generated as metals by the slag; the rest is mainly KCN/NaCN. The lower areas of the blast furnaces are characterized by a higher amount of K/Na and KCN/NaCN. Because of the drop in the process temperature below 1000°C, the stability of cyanides and metallic alkalis decreases. In connection with the lower reduction potential of the process gas (higher CO₂ and H₂O contents), carbonates become more

stable. Gaseous compounds rise inside the reactor, while solid and liquid compounds descend in the reactor (65 wt.-%) and ascend as little droplets (35 wt.-%).³⁶ Like in industrial operations, an increase of the alkali load in the middle of the BF can be observed. The maximum occurs in a temperature range between 650°C and 1050°C. For the basic model, a load of nearly 20 kg K+Na (19.9 kg/tHM) is calculated. The alkali load decreases up to the top area. Finally, the alkali flow exits the reactor by the top gas (0.614 kg K+Na/tHM). The molar ratio between cyanides and carbonates in the top gas is nearly 1:2 (32 molar-% to 68 molar-%). However, this ratio is highly dependent on the temperature profile of the top zone.

For the description of the horizontal alkali distribution in the BF, two separated areas—a cold one outside and a hot one at the centre—are defined by the multi-stage model (see Figure 4-5). The temperature difference between the gas flow (homogeneous gas temperature for the cold and the hot zone) and the reaction areas is ± 150 °C. This leads to different equilibria for the alkali compounds at the centre and the edge zone. The calculations of the basic model show different values for the hot and cold areas (see Table 4-4 and Figure 4-7), the total load, and the ratio. The alkalis enter the lowest reaction areas from the slag zone with a ratio of the elements K and Na of 50%/50%. The alkali load of the top gas is the sum of zone 1.

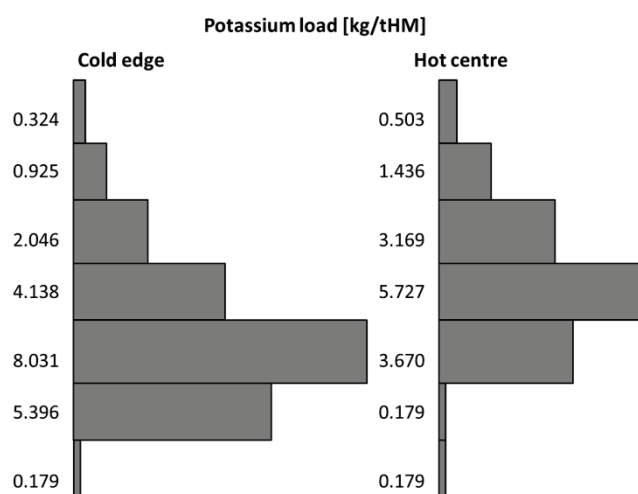


Figure 4-7: Distribution of alkali compounds for the standard blast furnace ⁴³

Table 4-4: Specific alkali load and ratios of the outer cold and inner hot zones (standard blast furnace for slag temperature 1420°C and $B_2=1$)⁴³

Reaction Area	Temperature [°C] (hot/cold area)	K-load [kg/tHM and %]		Na-load [kg/tHM and %]	
		cold area (edge)	hot area (centre)	cold area (edge)	hot area (centre)
Zone 1	300/50°C	0.32 kg (39%)	0.50 kg (61%)	0.19 kg (37%)	0.33 kg (63%)
Zone 2	550/250°C	0.93 kg (39%)	1.44 kg (61%)	0.56 kg (37%)	0.95 kg (63%)
Zone 3	650/350°C	2.05 kg (39%)	3.17 kg (61%)	1.23 kg (37%)	2.10 kg (63%)
Zone 4	950/650°C	4.14 kg (42%)	5.73 kg (58%)	2.47 kg (38%)	4.06 kg (62%)
Zone 5	1050/750°C	8.03 kg (68%)	3.67 kg (31%)	4.77 kg (58%)	3.52 kg (42%)
Zone 6	1250/950°C	5.40 kg (97%)	0.18 kg (3%)	3.23 kg (78%)	0.94 kg (23%)
Zone 7	1550/1250°C	0.18 kg (50%)	0.18 kg (50%)	0.13 kg (50%)	0.13 kg (50%)

In reaction area 6 to 5 the cold area has a higher alkali load (temperature range of appr. 1000°C). This peak changes in reaction area 4 to 1, where the hot area has the higher alkali load. The main alkali discharge from zone 1 to the top gas comes from the hot area (more than 60 %).

To summarize the results of the standard BF model, Figure 4-8 illustrates the input and output flows. The left side shows the input data of the charged materials. The data is based on industrial measurements. The mass of the single burden fractions is shown in kg/tHM. The ferrous burden is dominated by sinter. The fuel rate is typical for European BFs with ~500 kg coke+coal/tHM. The load of Na and K is shown in kg/tHM. In addition, the ratio of the alkalis in the burden fraction compared to the total load is mentioned. Coke and sinter can be seen as the main sources for K and Na. On the right side of the figure, the output streams are presented. The hot metal is the biggest fraction, but it does not contain alkalis. The slag fraction carries the highest alkali load. The top gas fraction (mass is shown for dust plus sludge) is separated into dust, sludge, and washing water. Here, the total Na or K in the products as well as the ratio to the total alkali output are mentioned. The masses are from measured industrial data. The alkali load of the products is calculated by the standard BF model.

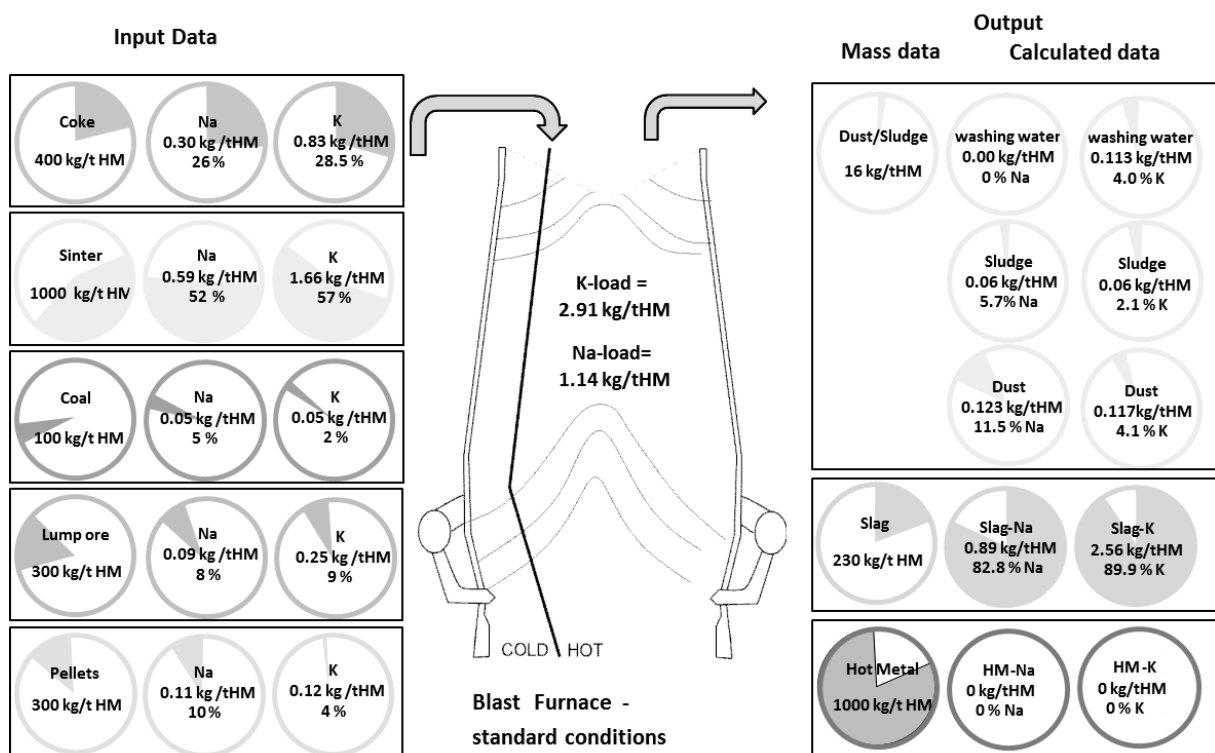


Figure 4-8: Alkali flow of standard 50 tHM/h blast furnace

4.2.5 Validation of Standard Model

For validation of the basic model, a comparison with industrial data and trends from literature was essential.

Validation of the output streams using industrial data:

The data from industrial operations show that the alkalis are divided into two main fractions: the slag phase and the top gas. The top gas fraction is separated during waste gas treatment into dust, sludge, and washing water. In particular, the industrial values give a total K input of 2.9 kg K (all values in this chapter are for one ton of hot metal). Whereas 2.48 kg of K is dissolved in the slag phase as $K_2O \cdot SiO_2$, the rest (0.067 kg K) enter the top gas as carbonates, cyanides, and metals. The behaviour of Na is similar. The total Na input is 1.1 kg. It is separated into the slag phase (0.85 kg Na) as $Na_2O \cdot SiO_2$. The rest is discharged as carbonates, cyanides, and metals by the top gas (0.051 kg Na). All the data are for a 50 tHM/h BF with input material and process parameters similar to the standard BF in Table 4-1.

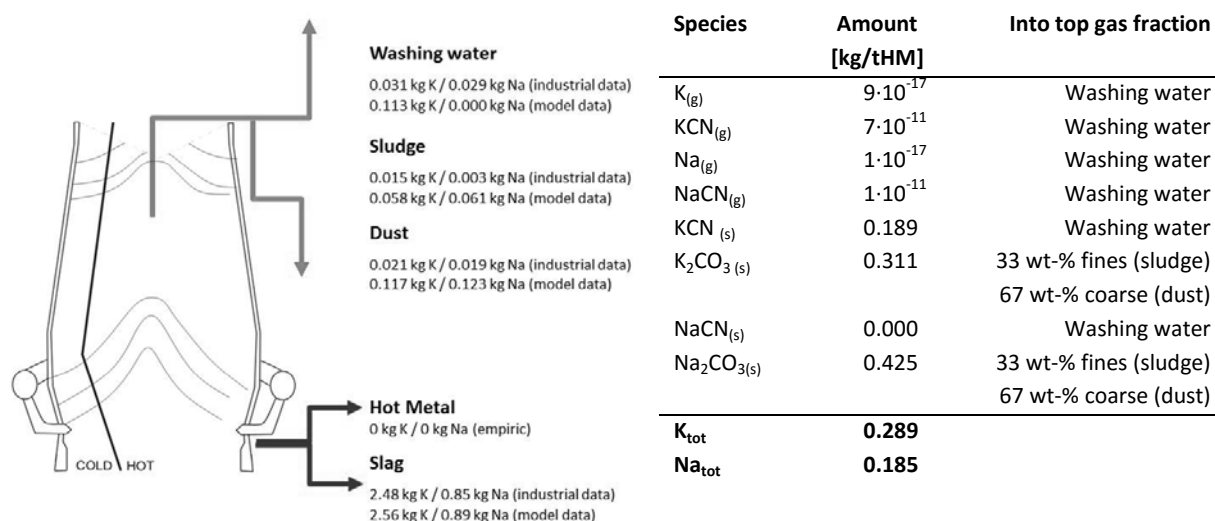


Figure 4-9: Comparison of calculated values (see values of single compounds in the table and the allocation to top gas fractions on the right) with analysis from industrial operation⁴³

To compare the measured data with the calculated values, Figure 4-9 provides an overview. For the slag phase, the model calculation gives a value of 2.56 kg/tHM K and 0.89 kg Na. This means a deviation between the measured and calculated data of <4%. In this context, Biswas²⁸ determines that equal inputs of K and Na lead to equal amounts in the slag. Although this is not seen in all BFs (Table 3-2), even in the calculations performed for this research, the ratio of alkalis from the input material into the slag phase is similar with 80–90%.

For the top gas, the individual treatment steps have to be considered. The top gas is treated using several cleaning steps: cyclones, electrostatic filters, and washing units. This waste gas treatment produces dust, sludge, and washing water as solid and liquid (aqueous solution) leftovers. These cleaning steps also separate the alkali compounds from the gas flow—particularly 0.021 kg/tHM K (0.019 kg Na) into the dust fraction, 0.015 kg/tHM K (0.003 kg Na) into the sludge, and 0.031 kg/tHM K (0.029 kg Na) into the washing water of the wet cleaning unit.

In the alkali model, the K/Na compounds are linked to the specific top gas fractions: 67% of the solid carbonates in the top gas enter the dust phase (coarse particles), 33% of the solid carbonates enter the sludge phase (fines particles), and the cyanides and metal compounds enter the washing water. The results for the calculated standard BF are summarized in Figure 4-9 (right). The amount of metallic K/Na and NaCN is low ($<10^{-10}$ kg/tHM). The thermochemical stable product is mainly solid carbonate. Here 0.31 kg $K_2CO_{3(s)}$ and 0.425 kg $Na_2CO_{3(s)}$ enter the dust and the sludge. At the edge of the top zone at $<150^\circ\text{C}$, even KCN is stable. This cyanide enters the washing water. NaCN shows no stability under top gas conditions. In total, 0.289 kg K and 0.185 kg Na leave the reactor by the top gas.

If you carefully weigh the calculated as against the measured data of Figure 4-9, the difference is significant in some aspects. For the K balance, the calculated values are up to five times higher; for Na, it is even more. This discrepancy is mainly caused by the mass balance of the industrial data,¹¹⁶ whereas alkali input and output usually show a deviation of $>10\%$ during industrial operation. After the evaluation of the output streams, the internal flows are examined more closely.

Evaluation of the internal flows and alkali accumulation in the reactor:

A main task of the alkali model is allowing a look inside the reactor to provide knowledge about the K and Na flow. The following methods of determining the alkali distribution in the reactor are mentioned in the reviewed literature: On the one hand, an analysis of sampled material according to the K and Na content is possible after a BF shutdown.^{119,137} On the other hand, models¹¹⁹ were also developed to predict the distribution.

For validation of the internal alkali cycle, mainly sources from the reviewed literature were employed. Figure 4-10 summarizes data from the literature and the model¹⁰⁹ (Figure 4-10 [middle]), and from industrial data¹¹⁹ (Figure 4-10 [right]). As a result of these investigations, an enrichment of K in the coke ash (middle) or total alkali oxides in the coke ash (right) was clearly measurable. This enrichment is confirmed by the calculated values for K+Na (Figure 4-10, left). However, the data from the literature focuses only on the alkali load in the coke fraction (the developed alkali model focuses on the total mass flow through a fixed region in the BF and does not mention the fractions of coke or ferrous burden material, which are in that region). For a thermochemical prediction of values like the K content in the coke ash, additional information about the burden movement would be necessary, which was not mentioned in the model of this work.

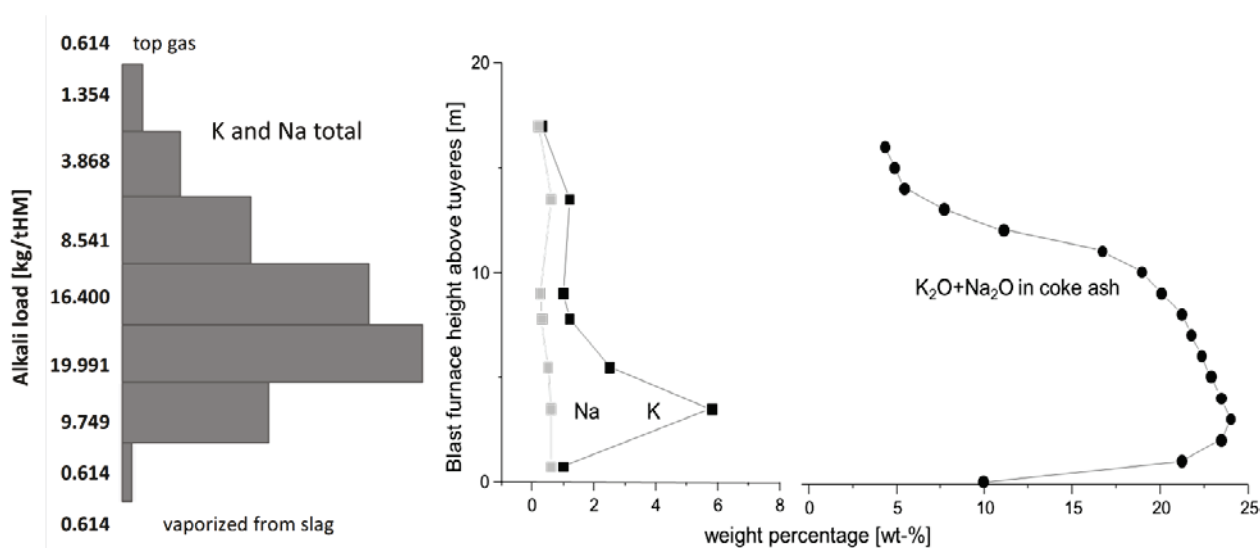


Figure 4-10: Alkali load (total potassium and sodium) for a basicity $B_2=1$ and a slag temperature of 1420°C (standard model), and comparison with the alkali distribution (middle: total K/Na in coke; right: sum of K/Na-oxidic in the coke ash) over the blast furnace height based on industrial investigations^{36,109,119}

Other investigations by an experimental BF¹³⁸ also show the increase of K_2O and Na_2O in SiO_2 -based fluxes like dunite, olivine, and gravel over the reactor height. Figure A-8 (see Appendix) presents the chemical analysis of these materials after the operation. The rise in alkali content is linked to the enrichment of K/Na-containing compounds in the process gas. Especially for high SiO_2 -bearing gravel, the K_2O content enlarges by the factor 10. However, these trends can be seen as a confirmation of the basic outline of the standard alkali model.

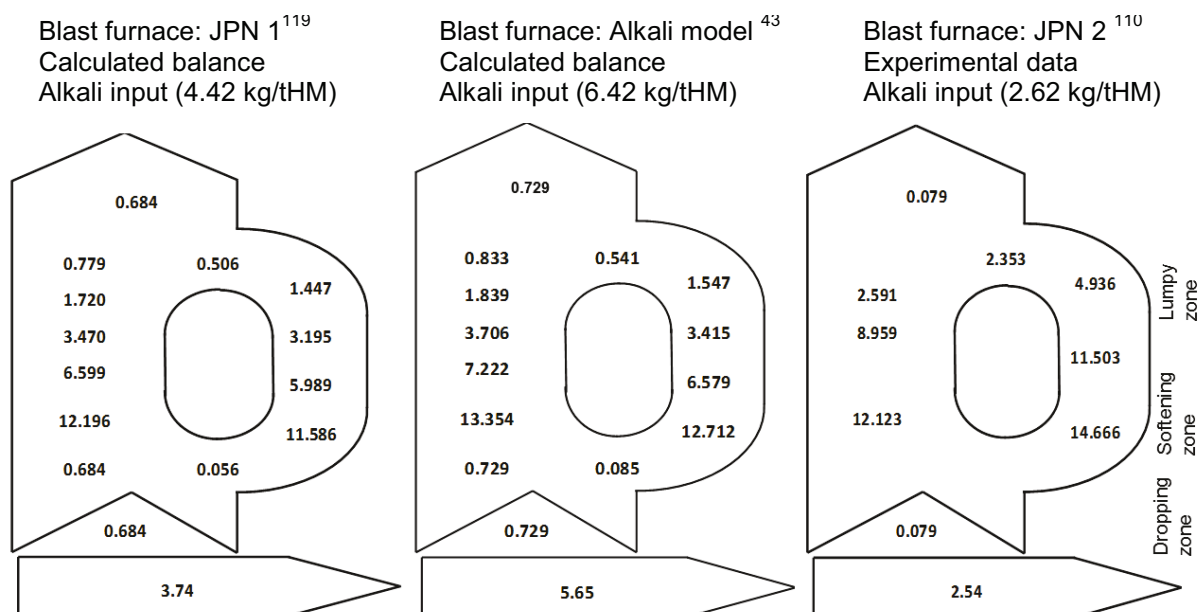


Figure 4-11: Comparison of alkali flows [kg K/tHM] between own alkali model (middle for standard blast furnace with high alkali input), prediction from other models (left), and from industrial data (right)

In general, for the analysis of the accumulation of alkalis in the reactor, several complex methods can be performed. Figure 4-11 shows three different alkali balances from three different approaches (calculated from model, own calculations, and experimental data). The basis for all three balances is a small-scale BF (approximately 50 tHM/h). Although the load varies between 2.6-6.4 kg K+Na, the enrichment is determined clearly in all three methods. The values of the internal alkali flow are linked to certain zones in the BF (dropping, softening, and lumpy zones). Especially the discrepancy between calculated values (left and middle) and the experimental data show the complexity of the alkali balance. However, the model reaches empirically determined values for industrial plants (11–19 kg/tHM) in the lower shaft region.

4.2.6 Parameter Analysis with Focus on Slag Properties

For the parameter analysis, four different variations of the standard model were performed. First, two examples of a BF with small variations in pressure and slag composition plus tapping temperature will be presented. Second, the impact of slag temperature on alkali generation and enrichment will be shown. Finally, the slag basicity and its influence on the alkali distribution will be examined.

Results of BF—variation 1 (hot blast pressure):

In the following, an example of a small modification of the pressure profile in the hearth is presented. According to industrial conditions a pressure drop through the stock and the tuyeres of 0.5 bar is considered. This leads to a lower pressure at the slag phase compared to the standard model. For the calculation, the pressure of 2.15 bar (see Table 4-3 at the slag zone) is replaced by a reduced value of 1.65 bar. The data for the input and output materials (see Table 4-1), the process parameters (see Table 4-2) and the reactor profiles (see Table 4-3 except the slag zone pressure) remain the same as for the standard blast furnace in chapter 4.2.1. Figure 4-12 shows the results of the BF-variation 1 (values and black columns) in contrast to the standard blast furnace (grey columns). The lower pressure in the hearth leads to a higher alkali generation by the slag phase due to Equation 4-1 and 4-2. The amount increases by 37% from 0.61 to 0.84 kg Na+K per tHM. Consequently, also the load in the higher regions rises.

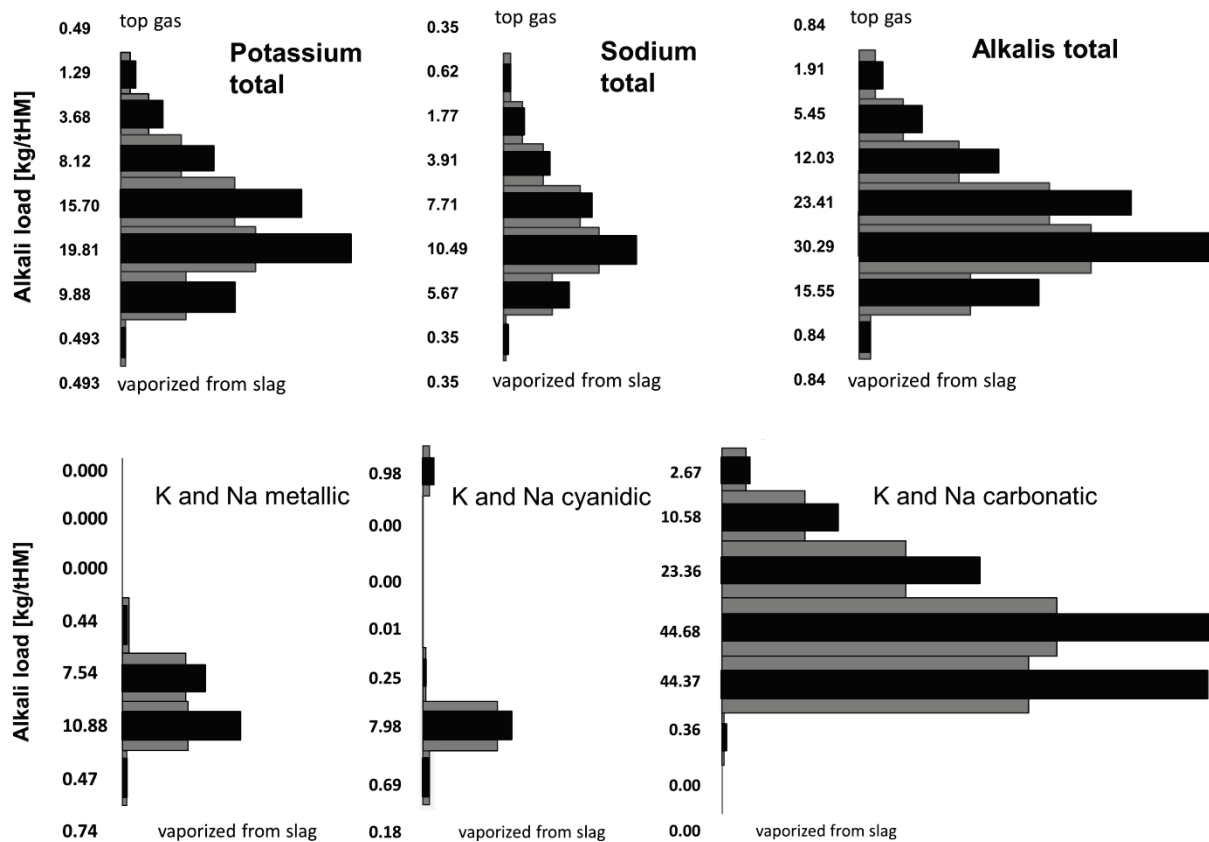


Figure 4-12: Alkali distribution over the furnace height in kg/tHM (sum of cold and hot areas; values and black columns for BF-variation 1, grey columns for the standard BF)

The peak in zone 5 increases by 50% from 20 kg to 30.3 kg Na+K per tHM. The stability areas for cyanides and carbonates remain constant for both cases. Generally, all compounds rise by the lower pressure in the hearth, although the pressure, gas and temperature profile of the reactor is not changed compared to the standard model. Variation 1 is seen as better model than the standard BF due to the implementation of the pressure drop through the stock and the tuyeres. Additionally, it shows the need of further examinations, especially of the dust rate.

Results of BF—variation 2 (slag properties):

In the following, an example of a small variation of slag parameters is presented. Table 4-5 shows the variation of T_{slag} of +5K and an increase in slag basicity to $B_2= 1.16$ with an industrial near-slag analysis containing CaO, MgO, SiO₂, Al₂O₃, MnO, S, TiO₂, and other elements. The top gas and hot blast properties and, consequently, the temperature, pressure, and gas profiles remained the same. The result of the K distribution over the BF height is shown in Figure 4-13. In addition, the amounts of metallic and cyanide K compounds are illustrated.

Table 4-5: Process parameters of the blast furnace—variation 1 (including the parameters of the standard blast furnace)

Hot metal/ Slag		Slag composition	
Temperature [°C]	1425 (1420)	CaO [%]	44 (50)
Slag basicity (B_2)	1.16 (1.0)	SiO ₂ [%]	31 (50)
Productivity [tHM/h]	50	Al ₂ O ₃ [%]	12
Slag volume [kg/h]	13500	MgO [%]	6
		K ₂ O+MnO+S+TiO ₂ +Fe ₂ O ₃ +Na ₂ O [%]	7

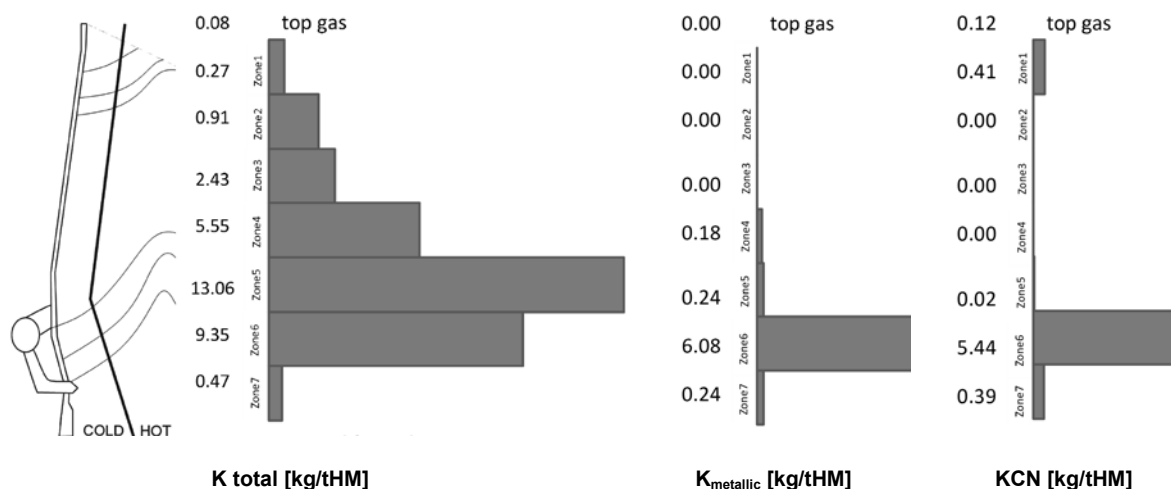


Figure 4-13: Distribution of total K and selected K compounds in the different reaction areas of the blast furnace (variation 2) in kg/tHM (sum of cold and hot columns)⁴³

Comparing the results of the standard BF (Figure 4-6) and variation 2 (Figure 4-13), the following statements can be made: By the defined slag variation, the total generated alkalis already rise by 30%. In particular, the K peak increases from 11.7 to 13.1 kg/tHM. The stability areas for K_{met} and KCN are similar to the standard BF because of the same gas conditions. Only the load is higher in variation 2 because of the higher alkali generation from the slag phase.

Variations 1 and 2 of the BF were important approaches for the model development and for the evaluation of process parameters. The slag temperature and basicity will be discussed next.

Evaluation of slag properties—temperature:

The next important step was evaluation of the slag parameters on alkali accumulation. As discussed by several authors,^{96,107,109,113} the slag parameters have a major influence on alkali flow inside the reactor. In particular, the temperature plays a major role in the equilibrium constant (Equation 4-3) and the evaporation rate (Equation 4-7). To determine the effect in the alkali model, calculations were performed with different slag temperatures. Figure 4-14 shows the mass transport of the alkalis and their compounds (derived from all compounds) in correlation with the slag temperature. The continuous lines with spotted points show the K/Na emission by the slag phase. Lower slag temperatures lead to less K/Na evaporation. It rises with the temperature. The dotted lines with the spotted points describe the amount of K (black) or Na (grey) that leaves the reactor with the top gas. The gradient is smaller than the evaporated masses in the BF hearth because of the influence of other parameters like top gas composition, temperature, and pressure. The lines with square points are linked to the enrichment in zone 5 (1050°C/750°C) for both K and Na. The enrichment reaches a total value of approximately 20–25 kg alkalis per tHM. Zone 5 was chosen for the evaluation because this area is also known by other authors^{36,139} as the region with the highest alkali load.

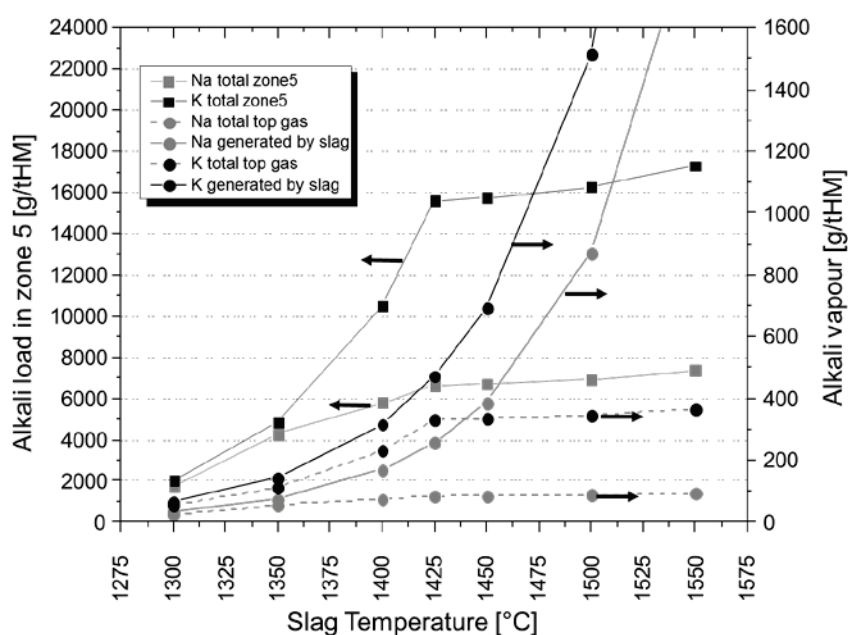


Figure 4-14: Influence of slag temperature on the alkali content in the reactor with the alkali load in zone 5 (square points), and the alkali vapour (spotted points) from the slag phase (continuous lines) and the top gas (dotted lines)⁴³

Evaluation of slag properties—basicity:

Another main factor for the alkali flow in the BF is the slag basicity. Acid compounds like silica lead to a higher discharge of K and Na by the slag phase and less evaporation into the reactor. Other slag compounds influence the evaporation due to their optical basicity¹⁰⁹ (see Equations 4-5 and 4-6). Table 4-6 summarizes the performed calculations for different slag compositions based on the basic model and a temperature of 1450°C. The calculations were carried out for the standard BF with five theoretical slag compositions. Slags 1 to 3 are simple two-component slags

with SiO₂ and CaO. The contents vary between 45–55%, while the basicity varies from 0.82–1.22. The change of the SiO₂ and CaO leads directly to a change in the alkali evaporation. At a basicity of 1.22, the evaporation rate is twice as high as at 0.82. The higher alkali flow from the slag into the reactor leads to a higher enrichment in the stack and bosh regions. The K load for zone 3 (lower stack region) is shown in Table 4-6. Like the evaporation, even the mass flow is twice as high with a higher basicity. For slags 4 and 5, Al₂O₃ and MgO were considered as well. The SiO₂/CaO ratio remains the same; up to 15% Al₂O₃ and 10% MgO are added. It is seen that the acidic character of Al₂O₃ leads to less K in the reactor by slag 4 compared to slag 2. In contrast to Al₂O₃, MgO acts as a basic compound in the slag and an addition leads to a higher formation of K by the slag. Moreover, the alkali load in the reactor rises with slag 5 compared to slag 2 or 4.

Table 4-6: Effect of slag composition on K/Na content in top gas and in the lower stack region of a blast furnace (zone 3)⁴³

Slag No.	Slag Composition (CaO/SiO ₂ /MgO/Al ₂ O ₃)	Basicity B ₂ /B ₄	Optical Basicity Λ	K in top gas [kg/tHM]	K enrichment [kg/tHM]
Slag 1	45%/55%/0%/0%	0.82/0.82	0.64	0.31	3.9
Slag 2	50%/50%/0%/0%	1.00/1.00	0.66	0.44	5.6
Slag 3	55%/45%/0%/0%	1.22/1.22	0.69	0.66	8.3
Slag 4	40%/40%/5%/15%	1.00/0.82	0.66	0.42	5.3
Slag 5	40%/40%/10%/10%	1.00/1.00	0.67	0.49	6.3

Review on a parameter study of the alkali model and further work:

To sum up, the following statements can be made after the parameter study:

- Although the temperature and gas profiles of the reactor remain the same, a change in the slag properties leads to a significant change in the alkali load of, for example, the stack and bosh regions.
- The slag model has to be developed further. The literature²⁸ shows that the alkali content of the outgoing slag seldom exceeds 2 wt-%. So, a maximum alkali load is seen in industrial operations. This maximum capacity of the slag phase is not implemented yet.
- The change of K₂O/Na₂O activity from the cohesive zone to the hearth is not considered yet. Instead, it is fixed by a stable value.
- By means of this model, the determination of areas with a high alkali attack on coke, burden material, and refractories is possible for different operation modes.
- The model also shows that a higher slag temperature can enrich the alkali load by up to 500%; in particular, there is a theoretical increase of T_{Slag} from 1300°C to 1600°C. Moreover, the basicity changes the evaporation of K from 0.31 kg/tHM (B₂=0.82) to 0.66 kg/tHM (B₂=1.22), which is more than the double. Overall, a low tapping temperature and a low basicity lead to higher discharge of K and Na by the slag phase and a decrease in the alkali load of the reactor.

4.3 Alkali Model for Smelting Reduction

Similar to the BF, other ironmaking reactors were examined as well. Especially because smelting reduction processes have not been evaluated with regard to alkalis so far, this topic was a major point of interest. For the evaluation of the alkali balance in smelting reduction processes (COREX® or FINEX®), the melter gasifier was examined more closely.

4.3.1 Fundamental Layout of the Alkali Model for the COREX® or FINEX® Process

For thermochemical reasons, the alkali carbonates and silicates are stable in the reduction steps of the process (see Figure 2-5 and Figure 2-6). Only afterwards in the melter gasifier do the high temperature and reducing compounds in the process gases become dominant. Based on these considerations, similar to the BF, a model for the melter gasifier was created. Again, the two main parts of the simulation are an empirical slag model (see Chapter 4.2.2) and a multi-stage reactor for the thermochemical calculation of stable alkali compounds (see Chapter 4.2.3).

Once again, the silicates reach the melter gasifier hearth, where they are reduced and boiled. The conditions in the melter gasifier and BF hearth are similar with regard to alkalis due to the similar reactor layout (as an in-bed reactor⁵¹). Consequently, the properties of hot metal (C=4.6/4.5%, Si=0.3/0.5%, Mn=0.3/0.1%, P=0.07/0.11%, S=0.03/0.02% for BF/melter gasifier)^{9,55} and the slag are similar. The FeO content of the final slag and the basicity B_2 are low (approximately 1.1–1.3). The tapping temperature is lower for the BF (1420–1450°C versus 1500°C for the melter gasifier).

These similarities and discrepancies lead to both similar and different aspects in the field of alkali reactions. Derived from the different paths concerning the gas conditions and the reaction equilibria in Figure 3-4, the following statements are defined:

- The alkalis enter both reactors mainly as silicates (K_2SiO_3 , Na_2SiO_3) via the burden material (gangue, binder) and fuels (coal/coke ash). Due to the thermochemical stability, they do not react until the hearth area. In the hearth, the alkalis dissolve in the slag phase and are partially reduced by the high carbon activity. Carbonates and oxides play a minor role for the alkali input.
- The alkalis evaporate from the slag phase into the reactor as metals or cyanides. They ascend in the reactor and get oxidized by CO_2 and H_2O (as well as by FeO). The lower temperature in the upper reactor areas leads to condensing and solidification.
- The melter gasifier is shorter, and it has a higher top temperature and pressure in comparison to the BF. This leads to a higher alkali load of the generator gas and less alkali enrichment in the melter gasifier. However, the slag is the main source for alkali discharge, as seen in the BF.
- Regards to the cyanide formation, a higher load of KCN and NaCN is expected in the BF. This is caused by the higher N_2 -content of the process gas. Own calculations (see chapter 4.4.2) also show a higher cyanide load in the BF. However, the formation of cyanides is a complex topic, which still has to be studied.

- In general, two types of alkali cycles are known: an internal and an external alkali cycle. In the BF, an internal circle forms over the reactor height. In addition, in the BF process, the recycling of dust by the sinter plant leads to the repeated input into the process chain (external cycle).

For the melter gasifier, an internal cycle also forms over the reactor height. Furthermore, two kinds of external cycles exist. The first one is connected with the hot gas cyclone. It separates the dust from the generator gas directly after the melter gasifier and feeds it back into the reactor. However, the melter gasifier, including the hot gas cyclone, is only a part of the total process. The second external cycle is formed by interaction with the reduction stage because the COREX® and FINEX® processes are both two-stage processes with a reduction and a smelting stage. After the melting aggregate and the hot gas cyclone, small amounts of dust can remain in the reduction gas. This dust can be filtered by the bulk in the reduction stage and the dust gets deposited at the solid ore/sponge iron. After the reduction stage, the solids are again charged into the melter gasifier by the iron carrier (e.g. DRI or HCI). This interaction between the reduction and smelting stages is not a part of this work.⁵⁵

A comparison between the melter gasifier and the BF based on the alkali distribution is discussed in Chapter 4.4.2.

4.3.2 Data Input and Outline of the Melter Gasifier

In this chapter, the input data and the profiles for the melter gasifier simulation are discussed.

Analysis and input masses: The masses of the charged materials per ton of hot metal (tHM) and the chemical analysis (K- and Na-content in wt-%) are the initial parameters for the simulation. They are inserted by an input sheet. For further calculations, all charged alkalis are seen as alkali silicates. All alkalis will descend in the reactor and get dissolved in the slag phase of the melter gasifier hearth. The input and output analyses for the melter gasifier are derived from industrially charged materials and products,⁵⁵ and summarized in Table 4-7.

Table 4-7: Exemplary data of potassium and sodium in input and output materials derived from industrial data⁵⁵ for the melter gasifier model

Charged materials	Input masses [kg/tHM]	Chemical analysis	Input alkali metals [kg/tHM]
HCl	1500	0.01% K/0.02% Na	0.13 kg K/0.23 kg Na
Additives (Quartz)	150	0.28% K/0.00% Na	0.43 kg K/0.00 kg Na
Coal	650	0.28% K/0.06% Na	1.85 kg K/0.38 kg Na
Coal (PCI)	150	0.05% K/0.05% Na	0.08 kg K/0.08 kg Na
Total Input			2.49 kg K/0.69 kg Na
Product	Output masses [kg/tHM]	Chemical analysis	Output alkali metals [kg/tHM]
Hot Metal	1000	<0.003% K+Na	0
Slag	300–330	0.75% K/0.21% Na	2.25–2.45 kg K/0.62–0.69 kg Na
Dust after hot gas cyclone	2.5–3.1	7.92% K/5.56% Na	0.20–0.25 kg K/0.14–0.17 kg Na
Average Output			2.56 kg K/0.82kg Na
Discrepancy			0.07 kg K/0.13 kg Na

Although the materials and analyses vary in the BF and melter gasifier model, all alkalis enter the slag phase as silicates in both models.

Temperature, pressure, and gas composition:

The temperature, pressure, and gas profiles are derived for all reaction zones from the generator gas and hot blast parameters. All used process parameters are summarized in Table 4-8.

Table 4-8: Process parameters for the outline of the profiles of the melter gasifier

Generator gas properties		Blast properties		Hot gas cyclone	
GG temperature [°C]	1050	Temperature [°C]	25	HGC temperature [°C]	735
CO [vol-%]	64.2	Blast pressure abs. [bar]	5.5	Top pressure abs. [bar]	5.5
H ₂ [vol-%]	16.0	Gas volume [m ³ /tHM]	400	Gas volume [m ³ /tHM]	2250
CO ₂ [vol-%]	13.3	Blast humidity [%]	0		
H ₂ O [vol-%]	6.3	O ₂ content [vol-%]	99.5		
N ₂ [vol-%]	2	Flame temperature[°C]	2000		
Top pressure abs. [bar]	4.5				
Gas volume [m ³ /tHM]	1500				
Hot metal/Slag			Slag composition		
Temperature [°C]	1500		CaO [%]	40	
Slag basicity (B ₃)	1.43		SiO ₂ [%]	35	
Productivity [tHM/h]	180		Al ₂ O ₃ [%]	15	
Slag volume [kg/h]	58500		MgO [%]	10	
			Rest (K ₂ O, MnO, S, TiO ₂ , Fe ₂ O ₃ , Na ₂ O)	0	

For the gas composition, all specific gases are calculated as kmol/h (see Chapter 4.2.1 for the BF). The profile of the gas composition is fitted between the raceway zone (lowest zone defined by the blast) and the dome area (highest zone defined by the generator gas) by a characteristic trend curve. The basis for the trend is taken from literature^{53,59} (see Figure 2-6).

Table 4-9: Reaction zones of the standard melter gasifier, including temperature, pressure (absolute), and gas composition derived from industrial data^{21,28}

Reaction Area	Melter Gasifier zone	Temperature (hot/cold area)	Pressure (abs.)	Gas composition [mol-%]
HGC	Hot gas cyclone	735°C	5.5 bar	64% CO, 13% CO ₂ , 16% H ₂ , 6% H ₂ O, 2% N ₂
Generator gas	Dome/freeboard	1050°C	4.5 bar	64% CO, 13% CO ₂ , 16% H ₂ , 6% H ₂ O, 2% N ₂
Zone 1	Dome/freeboard	1200/900 °C	4.5 bar	64% CO, 13% CO ₂ , 16% H ₂ , 6% H ₂ O, 2% N ₂
Zone 2	Dome/freeboard	1200/900 °C	4.5 bar	64% CO, 13% CO ₂ , 16% H ₂ , 6% H ₂ O, 2% N ₂
Zone 3	Dome/freeboard	1100/800°C	4.5 bar	70% CO, 13% CO ₂ , 12% H ₂ , 5% H ₂ O, 2% N ₂
Zone 4	Upper char bed	900/600 °C	4.55 bar	76% CO, 10% CO ₂ , 10% H ₂ , 4% H ₂ O, 2% N ₂
Zone 5	Upper char bed	1100/800 °C	4.8 bar	86% CO, 3% CO ₂ , 8% H ₂ , 3% H ₂ O, 2% N ₂
Zone 6	Lower char bed	1350/1050 °C	5.0 bar	99.75% CO, 0.25% N ₂
Zone 7	Lower char bed	1450/1750 °C	5.3 bar	99.75% CO, 0.25% N ₂
Slag zone	Hearth	1500 °C	5.3 bar	99.75% CO, 0.25% N ₂

The approach for the temperature and the pressure profile is similar. For the implementation of a horizontal temperature profile, a temperature range can be added to simulate the cold centre and hot edge zones ($\pm 150\text{K}$ for the melter gasifier). The difference to the BF (cold edge-hot centre) is caused by the central charging of cold coal briquettes from the top. Table 4-9 shows the temperature, pressure, and gas composition for all reaction zones, the slag zone, and the generator gas (sum of zone 1 cold+hot). In addition, the conditions for a further reaction zone—the hot gas cyclone (HGC)—are included.

For the slag zone, the slag temperature, productivity, and slag composition are mentioned in Table 4-8. These values are directly linked to the activity a_{K2O} in the slag phase.

Dust ratio and separation degree of HGC: For the construction of the alkali model and particularly the formation of a circulation, a kinetic factor called dust ratio was included. It gives the ratio of an ascending dust fraction compared to the dust, which is deposited and descends in the reactor. The dust factor has to be inserted as an input parameter. Based on the literature and the calculations performed as part of this research, the dust factor for a successful model is between 30–40 mol-%. More details have already been discussed in the description of the multi-stage model in Chapter 4.2.3. For the HGC, the separation rate had to be included. The value for the separated dust fraction, which moves back into the reactor by feeds, is fixed at 90%. However, variations of the separation rate were used to evaluate the impact on alkali enrichment in the reactor.

4.3.3 Results of the Standard Melter Gasifier

For the evaluation of the alkali balance of the melter gasifier, a closer look at the alkali distribution, and the alkali flows of input and output materials was taken.

The results for the standard melter gasifier are shown in Figure 4-15. At the top, the comparison between K and Na is mentioned, as well as the total sum of the alkali load. At the bottom, the three most important classes of alkali compounds are illustrated (left: metallic K+Na; middle: cyanide K+Na; right: carbonate K+Na). Based on these results, the following statements are made: The ratio of cyanides is lower at the bottom of the melter gasifier, but they are still stable. Above the lower char bed area, the amounts of cyanides are negligible. The carbonates behave similarly to those in the BF; the maximum is in the upper char bed region and the value decreases in the dome. In total, the load of carbonates is lower than in a comparable BF. Metallic K and Na are the main compounds in the dome area. They finally leave the melter gasifier by the generator gas as a main alkali compound (>90% of K and 60% of Na are charged out as gaseous metals).

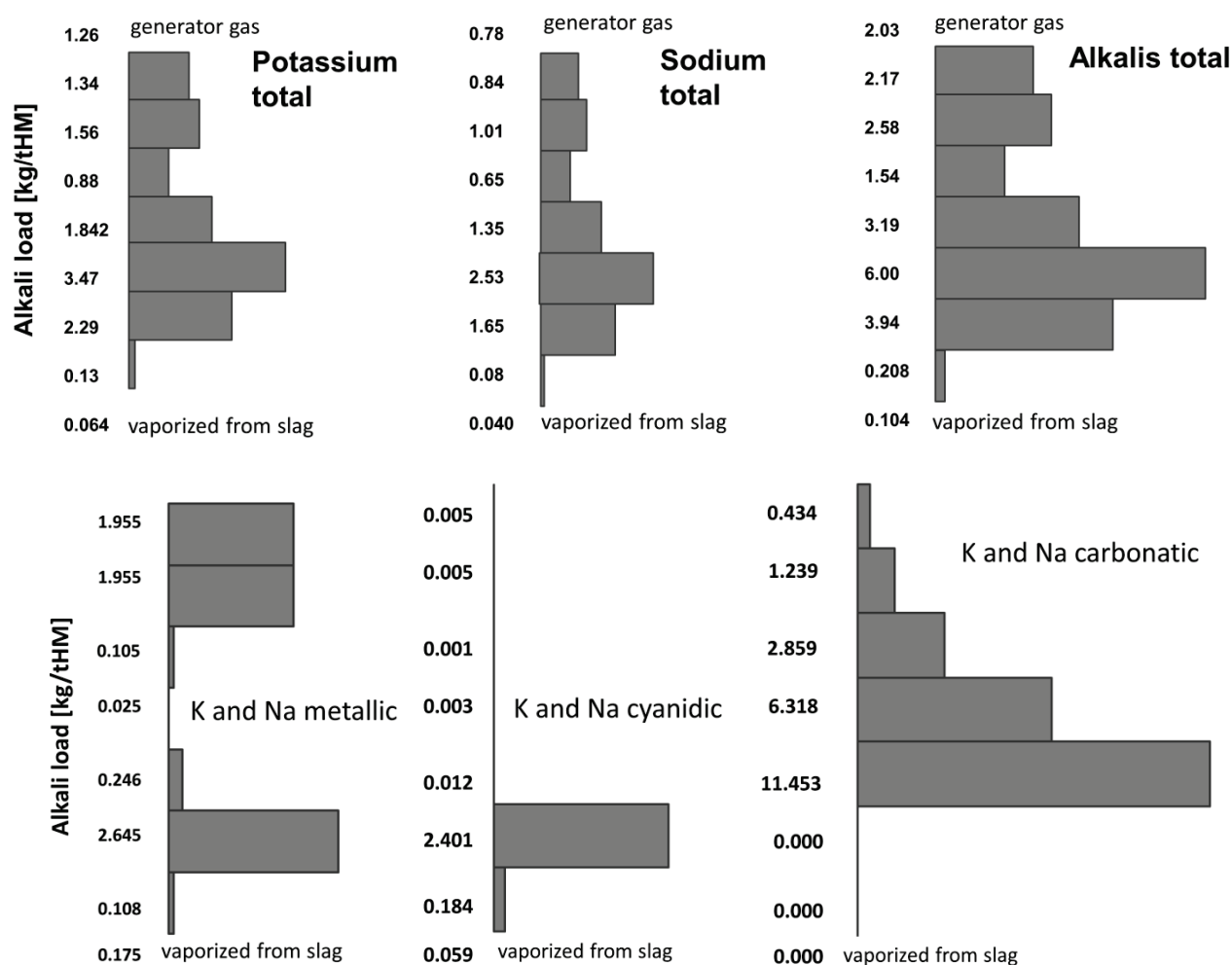


Figure 4-15: Alkali load for the standard melter gasifier (180 tHM/h, $T_{\text{slag}}=1500^{\circ}\text{C}$, $B_2= 1.1$, sum of cold and hot areas)

A special aspect of the melter gasifier model is the waste gas treatment by an HGC. In the HGC, the dust-loaded gas stream is calculated again for a temperature of 735°C . The gas composition remains constant for the generator gas and the HGC. An important factor is the separation degree of the cyclone (90% of the total solid and liquid alkali loads are removed from the stream and recycled). The HGC lowers the alkali load in the stream from 2.03 kg/tHM to 0.2 kg/tHM. The remaining dust (1.83 kg/tHM) is fed into zone 2. Figure 4-17 shows the effect of the dust recycling and a second alkali peak forms in the dome area. The main compound of this peak is metallic K/Na due to the high temperature and CO content in the process gas. To evaluate the influence of the external dust recycling, a variation of the separation degree of the HGC was performed. Through the change in the separation rate from 90% to 95%, the alkali load in the generator gas increases by more than 90% from 2.03 kg/tHM to 3.87 kg/tHM.

In addition to Figure 4-8 (BF), Figure 4-16 shows the mass balance of the standard melter gasifier. The input materials are on the left side, including the amount and ratio of the input masses (HCl, coal, coke, fluxes) and the ratio of the total alkali load for each mass fraction. On the left side at the bottom, the output data derived from the industrial operations of hot metal, slag, and dust (including the ratio of total output) is visualized. At the top, the calculated amount of K/Na in the different fractions including the ratio is shown (the dust of the external circulation of the HGC is also mentioned).

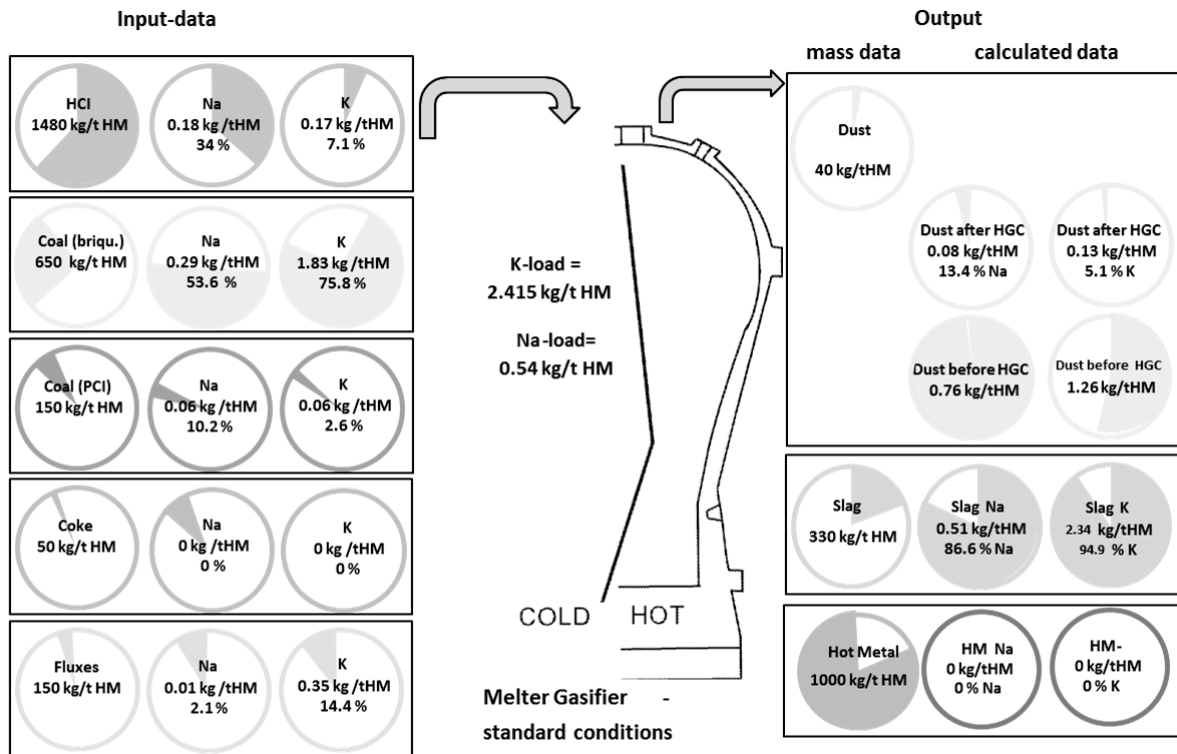


Figure 4-16: Alkali balance for the standard melter gasifier with input data and output masses from industrial data and calculated K/Na in the slag and dust

4.4 Discussion about Alkali Model

In the following chapter the outcome of the alkali model for both reactors is discussed.

4.4.1 Background of the Standard Blast Furnace Model

For the standard process a blast furnace with high alkali load (4.1 kg K+Na per ton hot metal) was chosen. The reason therefore is the local iron production by blast furnaces with high alkali-bearing materials. Consequently, the slag basicity B_2 is below 1, which is not typical for European blast furnaces. A slag with high silicon content has a high capacity for alkalis, which leads to a minor K/Na-emission into the reactor. However, the higher basicity combined with the lower content of alkalis in the charged material will lead to a similar dimension of the alkali cycle for other European blast furnaces. This is confirmed by data from literature (see Figure 3-8) and own investigations (see chapter 4.2.6). Another aspect for the evaluation is the size of the blast furnace. The standard model deals with a productivity of 50 tHM/h. This value is low compared to modern blast furnace operations. The size was chosen because of two different reasons. First, the production with furnaces of 50 tHM/h productivity is typical for local steel producers. The data from the local blast furnaces were essential for the model development. Second, the literature for the evaluation is based on blast furnace data with a similar size.^{110,119} The typical productivity of modern blast furnaces is up to 400 tHM/h. In the model the higher productivity will increase the total alkali flow in the reactor. The amount of alkalis per ton hot metal will depend on the gas volume in the reactor and can vary compared to the standard blast furnace. This point was also considered for the comparison between the blast furnace and the melter gasifier in the following chapter.

4.4.2 Comparison between Blast Furnace and Melter Gasifier

There are several differences between the two ironmaking reactors (see Chapter 2.1). For instance, the firing is done by tuyeres for both reactors but with different gas agents (BF: 23% O_2 and 77% N_2 ; melter gasifier: 99.5 % O_2). Furthermore, the diagrams in Figure 2-3 and Figure 2-6 show the differences in the temperature, pressure, and gas profiles. The pressure is lower for the BF operation. Starting from 2.15 bar at the raceways, the pressure drops to 1 bar at the top. The melter gasifier starts with 5.3 bar and shows 4.5 bar in the dome. The temperature is similar for both reactors at the hearth (although the tapping temperature for the melter gasifier is higher—1500°C versus 1450°C). It drops in the higher areas to $T < 1000^\circ\text{C}$. This decrease in temperature continues for the BF to a top gas temperature of 150°C.

Table 4-10: Important differences in the process layouts of the standard reactors

	Blast furnace	Melter gasifier
Slag temperature	1420 °C	1500 °C
Basicity $B_2/B_3/B_4$	1 / 1 / 1	1.1 / 1.4 / 1
Rising dust ratio	35 wt-%	35 wt-%
Productivity	50 tHM/h	180 tHM/h
Blast volume	1000 Nm ³ /tHM	400 Nm ³ /tHM
Hot gas cyclone	no	yes

For the melter gasifier, the dome at the top shows a higher temperature (1050°C) compared to the char bed (850°C). The process gas is characterized by a high nitrogen content (~50%) for the BF. The GOD increases over the furnace height (CO and H₂ are decreasing, CO₂ and H₂O are increasing) up to ~50%.

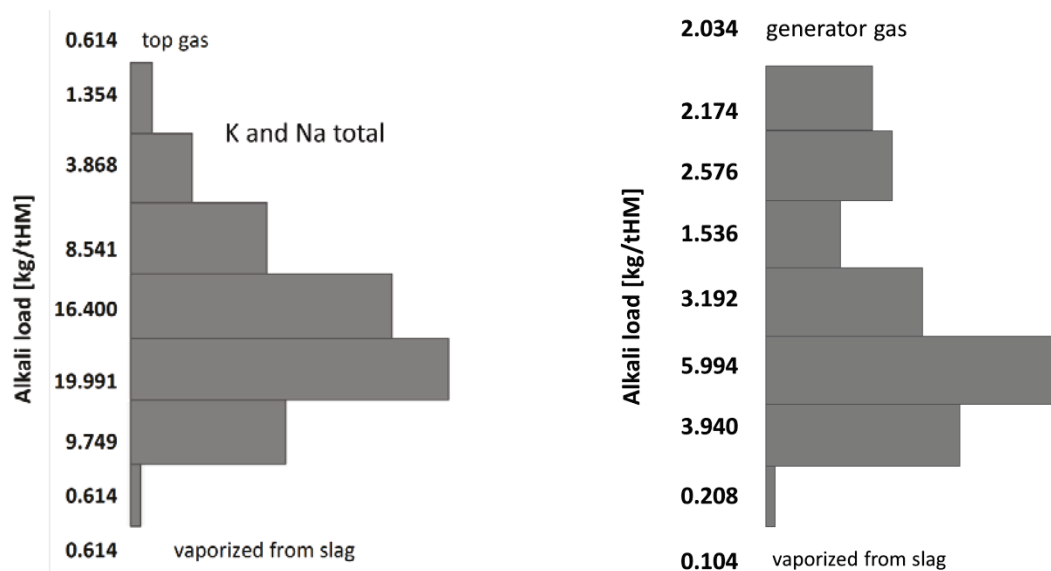


Figure 4-17: Alkali load (total potassium and sodium) for the blast furnace (left) and the melter gasifier (right)

In contrast, the melter gasifier shows no N₂ and mainly CO for the lower areas. The CO content only drops to values >65% in the dome area, which means a GOD of 10–15%. One important part of the melter gasifier is the HGC, which is located after the generator gas pipe. It separates the dust from the gas phase (separation degree of 90% for the model). The dust is recycled into the process by feed ducts, which are located above the char bed (see Figure 2-6). For the calculation, this recycled dust is considered in reaction zone 2. The temperature for the HGC was defined with 735°C for the calculation of the equilibrium.

For a comparison of the alkali flow in the BF and the melter gasifier, calculations were performed until the steady state for both reactors. Although both reactors are based on a similar multi-stage model, the following additional discrepancies in the process conditions have to be considered (see Table 4-10). The slag properties are quite different for temperature and composition. The melter gasifier slag is hotter and has a higher basicity caused by the higher ratio of MgO. The results for the alkali load over the reactor height are visualized in Figure 4-17 for the BF (left) and the melter gasifier (right). The enrichment is measurable for both reactors. From the start at the lowest zone (slag area), the BF shows higher values for the evaporated alkalis. The higher amount of gas and the lower pressure from the tuyeres are the main reasons. Both lead to the favoured transport of K and Na from the slag into the gas phase above the furnace hearth. Slag properties like a lower tapping temperature and similar basicity B₄ theoretically lower the alkali emission, but have minor consequences in these cases.

Table 4-11: Comparison of the main findings by the alkali model for blast furnace and melter gasifier

	Blast furnace	Melter gasifier
General	The high range of process gas composition, pressure, and temperature over the furnace height lead to the formation of complex alkali cycles. The enrichment is significant. The model simulates the concentration of alkali compounds in specific BF areas.	The melter gasifier is characterized by a dome region with high temperature. The process gas is defined by a high CO content (high reducing conditions). The recycling of dust from the HGC leads to a second peak in alkali enrichment above the upper char bed area.
Cyanides	The high ratio of N ₂ in the process gas leads to the formation of cyanides in the lower zones, as well as in the top region. The cyanides in the top region are separated mainly by the washing water from the waste gas flow.	Due to the injection of 99.5% oxygen through the tuyeres, the amount of alkali cyanides is negligible compared to other alkali compounds.
Top gas	The temperature of approximately 150–300°C (160 °C for the final top gas, 300 °C for the gas in the hot reaction zone) and the high amount of oxidizing compounds in the top gas (CO ₂) lead to the stability of mainly carbonates. They mainly get separated from the waste gas flow by the dust or sludge fraction.	The top gas is characterized by a high temperature (>1000°C) and a high CO content. This leads to a high ratio on metallic alkali vapour compared to other alkali compounds. A significant increase in K/Na is caused by the recycling of dust from the HGC.
Emissions by the slag phase	The slag is the main source for alkali generation into the furnace. The basicity and the temperature are the main parameters for the K ₂ O/Na ₂ O activity and, consequently, the evaporation. The amount of metallic and cyanide vapour is similar with regard to the hot blast composition.	The slag is the main source for alkali generation into the reactor. The basicity and the temperature are the main parameters for the K ₂ O/Na ₂ O activity and, consequently, the evaporation. The amount of metallic vapour is higher than for the cyanide compounds. In addition, the total alkali evaporation is less due to the lower gas rate from the tuyeres (only 30% of hot furnace blast volume)

A main goal of the alkali model for the melter gasifier is to predict the alkali output by the slag phase and the top gas (BF) or generator gas (COREX® and FINEX® processes). The correlation between composition and emitted fraction (carbonates in dust or sludge, metals and cyanides in washing water³⁶) allows the forecast of K/Na in the top gas treatment system. In Table 4-11, the main finding of the alkali models for the BF and the melter gasifier are compared based on several significant categories.

4.5 Results of Alkali Model: Future Potentials

The alkali model for ironmaking reactors enables a specific focus on the behaviour of K/Na compounds in the BF and in smelting reduction processes. It predicts the stability of alkali compositions as well as the enrichment in specific areas of the reactor. The comparison with industrial data shows analogies of the calculated values.⁴³ However, continuous improvement and development of the model is necessary.

The next steps should focus on the interaction of alkali metals with halogens (Cl, F) and the behaviour of other circulating elements (Zn, Pb) in ironmaking processes. Previous research by several authors^{36,113} has already focused on the accumulation of halogens in the reactor and in the gas treatment system. Figure 4-18 shows the circulation of chlorine in a BF, where KCl, NaCl, and HCl are stable compounds. In the next step of alkali modelling, the stability of these compounds will be considered. The similarity of measured Cl flows to the developed alkali model is clearly visible. Preliminary studies have already confirmed the approach of Cl/F modelling by the alkali model. The chlorides and additional fluorides are formed as stable compounds over the BF height. They descend or ascend with the gas stream and the bulk. However, the thermochemical stability of these compounds has to be linked to kinetic approaches to get a better and process-near picture of the chlorine accumulation.

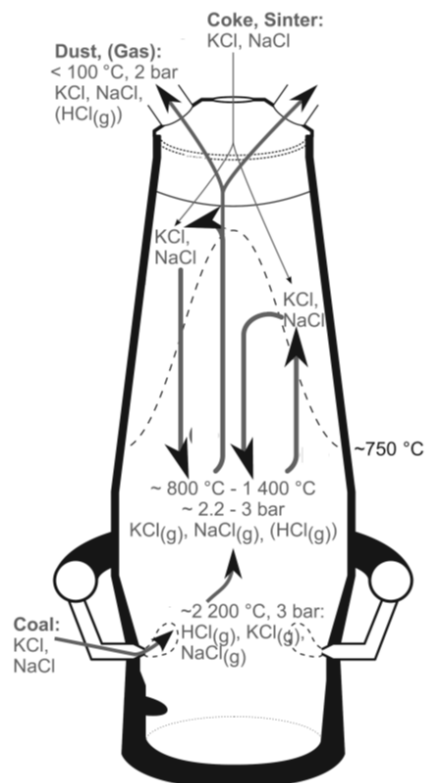


Figure 4-18: Chlorine in the blast furnace, including the interaction with alkalis¹¹³

5 Microscopic Effect of Alkalis on Reduction, Disintegration and Melting

Next, he must have knowledge of Drawing, that he can draw plans of his machinery.

Georgius Agricola, De Re Metallica

This chapter deals with the investigations on the microscopic effects of alkalis on the ferrous burden materials. By the adoption of common methodologies as well as the development of new approaches for the investigation of alkalis, the reproductive measurement of different iron carriers was performed under the influence of alkalis. To get an overview about the total project, the following aspects are investigated in the following chapters:

- Investigated materials and methodology (Chapter 5.1)
- The assimilation of alkalis in ferrous burden material by different morphological phases (Chapter 5.2)
- The influence of K and Na on indirect reduction of the iron oxides by reduction gases containing CO and H₂ (Chapter 5.3)
- Mechanical stability, particularly abrasion, sticking, and a disintegration tendency (Chapter 5.3.3)
- The effect of alkalis on the formation of metallic iron (Chapter 5.3.4)
- The softening and melting behaviour of reduced burden material under the influence of alkali metals (Chapter 5.4)

5.1 Methodology for Investigations of the Samples of Ferrous Burden Material

For these investigations, representative samples of ferrous burden materials (lump ore, pellets, sinter) used in the BF and smelting reduction processes were taken. For lump iron ore, hematitic as well as limonitic ore was chosen; for the pellets and for the sinter, two different blends were investigated. The chemical composition of the raw materials is summarized in Table 5-1. The hematite raw ore shows a high content of iron oxide, while the gangue has a very low basicity (high content of acid compounds SiO_2 and Al_2O_3). The amount of K and Na is high (approximately 0.1% K_2O), which is typical for ores from iron-banded formations.⁹⁵ The surface area is low, which indicates a dense, hematite structure. The limonitic ore shows a high Fe content and a high LOI (which represents the bounded water). The basicity is low (high SiO_2 and Al_2O_3 contents). The surface area is high, which is typical for ores with a high ratio of limonite. K_2O and Na_2O have already been washed away during weathering, so they are not present. For the pellets, two different brands were chosen. Pellet 1 is characterized by an acidic binder (very high SiO_2 content) and a high amount of alkalis. Pellet 2 is a basic pellet (higher CaO content) with a lower amount of alkalis. Both pellets show a low surface area, and their Fe content is high and LOI is low (indicating hematite as the main iron carrier). For the sinter samples, two industrially used materials were chosen. Both show a similar Fe content. Sinter 1 shows a lower basicity and double the amount of alkalis than sinter 2. The surface area is very low and it was not measurable by BET measurement (Brunauer-Emmett-Teller analysis).

Table 5-1: Chemical composition and specific surface area of the investigated raw materials

	Specific surface area [m^2/g]	Fe_{tot} [%]	Fe^{2+} [%]	Al_2O_3 [%]	CaO [%]	K_2O [%]	Na_2O [%]	MgO [%]	SiO_2 [%]	LOI [%]	B_2	B_4
Hematite	0.42	67.0	1.01	0.71	0.02	0.118	0.1	0.01	2.6	0.34	0.0	0.0
Limonite	3.74	63.3	0.76	1.1	0.01	0.004	0.01	0.01	1.68	6.36	0.0	0.0
Pellet 1	0.23	64.6	1.38	0.38	0.17	0.08	0.05	0.33	6.34	0.06	0.0	0.1
Pellet 2	0.4	65.4	0.26	1.28	2.26	0.02	0.02	0.01	2.1	0.19	4.5	1.3
Sinter 1	n.a.	52.41	5.4	2.25	9.72	0.54	0.072	2.99	7.9	0	1.23	1.25
Sinter 2	n.a.	52.69	5.6	1.74	12.07	0.303	0.046	3.14	6.7	0	1.80	1.80

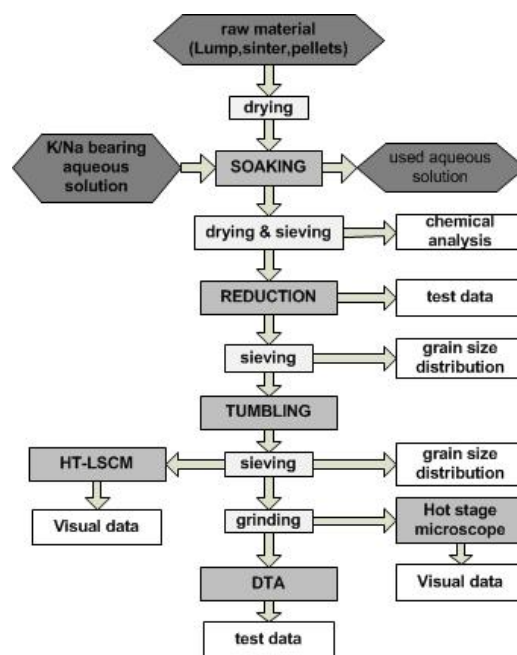


Figure 5-1: Flow sheet for the evaluation of ferrous burden material affected by alkalis

Prior to the investigations, all samples were leached with K and Na separately, following a standardized methodology (see Figure 5-1). First, the raw material is dried before being soaked in an aqueous solution containing either NaOH or KOH. Pre-tests were performed using NaCO_3 , which showed the same assimilation of Na as NaOH. After a soaking time of 14 days, the samples were taken out and dried. A chemical analysis was done to determine the assimilation of K and Na. The reduction tests with the treated samples were carried out to determine the change in reducibility in comparison to non-treated materials. To determine the mechanical stability, the reduced samples were sieved and tumbled according to the standard ISO 4701:2008.¹⁴⁰ The measured grain size distributions were compared to values before reduction and to the values of untreated materials. To evaluate the softening and melting behaviour, the reduced samples were tested by hot stage microscopy, high-temperature laser-scanning confocal microscopy (HT-LSCM), and differential thermal analysis (DTA). Especially the results of the DTA were considered for characterization of the influence on melting and softening by alkali treatment. In the following chapters, the methodology of the single steps is described, including the main influences and results of the alkali addition to ferrous burden materials.

5.2 Alkali Assimilation of Ferrous Burden Material

Derived from the gas atmosphere in ironmaking processes, a specific methodology for the soaking of materials was developed. In industrial processes, alkalis often occur as gases and impregnate solid particles like burden materials and coke. For instance, this relation is seen in the BF shaft. Hence, a methodology was developed that shows the fluid-solid reaction between burden material and alkali vapour, similar to that seen in the BF shaft. The soaking of solid ferrous material in an aqueous solution was an approach to simulate the interaction between fluid (alkali vapour in the process gas) and the solid particles (burden material). Similarly to the

BF shaft, the alkalis move from the fluid into the solid material by diffusion. Compared to the literature,^{125,126} this procedure is the best way to visualize the real process (no synthetic phases and no input of halogenides, which also affect the reaction mechanisms). The solution was prepared using distilled water and 5 molar KOH or NaOH separately. The raw material was sieved (grain size between 10–12.5 mm) and dried (24 h at 105 ±5°C¹⁴¹). The dried material was then put into the solution and the soaking continued for 14 days. The samples were dried and analysed with regard to their alkali assimilation. Table 5-2 shows the analysis for lump ore, pellets, and sinter for the raw material and the 5-molar treated materials. In addition, Figure 5-2 shows the increase during the alkali treatment. Soaking was also carried out in 1 and 2.5 molar solutions as well to verify the trends.

Table 5-2: Chemical analysis of K/Na of untreated and treated raw materials

	Specific surface area [m ² /g]	Untreated K ₂ O [%]	K-treated (5-molar) K ₂ O [%]	Untreated Na ₂ O [%]	Na-treated (5-molar) Na ₂ O [%]
Hematite	0.42	0.118	0.37	0.1	0.2
Limonite	3.74	0.004	0.87	0.01	1.16
Pellet 1	0.23	0.08	1.965	0.05	1.139
Pellet 2	0.4	0.02	1.085	0.02	0.939
Sinter 1	n.a.	0.54	0.92	0.072	0.89
Sinter 2	n.a.	0.303	1.176	0.046	1.158

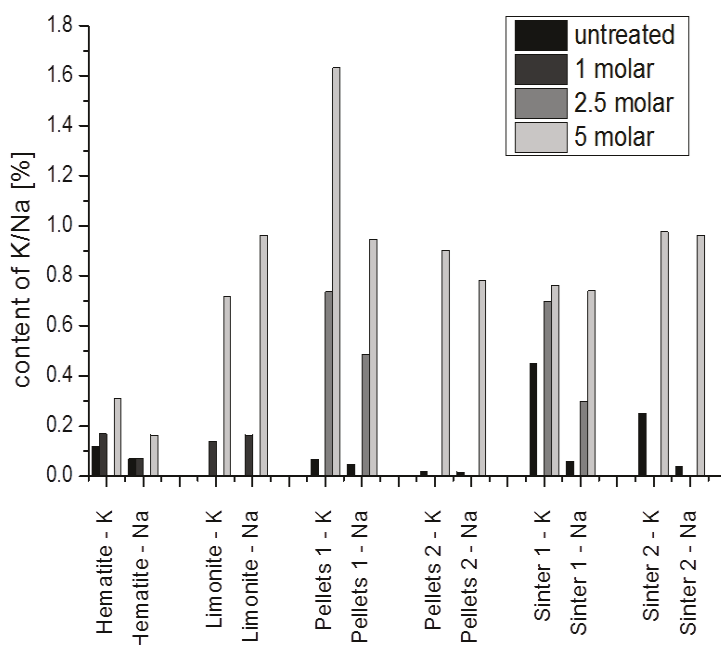


Figure 5-2: Alkali content of the ferrous material in correlation with the molarity of the solution

All materials show an increase during soaking; the tendency follows a linear correlation between alkali assimilation and the molarity of the solution (which is similar to the assimilation in industrial processes by the partial pressure of alkalis in the gas phase¹⁰⁹). To get an overall

view on the different materials, additional analysis by microprobe was performed. These results are shown for the burden materials separately.

Hematite lump ore: During treatment, an increase of K and Na in the ore was detectable. Although the total increase is not high because of the dense structure, especially the gangue is affected by K and Na. However, the gangue already shows a higher amount of K before the saturation.

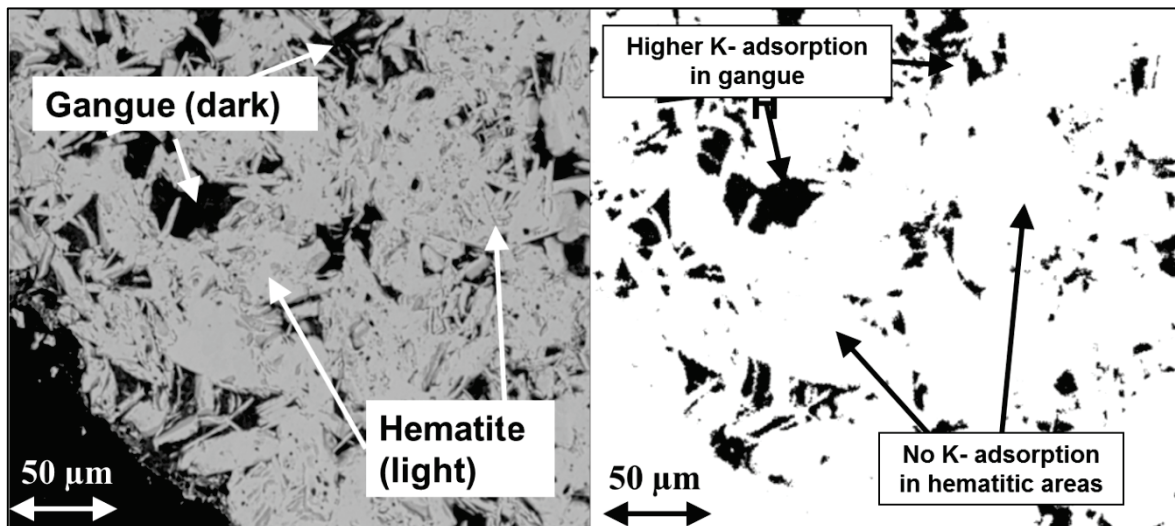


Figure 5-3: Mineralogical structure (left) and K distribution after treatment (right) in hematite lump ore

Limonitic lump ore: The limonitic lump ore shows higher assimilation compared to the hematite. This is mainly due to the higher surface area, which leads to high amounts in the porous limonite for K as well as Na. Figure 5-4 shows the major assimilation in the limonite and the minor assimilation in the hematite. Compared to the original raw ore, which consists of hardly any K and Na, the total assimilation was very high (nearly 1% in a 5-molar solution). The distribution of Na over the particle is similar to that of K.

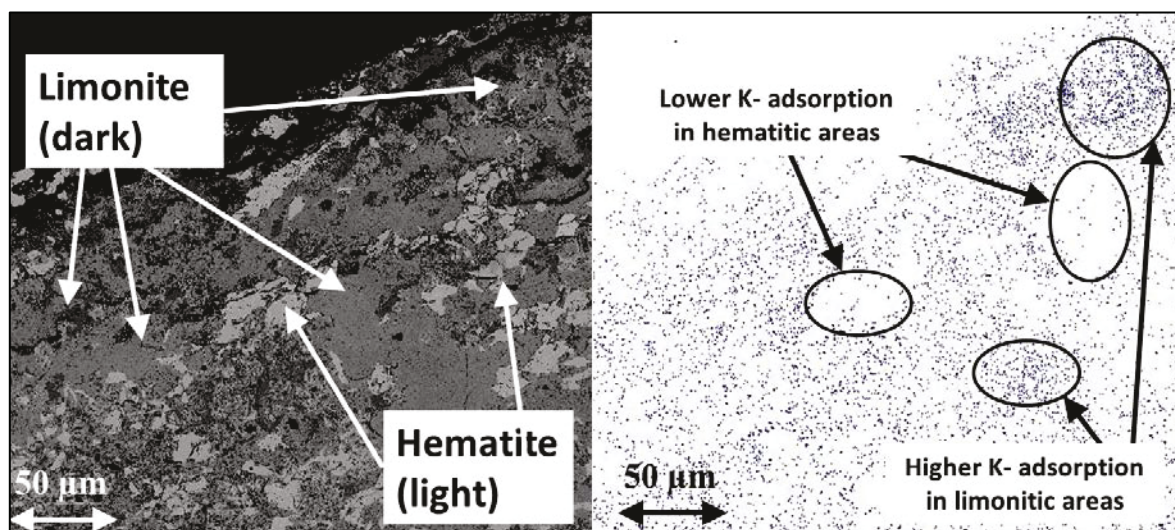


Figure 5-4: Mineralogical structure (left) and K distribution after treatment (right) for limonitic lump ore

Pellets/Sinter: Both pellets and sinter show high assimilation of alkalis. In contrast to the lump ores, the specific surface area is very low; hence, it cannot be the reason for the high alkali increase. Absorption instead of adsorption on the inner surface is the main process during treatment. Investigations by microprobe (see Figure 5-5) show the K especially in the glass and gangue phases. In the sinter, the calcoferrite and hematite—and the hematite grains for pellets—are less affected by the alkali treatment.

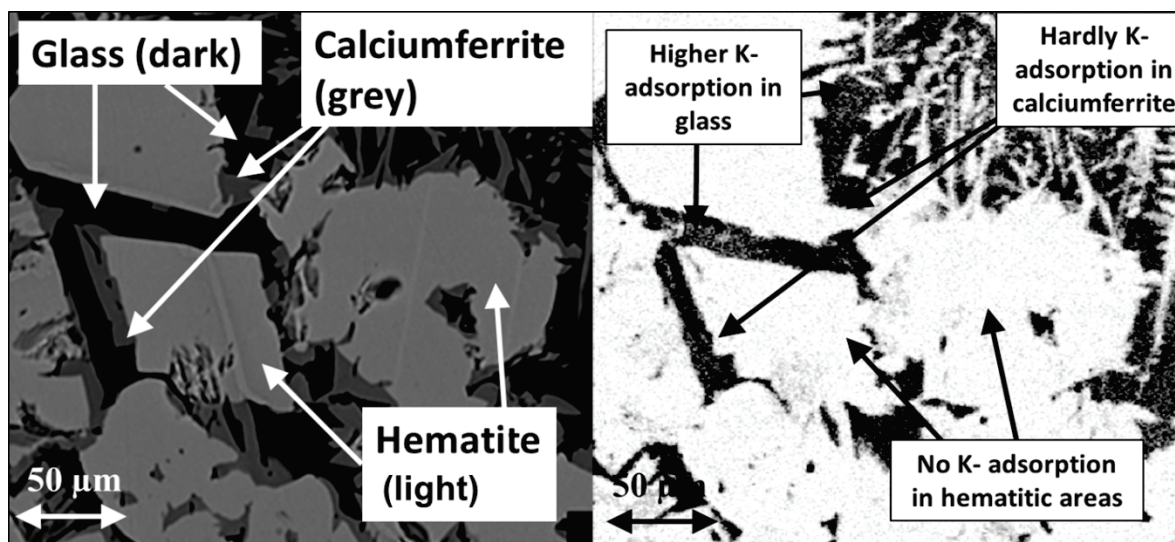


Figure 5-5: Mineralogical structure (left) and K distribution after treatment (right) for Sinter 1

For the alkali treatment, it was important to eliminate the effect of the basic solution (OH⁻ in aqueous solution) and of the water itself on the ferrous material. Therefore, tumbling was carried out after the soaking, but no effects on the mechanical properties of the binding forces—for example, in the glass phase—were measureable between untreated and treated material. Table 5-3 shows an overview of the assimilation investigated by chemical analysis, scanning electron microscope (SEM), and microprobe.

Table 5-3: Summary of the K/Na content in different iron carriers under the influence of alkalis

Type of ferrous burden	Mineralogical phase	Untreated	K-treated	Na- treated
Hematite	hematite	no	very low	very low
	gangue	low	medium	medium
Limonite	limonite	no	medium	not measured
	gangue	no	medium	not measured
Pellets	hematite	no	low	low
	glass	low	very high	very high
Sinter	hematite	no	no	no
	calcoferrite	no	low	low
	glass	medium	very high	low

5.3 Influence of Alkalis on Reduction Reactions and Mechanical Stability

The effect of K and Na on reduction is determined by reduction tests under reducing atmospheres (gas mixtures with CO, H₂, CO₂, H₂O, and N₂) and specific temperature regimes. In total, three different reduction tests were performed: a standardized test (ISO 4695) and two types of process-near tests (BF conditions, smelting reduction conditions). They were operated with untreated and alkali-treated materials. The outcome of the tests gives an explanation about the effect of K and Na on reduction reactions.

5.3.1 Testing Equipment and Programs for Reducibility and Mechanical Stability

The reduction is carried out in a fixed-bed reactor with a diameter of 75 mm. Figure 5-6 shows a scheme of the reduction facility, including the gas supply units (mixing of the single gas compounds CO, CO₂, H₂, H₂O, and N₂). The gas mixture enters the vertical reactor from the bottom and the sample is positioned on a grid above the gas-preheating zone. The reactor retort is electrically heated in a three zone-tubular furnace. The reduction is operated in a batch mode. The exhaust gas leaves the reactor at the top. The weight loss is recorded by a weighing device and is used to determine the change in the RD over time. The most important values for the determination of the reducibility are the RD₈₀ (needed time to reach an 80% RD) and the reduction rate $\left(\frac{dRD}{dt}\right)_{40}$ (rate at a 40% RD). The main technical data is shown in Figure 5-6 and Table 5-4.

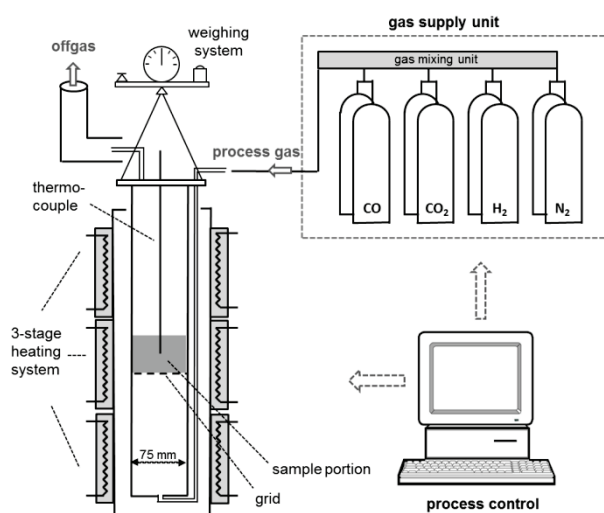


Table 5-4: Technical data and values¹³¹

Sample mass	500	[g]
Max. testing temperature	950	[°C]
Grain size (input material)	10–12.5	[mm]
Reduction degree	$RD = \left(\frac{O_{removed}}{O_{total}}\right) \cdot 100$	[%]
Time for RD = 80%	RD ₈₀	[min]
Reduction rate	$\left(\frac{dRD}{dt}\right)_{40} = \frac{33.6}{t_{60} - t_{30}}$	[%/min]

Figure 5-6: Testing device (retort) for the reduction of iron ores¹³¹

To get an overall picture of the reduction behaviour, standardized and process-near tests were performed. The standardized test follows ISO 4695¹⁴² and is carried out under a CO atmosphere at 950°C. Although this test delivers important values for the characterization of the material, it does not visualize the real process conditions in ironmaking reactors like a BF very well. Consequently, two adapted reduction tests were established to perform the tests under process-near conditions; one under BF process-near conditions (BF) and one under smelting reduction

process-near conditions (SR). The modified temperature profiles, gas composition, and gas flow rates are summarized in Table 5-5 for all testing types. For further information about process-near tests, see Hanel.⁸⁰

Table 5-5: Parameters of the standardized and process-near reduction tests

Test	Step	Temperature [°C]	Flow rate [NI/min]	Gas composition [vol.-%]	Time [min]
ISO 4695	0	AT to 950°C	50 NI/min	100% N ₂	ca. 60
	I	950°C	50 NI/min	40% CO, 60% N ₂ ,	RD ₈₀
BF near process condition	0	AT to 300°C	25 NI/min	100% N ₂	ca. 20
	I	300–500°C	50 NI/min	24% CO, 23% CO ₂ , 3% H ₂ , 50% N ₂	30
	II	500–950°C	50 NI/min	Continuous from phase I to phase III	60
	III	950°C	50 NI/min	42% CO, 5% CO ₂ , 3% H ₂ , 50% N ₂	RD ₈₀
SR near process conditions	0	AT to 300°C	25 NI/min	100% N ₂	ca. 20
	I	300–500°C	25 NI/min	39% CO, 46% CO ₂ , 15% H ₂	20
	II	500–800°C	25 NI/min	Continuous from phase I to phase III	40
	III	800°C	25 NI/min	65% CO, 10% CO ₂ , 25% H ₂	RD ₈₀

*AT....ambient temperature

As a consequence of the modified process conditions, new mechanisms occur during the iron ore reduction. The Baur-Glaessner diagram illustrates the single steps from oxide to metal for the modified tests. The dotted lines show the stability fields for pure H₂/H₂O or CO/CO₂ mixtures, while the black line shows the equilibrium lines for the gas mixture at the beginning of the test. In contrast to ISO 4695 (pure CO, which directly leads into the stability area of metal iron), a reduction route through a changing gas and temperature profile is performed.

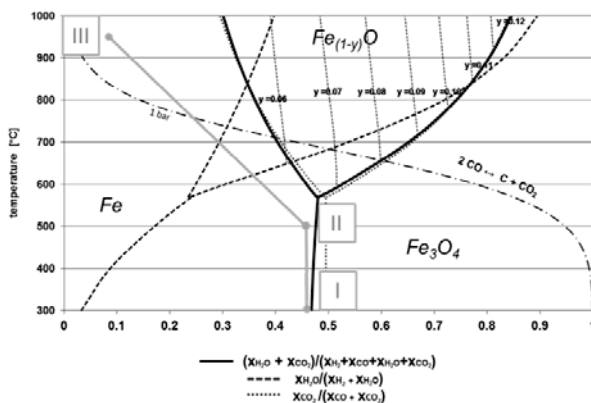


Figure 5-7: Process route of the blast furnace process-near reduction test (BF) in the Baur-Glaessner diagram

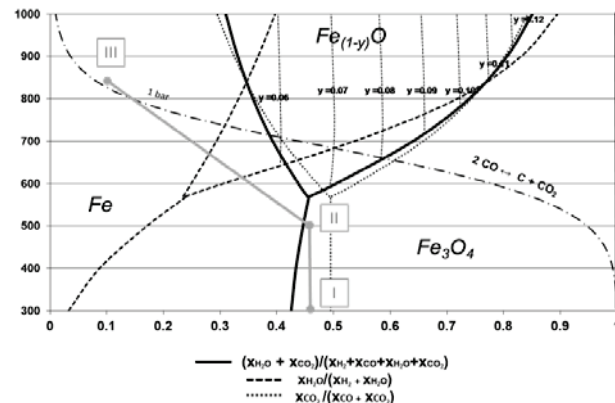


Figure 5-8: Process route of the smelting reduction process-near reduction test (SR) in the Baur-Glaessner diagram

The main differences between BF and SR tests are the lower temperature for the SR test, the higher ratio of H₂ in the process gas, and that no nitrogen is present during reduction. Moreover, the path in the Baur-Glaessner diagram is different for the two procedures. In the BF test, the process conditions of the reduction gas leads to the formation of iron from the beginning. During

the SR test, magnetite is formed in the first reduction phase. Further effects of the different process conditions on the burden materials will be discussed in the following chapters.

In addition to the reduction tests, research also focused on mechanical stability. Therefore, tumbling tests with a drum (for specific data, see Figure 5-9 and Table 5-6) were performed with the reduced materials. The mechanical parameters were adapted to industrial near-process conditions (see Hanel⁸⁰) that are mainly derived from ISO 4696-1.¹⁴³ In general, all tendencies are calculated by the ratio between a specific mass fraction m_i and the total mass m_0 . The mass fractions are for the disintegration (m_1) a particle size <6.3 mm, for the abrasion (m_2) a particle size <0.5 mm, and for sticking (m_3) a particle size >12.5 mm.

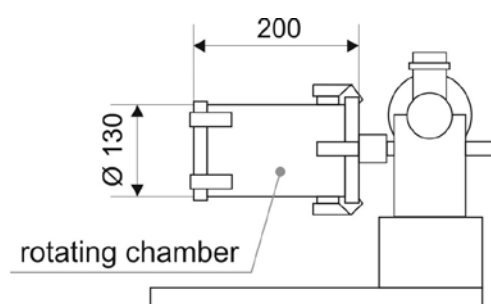


Figure 5-9: Schematic picture of the tumbling drum, including the dimensions¹³¹

Table 5-6: Testing conditions of the tumbling tests and equations for the evaluation¹³¹

Rotations	900	[---]
Rotation velocity	30	[U/min]
Disintegration tendency (DT)	$DT = \frac{m_1}{m_0} \cdot 100$	[%]
Abrasion tendency (AT)	$AT = \frac{m_2}{m_0} \cdot 100$	[%]
Sticking tendency (ST)	$ST = \frac{m_3}{m_0} \cdot 100$	[%]

5.3.2 Results of the Reduction Tests

In this chapter, the influence of different process conditions and the effect of alkalis on different iron carriers (lump ore, pellets sinter) are discussed. In general, all materials are affected by alkalis. First, the performance under ISO and BF conditions is discussed, then a comparison to SR-conditions for exemplary materials is carried out as well as an evaluation of the results based on kinetic aspects. All reduction curves of the investigated materials showing the process data for temperature and gas flow as well as the measured RD as a function of time are presented in Figures A-1 to A-4.

Lump ore (hematite and limonite):

The change in reducibility is directly linked to the assimilation of K and Na in the material. Limonitic ore shows a higher increase due to its higher specific surface and porous limonite in the microstructure than hematite ore. Under ISO conditions, both K and Na accelerate the reduction (K/Na assimilation in ore approximately 0.7/1%). Moreover, under BF near-conditions, K and Na accelerate the reduction in a similar way. The reduction curves can be seen for both tests in Figure 5-7 for limonitic ore (and in Figure A-1 for all lump ores). To determine the representability, several tests were performed, which show a deviation in reducibility by a maximum of 3%. Interestingly, there are nearly the same reduction curves for K and Na, which may be the effect of the gas diffusion as a limiting kinetic step (evaluation at the end of this chapter). For hematite iron ore, the same trend was determined, although the increase was less due to the lower content of alkali assimilation of the particles.

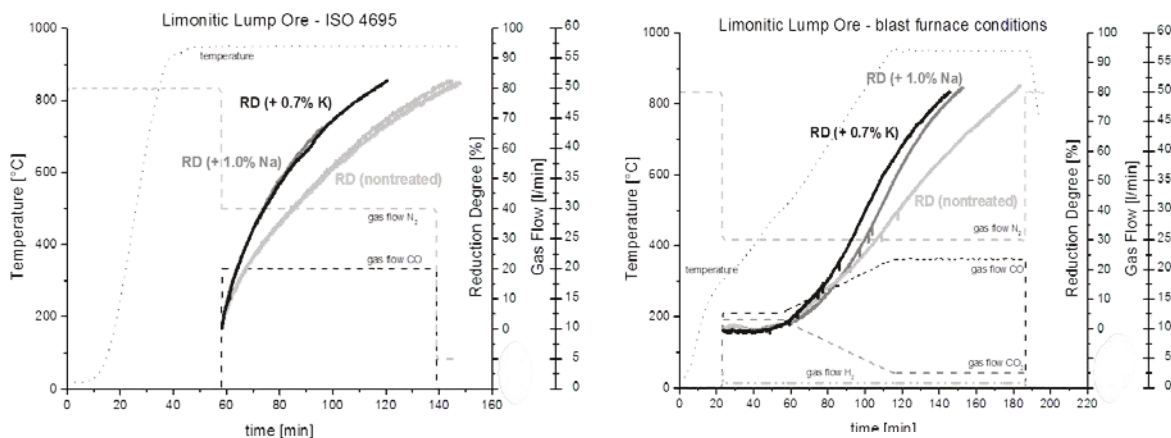


Figure 5-10: Process data and reduction curve for limonitic lump ore under ISO (left) and BF (right) conditions and the addition of K or Na

Pellets (acid pellet 1 and basic pellet 2): The pellets also show an increase in reducibility. Especially under a pure CO atmosphere (ISO tests), this change is significant. Under BF conditions, the effect is less. Although the reaction rate accelerates for both brands, the curves seem to vary. Pellet 1 shows a change in the kinetic limiting step for untreated material (see light grey curve in Figure 5-11, left) from diffusion-limited to reaction-limited. In general, the diffusion is fast for pellets and the chemical reaction is the limiting step. For K/Na-treated materials, the diffusion seems to be the limiting step for the total time, which indicates the effect of K/Na on the chemical reaction (reduction of iron oxide). For basic pellet 2, the chemical reaction is the limiting step during the total testing time, which also leads to acceleration by alkalis from the beginning.

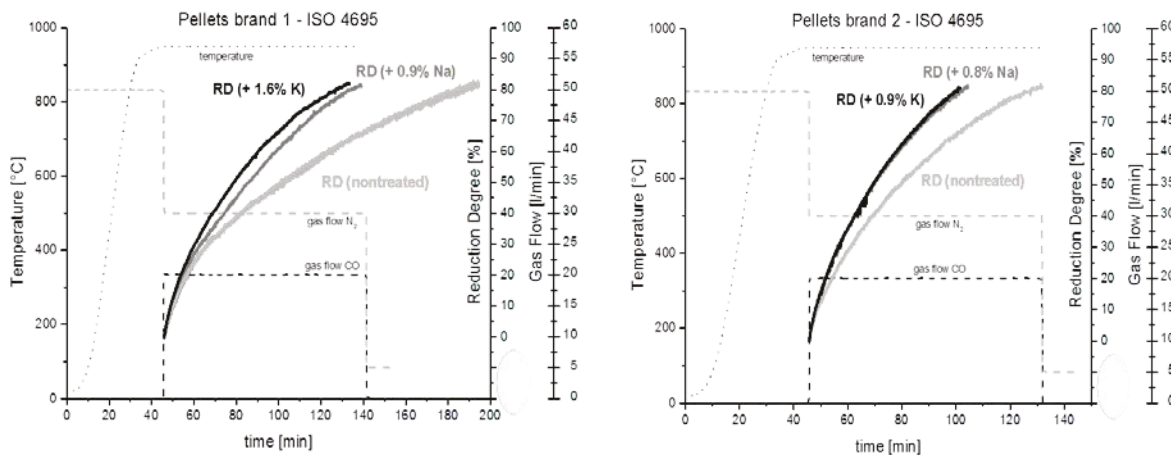


Figure 5-11: Process data and reduction curve for acid pellet 1 (left) and basic pellet 2 (right) under ISO condition (pure CO) and the addition of K or Na

Sinter (blends 1 and 2): Sinter is known to be a well-reducible material. However, an acceleration of reduction was also observed (see Figure 5-12 for sinter 2). Although the chemical composition and microstructure varies between the two blends, the behaviour with alkali treatment shows the same trends. Under pure CO, the effect was higher than under BF conditions, where the differences are not significant. From the kinetic point of view, a

performance similar to pellets was observed. The increase of the reduction rate was smaller than during the testing of lump ores, which indicates diffusion as a limiting step during sinter reduction. The ISO test delivers an interesting result: It shows different increases in reducibility, even though the assimilation of K and Na is of nearly a similar quantity. A possible reason is the already high K-content in the untreated sinter samples. This indicates that not only is the assimilation important, but also the absolute content of K or Na plays a role in the reduction process.^{98,144}

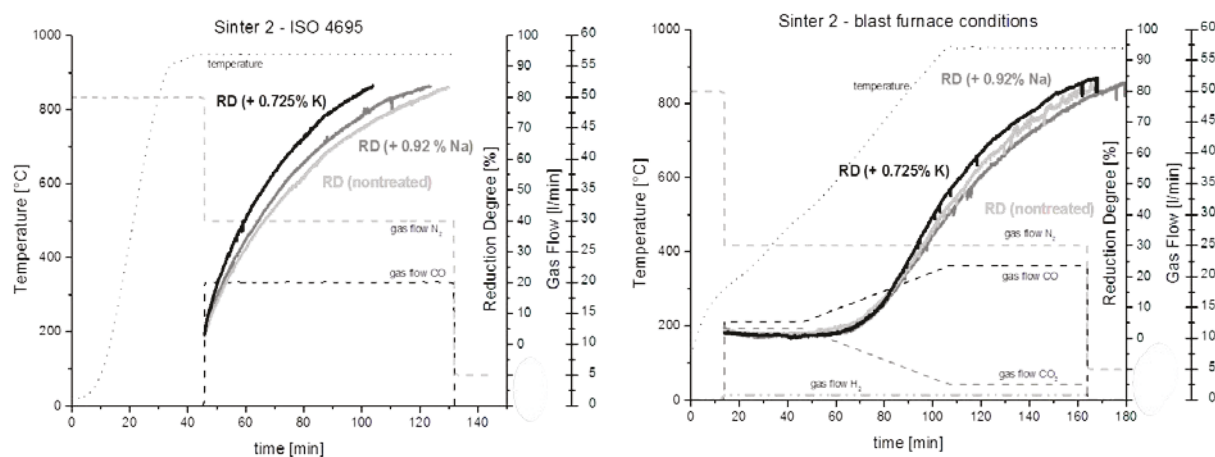


Figure 5-12: Process data and reduction curve for sinter 2 under ISO (left) and BF (right) conditions, and the addition of K or Na

Reduction under smelting reduction near-process conditions (SR): In addition to the ISO and BF tests, tests with higher H₂ and no N₂ were performed to show the reduction behaviour and effects of alkalis under testing conditions similar to conditions during smelting reduction processes. The results were similar to those of the BF tests. The effects of K and Na are less than for ISO conditions. The reason is the variation of the material properties. Sinter and pellets were less affected than lump iron ores. Figure 5-13 shows the reduction curves for hematite lump ore and basic pellet brand 2. Overall, the SR tests show an interesting trend: that the effect of K and Na decreases with lower CO content in the reduction gas.

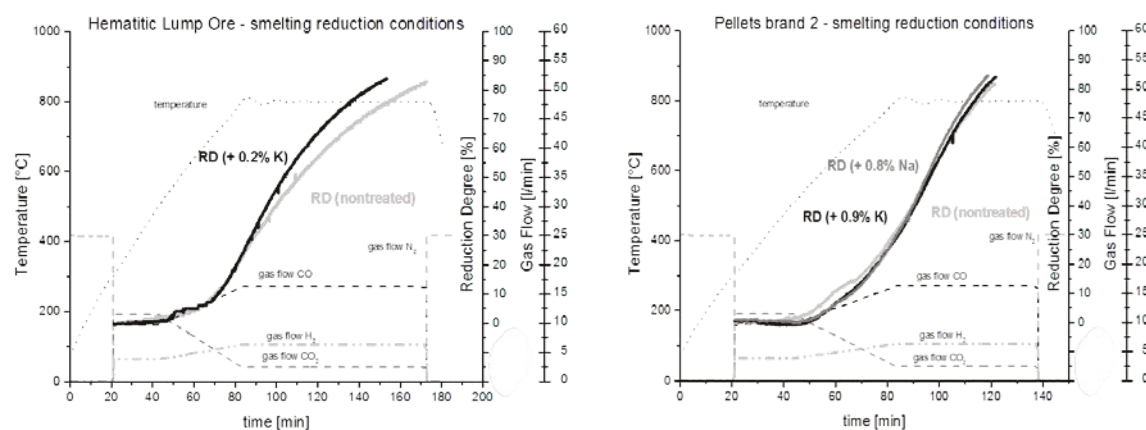


Figure 5-13: Process data and reduction curve for hematite lump ore (left) and basic pellet 2 (right) under smelting reduction near conditions and the addition of K or Na

Conclusion and discussion of the reduction tests: For the evaluation of the specific effects of K and Na, several kinds of ferrous burden material as well as several different reduction conditions were investigated. Table 5-7 shows a summary of the performed tests, particularly the reduction rates $\left(\frac{dRD}{dt}\right)_{40}$ and the reduction time RD_{80} . Sinter samples show the highest reducibility. In addition, pellets are characterized by high reduction rates. However, the addition of alkalis (both K and Na) leads to an acceleration of the reduction for all materials under CO-containing atmospheres.

Table 5-7: Summary of reduction times and reduction rates of the performed tests

Sample	Reduction test at ISO conditions						Reduction test at industrial-scale conditions (BF)					
	Non-soaked material		K-soaked material		Na-soaked material		Non-soaked material		K-soaked material		Na-soaked material	
	$\left(\frac{dRD}{dt}\right)_{40}$	RD_{80}	$\left(\frac{dRD}{dt}\right)_{40}$	RD_{80}	$\left(\frac{dRD}{dt}\right)_{40}$	RD_{80}	$\left(\frac{dRD}{dt}\right)_{40}$	RD_{80}	$\left(\frac{dRD}{dt}\right)_{40}$	RD_{80}	$\left(\frac{dRD}{dt}\right)_{40}$	RD_{80}
Hematite ore	0.70	133	1	96	0.68	135	0.59	222	0.73	184	0.53	225
Limonitic ore	1.04	81.5	1.5	56	1.66		0.86	155	1.38	116	1.39	125
Pellet brand 1	0.60	141	1.14	79.5	0.89	86	1.05	169	1.19	125	1.07	133.4
Pellet brand 2	1.11	79	1.66	53.3	1.58	55.2	1.22	128	1.36	120	1.19	127
Sinter 1	1.34	69	1.92	48	1.37	66.5	1.27	145	1.35	136.5	1.46	134
Sinter 2	1.26	74	1.81	50	1.43	64	1.14		1.29	148	1.02	154.8

The comparison of the alkali assimilation with the change in reducibility (see Figure 5-14) shows the correlation under ISO conditions with high CO content. The black points (■) show the tests under ISO condition, the red points (•) under BF-near testing conditions, and the blue points (Δ) under SR-near testing conditions. The decreasing content (as well as partial pressure) of CO leads to less change in reducibility resulting from alkali conditions. This comparison of the performed tests is an important basis for scientific evaluation of the microscopic processes, which will be discussed in Chapter 5.3.3, in combination with mineralogical investigations and determination of the mechanical stability.

The effects of alkalis on the reducibility of burden materials can be summarized as follows:

- Hematite lump ore: less assimilation but change in reducibility effect under all performed testing conditions
- Limonitic lump ore: significant change in reducibility under all performed testing conditions
- Pellets: higher reducibility by K or Na addition, especially under a pure CO atmosphere (ISO conditions)
- Sinter: higher reducibility under ISO conditions and by the addition of K; no significant effects for other tests

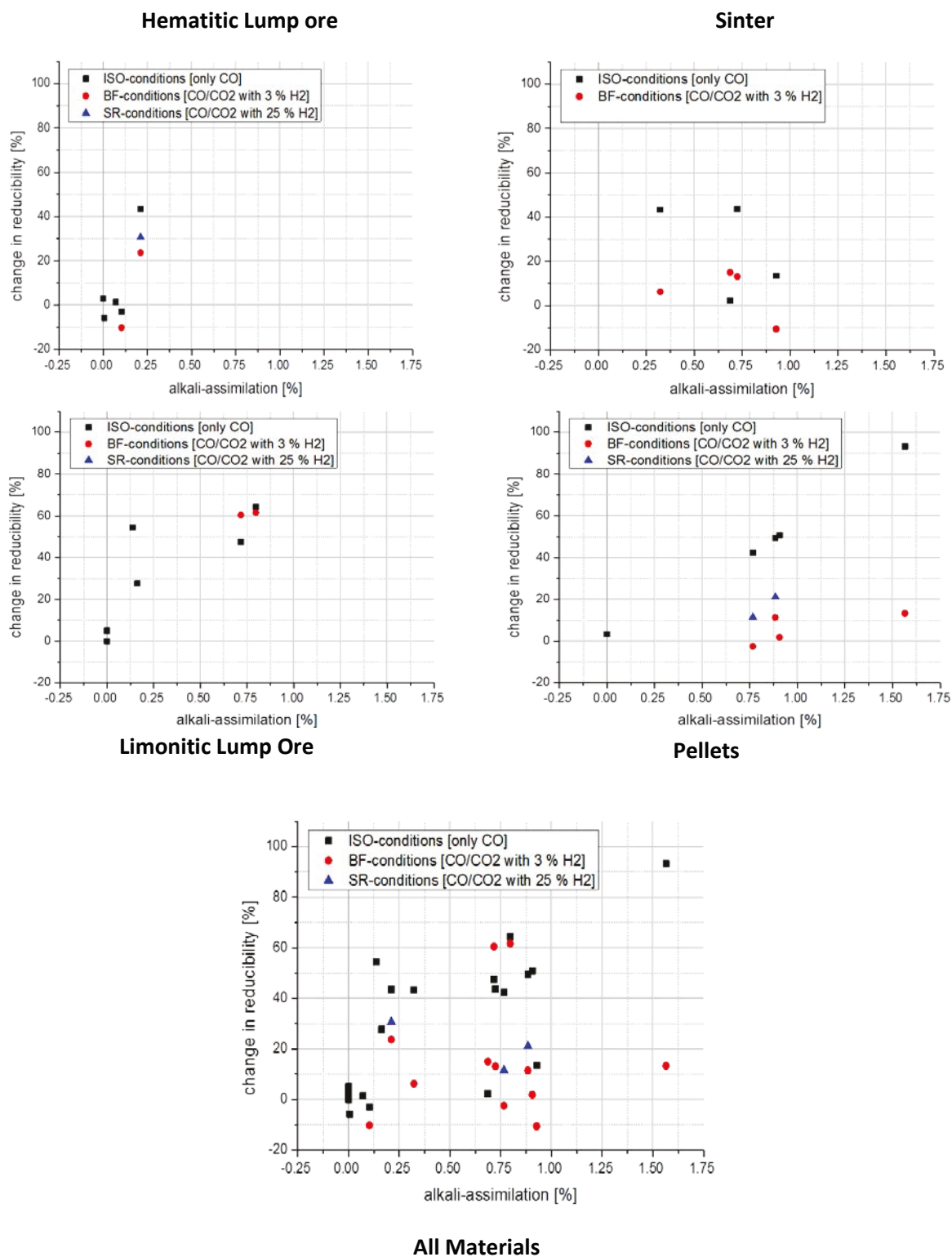


Figure 5-14: Relative change in reducibility by the addition of alkalis for different materials

5.3.3 Influence of Alkalis on Mechanical Stability during Reduction

In this chapter, the influence on mechanical stability is evaluated. In particular, the focus is on sticking, abrasion, and a disintegration tendency during reduction processes. The data is measured by tumbling and sieving.

Disintegration: The disintegration is evaluated by the disintegration tendency (DT), which describes the ratio of material after tumbling <6.3 mm; for this fraction, the crack is induced in the centre of the particle, which mainly indicates weakening and disintegration, not abrasion mechanisms. However, the disintegration is caused by two different mechanisms, whereas the first one depends on the process conditions (e.g. higher values for SR-near process conditions) and the specific effect of K and Na (summarized for all materials in Figure 5-15). No disintegration was detected for lump ore. All brands and blends of pellets and sinter show a lower stability under the influence of alkalis. One exception is the sinter under process-near conditions (BF, SR), where an increase in structural stability is detected. The reason is the softer structure under the influence of alkalis. Especially in the gangue and the glass phases, the stress induced by the formation of metallic iron during reduction below 950°C, is lowered. This is also discussed in Chapters 5.3.4 and 5.4 in comparison with the softening behaviour and microscopic investigations.

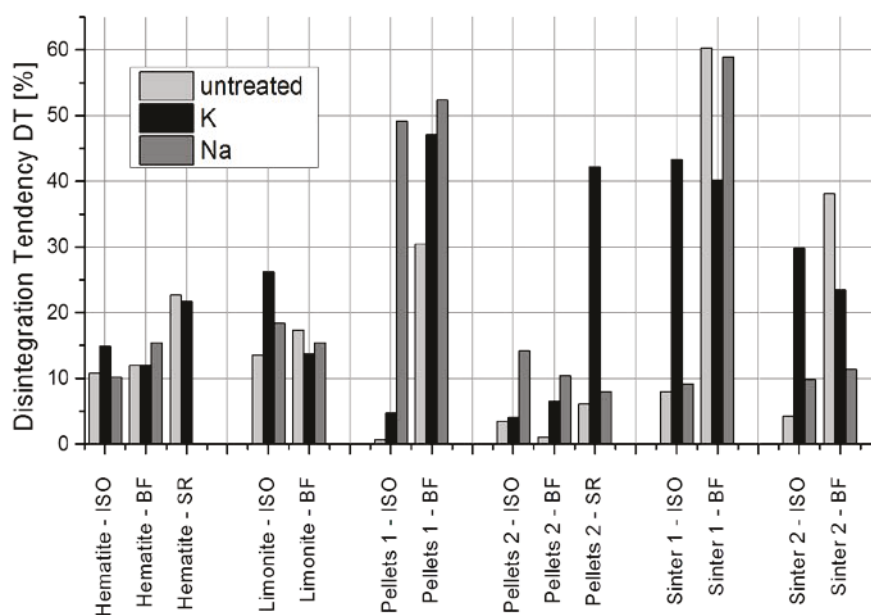


Figure 5-15: Summary of the disintegration tendency (mass ratio <6.3 mm) for ferrous burden material (untreated and alkali-treated)

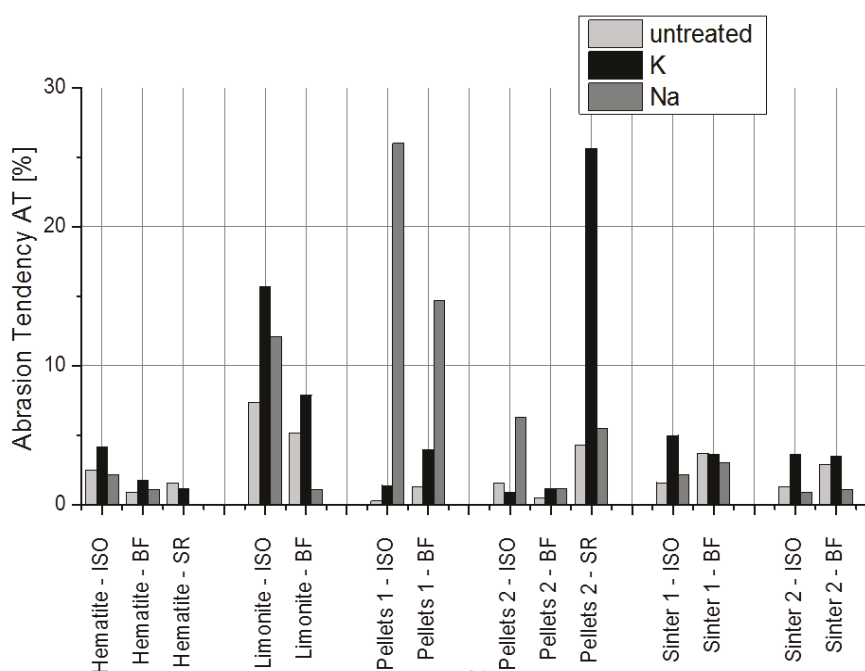


Figure 5-16: Summary of the abrasion tendency (mass ratio <0.5 mm) for ferrous burden material (untreated and alkali-treated)

Abrasion: The abrasion is evaluated by the abrasion tendency (AT), which describes the ratio of material after tumbling <0.5 mm. The fines are generated from the particle surface by mechanical forces during reduction and tumbling. Following the addition of alkalis, an increase in the fines ratio is detected (see Figure 5-16). Especially lump ores and pellets show a significant change, whereas pellet 1 (acid) was affected by Na massively. The weakening of the surface by a faster nucleation mechanism as well as increased whisker formation are the main reasons for this. For sinter, no significant change in AT was observed. This might be because of the already high DT and low sticking tendency (hardly any whisker formation).

Sticking: The formation of metallic fibres on the particle surface during reduction and the following agglutination of the material bed is generally known as sticking (further information is available in the literature^{145,146}). The sticking tendency (ST) is defined as a ratio of material >12.5 mm after reduction and tumbling. Similar to the abrasion tendency, lump ore (especially limonitic) and pellets were affected by alkali addition. For pellets, the effect of swelling also needs to be considered, which was not part of the performed work¹³⁰ (also see Chapter 3.3). Sinter has no sticking tendency. The trends are summarized in Figure 5-17.

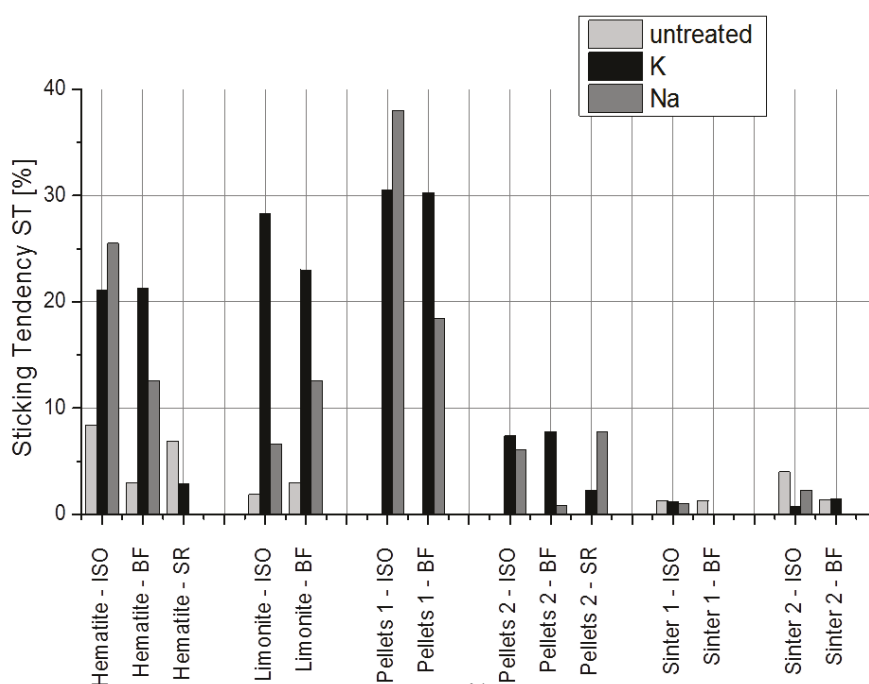


Figure 5-17: Summary of the sticking tendency (mass ratio >12.5 mm) for ferrous burden material (untreated and alkali-treated)

A summary of the determined values for DT and AT is given in Table 5-8. In general, a weakening of the particles by K/Na is observed. Only for process-near conditions was an improvement in the mechanical behaviour determined; the reason is the earlier start of softening of the Fe-Ca phases by the addition of K/Na. This makes the structure more flexible, and crack formation and growing is limited. Additional research of pellets and sinter has been done in the past by other authors.^{127,130,147} Alkalies lead to swelling and, sometimes, to complete destruction of the particles. These outcomes were also confirmed by the performed work.

Table 5-8: Summary of disintegration and abrasion tendencies under ISO and BF conditions

Sample [value in %]	Reduction test at ISO conditions						Reduction test at industrial-scale conditions (BF)					
	Non-soaked material		K-soaked material		Na-soaked material		Non-soaked material		K-soaked material		Na-soaked material	
	<i>DT</i>	<i>AT</i>	<i>DT</i>	<i>AT</i>	<i>DT</i>	<i>AT</i>	<i>DT</i>	<i>AT</i>	<i>DT</i>	<i>AT</i>	<i>DT</i>	<i>AT</i>
Hematitic ore	10.8	2.4	14.9	4.2	10.2	2.2	12.0	0.9	12.0	1.8	11.7	1.0
Limonitic ore	13.5	7.4	26.2	15.7	18.4	12.1	14.4	5.2	13.8	7.9	15.5	1.1
Pellet brand 1	0.7	0.3	4.7	1.4	49.2	26.0	30.5	1.3	47.1	4.0	52.4	14.7
Pellet brand 2	3.5	1.6	4.1	0.9	14.2	6.5	1.1	0.85	6.5	16.7	10.5	1.2
Sinter 1	8.0	1.6	43.3	5.0	9.2	2.2	60.3	3.7	40.2	3.6	58.9	3.0
Sinter 2	4.3	1.3	29.8	3.6	9.8	0.9	38.1	2.9	23.5	3.5	11.4	1.1

5.3.4 Morphological Investigation of Reduced Samples

For a comprehensive understanding of reaction mechanisms and especially the effect of alkalis, morphological investigations and a comparison with similar work from the literature were performed. After the tests, polished sections of the reduced materials were prepared and studied by optical microscopy.¹⁴⁸ Investigations on reduced pellets (see Figure 5-18) show the bigger size of the metallic nuclei (white) in the Na-treated material (right). A possible reason for the bigger metal grains is the earlier formation of a stable metal nucleus in the Na-treated structure. These stable grains can also describe the increase in reducibility from the beginning, in connection with the catalytic effect of metallic iron on reduction reactions (see Chapter 5.3.2). Both K and Na lower the nucleation energy for metallic iron.

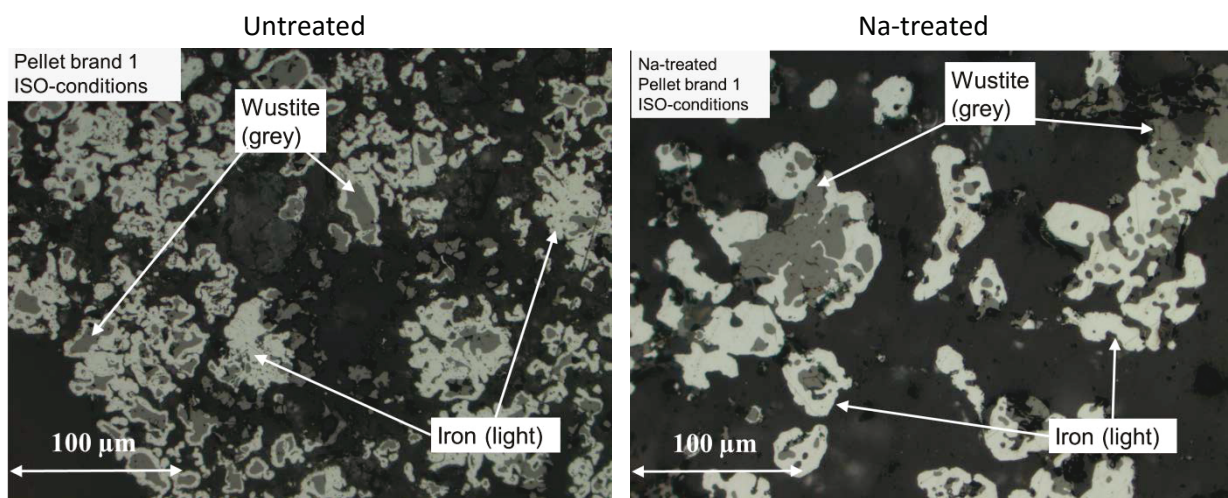


Figure 5-18: Morphological comparison of untreated pellets with Na-treated pellets after reduction under ISO conditions

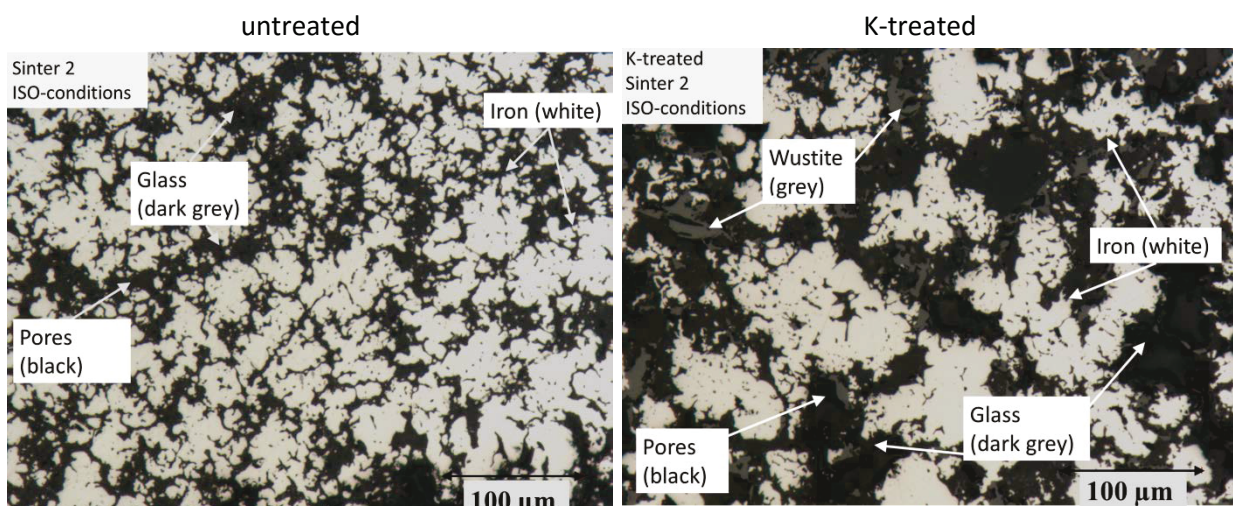


Figure 5-19: Morphological comparison of untreated sinter with K-treated sinter after reduction under ISO conditions

Furthermore, the bigger size of the stable metal grains (as well as the faster growth) can be the reason for the particle weakening (leading to more stress inside the particle) and the sticking or abrasion (bigger nuclei for whisker formation at the surface area). These findings match with the mechanical values determined in Chapter 5.3.3 (especially pellet brand 1 of Figure 5-18 shows a high tendency for sticking and abrasion). Moreover, for sinter, this trend of bigger metallic grains was observable (see the left side of Figure 5-19 for untreated and the right for K-treated reduced materials).

5.3.5 Comparison with Literature and Discussion of Results

For the interpretation of the testing results, the literature is examined closely. This enables an insight into the fundamentals of iron ore reduction and the establishment of new knowledge.

Investigations and findings by other authors:

The effect of alkalis on iron ore reduction has already been discussed by several authors. However, most of the work was performed on artificially created material (the alkali carrier was melted together with an iron carrier before reduction) or non-process-near reduction conditions. This research focuses on the simulation of industrially used materials under both process-near conditions and K/Na load. This leads to difficulties for the direct comparison of the results, but the trends are similar. Authors like Pan,¹²⁵ Gougeon,¹²⁶ Bahgat,¹²⁴ Nakagawa,¹⁴⁹ and Al-Ajeel¹⁵⁰ show the effect of K and Na on the reducibility. Figure 5-20 to Figure 5-23 show exemplary graphs of these investigations. For Al-Ajeel,¹⁵⁰ the increase in reducibility is due to the catalytic effect on the Boudouard reaction. The tests were performed on ore-coke mixtures. The acceleration is derived from the faster carbon gasification under the influence of K. This outcome is not verified by the actual investigations, because no solid or fixed carbon was present during the ISO, BF, or SR tests (only CO and CO₂ as carbon carriers). This falsifies all theories that link the increase in reducibility to catalytic effects on the Boudouard reaction. Another theory presented by Nakagawa relates to the surface change on the addition of K. The grain boundaries of wuestite (after reduction from magnetite) show an irregular and strongly eroded shape with a bigger contact area for further reactions. However, this effect was not detected by the transformation to metallic iron. Moreover, the use of KCl is an approach that does not lead to the effect of K on iron reduction only (dissolved Cl ions also have a big influence on reaction mechanisms).¹⁴⁹ Besides, Gougeon¹²⁶ sees a change in the surface area as a main factor for the increasing reducibility. The relatively big K atoms (effective ionic radius for K⁺=0.138nm, N⁺=0.102 nm, Fe²⁺=0.063 nm^{151,152}) infiltrate the outer layers of the Fe-O lattice, which leads to local expansion. The Fe-O bond is thereby weakened.

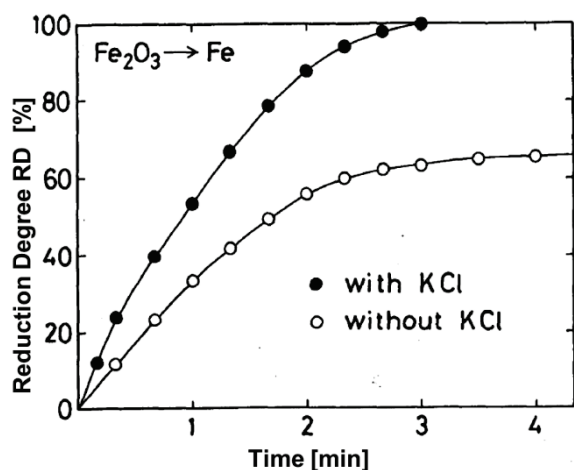


Figure 5-20: Effect of KCl addition on reduction degree under CO/CO₂ atmosphere at 900°C¹⁴⁹

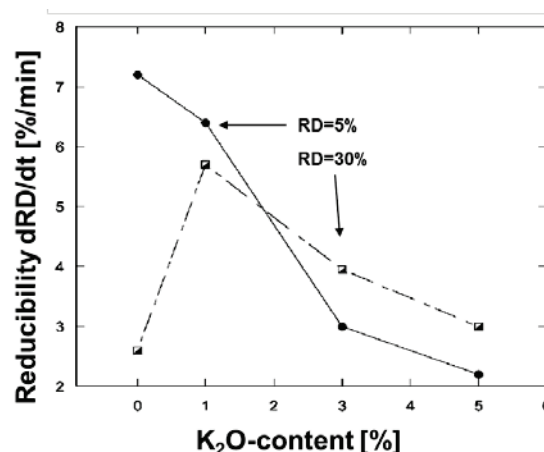


Figure 5-21: Change in reduction rate by the addition of K₂O at 800°C at a reduction degree of 5 and 30%¹²⁴

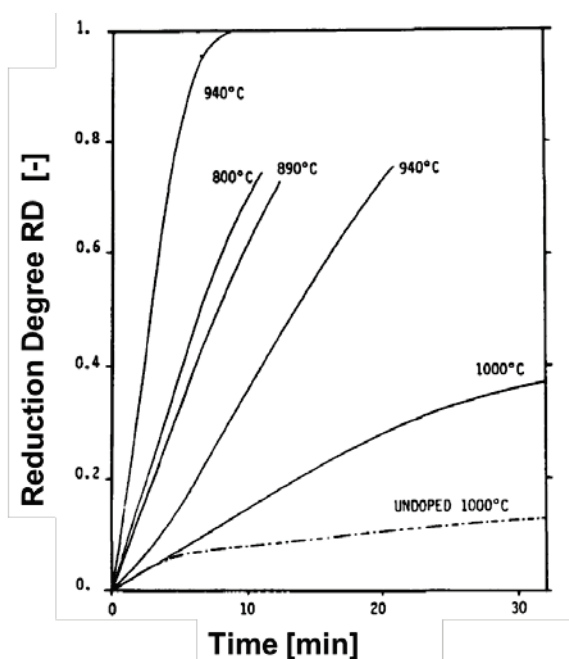


Figure 5-22: Reduction curves for doped iron oxide under CO, CO₂, H₂ and N₂ atmosphere at different temperatures¹²⁶

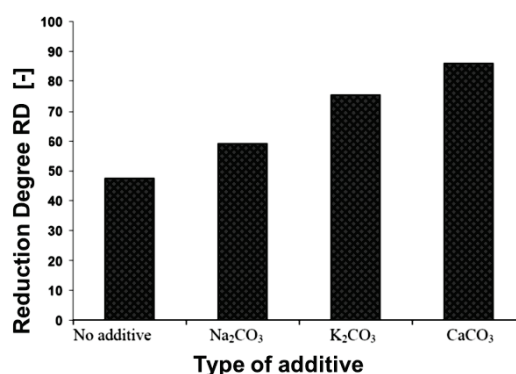


Figure 5-23: Effect of different carbonates on the reduction degree at 1000°C and 5% additives after 150 minutes¹⁵⁰

Gougeon¹²⁶ also demonstrates that already-reduced material can be soaked in alkali solution a second time. In subsequent tests, a faster reaction is seen. This leads to the theory that alkali ions do not affect the Fe-O bond. Moreover, a change in nucleation energy and growing was mentioned as a reason for faster reduction. In addition, tests with varying H₂ as the reducing gas were performed; no changes in the reaction velocity for treated and untreated materials were observed (the effect of H₂ will be discussed in Figure 5-24). Moreover, Pan¹²⁵ and Bahgat¹²⁴ performed reduction tests with sintered (Pan) and K₂CO₃-treated (Bahgat) materials. Although the sintering does not illustrate the actual process, K/Na shows similar effects. The reducibility increases to a maximum at its total alkali content of approximately 1–3%. With higher content, the reaction rate decreases again. This is described by a lower softening temperature (low melting K-/Na-containing phases) and clogging of the fine pores (confirmed by a lower surface

area). Both also discovered more whisker formation and sticking (similar to the tests in Chapter 5.2.3). To determine the real reaction mechanisms, first, a comparison of the activation energy has to be conducted (see data from Pan for Fe₂O₃ reduction and Bahgat for FeO reduction in Table 5-9). The energy was calculated using an Arrhenius plot, which shows a significant minimum of 1–3% of K₂O or Na₂O. This leads to the theory about a catalytic effect during reduction.

Table 5-9: Comparison of activation energy for iron oxide reduction

Reduction degree [%]	Reduction of Fe ₂ O ₃ (Pan ¹²⁵)				Reduction of FeO (Bahgat ¹²⁴)			
	0% Na ₂ O	1% Na ₂ O	3% Na ₂ O	5% Na ₂ O	0% K ₂ O	1% K ₂ O	3% K ₂ O	5% K ₂ O
5	36 kJ/mol	26 kJ/mol	29 kJ/mol	43 kJ/mol				
15					35 kJ/mol	16 kJ/mol	22 kJ/mol	24 kJ/mol
30	19 kJ/mol	10 kJ/mol	2.35 kJ/mol	3.4 kJ/mol				
80	8.8 kJ/mol	3.75 kJ/mol			25 kJ/mol	57 kJ/mol	60 kJ/mol	68 kJ/mol

Moreover, Luo¹⁵³ and Knell¹⁵⁴ describe a catalytic effect of K-dotted Fe oxides for the shift reaction (see Equation 5-1). In that context, it needs to be considered that metallic iron also acts as a catalyst during reduction. For instance, Fe_{met} is used during the Fischer-Tropsch synthesis (Equation 5-2). Knell determines this effect on the higher ion exchange rate for Fe³⁺ and Fe²⁺ in K-treated iron carriers (however, this does not describe the passivity of K during reduction by H₂). For the evaluation of the performed reduction tests, the two catalytic effects of K/Na and Fe_{met} have to be considered.



In addition to these thermodynamic aspects, kinetic considerations also have to be included. Especially if a view on H₂ reduction is taken, it will lead to an understanding of reduction kinetics in the particle. For instance, the performed tests under process-near conditions (BF, SR) show less influence of alkalis on reducibility compared to the standardized tests (ISO 4695) with pure CO. To check the specific influence of a single reducing gas, modified ISO 4695 tests with pure H₂ were performed (same temperature, gas flow, and pressure). The result (see Figure 5-24) shows that H₂ reduction is not affected by the addition of K or Na (also confirmed by process-near reduction tests and literature¹²⁴).

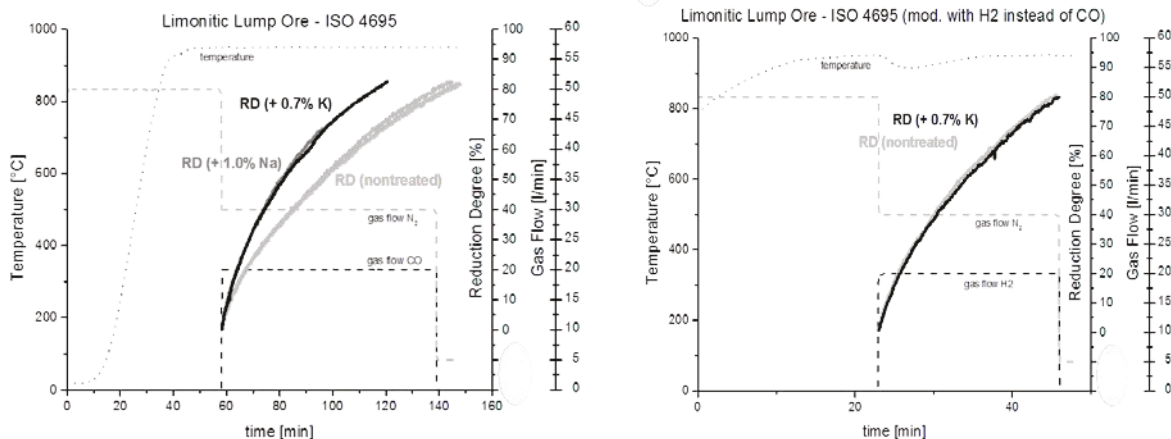


Figure 5-24: Reduction of lump ore with pure CO (left) and pure H₂ (right) atmospheres (testing conditions derived from ISO 4695)

Two mechanisms can be the reason for this. On the one hand, the kinetics of hydrogen plays a role. H_2 is characterized by faster diffusion; in most cases, iron ore reduction by hydrogen is controlled by the kinetics of the chemical reaction. CO reduction can be limited by diffusion as well as by chemical reaction kinetics. It can be determined that no change in limiting kinetic steps and no change in the chemical reaction (iron oxide reduction by hydrogen) have taken place. For CO reduction, the evaluation of kinetics is more complex. However, pellet brand 1 (see Figure 5-11 left) supports important information. A clear change (a buckle) of the reduction rate under a pure CO atmosphere and, derived from that, the limiting kinetic step are visible after a few minutes. This indicates a change from a diffusion-limited to a chemical reaction-limited process. Untreated pellet brand 1 is first limited by the transport of CO to and CO_2 from the reaction area (the reaction rate is high). After a few minutes, this changes to a limitation by the chemical reaction. The fact that pellets have a high surface area for the reaction confirms the diffusion as a limiting step for the start of pellet brand 1 (and for the total reduction time of pellet brand 2). According to the effect of K/Na, the change in the limiting kinetic step is not observed. Both pellets show an increase in the reduction rate (although pellets are already characterized by a high reducibility). This indicates the chemical reaction to be the kinetic step, which is influenced by alkalis.

Conclusion and final interpretation:

The combination of the discussed ideas and facts leads to the theory that alkalis destabilize the C-O bound of the CO (the reason for faster reduction). The following points confirm this theory:

- Lower activation energy (see Table 5-9 and the literature^{125,124})
- Chemical reaction as the influenced kinetic step (comparison of ferrous burden materials, especially pellet brand 1; for an example, see Figure 5-11)
- Bigger metallic grains observed by petrographic investigations (see Figure 5-18 and Figure 5-19; this also leads to less mechanical stability, as mentioned in Chapter 5.2.3)
- Different effects of H_2/CO in the reduction gas (see Figure 5-24)

All these research results were derived from following key aspects:

The saturation was carried out with OH solutions for both KOH and NaOH. Hence, it is assumed that the hydroxide solution changes the original ferrous materials and leads to changes in reduction behaviour. This statement can be falsified as the OH content is similar for two solutions with the same content of KOH or NaOH (5-molar), but the change in reducibility is slightly different. So, a constant change in basicity does not lead to a consequent change in reducibility or mechanical properties. Moreover, tumbling tests were performed directly after the aqueous treatment. These have not shown changes compared to the original material. In addition, saturation tests with aqueous $NaCO_3$ solutions were performed with the same molarity of Na. The results were similar as those for material under $NaCO_3$ treatment and NaOH treatment for the same Na content.

The statement that a catalytic effect on the Boudouard reaction leads to changes can be negotiated with regard to the absence of carbon in the tests. However, a specific effect on CO reduction was detected (decreasing influence of alkalis with decreasing CO content in the reduction gas). This aspect is seen as controversial in the literature.^{124,126} The investigations for this research determine that alkalis and CO influence each other during iron ore reduction, but alkalis and hydrogen do not. This is also confirmed by the ISO tests under pure CO, which show

the biggest change in reactivity. Although the partial pressures and temperature profiles are complex for the performed tests, the independence of alkalis during H₂ reduction is definitive. Moreover, the trends are similar for all materials, although the structures and chemical compositions are very different for pellets, lump ores, and sinter samples.

Inorganic chemistry¹⁴⁴ can support important facts relating to the evaluation of the microscopic mechanisms. Due to the electropositive characteristics of K/Na atoms, the low electronegativity can affect the partially polar CO molecule (an effect at the non-polar H₂ can be denied) and leads to fluctuations of the electron cloud of the compound. This behaviour is presented schematically in Figure 5-25. Moreover, the formation of the interim product Na₂O (FeO+2Na) and the further easier reduction by CO (Na₂O+CO leads to 2 Na + CO₂) can play a possible role in the reducibility.

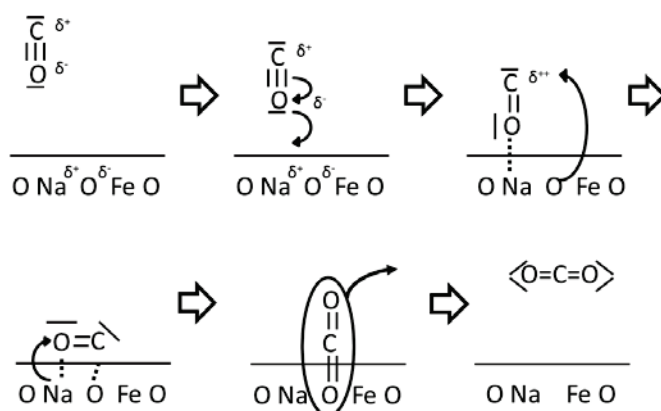


Figure 5-25: Influence of alkali on the chemical mechanisms during reduction by CO

The change in the crystallographic structure of the solid material as a reason for the accelerated reducibility is seen as a minor factor (see hydrogen reduction, which was not affected by alkalis, although they were clearly detectable in the material structure).

5.4 Effects of Alkalis on Softening and Melting Behaviour

Alkali metals are known to have lowering effects on the melting temperature of burden material. To evaluate this effect on the softening and melting of iron carriers, particularly under the influence of alkalis, investigations were performed. Especially the cohesive area of the BF is important for the process behaviour due to the lowering of the softening temperature by K/Na (see Figure 3-13) and the connected worse BF performance caused by a wider temperature range for full melting (higher pressure drop in cohesive zone).⁸² The investigations were linked to the melting temperatures of alkali-bearing oxides. Na and K can penetrate the particle, especially in the gangue and glass phases (confirmed by microprobe; refer to Chapter 5.2). The methodology is a further development of the performed reduction and tumbling tests (see Chapter 5.3). It helps to gain information about affected materials in the cohesive and melting zone.

5.4.1 Preparation of Material and Methodology

To simulate the behaviour in the melting zones of the reactor, partially reduced material (approximately 80% RD) was taken as input material (reduced material from previous chapter; also see Figure 5-1) for softening and melting tests. Data from the literature show similar RDs for the area directly above the cohesive zone.^{28,82}

All iron carriers from Chapter 5.2 were studied (for the chemical analysis, see Table 5-10). The RD was similar at ~80% for all samples.

Table 5-10: Chemical analysis of partially reduced iron carriers for the softening and melting tests

	Fe _{tot} [%]	Basicity B ₄ [-]	Untreated K ₂ O [%]	K-treated (5-molar) K ₂ O [%]	Untreated Na ₂ O [%]	Na-treated (5-molar) Na ₂ O [%]
Hematite	82.5	0.01	0.145	0.456	0.123	0.246
Limonite	80.9	0.01	0.005	1.112	0.013	1.482
Pellet 1	79.6	0.07	0.099	2.421	0.062	1.403
Pellet 2	80.3	0.67	0.025	1.332	0.025	1.153
Sinter 1	61.6	1.25	0.634	1.08	0.085	1.045
Sinter 2	61.9	1.8	0.356	1.381	0.054	1.36

The task for the research was evaluation of the influence of alkalis like K and Na on the softening and melting behaviour, according to three special points of view: the change in transformation temperature, the effect on specific morphological phases (e.g. gangue or glass), and the differences between different iron carriers and types of alkalis (Na, K).

Investigations were carried out using HSM, HT-LSCM, and DTA. Supporting information was delivered by chemical analysis and SEM. The testing conditions were adapted to industrial conditions (see Figure 2-3 and Table 5-11).

The reduced material was prepared due to their use in the different methods. For the investigations with the HSM and the DTA, the material was ground to a grain size $<50\ \mu\text{m}$. For the HT-LSCM, the material was cut into cylindrical samples with a diameter of $\sim 7\ \text{mm}$ and a height of 5 mm.

5.4.2 Methods of Testing (Softening and Melting Temperature)

First, several methods of testing were performed to find a successful methodology for simulation of the cohesive zone according to the alkali load. However, the less successful methods were used to gain supporting information.

HSM (hot stage microscopy): A HSM is used to measure the melting and wettability of substances on solid materials (e.g. slag on refractory material). Therefore, the investigated substance is located on the material, charged into a tube furnace, and heated up. The shape of the materials is recorded with a camera, which analyses the change in the size of the shape. For further information, see the literature.¹⁵⁵ One method that was also used for the defined task is to press pulverized material into a cone or cylinder. During heating up, the shape of the cone changes. The shape of the investigated material can be linked to specific temperatures like deformation, softening, hemispherical, and flowing (melting) temperature.^{156,157}

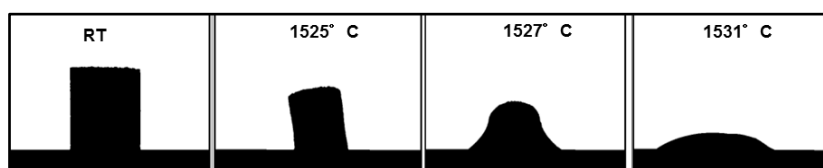


Figure 5-26: Exemplary result of the melting behaviour recorded by hot stage microscopy (left: ambient temperature, softening point at 1525°C , hemispherical point at 1527°C , and flowing point at 1531°C)¹⁵⁸

HT-LSCM (hot temperature laser scanning confocal microscopy):

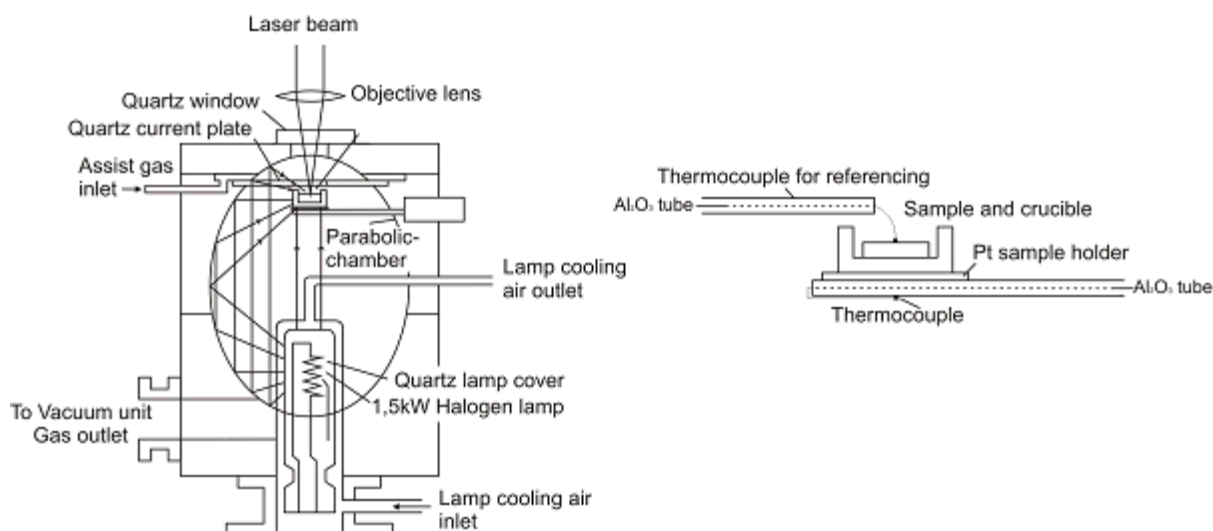


Figure 5-27: Schematic picture of the HT-LSCM, including the sample holder (Al_2O_3 crucible)¹⁵⁹

With HT-LSCM, it is possible to examine a material’s surface at temperatures up to 1700°C. This is normally not possible with an optical microscope because of the emission of tempering colours by ferrous materials starting with $T > 200^\circ\text{C}$. Therefore, the sample surface is scanned by a laser that is controlled by mirrors. The laser initiates a local, fluorescent radiation that is intensified and detected by a photomultiplier. A schematic image of the setup is shown in Figure 5-27, including the sample holder system. For further information on the technical details and procedures, see the reviewed literature.³³

DTA (differential thermal analysis): The DTA is based on a simultaneous gravimetric analysis with a reference sample. Based on the comparison of the energy consumptions of two samples that are heated up under similar conditions (pressure, atmosphere, gas flow), it is possible to determine phase transformations of the investigated sample at certain temperatures (including solid-liquid transformations). The reference material itself undergoes no transformation. In particular, the difference in heat consumption is measured, which also allows statements about endothermic or exothermic reactions. The two types of DTA signals are shown in Figure 5-27.

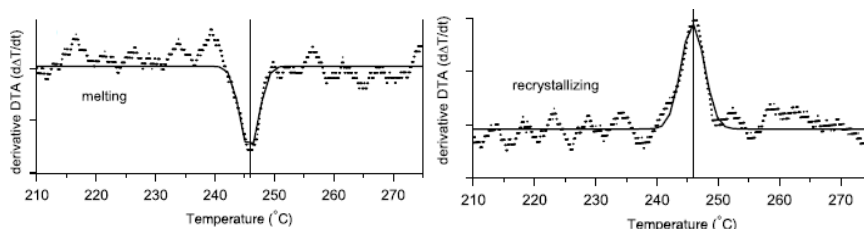


Figure 5-28: Exemplary schemata of DTA curves for phase transformations (endothermic reaction for melting [left] and exothermic reaction for recrystallization [right])¹⁶⁰

By these tests, it is possible to determine the transformation temperatures of the reduced materials, including the melting temperature. Afterwards, it is possible to compare alkali-treated material with untreated materials.¹⁶¹ For the interpretation of the results (see Table 5-12 and Figure 5-14), it has to be considered that the measurements were carried out using different DTA facilities with different measured temperature ranges.

Table 5-11 presents a summary of the main parameters for the testing procedures of HSM, HT-LSCM, and DTA measurements.

Table 5-11: Process conditions for the softening and melting tests

	Sample mass [g]	Temperature range [°C]	Heating rate [K/min]	Atmosphere [%]	Measured value
HSM	0.250	0–1600	10	100% N ₂	Optical (sample profile)
HT-LSCM	approx. 25	0–1500	5	100% Ar	Optical (sample surface/section)
DTA	0.250	0–1600	10	100% N ₂ (70 ml/min)	Heat (changes to reference sample)

5.4.3 Influence of Alkalis on Melting and Softening Behaviour: Test Results

In the following chapter, the results of the individual methods are summarized.

HSM (hot stage microscopy): The results of the HSM were derived from transformation points. These points were measured by a camera as per Figure 5-29. The research focused on partially reduced limonitic ore (top) and the basic pellet brand 2 (bottom). Untreated, K-treated, and Na-treated samples were observed. The measured temperature values for the softening and melting (flowing) points are also included in Table 5-12. To sum up, no significant difference between the softening and melting temperatures of treated and untreated materials was measured. So, the HSM is not the appropriate method for evaluation of the influence of alkalis. These tests mainly revealed that the metallic iron seems to be definitely not influenced by alkalis. This statement can be derived from the stability of all cylinders up to $\sim 1530^{\circ}\text{C}$, the T_m of pure metallic iron. Another outcome refers to the previously performed reduction tests. Investigations on ISO-reduced materials and on material that was reduced under process-near conditions (BF conditions) show no differences during melting. This confirms the independence of metallic iron in reduction.

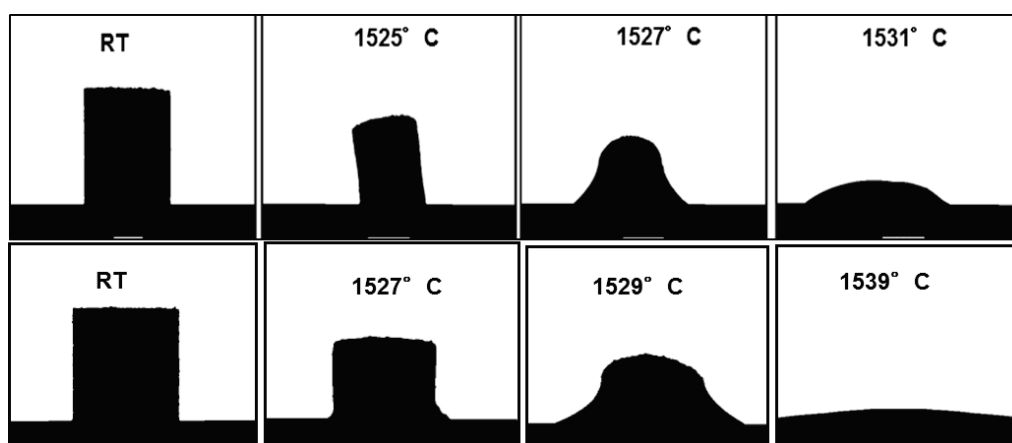


Figure 5-29: Exemplary result of the melting behaviour recorded by hot stage microscopy (top: partially reduced limonite, Na-treated; bottom: partially reduced pellets, K-treated)¹⁵⁸

HT-LSCM (hot temperature laser scanning confocal microscopy): Observations by HT-LSCM were carried out using three different samples: limonitic lump ore, pellet brand 2, and sinter blend 2. The reduced materials behaved similarly in the equipment. For example, Figure 5-30 shows monitored pictures of pellet brand 2. The metallic fraction was clearly visible (white areas) the whole time. This also confirms the findings from the HSM: that the metallic structure is stable up to 1530°C . Moreover, the pores (black) and the oxidic areas (dark grey for glass and gangue, light grey for wuestite) were clearly visible.

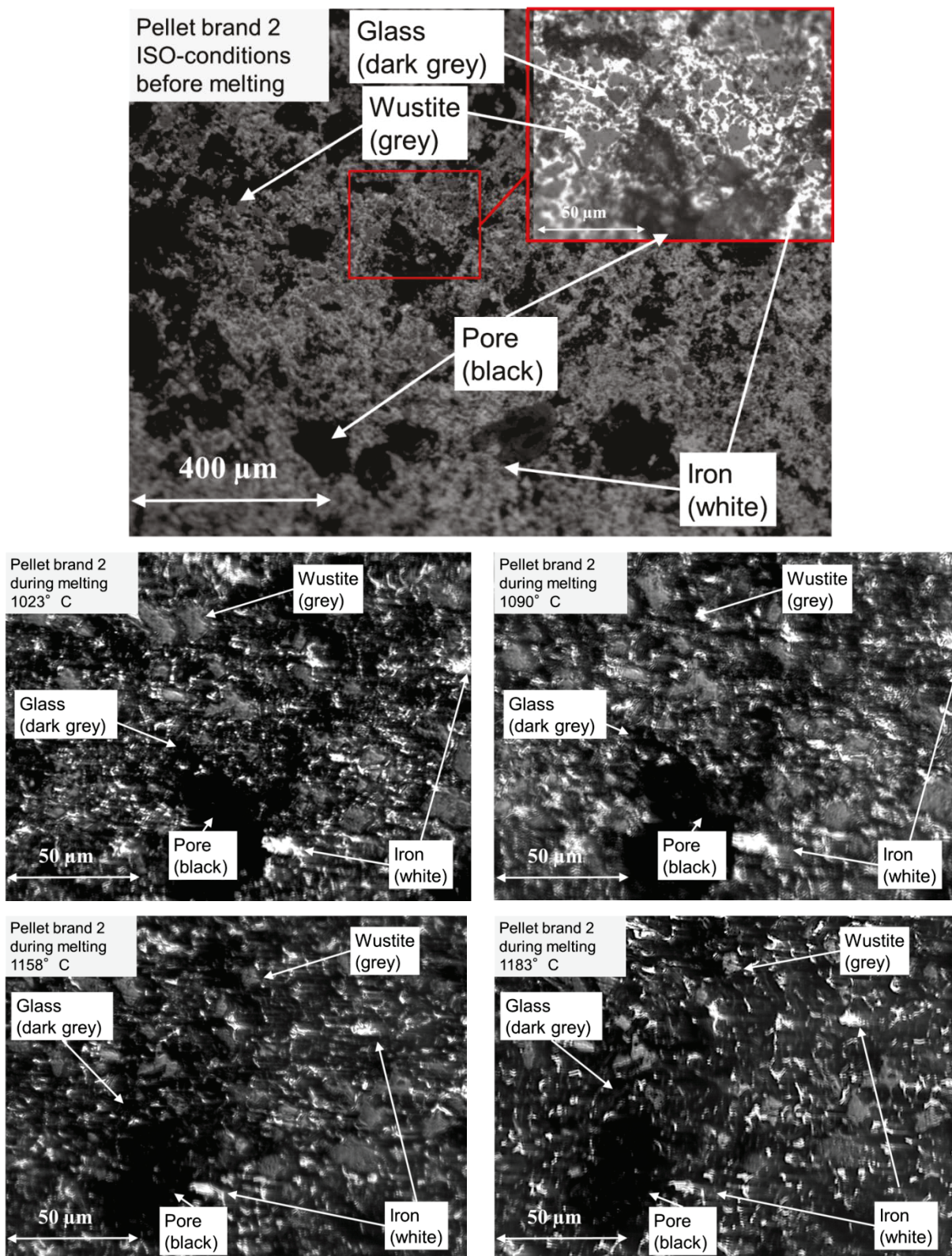


Figure 5-30: Observation of reduced pellets by HT-LSCM before heating up (light microscopy) to 1023°C, 1090°C, 1158°C and 1183°C

However, a serious problem occurred during the operation. For a successful test, the HT-LSCM needs a plane surface of the sample. This can be achieved up to temperatures of 1100°C. Above this temperature, the softening of oxidic phases starts and the surface becomes irregular. No picture of the sample can be recorded anymore. However, the results of pellets (Figure 5-30), limonitic lump ore (see Figure A-5), and sinter (see Figure A-6) are included in this work because they give supporting information about the microstructure.

DTA (differential thermal analysis): Investigations using DTA have been performed with the limonitic lump ore, both pellets brands, and both sinter blends. Furthermore, a comparison between untreated, K-treated, and Na-treated samples proved successful. Figure 5-31 illustrates all measured DTA curves. For all figures, the curves for untreated (light grey), K-treated (black), and Na-treated (dark grey) samples are included. The corresponding values are summarized in Table 5-12. For the measurements, only material from the ISO reduction tests was taken. Additional tests with material from the BF reduction test shows no difference.

A careful look at the main outcomes shows that especially the transformation temperatures of the iron-bearing phases dominate the curves. The limonitic lump ore and pellet 2 were heated up to 1600°C. So, the melting of the metallic iron can be seen clearly at 1530°C. Here, a high amount of energy is consumed. Another transition temperature, which is visible in every measurement, is the γ - δ transformation of iron. Due to its characteristic as a solid-solid transformation, the consumed energy is smaller than in the melting point. With regard to oxides, evaluation of the results becomes more difficult. The FeO-bearing phase is dominant in every material due the partial reduction of ~80%. The melting point of FeO is between 1250–1350 °C, depending on how the FeO is bounded in the different phases. For instance, the limonitic lump ore has dense wuestite cores and it shows a defined transition at ~1350°C. However, the sinter shows a lower FeO point because of the correlation with calcioferrites. The pellets and sinter samples show multiple phase transformations between 1150 and 1350°C. Overall, the measurement of the phase transformation was representative (see repeated tests in Figure 5-31) and the determination of the transition temperature was precise (see evaluation in next chapter).

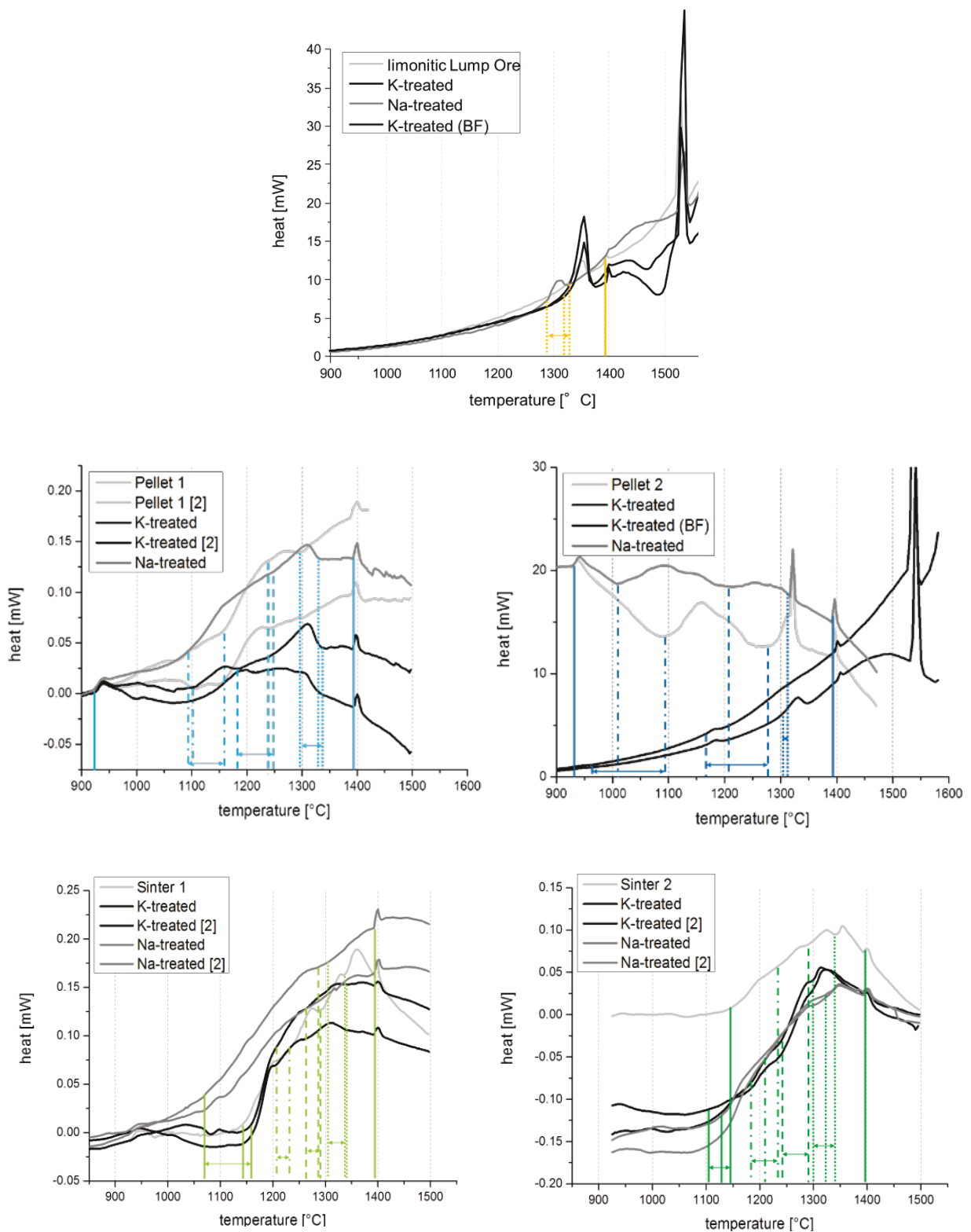


Figure 5-31: Comparison of the recorded DTA curves for reduced ferrous materials (untreated and treated)

5.4.4 Influence of Alkalis on Melting and Softening Behaviour: A Comparison with Literature and Data Evaluation

In this chapter, the results of the melting tests are summarized and analysed.

5.4.4.1 Evaluation of Testing Results and Comparison of Different Methods

In general, DTA was the most successful tool for determining the specific influence of K/Na on the melting behaviour. The results of the HSM only showed the melting temperature; the softening temperature was measured at nearly the same range (see Table 5-12 [top]). This is caused by the metallic fraction (iron) in the reduced material, which stabilizes the cylinder during the heating up phase. The metallic iron starts to melt at a temperature of $\sim 1530^{\circ}\text{C}$ (theoretically at 1536°C for pure iron). Measured values above 1536°C (e.g. K-treated samples in Table 5-12) show the difficulty of this measuring method. Consequently, this methodology was only used for supporting information, but not for reaching the determined task. Similarly, the HT-LSCM only delivers optical information about the materials' surface during heating up; specific deformation or melting temperatures are difficult to measure (see Figure A-5 to A-6 and Figure 5-30). Observation of the partially reduced material above 1300°C (depending on material source) is hardly possible. The reason therefore is the softening of oxidic compounds, which makes the flat surface irregular. However, a flat surface is important for the measurement. A successful approach involved determining the transformation temperatures using DTA. Due to a precise measurement (calibration with cobalt [Co] ensures reproducibility of $\pm 1\text{K}^{158}$), representative results are available. This enables the comparison between treated and untreated materials. All transformation temperatures are summarized in Table 5-12 (bottom).

Limonitic lump ore: The limonitic lump ore is characterized by small amounts of acid gangue. During HSM, no significant changes were visible with the addition of alkalis (see temperatures in Table 5-12 [top]). This is caused by the stable metallic fraction up to 1530°C . This relation can be confirmed with the observation by HT-LSCM, which shows stable metallic iron spots up to 1400°C (see Figure A-5 [white areas]). The DTA shows all phase transformations up to $\text{Fe}_{\text{met}(\text{liquid})}$. This enables an interpretation of all transformations in correlation with the chemical analysis (see Table 5-10). The most important peaks are caused by the melting of Fe_{met} (measured: $1520\pm 5^{\circ}\text{C}$) and FeO (measured: $1326\pm 50^{\circ}\text{C}$). Phase transformations of the solid metallic fraction cause lower peaks: α - γ transformation at $920\pm 5^{\circ}\text{C}$ and γ - δ transformation at $1394\pm 2^{\circ}\text{C}$. Derived from Table 5-12, it can be seen that only FeO is affected by the addition of alkalis; the metallic fraction appears unaffected. For Na-treated material, the increase by 1.5% Na leads to a drop of nearly 50°C in the transformation temperature for $\text{FeO}_{(\text{s})}$ - $\text{FeO}_{(\text{l})}$. This trend was not detectable for K-treated material. The low ratio of non-ferrous compounds leads to hardly detectable and non-significant transformation peaks of the gangue phase. As mentioned, tests with reduced materials from ISO reduction and process-near reduction (BF conditions) were carried out. It was observed that the method of reduction has no influence on the metal's behaviour during melting (see Figure A-5 for limonitic lump ore).

Table 5-12: Comparison of transformation temperature influenced by alkalis¹⁵⁸

Method	Material	Temperature (Phase transformation)	Untreated T [°C]	K-treated T [°C]	Na-treated T [°C]	
Hot stage microscopy (HSM)	Limonitic ore	Softening	1528/1526	1528/1530	1525	
		Melting	1530/1530	1541/1546	1531	
	Pellet brand 2	Softening	1526/1525	1527/1527	1524	
		Melting	1531/1532	1539/1527	1530	
Differential Thermal Analysis (DTA)	Limonitic ore	Fe _{met} (α-γ)	920	915/918	915	
		Na-silicate			1091	
		SAF	1326	1327/1339	1287	
		Fe _{met} (γ-δ)	1394	1396/1396	1395	
		Fe _{met} (δ-liquid)	1520	1518/1525	1523	
	Pellet brand 1	Fe _{met} (α-γ)			926/922	925
		SAF	1159/1160	1100/1119	1089	
		SAF	1248/1239	1214/1185	1254	
		FeO	1301	1326	1331	
		Fe _{met} (γ-δ)	1397/1396	1393/1395	1393	
	Pellet brand 2	Fe _{met} (α-γ)	930	925/926	930	
		CAF	1080	962	1007	
		FeO	1299	1165/1180	1208	
		Fe _{met} (γ-δ)	1394	1397/1397	1393	
		Fe _{met} (δ-liquid)	-	1530/1531		
	Sinter 1	CSF	1143	1159/1160	1054/1091	
		CSF	1237	1220/1205		
		CSF	1290	1265/1264	1290	
		FeO-based phase	1340	1345/1341	1307	
		Fe _{met} (γ-δ)	1392	1393/1393	1397/1395	
	Sinter 2	CSF	1148	1103/1092	1132/1135	
		CSF	1235	1185/1183	1212/1216	
		CSF	1295	1243/1242		
		FeO-based phase	1346	1300/1301	1322/1331	
Fe _{met} (γ-δ)		1392	1392/1396	1392/1395		

Pellets: Two different pellet brands were investigated (pellet brand 1 with acid gangue and pellet brand 2 with basic gangue). Observations by HSM show behaviour similar to the limonitic lump ore (stable cylinder up to 1530°C; no difference between treated and untreated material). The measurement by the HT-LSCM (see Figure 5-30) only shows results until 1200°C; afterwards, the softening binder or oxides do not allow a clear picture of the flat surface. After the test, it was seen that the gangue and FeO phases sank below the original surface level (metallic iron was still at the same height). In addition to the recorded HT-LSCM pictures, a SEM measurement was carried out to confirm the stability of alkalis in the material during heating up (normally the boiling temperature of K/Na is <900°C). The results of the metal-rich and oxide-rich areas are summarized in Table 5-13, and they confirm the presence of the K/Na in the material up to nearly 1500°C. An enrichment of 4.7% Na in total was measured for the oxide-rich phase.

Table 5-13: Analysis of melted material (based on partial reduced pellet brand 2, Na-treated) by SEM measurement¹⁵⁸

	O [%]	Na [%]	Al [%]	Si [%]	Ca [%]	Ti [%]	Mn [%]	Fe [%]
Metal-rich area	2,43	-	0,56	0,23	0,14	-	-	96,64
Oxide-rich area	32,68	4,7	11,85	8,72	9,11	0,15	0,86	31,93

The DTA results show similar results as for the limonitic ore. The main phase transformations can be linked for both brands to the metallic phase transformations (α - γ transformation: $925\pm 5^\circ\text{C}$; γ - δ transformation: $1395\pm 2^\circ\text{C}$; δ -liq transformation: $1330\pm 1^\circ\text{C}$). Other phase transformations are linked to the behaviour of oxidic systems (gangue, binder, and FeO phases). These oxidic systems are also the main difference between the two pellets brands.

Sinter: For the research on sinter, two different types based on two different blends were investigated (sinter 1 with basicity $B_2=1,2$ and sinter 2 with basicity $B_2=1,8$). In addition, for sinter, the observation by the HT-LSCM (see Figure A-6) was unsuccessful due to the sinking of the oxidic phases (gangue, glass, calcioferrites, FeO) at temperatures $>1200^\circ\text{C}$. The DTA delivers useful information due to the effect of alkali addition. Apart from metallic transformation (see limonitic lump ore and pellets brands), all oxidic transformations were affected by alkalis (K and Na). This effect is even higher than for the pellets brands.

5.4.4.2 Discussion of the Melting Tests and Conclusion

In the following, the main outcome of the softening and melting tests is summarized and discussed.

According to the methodology, the DTA analysis is the best way to determine the influence of alkalis on the melting behaviour of ferrous (partially reduced) burden material. Besides the chemical analysis and SEM investigations, HSM and observation by HT-LSCM are supporting methods that help to confirm the results of the DTA and supply additional information.

Due to the determined results, it may be assumed that alkalis have no influence on the metallic phases but high influence on the oxidic compounds of the iron carrier. Nearly all investigated materials show a constant transformation temperature for both treated and untreated materials (α , γ , δ , liq transformations). Only slight discrepancies can be seen between theoretical values⁷⁵ and measured data. To confirm this outcome, the results from Table 5-12 can be compared to the Fe-O binary system of Figure 5-32. These also fit the results of the HSM and HT-LSCM.

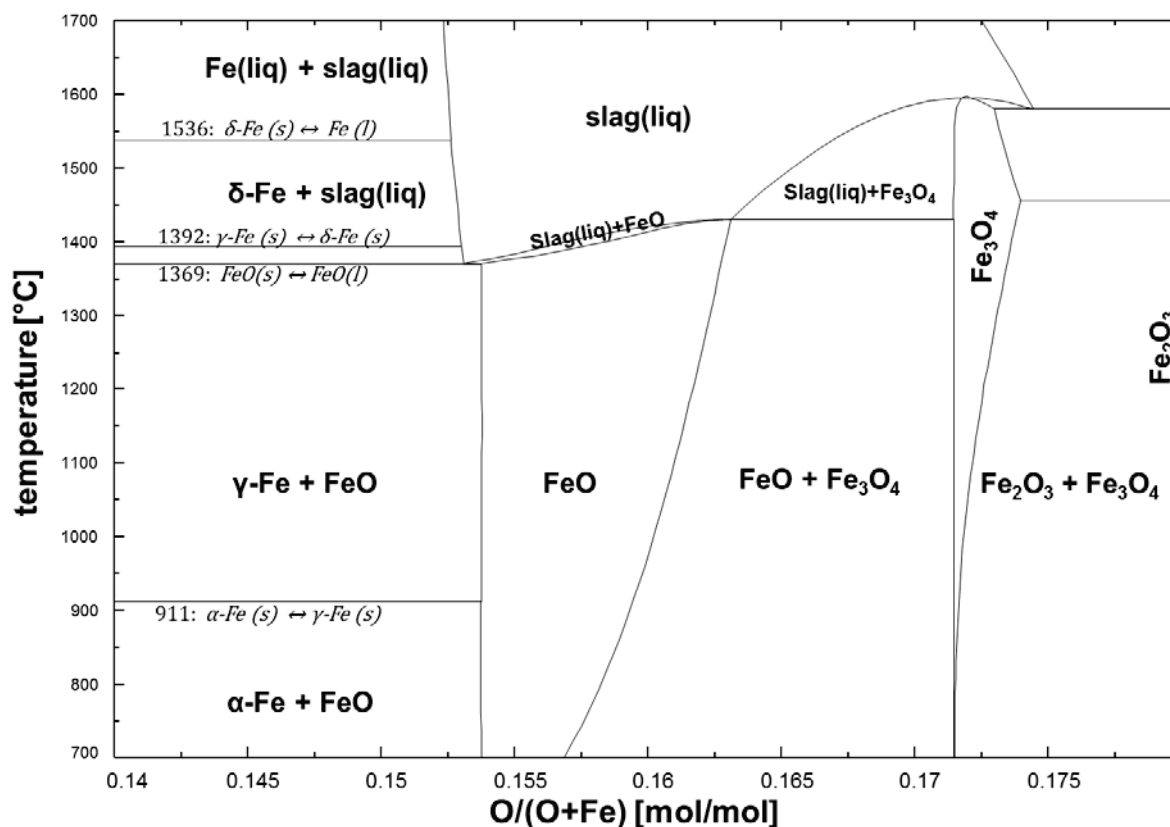


Figure 5-32: Fe-O binary system including the phase transformations and temperatures⁷⁵

However, the oxidic compounds are highly affected by alkalis, which can be seen in a significant change of the transformation temperatures. To get an impression of the impact of K/Na on the transformation temperatures, Figure 5-33 compares the two binary diagrams FeO-SiO₂ and FeO-Na₂SiO₃ to visualize the change in the stability areas by addition of Na₂O.

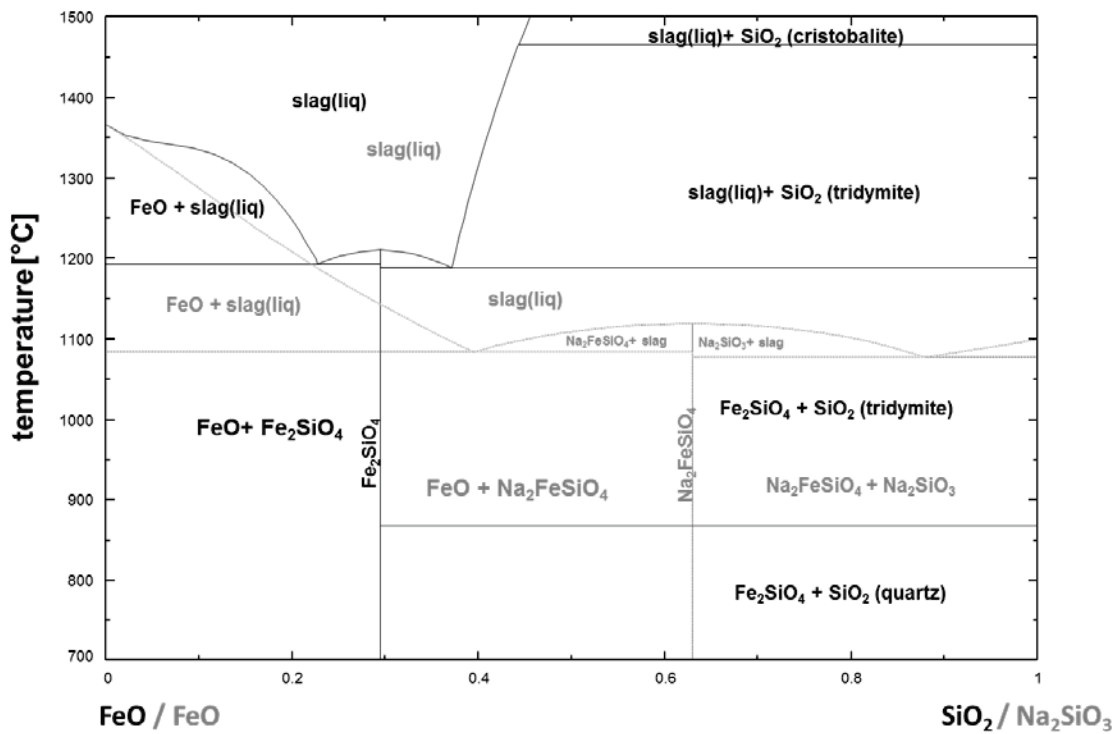


Figure 5-33: Comparing the binary systems of FeO-SiO₂ (black) and FeO-Na₂SiO₃ (grey)⁷⁵

The oxidic systems are of particular interest. Therefore, Table 5-14 selects the oxidic compounds of the reduced and investigated materials, and places these in relation with ternary systems. Although the materials are inhomogeneous due to their origin as industrially used iron carriers, the approach for the interpretation needs to use multiple-compound systems. The most important ternary systems are CaO-Al₂O₃-SiO₂ (CAS), CaO-SiO₂-FeO (CSF), CaO-Al₂O₃-FeO (CAF), and SiO₂-Al₂O₃-FeO (SAF). According to the basicity, especially limonite and the pellets have acidic characteristics (high SiO₂ and Al₂O₃). The amount of FeO is high in all samples due to the partial reduction of the total material RD ~80% before melting).

Table 5-14: Comparison between the oxidic systems of the iron carriers (C-CaO, A-Al₂O₃, S-SiO₂, F-FeO)

	CAS [%]	CSF [%]	CAF [%]	SAF [%]
Limonite	0.4/39.4/60.2	0.1/9.4/90.6	0.1/6.3/93.6	8.8/6.1/85.4
Pellet 1	2.5/5.5/92.0	0.7/27.4/71.8-	1.0/2.2/96.8	27.2/1.6/71.2
Pellet 2	40.1/22.7/37.2	10.7/9.9/79.4	11.1/6.3/82.6	10.4/6.3/83.3
Sinter 1	48.9/11.3/39.8	31.3/25.4/43.3	38.2/8.8/53.0	33.4/9.5/57.0
Sinter 2	58.9/8.5/32.7	37.4/20.7/41.9	44.1/6.4/49.5	30.5/7.9/61.6

An evaluation of the materials in correlation with the literature and the data from Table 5-12 and Table 5-14 is conducted in the following chapter. To evaluate the results from DTA, a closer look at ternary systems and data from the literature is essential. Afterwards, the transition temperatures were linked to specific phases (see Table 5-12).

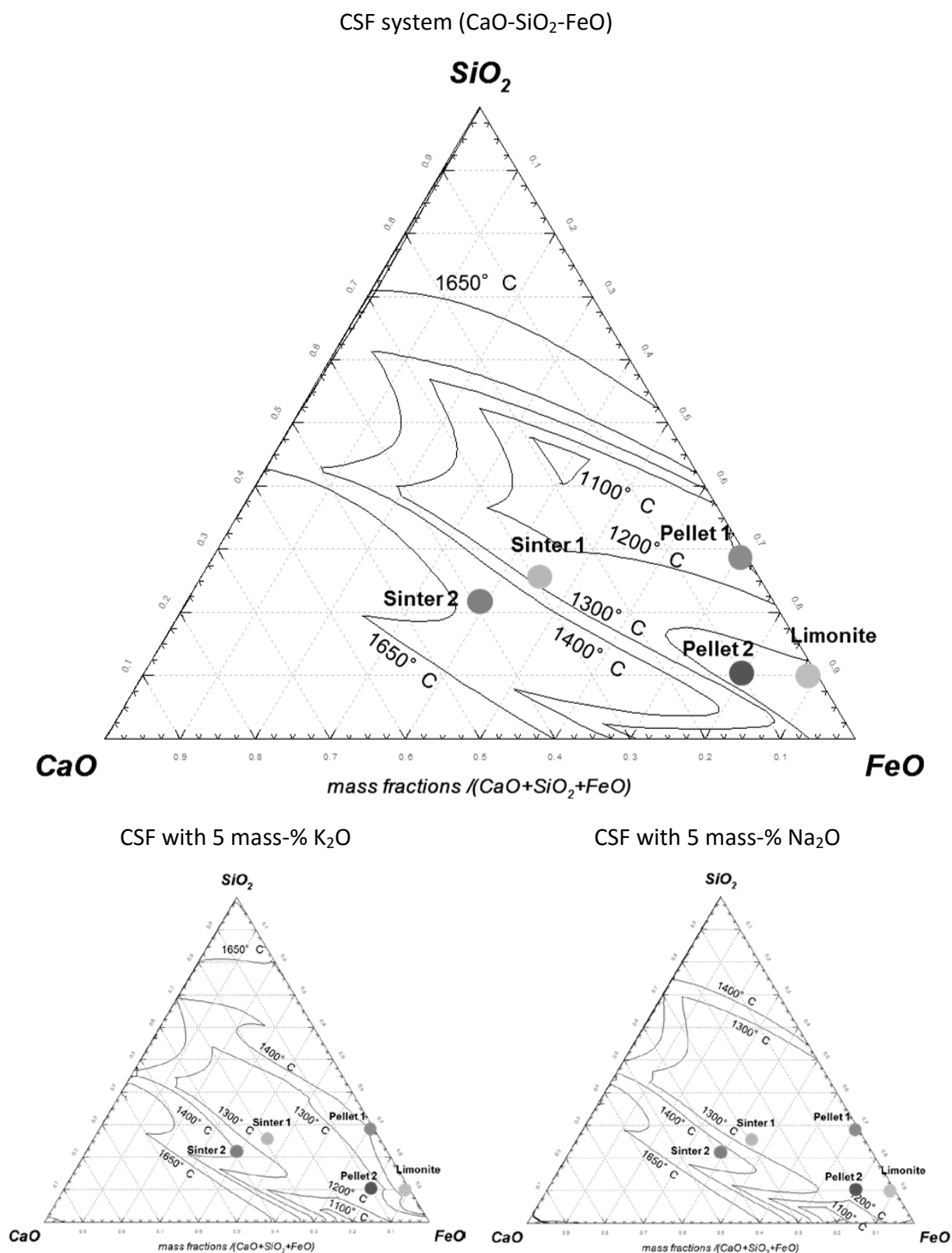
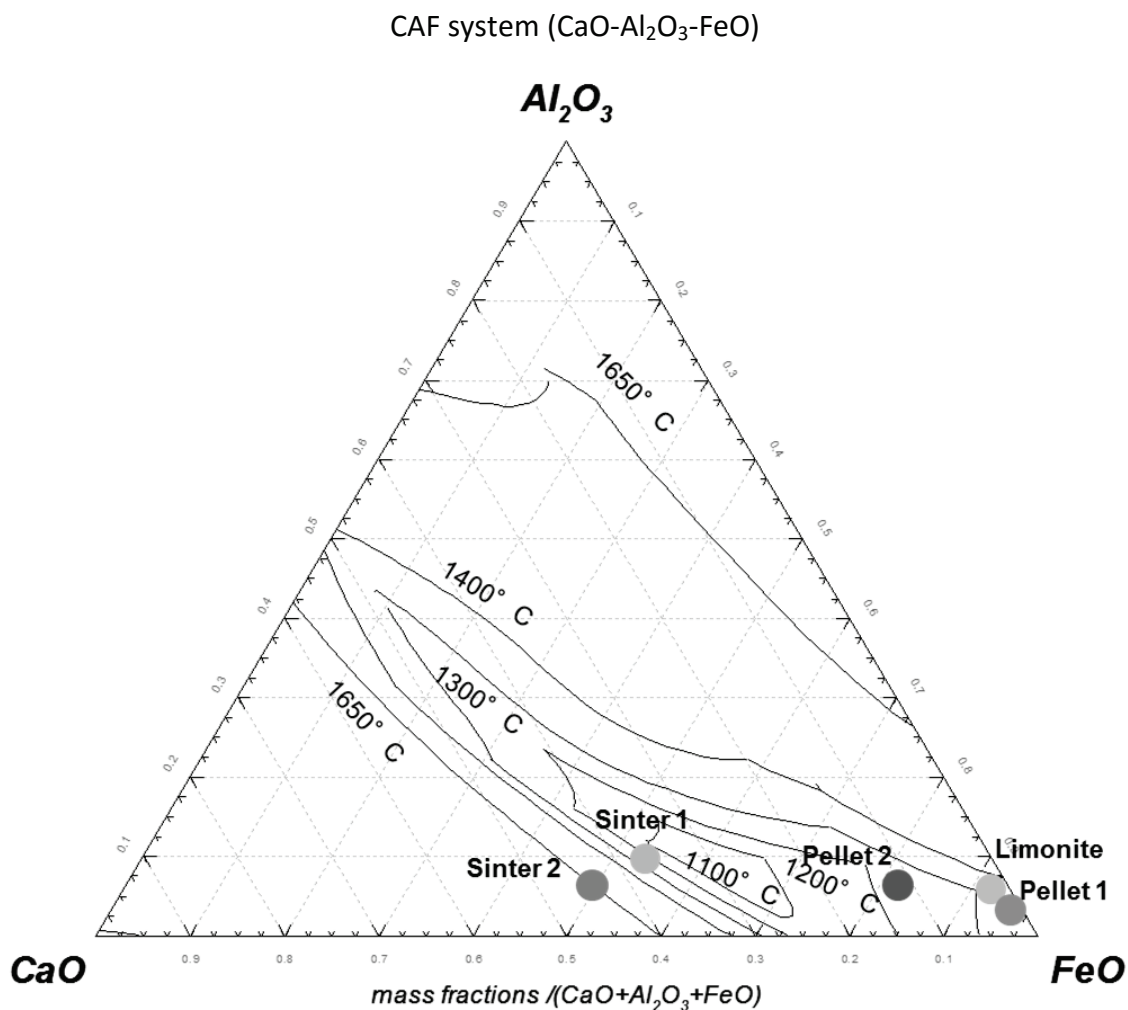
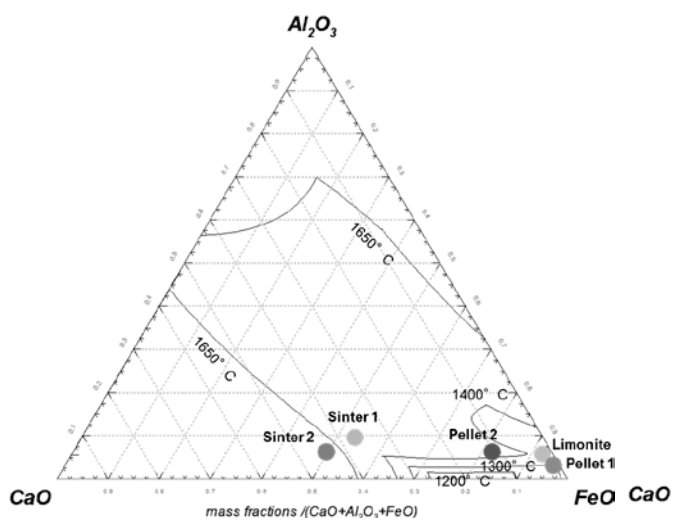


Figure 5-34: Ternary system CSF with the liquidus lines for 1000–1600°C, and the modifications with 5 wt-% K₂O and Na₂O (chemical composition of the oxidic compounds of the investigated materials marked as points)



CAF with 5 mass-% K₂O



CAF with 5 mass-% Na₂O

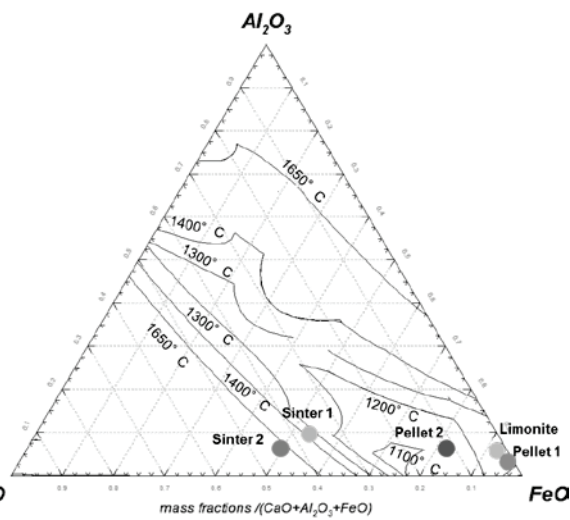


Figure 5-35: Ternary system CAF with the liquidus lines for 1000–1600°C, and the modifications with 5 wt-% K₂O and Na₂O (chemical composition of the oxidic compounds of the investigated materials marked as points)

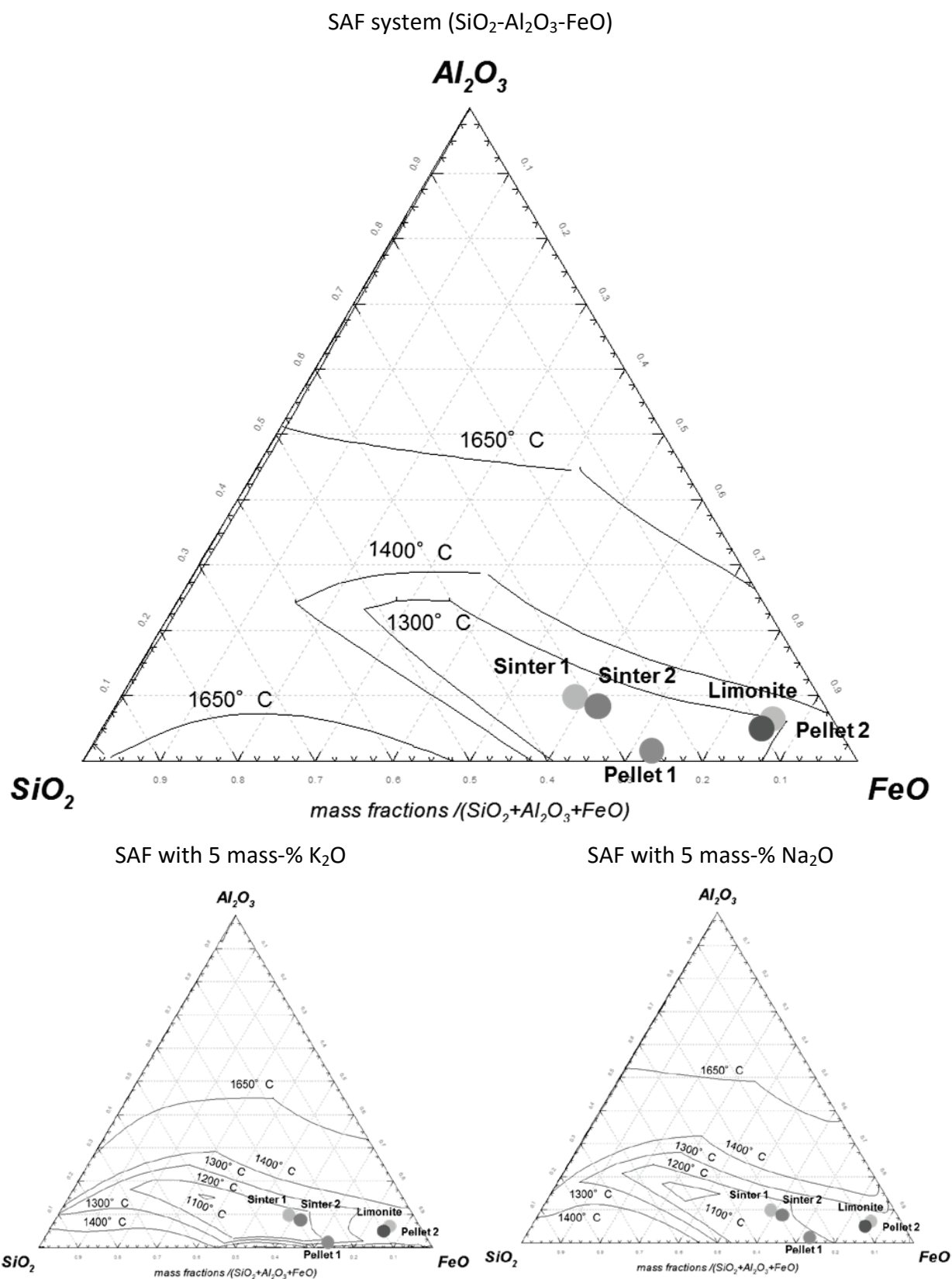


Figure 5-36: Ternary system SAF with the liquidus lines for 1000–1600°C, and the modifications with 5 wt-% K_2O and Na_2O (chemical composition of the oxidic compounds of the investigated materials marked as points)

Limonitic lump ore: To evaluate the acid limonitic lump ore, the $\text{SiO}_2\text{-Al}_2\text{O}_3\text{-FeO}$ system was studied (SAF system). On the addition of K, no significant change was observed. This is also confirmed by the ternary system with K_2O addition (see Figure 5-34, Figure 5-35, and Figure 5-36). In contrast, Na addition led to a decrease in the transformation temperature (the T_m decreases in the SAF system by 40–60°C, which is also measured by DTA). A low-melting Na_5SiO_3 phase (1090°C) was also formed by Na treatment (see Table 5-12); a low-melting K_2SiO_3 phase (976°C) was not detected. In general, an addition of 1–1.5% Na/K led to a drop in the melting temperature of 40–60°C for almost all oxidic phase transformations.

Pellets: Acidic pellet 1 was also evaluated by an SAF system. For the oxide phase (untreated sample), a transformation temperature of ~1200°C was expected; the DTA measurement gives temperatures of 1160 to 1240°C. For the K-treated samples, a drop in T_m of 40–60°C was observed for oxidic compounds (similar to limonitic ore). A decrease of 70–80°C was also observed for Na-treated materials. So, acid pellets can be seen as significantly affected by alkali elements according to the melting behaviour.

For the basic pellet 2, a CAF system was taken for the evaluation of the melting behaviour (see chemical analysis in Table 5-10). The addition of K shows a decrease in T_m for oxidic compounds (similar to acidic pellet) of >100°C (formation of a low-melting $\text{K}_2\text{O-CAF}$ phase and formation of a $\text{FeO-K}_2\text{O}$ -rich phase at 1164°C). Moreover, the Na-treated samples melted at lower temperatures ($\Delta T \sim 85^\circ\text{C}$). The formation of a $\text{Na}_2\text{O-CAF}$ phase (1006°C) and a $\text{FeO-Na}_2\text{O}$ -rich phase (1208 °C) are the reasons for this.

For the pellets, trends and data from the literature¹⁶² are taken as supporting information to validate the measured results. So, Figure 5-37 compares the melting of acidic and basic pellets (untreated) by the measurement of the pressure drop. The softening (layer thickness) starts at ~1100°C and ends at ~1400°C, whereas the pressure drop in acidic pellets is more significant. Own investigations have shown a melting area for untreated materials from 1160–1300°C (acidic) and 1080–1300°C (basic).

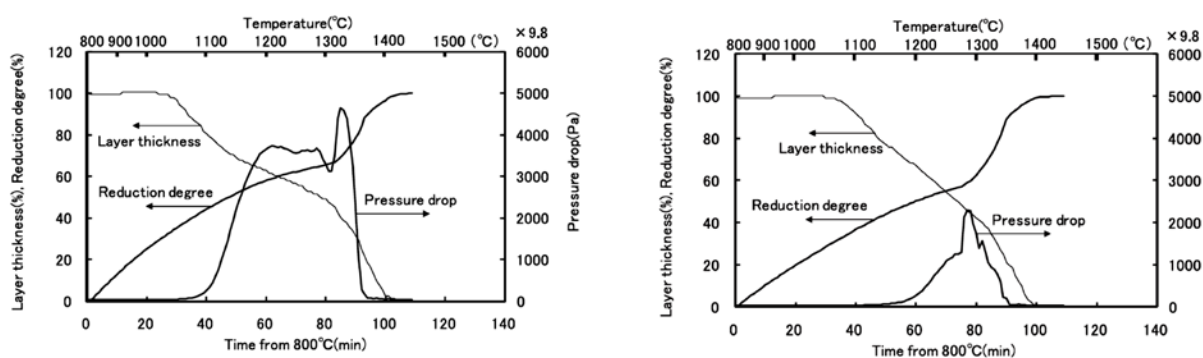


Figure 5-37: Pressure profile during a melting test for an acidic pellet grade (left) and a basic pellet grade (right)¹⁶²

Sinter: The sinter samples show differences related to the basicity. Sinter 1 ($B_2=1.3$) was evaluated in comparison with a CSF ternary system. The measured transformation temperatures (1143°C, 1237°C, 1290°C and 1339°C) can be linked to different kinds of calcioferrites or calciosilicoferrites as the main compounds of sinter samples. Calciosilicoferrite melts at $\sim 1220^\circ\text{C}$ (kirschsteinite (CaFeSiO_4): 1223°C; ferroankermanite ($\text{Ca}_2\text{FeSi}_2\text{O}_7$): 1220°C), calcioferrites at $\sim 1130^\circ\text{C}$. These melting points are shifted downwards by alkali addition. K leads to a drop of up to 20°C, while Na shows a higher effect with a ΔT of 30–85°C. Sinter 2 ($B_2=1.8$) confirms the test results of sinter 1. The transformation points are at 1148°C, 1235°C, 1295°C, and 1346°C (see calcioferrites and calciosilicoferrites). In this sample, the effect of K was higher; the transformation temperatures were lowered by 45–55°C. The Na also shows a shift of 15–25°C for oxidic phases.

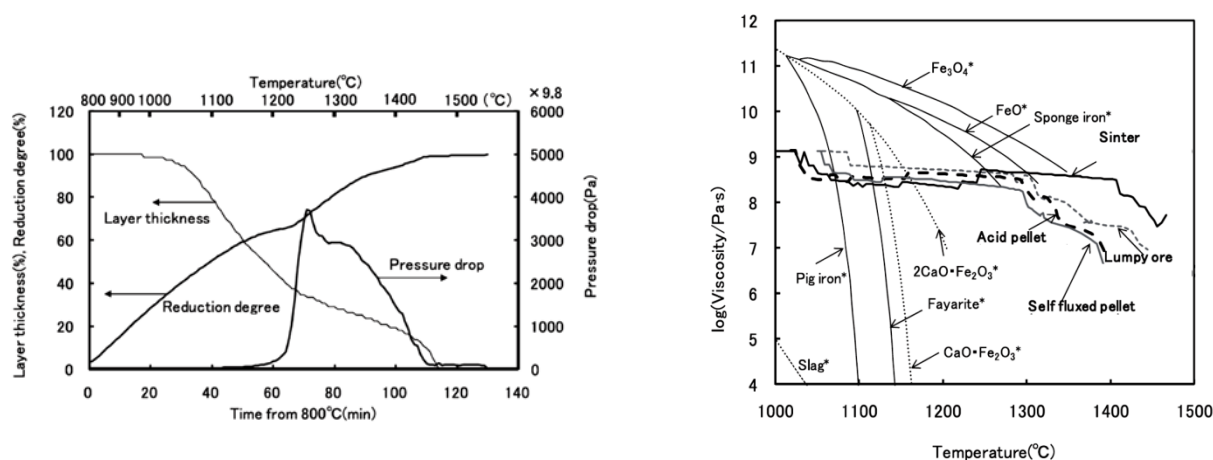


Figure 5-38: Pressure profile during a melting test for a sinter sample with $B_2=2.1$ (left), and comparison of different burden materials and pure substances by viscosity measurement (right)¹⁶²

A comparison with the reviewed literature shows the main softening phase at 1100–1200°C, and the final stage at $\sim 1450^\circ\text{C}$ for a sinter sample with basicity $B_2=2.1$ (see Figure 5-38 [left]). Furthermore, Figure 5-38 (right) shows a comparison of different values for the viscosity of burden materials and pure substances (marked with *). The softening and melting ranges of pure oxidic compounds are located between 1100–1200°C. The stable trend for ferrous materials such as sinter, lumpy ore, and pellets are linked to the stability of Fe_{met} up to temperatures of 1500°C. These trends can be confirmed by the investigations of this research, using HSM and HT-LSCM, where a stable structure was possible up to 1500°C. Other authors³⁶ have also reached similar results for transformation temperatures. Especially the bigger peaks for phase transformations linked to iron were also detected by former research; the oxidic conversions were more difficult to detect.

The following main statements about the effect of alkali metals on softening and melting behaviour can be determined after the evaluation of the melting tests:

- Alkali metals do not influence the melting and transformation temperatures of metallic iron.
- The softening and melting behaviour is independent of the former method of reduction.
- Oxidic systems are affected by alkali addition significantly. All phase transformations of oxides (wuestite, gangue, glass, calcioferrites) are changed by the addition of K or Na.
- Measurement by DTA is a good method to evaluate the influence of alkalis on melting behaviour. The transformation temperatures can be determined and the reproductivity is high.
- HSM and HT-LSCM can support additional data compared to DTA, but they are not good methods for measuring the alkali effect.
- Ternary systems can support information for the evaluation of unknown phase transformations.

6 Summary, Conclusion, and Outlook

Lastly, there is the Law, especially that dealing with metals, that he may claim his own rights, that he may undertake the duty of giving others his opinion on legal matters, that he may not take another man's property and so make trouble for himself, and that he may fulfil his obligations to others according to the law.

Georgius Agricola, De Re Metallica

Within this thesis, two major goals were achieved. First, an alkali model for ironmaking processes was developed. Based on an empirical data and multi-stage model with thermochemical calculations, a clear picture of the stability areas of alkali compounds in specific zones of ironmaking reactors can be drawn. Second, a new approach involving experimental simulations on industrially used ferrous burden materials was used to evaluate the effect of K and Na on assimilation, reducibility, mechanical stability, and softening or melting.

6.1 Macroscopic Correlations between Process Parameters and Alkali Behaviour

The alkali balance of ironmaking reactors has always been a problem because of the formation of internal and external alkali cycles, and the accumulation of alkali compounds inside the reactor. Furthermore, harmful compounds like cyanides can form under reducing conditions similar to those in the BF. The development of an alkali model was an approach to link thermochemical fundamentals (reactions and stability of alkali compounds) with the critical mass balance of ironmaking reactors (multi-stage layout of reactor model).

The alkali model was designed for the BF and a smelting reduction process. The focus was on K and Na, and their compounds. By estimating a standard process and a parameter study, a better understanding of the alkali flows inside the reactors has been achieved.

A summarizing example of a standard model BF with a total alkali load of 4.1 kg K+Na/tHM is shown in Figure 6-1. The mentioned alkali compounds and their stability over the BF height are included.

Furthermore, the main discharge by the slag phase and the enrichment of alkalis in the lower shaft region are visualized. In

addition, the validation with industrial data and literature confirms the basic layout of the alkali model. For the smelting reduction processes, the melter gasifier of the COREX or FINEX® process was examined closely. Similar to the BF model, a multi-stage model was developed and evaluated.

The alkali model for ironmaking processes is a new tool for the evaluation of alkali flows in a reactor. It allows the calculation of mass flows based on thermochemical fundamentals and the interpretation of different process parameters. For instance, the parameter study has shown that slag properties like tapping temperature or basicity are directly linked to the alkali peak in the BF shaft. This model is also useful for the evaluation of cyanides. The amount of cyanides in the washing water can be calculated. The temperature distribution at the top influences the amount of cyanides significantly.

However, the model is still not complete. Further developments are planned for both the BF and the smelting reduction processes. The implementation of halogens and zinc has already led to successful results and additional information. These results were not included in this work. In the field of smelting reduction, modifications and connections with the reduction stage, and further gas flows have to be performed in subsequent projects.

6.2 Microscopic Correlation between Iron Ore Reduction and Alkalis

The microscopic research of the alkali effect on burden material was carried out to gain knowledge about the influence of K and Na on different aspects during ironmaking: the assimilation of alkalis, reducibility, mechanical stability, and, finally, the softening and melting behaviour.

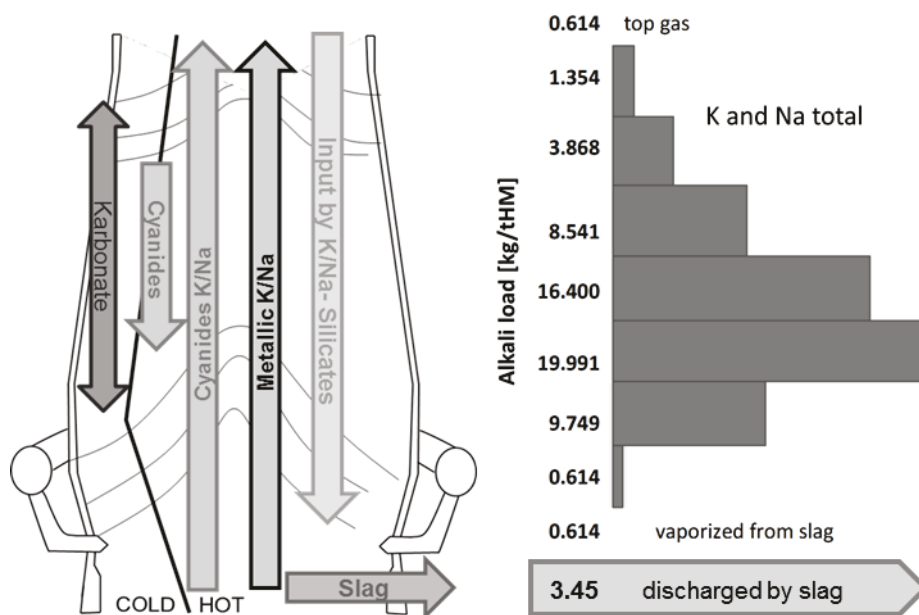


Figure 6-1: Exemplary illustration of the alkali distribution and the alkali compounds for a 50 tHM/h blast furnace and a load of 4.1 kg alkalis per tHM

Table 6-1: Summary of the investigations on the effect of alkali metals on ferrous burden material

	Assimilation of alkali metals	Reduction and Mechanical Stability during Reduction	Softening and Melting Behaviour
Lump Ore	<p>Differences were seen between dense hematite and porous limonite.</p> <p>Limonitic ore: The alkali assimilation was high for both K and Na. The reason can be derived from the highly specific surface. The assimilation was high in the limonitic and gangue phases. Hematite structures were less affected.</p> <p>Hematite ore: The hematite showed little assimilation for alkalis due to its dense structure. Only in the gangue was a small increase by the alkali treatment detectable.</p>	<p>Tests were performed with limonitic and hematite lump ore separately.</p> <p>Limonitic ore: The treated materials show an increase in the reducibility of 50–60% during the standardized ISO-test. Also, higher sticking and abrasion tendencies were measured during reduction. The reduction under process-near conditions also showed an increase in reducibility (less than for ISO tests, though).</p> <p>Hematite ore: A clear rise in reducibility was measured during the reduction tests. Although this increase was visible for all tests, the effect of alkalis was higher in the ISO test than in the BF and SR tests. The mechanical properties were nearly equal for untreated and treated materials; only the sticking tendency increased by K/Na addition.</p>	<p>The melting tests showed a decrease in the T_m of the oxidic phases of 40–60°C by the addition of K/Na. However, the metallic iron was unaffected and has given stability to the sample up to 1500°C.</p>
Pellets	<p>All pellets samples showed an enormous assimilation of K/Na, especially in the glass and gangue phases.</p>	<p>The reducibility increased in the ISO test. The effects of alkalis in the process-near reduction tests were minor. According to the mechanical stability, the sticking, degradation, and abrasion increased.</p>	<p>The melting behaviour was investigated by HSM, HT-LSCM, and DTA. The DTA showed the best results. The metallic transformations were not affected by alkalis, but the oxidic phase transitions were shifted to lower temperatures for the treated materials (lowering by 40°C to >100°C). The visualization by HT-LSCM was not successful due to the softening of the glass phase.</p>
Sinter	<p>The sinter showed assimilation especially in the gangue and glass phases. The calcioferrites and ferrous phases were less impregnated.</p>	<p>During reduction, an increase in reducibility was measured (more for the ISO test, minor for the BF and SR tests). The mechanical properties changed with regard to particle disintegration (both lower and higher disintegration depending on the testing conditions). Abrasion and sticking did not change significantly.</p>	<p>In the field of melting behaviour, again, all oxidic phases were shifted to lower melting temperatures. The quantity was similar for all phase transformations (drop of 20–55°C by the addition of alkalis).</p>

Common methods as well as new approaches were used. The assimilation was carried out by an aqueous treatment with K- or Na-bearing solutions. The reduction tests were performed by standardized ISO tests and they adopted industrial-near testing regimes. For the evaluation of mechanical stability, sieve analysis and standardized tumbling tests were used. Finally, the determination of the melting behaviour was performed by three different methods: HSM, HT-LSCM, and DTA.

Six different industrially used iron carriers were investigated to determine the basics of alkali interaction (two lump ores, two pellet brands, two sinter blends). Moreover, a classification of these materials with regard to alkali attack was possible. The summary of the microscopic research on burden material and their interaction with alkalis is shown in Table 6-1.

In general, the following statements can be determined:

- The assimilation is mainly caused by the K/Na impregnation in the gangue and glass phases. The effect of the specific surface was important for only the lump ores. K and Na were able to diffuse into the particles' core and dense structures.
- The effect of alkalis on iron ore reduction was studied precisely. Especially the influence on the CO reduction was a new outcome and it was widely debated in previous literature. An interesting finding of the investigations was that alkali metals hardly influence the reduction speed with H₂. Moreover, findings due to reduction kinetics were found. They assume that alkali metals can change the limiting step and consequently the whole reduction mechanisms. These results can support information about the reduction kinetics for future research. The mechanical properties after reduction changed enormously in some cases. However, the quantitative change in abrasion, disintegration, and sticking tendency depends on the original material.
- For the evaluation of the melting behaviour and the influence of alkalis, measurements with the DTA have produced the best results (supporting information by tests with HSM and HT-LSCM). The stability of the metallic iron was visible up to 1530°C and an effect of K/Na on the metallic fraction was not detected (low solubility of Na/K in metallic iron). However, a significant change of the phase transformations of oxides (e.g. gangue, glass, calcioferrites, FeO) was measured for all materials. The melting temperature was shifted to lower temperatures with the addition of K/Na for most materials.

This thesis represents a new methodology for the characterization of ferrous burden materials with regard to alkalis. The combination of standardized methods (tumbling and reduction tests) and new approaches (alkali treatment, DTA analysis with partially reduced materials) led to successful results. On the one hand, knowledge was gained about the effects of K and Na. For instance, acid pellet brands showed higher degradation during reduction than did basic pellets. On the other hand, new theories about the fundamentals of reduction kinetics were stated. Alkali metals seem to accelerate the CO reduction because of their electropositive characteristics.

Moreover, in the future, the microscopic evaluation of input materials is essential. Material properties like abrasion, reactivity, and softening behaviour are directly linked to the process performance and can be changed by harmful elements like alkalis (K, Na) or halides (Cl). Qualitative and quantitative characterization plays a key role for a successful ironmaking process.

6.3 Outlook and Future Potentials

To sum up, the thermochemical modelling and experimental simulations give rise to a clear picture about alkali metals in ironmaking processes. Alkalis offer both opportunities and threats for the future of ironmaking.

The performed work delivers fundamental data about alkalis and it can be a starting point to lower the impact of the following issues:

- Fuel consumption
- Emissions (cyanides in the waste gas)
- Generation of dust and fines
- Usage of domestic or Fe-rich iron ores with higher K/Na content (e.g. RSA, AUT, etc.)

Alkalis offer an opportunity with regard to their use as fertilizers. K in potash is an important resource for agriculture and it is normally produced by mining (see open bit mine in Figure 6-2). For example, consider the K consumption of China. In 2006, around 11 mio. t. of K was used for fertilizing, whereas 8 mio. t. had to be imported. Assuming that 90% of the K in the sinter dust is processed, annual production of 500 kt KCl would be possible. Furthermore, this is linked with a potential of 600 kt K₂SO₄. In that case, the separation, modification, and usage of K-bearing waste material (dust, sludge) are of interest to partially substitute the primary source potash.



Figure 6-2: open-bit mining for potash production

163

Another future aspect is industry 4.0. Nowadays, industry 4.0 summarizes technological opportunities for the industrial production like autonomous robots, additive manufacturing, system integration, big data mining, smart products, social machinery, virtual production and the internet of things. Figure 6-3 demonstrates the evolution of industrial processes. Starting from the 1st industrial revolution it shows the way towards modern production methods. The implementation of advanced technologies is the major step for the 4th industrial revolution. In this context, the simulation of processes plays a key role. Simulations have to be based on models, which represent the real process. Programs should be able to deal with huge volumes of industrial data as well as mathematical, chemical and physical fundamentals. Furthermore, the structures of such models have to be as simple as possible to lower the calculation time, which is important for the applicability of software tools. For instance, the alkali model can contribute information to the blast furnace simulation. It enables the virtual view on the material flow in the reactor – based on thermodynamical fundamentals and industrial data.

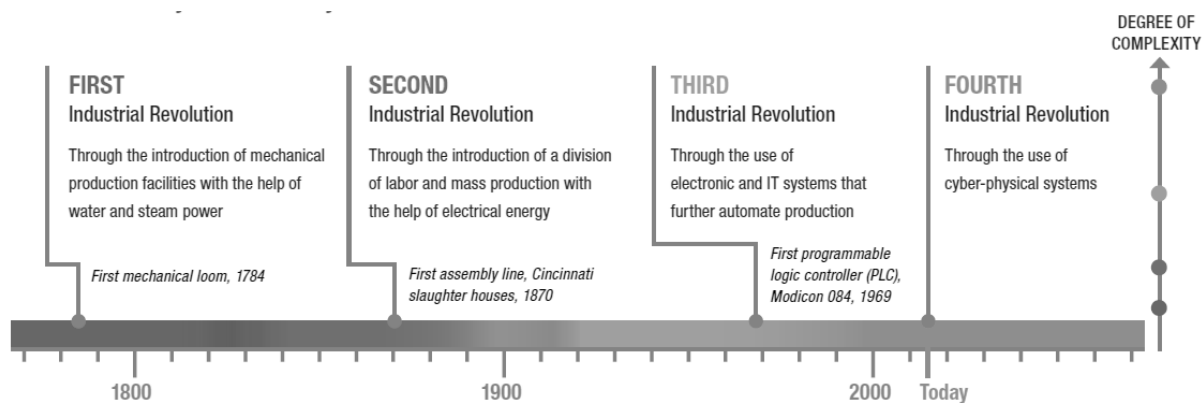


Figure 6-3: evolution of industrial production towards industry 4.0¹⁶⁹

For these topics, this thesis can deliver important information about the alkali behaviour in ironmaking reactors, new knowledge about the creation of suitable models for process simulation and, perhaps, new aspects of processing in the field of ironmaking.

7 References

- Grebe L.: Die Märkte für niedrig- und hochlegierte Stähle-heute und morgen, 1st Edition, Stahlhandels-Institut, Meerbusch, GER, (2015).
2. Vondran R.: Chances and challenges - economic and technical trends in the steel industry, *Stahl und Eisen*, 120, 2, (2000).
 3. Maddison A.: The World Economy: Historical Statistics, (2003).
available at http://archive.treasury.gov.au/documents/1042/HTML/docshell.asp?URL=02_Resource_commodities.asp (accessed 21 March 2016).
 4. Warings R.: Charakterisierung anthropogener Ressourcenlagerr in Österreich am Beispiel Stahl-eine Bottom up Analyse, *Master Thesis*, University of Natural Resources and Live Science Vienna, AUT, (2015).
 5. Pichler A.: Iron Balance Study for Austria, *K1-Met Scientific Exchange Day*, Leoben, AUT, (2016).
 6. World steel Association: Crude Steel Production 2015, (2016).
 7. World Steel Association: Economic sustainability, (2016).
available at <https://www.worldsteel.org/steel-by-topic/sustainable-steel/economic.html> (accessed 21 March 2016).
 8. US Geological Survey: Statista, (2016).
available at <https://www.statista.com/search/> (accessed 21 March 2016).
 9. Verein deutscher Eisenhüttenleute: Stahlfibel, Verlag Stahleisen GmbH, Düsseldorf, GER, (2002).
 10. Gocht W.: Handbuch der Metallmärkte, 2nd Edition, Springer, Berlin, GER, (1985).
 11. Clemens H.: Lecture in Physical Metallurgy 1- Introduction into materials, Montanuniversitaet, Leoben, (2009).
 12. Ashby M.F., D. R. H. Jones: Engineering Materials- An Introduction to Their Properties and Applications, 2nd Edition, Butterworth-Heinemann, Oxford, UK, (1996).
 13. Schenk J.: Erhöhung der Schrottsätze - Triebkraft und Grenzen, *VDEh- Ausschuss für Metallurgische Grundlagen*, Düsseldorf, GER, (2013).
 14. Paul G.: The Blue Economy. 10 Jahre. 100 Innovationen. 100 Millionen Jobs, Konvergenta Publishing, Berlin, GER, (2010).
 15. Neukirchen F., G. Ries: Die Welt der Rohstoffe, Springer, Berlin & Heidelberg, GER, (2010).

16. SteelBenchmarker™, (2016).
available at <http://steelbenchmarker.com/> (accessed 21 March 2016).
17. finanzen.net GmbH: Rohstoffe | Rohstoffkurse | Rohstoffpreise, (2016).
available at <http://www.finanzen.at/rohstoffe> (accessed 21 March 2016).
18. Genet M.: The Future of Steel- Impact of energy market developments on the steel industry, 74th Session of the OECD Steel Committee, (2013).
19. European Commision: Best Available Techniques (BAT) - Reference Document for Iron and Steel Production, Directive 2010/75/EU, Brussels, EU, (2012).
20. Längen H.B., M. Peters, P. Schmöle: Eisenerzeugung, *Stahl und Eisen*, 130, 4, pp. 36-64, (2010).
21. Gudenau H.W.: Eisenhüttenmännische Verfahrenstechnik - Vom Erz zum Stahl, Druck- & Verlagshaus MAINZ GmbH, Aachen, GER, (1989).
22. Paschen P.: Eisen-Ares-Mars: Metalle, Götter und Gestirne, *World of Metallurgy - Erzmetall*, 64, 6, (2011).
23. Rehren P., E. Pernicka: Coins, Artefacts and Isotops-Archaeometallurgy and Archaeometry, *Archaeometry*, 50, 2, pp. 232-248, (2008).
24. Strohmeier B.: DRI-based EAF-Steelmaking in Iran- Example Hormozgan Steel, 3rd ECC, Venice, ITA, (2016).
25. Schenk J.: Lecture in Ferrous Metallurgy I- Chemical/Physical Fundamentals, 4/1-4/86, Montanuniversitaet, Leoben, AUT, (2011).
26. Schenk J.: Lecture in Ferrous Metallurgy I- Reduction Metallurgy, 5/35-5/49, Montanuniversitaet, Leoben, AUT, (2011).
27. Schenk J.: Lecture in Ferrous Metallurgy I- Blast Furnace Technology, 5/77-5/105, Montanuniversitaet, Leoben, AUT, (2011).
28. Biswas A.K.: Principles of blast furnace ironmaking: Theory and practice, Cootha, Brisbane, AUS, (1981).
29. Feinman J.: Direct Reduction and Smelting Processes, AISE Steel Foundation, Warrendale, USA, pp. 741–780, (1999).
30. Feinman J., D. Mac Rae: Direct Reduced Iron: Technology and Economics of Production and Use, Iron & Steel Society, Warrendale, USA, (1999).
31. Schenk J.: Recent status of fluidized bed technologies for producing iron input material for steelmaking, *Particuology*, 9, pp. 14-23, (2011).
32. European Commision: Direktreduktion von Eisenerz: Eine bibliographische Studie, Stahleisen, Düsseldorf, GER, (1976).
33. Bernhard C., S. Michelic: Lecture in Process Routes for the Production of Selected Steels, Montanuniversitaet, Leoben, AUT, (2015).
34. Dahlmann P.: Steel's Contribution to a low-carbon Europe 2050: Technical and economic analysis of the sector's CO₂ abatement potential, *Steel Institute VDEh & Boston Consulting Group*, (2013).
35. Geerdes, M., H. Toxopeus, C. van der Vliet: Modern Blast Furnace Ironmaking-an Introduction, IOS Press BV, Amsterdam, NED, (2009).
36. Lin R.: Investigations of chlorine and alkali behaviour in the blast furnace and optimisation of blast furnace slag with respect to alkali retention capacity: Final report, Luxembourg, LUX, (2003).

37. Schenk J.: Lecture in Ferrous Metallurgy I- Ironmaking, 5/1-5/34, Montanuniversitaet, Leoben, AUT, (2011).
38. Gudenau H.W., K. Mavrommatis, A. Babich: Blastfurnaceprocess, RWTH, Aachen, GER, (2002).
39. Verein Deutscher Eisenhüttenleute: Grundlagen des Hochofenverfahrens, Physikalisch-chemische und physikalische Zusammenhänge, Stahleisen, Düsseldorf, GER, (1973).
40. Senk D., A. Babich: Eisenmetallurgie: Eisenreduktion und Schachtöfen, Stahleisen, Düsseldorf, GER, (2013).
41. Basu S., S. Seetharaman, A. K. Lahiri: Thermodynamics of Phosphorus and Sulphur Removal during Basic Oxygen Steelmaking, *Steel Research Int.*, 81, 11, pp. 932-939, (2010).
42. Seetharaman S., A. McLean, R. I. L. Guthrie, S. Sridhar: Treatise on process metallurgy, Elsevier, Oxford, UK, (2014).
43. Pichler A., J. L. Schenk, F. Hauzenberger, H. Stocker, C. Thaler: Thermochemical modelling of the alkali balance in blast furnaces, *Proceedings AsiaSteel 2015*, pp. 282–284, (2015).
44. Worldsteel Association: World Steel in Figures 2013, (2013).
available at <http://www.worldsteel.org/> (accessed 13 November 2013).
45. Midrex Technologies Inc.: MIDREX - World Direct Reduction Statistics 2012, (2012).
46. Harste K., H. B. Lungen: Steel production under economic extremes, *Stahl und Eisen*, 130, 8, pp. 45-54, (2010).
47. Stahlinstitut VDEh: Jahrbuch Stahl 2012, (2012).
48. Skorianz M., H. Mali, A. Pichler, F. Plaul, J. Schenk, B. Weiss: Reduction Behaviour and Structural Evolution of Iron Ores in Fluidized Bed Technologies. Part 1: Method for the Determination, *Steel Research Int.*, 87, 4, pp. , (2016).
49. Becher V.: Reaction Mechanisms involed in thermal and catalytic reforming of product gas from biomass gasification, TU München.
50. Midrex Technologies Inc.: MIDREX Statsbook 2014, (2014).
available at <http://MIDREX.com/assets/user/news/MIDREXStatsbook201411.pdf> (accessed 11 January 2016).
51. Schenk J.: Lecture in Special Metallurgical Processes, Montanuniversitaet, Leoben, AUT, (2015).
52. Kumar P., S. C. Barman, B. M. Reddy, V. R. Sekhar: Raw materials for COREX and their influence on furnace performance, *Ironmaking and Steelmaking*, 36, 2, pp. 87-90, (2009).
53. Wu S.-I., M.-y. Kou, J. Sun, W. Shen, K.-P. Du: Analysis of Operation Parameters Affecting Hot Metal Temperature in COREX Process, *Steel Research Int.*, 85, 11, pp. 1552-1559,(2014).
54. Skorianz M.: Classification of iron ores regarding their reduction behaviour in fluidized bed technologies, *PhD-Thesis*, Montanuniversitaet, Leoben, AUT, (2012).
55. Thaler C.: Entwicklung eines Modells zur Bilanzierung der Massen- und Energieströme für den FINEX®-Prozess zur Optimierung des Energieeinsatzes und Minimierung der Treibhausgasemissionen, *Master Thesis*, Montanuniversitaet, Leoben, AUT, (2010).
56. Prattes W.U.: Die technologische Entwicklung des COREX-Verfahrens, *Master Thesis*, Montanuniversitaet, Leoben, (2002).
57. Grill W.: COREX_FINEX-SVAI_ MetalsSymposium, *Siemens VAI Symposium*, (2009).
58. Du K., S. Wu, M. Kou, W. Shen, and Z. Zhang: Numerical Simulation of Liquid Iron Flow and Heat Transfer in the Hearth of COREX Melter Gasifier during Tapping Process, *Steel Research Int.*, 85, 3, pp. 466-476, (2014).

59. K. Du, S. Wu, Z. Zhang, F. Chang, and X. Liu: 'Analysis on Inherent Characteristics and Behaviour of Recycling Dust in Freeboard of COREX Melter Gasifier', *ISIJ International*, 54, 12, pp. 2737–2745, (2014).
60. Müller K.T.: Status of the ULCOS program, ThyssenKrupp, 2009.
61. Hismelt Sustainable Development Report; available at ftp://info.metallurgy.ac.at/redmet/Reduktionsverfahren/Hismelt-Sustainable-Development-Report_2007.pdf.
62. Yuan B., G.-M. Haarberg: Electrowinning of Iron in Aqueous Alkaline Solution Using Rotating Disk Electrode, *Revue de Métallurgie*, 10, pp. 455-459, (2009).
63. Lavelaine H., A. Allanore: Optimized Design of an Iron Electrowinning Cell, *Revue de Métallurgie*, 10, pp. 460–471, (2009).
64. Allanore A. , H. Lavelaine, W. Xuan: Application of Modeling to the Development of an Electrochemical Pilot Cell, *Revue de Métallurgie*, 10, pp. 440-454, (2009).
65. Sabat K.C., P. Rajput, R. K. Paramguru, B. Bhoi, B. K. Mishra: Reduction of Oxide Minerals by Hydrogen Plasma: An Overview, *Plasma Chem Plasma Process*, 34, 1, pp. 1-23, (2014).
66. Bäck E., A. Badr, J.-F. Plaul, A. Sormann: Überblick über die Entwicklung der Wasserstoff-Schmelzreduktion am Lehrstuhl für Metallurgie, *BHM Berg-und Hüttenmännische Monatshefte*, 154, 1, pp. 6-9, (2009).
67. Boundless.com, Mountain View, CA, USA, 2016.
68. Kondepudi D.: Introduction to modern thermodynamics, Wiley, Chichester, UK, (2008).
69. Froberg M. G.: Thermodynamik für Werkstoffingenieure und Metallurgen, (1993).
70. Atkins P.W., J. de Paula: Physikalische Chemie, 5th Edition, Wiley, Weinheim, GER, (2013).
71. von Bogdandy L., H.-J. Engell: The reduction of iron ores, Stahleisen, Düsseldorf, GER, (1971).
72. Weiss B. : Kinetics of iron fines reduction under fluidized bed conditions at elevated pressures, *PhD-Thesis*, TU Wien, Wien, (2008).
73. Eucken A.: Grundriß der physikalischen Chemie, 4th Edition, Akademische Verlagsgesellschaft, Leipzig, GER, (1934).
74. Turkdogan E.T.: Fundamentals of steelmaking, Institute of Materials, London, UK, (2010).
75. K. Hack and S.-M. Jung: 'FactSage', GTT Technology.
76. Fröber J., H.-W. Klapp, W. Kleppe, F. Oeters, M. Ottow, J. Selenz: Eisen und Stahl, 4th Edition, Carl Hanser, München, GER, (1986).
77. Skorians M., H. Mali, J. F. Plaul, J. L. Schenk, C. Thaler: Classification of fine ores regarding their reducibility with tests in a lab scale fluidized bed reactor and petrographical analysis, *Proceedings AISTech 2012*, Atlanta, (2012).
78. Diepschlag E.: Die Reduktion von Eisenerz unter Anwendung höherer Drücke, *Archiv für Eisenhüttenkunde*, 179, 5, (1936).
79. Tenebaum M.: Reduction of iron ores under pressure by hydrogen, *Transactions of the american institute of mining and metallurgy*, 135, 59, (1939).
80. Hanel M.B.: Characterization of Ferrous Burden Material for Use in Ironmaking Technologies, *PhD-Thesis*, Montanuniversitaet, Leoben, (2014).
81. Pichler A.: Entwicklung einer Methodik zur Bewertung der morphologischen Veränderung von Feineisenerzen während der Reduktion in einem Wirbelschichtreaktor, *Master Thesis*, Montanuniversitaet, Leoben, AUT, (2012).
82. Oeters F.: Metallurgie Teil 1: Eisenerzeugung, Stahleisen, Düsseldorf, GER, (1982).

83. Hofbauer H., F. Winter, A. Habermann, W. Steinbach, C. Stingl, and A. Thurnhofer: Grundsatzuntersuchung zur Wirbelschichtreduktion von Feinerzen, Final Report, TU Vienna, (2001).
84. Chatterjee A.: Beyond the Blast Furnace, CRC Press, Boca Raton, USA, (1994).
85. Steinbach W.: Reduktionskinetik von Feinerzen in der Wirbelschicht, *Master Thesis*, TU Wien, Wien, AUT, (1999).
86. Habermann A.: Kinetik der Eisenerzreduktion in der Wirbelschicht, *PhD-Thesis*, TU Wien, Wien, AUT, (2001).
87. von Bogdandy L., H.-J. Engell: Die Reduktion der Eisenerze: wissenschaftliche Grundlagen und technische Durchführung, Stahleisen, Düsseldorf, GER, (1967).
88. Feilmayr C., A. Thurnhofer, F. Winter, H. Mali, J. L. Schenk: Reduction Behaviour of Hematite to Magnetite under Fluidized Bed Conditions, *ISIJ International*, 44, 7, pp. 1125-1133, (2004).
89. Pichler A., J. L. Schenk, M. Skoriansz, J. F. Plaul, B. Weiss, H. Mali: Process behaviour of fine iron ores during reduction in a fluidized bed reactor and characterization of the morphological evolution, *Proc. ESTAD&JSI14*, pp. 100-102, (2014).
90. Szekely J., J. W. Evans, H. Y. Sohn: Gas-Solid Reactions, Academic Press, New York, USA, (1976).
91. Levenspiel O.: Chemical Reaction Engineering, John Wiley & Sons, USA, (1999).
92. Loo C.O., N. J. Bristow: Properties of iron bearing materials under simulated blast furnace indirect reduction conditions Part II: Reduction degradation, *Ironmaking and Steelmaking*, 25, 4, pp. 287-295, (1998).
93. Hack K.: Schlackenatlas Version 10.0, GTT-Technologies, (2014).
94. inmediaONE GmbH: Wissenmedia, available at <http://www.wissen.de/wortherkunft/alkali?keyword=alkali> (accessed 15 January 2014).
95. Klein C., A. R. Philpotts: Earth materials: Introduction to mineralogy and petrology, Cambridge University Press, New York, USA, (2013).
96. Altpeter, Beppler, Gerstenberg, Kannappel: Auswirkungen von Alkalien im Hochofen, *Stahl und Eisen*, 17, pp. 781-790, (1988).
97. Klein A.: Anorganische Chemie, TU Graz, (2013). available at http://www.uni-graz.at/~kleinaxe/AC1_Kap1.pdf (accessed 19 November 2013).
98. Wegscheider W.: Lecture in Chemistry II, Montanuniversitaet, Leoben, (2008).
99. Evans A.M.: Erzlagerstättenkunde, Enke, Stuttgart, GER, (1992).
100. Bailey J.: Iron and Manganese Ore Databook, Surrey, UK, (1992).
101. Noska T.: K₂O accumulation at the ATH-Hamborn BF: Project Proposal, *Internal Report Thyssen Krupp*, (2013).
102. Tauchner C.: Mineralogische Charakterisierung von Eisenerzen in Hinblick auf Gangartphasen, *Bachelor Thesis*, Montanuniversität, Leoben, (2015).
103. Schneiderhöhn H.: Erzlagerstätten, Gustav Fischer, Jena, GER, (1944).
104. Schneiderhöhn H., P. Ramdohr: Lehrbuch der Erzmikroskopie, Gebrüder Bornträger, Berlin, GER, (1931).
105. Hauzenberger F., J. Reidetschläger, J. L. Schenk, H. Mali: Methods for Assessing the Properties of Fine Iron Ores for Reduction Processes, *BHM Berg-und Hüttenmännische Monatshefte*, 149, 11, pp. 385-392, (2004).

106. Abraham K.P., L.I. Staffansson: The Alkali Problem in the Blast Furnace, *Scandinavian Journal of Metallurgy*, 4, pp. 193-204, (1975).
107. Gudenau H.W., K. Mavrommatis, A. Babich: Blastfurnaceprocess, RWTH, Aachen, GER, (2002).
108. Pilz K.: Verhalten von Kreislaufstoffen im Hochofenprozess, *Internal Report VAI*, (1998).
109. Ivanov O.: Metallurgische Grundlagen zur Optimierung von Hochofenschlacken mit Bezug auf die Alkalikapazität, *PhD-Thesis*, TUBA, Freiberg, GER, (2002).
110. Narita K.: Effects of alkalis and zinc on the wear of blast furnace refractories and the tuyere displacement, *Transactions ISIJ*, 21, pp. 839-846, (1981).
111. Krol L.: Angriff von Alkalien auf die Hochofenzustellungen aus Kohlenstoff und Graphit, *Archiv für das Eisenhüttenwesen*, 52, pp. 341ff, (1981).
112. Yusfin Y.S., P. I. Chernousov: The role of alkalis and conserving resources in blast-furnace smelting, *Metallurgist*, 43, pp. 54-58, (1999).
113. Bartusch H., T. Hauck, H.-G. Grabietz: Balancing and behaviour of chlorine in the Blast Furnace, *Stahl und Eisen*, 134, 1, (2014).
114. Pichler A., Stocker H.: Alkalienbilanz, *Internal Report Voestalpine*, (2013).
115. Besta P., A. Samolejová, K. Janovská, R. Lenort, J. Haverland: The effect of harmful elements in production of iron in relation to input and output material balance, *Metalurgija*, 51, 3, pp. 325-328, (2012).
116. Altland R., B. Beckmann, K.-P. Stricker: Verfahrensoptimierung am Hochofen durch kontrollierte Alkali- und Schlackenbedingungen, *Stahl & Eisen*, 119, 11, pp. 53-58, (1999).
117. Gudenau H.-W., M. Amatatsu, V. Stutz: Der Alkalienkreislauf im Hochofen, *Fachberichte Hüttenpraxis Metallverarbeitung*, 20, 1, pp. 2-10, (1982).
118. Davies J., J. T. Moon, F. B. Traice: Alkalis in the Blast Furnace, *Ironmaking & Steelmaking*, 5, 4, pp. 151-161, (1978).
119. Hatano M.: Investigation of the Influence of Alkali Circulation on the Blast Furnace Operation, *Trans.Jpn.Inst.Met*, 20, 10, pp.3-12, (1980).
120. Sulzbacher M.: Theoretische Überlegungen über das Verhalten von Alkalien im KR-Prozess, *Internal Report VAI*, (1984).
121. POSCO Inc.: Data from FINEX-Plant, *Internal Report*, (1998).
122. Meimeth S.: Energetische Nutzung von Kuppelgasen integrierter Hüttenwerke, *PhD-Thesis*, RWTH, Aachen, GER, (1996).
123. Pichler A., J. Schenk: Characterization of Kalabagh Iron Ore and reduction tests in a rotary kiln furnace and a TBRC, *Internal Report*, Montanuniversitaet, Leoben, AUT, (2013).
124. Bahgat M., K.S. Abdel Halim, H. A. El-Kelesh, M. I. Nasr: Metallic iron whisker formation and growth during iron oxide reduction: K₂O effect, *Ironmaking & Steelmaking*, 36, 5, pp. 379-387, (2009).
125. Pan W., Z. J. Ma, Z. X. Zhao, W. H. Kim, D. J. Min: Effect of Na₂O on the Reduction of Fe₂O₃ Compacts with CO/CO₂, *Metall and Materi Trans B*, 43, 6, pp. 1326-1337, (2012).
126. Gougeon M., B. Dupré, C. Gleitzer: An Investigation of the Critical Influence of Potassium on the Reduction of Wustite, *Metallurgical Transaction B*, 17B, pp. 657-663, (1986).
127. Ende H., K. Grebe, and S. Thomalla: Alkalien als Ursache von Schwell- und Zerfallvorgängen bei der Reduktion von Eisenerzpellets, *Stahl und Eisen*, 13, pp. 667-676, (1970).

128. Iljana M., O. Mattila, T. Alatarvas, V.-V. Visuri, J. Kurikkala, T. Paananen, T. Fabritius: Dynamic and Isothermal Reduction Swelling Behaviour of Olivine and Acid Iron Ore Pellets under Simulated Blast Furnace Shaft Conditions, *ISIJ Int.*, 52, 7, pp. 1257-1265, (2012).
129. Iljana M., O. Mattila, T. Alatarvas, J. Kurikkala, T. Paananen, T. Fabritius: Effect of Circulating Elements on the Dynamic Reduction Swelling Behaviour of Olivine and Acid Iron Ore Pellets under Simulated Blast Furnace Shaft Conditions, *ISIJ Int.*, 53, 3, pp. 419-426, (2013).
130. Möhlmann H., K. Koch, R. G. Ward: Untersuchungen zum Schwellverhalten bei der Reduktion mit Zuschlägen an Natrium Kalium Calcium Magnesiumoxid sowie Kieselsäure., *Arch. Eisenhüttenwesen*, 10, pp. 647-651, (1967).
131. Hanel M.: Characterization of burden material for ironmaking by means of reduction tests with morphological characterization, *ISIJ-VdEH-Jernkornet-Joint Symposium*, Osaka, JPN, (2013).
132. Pichler A.: Alkali-Model for Ironmaking Processes- User Manual, *Internal Report*, Montanuniversitaet, Leoben, (2015).
133. Rentz O., T. Spengler, S. Hähre, A. Sieverdingbeck: Prozessintegrierte Umweltschutzmaßnahmen in der Eisen- und Stahlindustrie, *Universitaet Karlsruhe*, (1997).
134. Fukutake T., Y. Takada, N.Tsuchiya, K. Okabe: The kinetics of potassium vaporization from the slags in the blast furnace, *Australia Japan Extractive Metallurgy Symposium*, pp. 269-280, (1980).
135. Friedrichs H.A., H. W. Gudenau, V. Stutz: Zur Verflüchtigung von Kalium aus Schlacken, *Archiv für das Eisenhüttenwesen*, 55, 4, pp. 137-142, (1984).
136. Choi J.Y., D. J. Kim, H. G. Lee: Reaction kinetics of desulfurization of molten pig iron using CaO-SiO₂-Al₂O₃-Na₂O slag systems, *ISIJ International*, 41, 3, pp. 216-224, (2001).
137. Lundgren M., L. S. Oekvist, B. Bjoerkman: Coke reactivity under blast furnace conditions and in the CSR/CRI test, *Steel Research int.*, 80, 6, pp. 396-401, (2009).
138. Li T.: Untersuchung des Verhaltens verschiedener SiO₂-MgO-Träger in Abhängigkeit von der Absinktiefe in einem Versuchshochofen inkl. Mikroskopiebericht, *Bachelor Thesis*, Montanuniversitaet, Leoben, AUT, (2015).
139. Hatano M.: Investigation of the influence of alkali circulation on the blast furnace operation, *ISIJ Int*, (1978).
140. International Organization for Standardization: ISO 4701:2008 Iron ores and direct reduced iron - Determination of size distribution by sieving, (2008).
141. International Organization for Standardization: ISO 10836 Iron ores- Method of sampling and sample preparation for physical testing, (1994).
142. International Organization for Standardization: ISO 4695 Iron ores - Determination of reducibility, (2007).
143. International Organization for Standardization: ISO 4696-1 - Iron ores for Blast Furnace Feedstocks - Determination of low-temperature reduction-disintegration indices by static method, (2007).
144. Lorenz I.P.: Vorlesung Anorganische Chemie- Koordinationschemie- Metallorganische Komplex-Katalyse: Grundlagen, Mechanismen und Modelle, Ludwig Maximilian Universität, München, GER, (2010).
145. Yi L., Z. Huang, T. Jiang: Sticking of iron ore pellets during reduction with hydrogen and carbon monoxide mixtures: Behaviour and mechanism, *Powder Technology*, 235, pp. 1001-1007, (2013).

146. Gudenau H.W., H.-P. Eisen, Y. Qi, G. Steinbeck: Sticking von Feinerz in der Wirbelschicht zur Schmelzreduktion, *Stahl und Eisen*, 111, 9, pp. 47-52, (1991).
147. ElKasabgy T.: A study of the mechanisms of degradation of iron ore pellets during reduction, *PhD-Thesis*, McMaster, Ontario, CAN, (1978).
148. Kolb F., A. Pichler, H. Mali, J. Schenk: Standardized Iron Ore Characterization Methodology for Metallurgy, *Practical Metallography*, 52, 1, pp. 5-20, (2015).
149. Nakagawa H., Y. Ono: Effects of potassium chloride on the reduction of iron oxides, *ISIJ Int.*, 25, 10, pp. 1021-1024, (1985).
150. Al-Ajeel W.A.: Effect of some alkali additives on the reducibility of al Huassainiyat iron ore, *Iraqi Bulletin of Geology and Mining*, 5, pp. 119-131, (2009).
151. Bhattacharyya A., J. Schenk, G. Rantitsch, C. Thaler, H. Stocker: Effect of alkaline elements on the reactivity, strength and structural properties of blast furnace cokes, *Metallurgija*, 54, 3, pp. 503-506, (2015).
152. Shannon R.D.: Revised effective ionic radii and systematic studies of interatomic distances in halides and chalcogenides, *Acta Cryst A*, 32, 5, pp. 751-767, (1976).
153. Luo M.: Fischer–Tropsch synthesis: Group II alkali-earth metal promoted catalysts, *Applied Catalysis A: General*, 246, 1, pp. 171-181, (2003).
154. Knell A., D. Monti, M. Maciejewski, A. Baiker: Catalytic dehydrogenation of 10,11-dihydro-5H-dibenz azepine (iminodibenzyl) to 5H-dibenz azepine (iminostilbene) over potassium-promoted iron oxides: effect of steam, potassium promotion and carbon dioxide treatment, *Applied Catalysis A*, 124, pp. 367-390, (1995).
155. Jülich Forschungszentrum: Hot Stage Microscopy available at http://www.fz-juelich.de/iek/iek2/EN/Forschung/Thermochemie/Methoden/Methoden_Uebersicht/ErhitzMikroskop/ErhMikroskop_node.html. (accessed 15 October 2013).
156. Patschger M.: Thermische Analyse, Otto Schott Institut für Glaschemie, Jena, GER.
157. Brandt F.: Brennstoffe und Verbrennungsrechnung, Vulkan Verlag, Essen, GER, (1999)
158. Kaltenböck I.: Erweichungs- und Schmelzverhalten von reduzierten Eisenträgern unter Berücksichtigung des Einflusses von Alkalien, *Master Thesis*, TU, Graz, AUT, (2014).
159. Michelic S., C. Bernhard, U. Dieguez Salgado, D. Loder: In-situ Beobachtung des Verhaltens nichtmetallischer Einschlüsse mittels Hochtemperatur-Laser-Scanning-Konfokalmikroskopie, *Gießereipraxis*, 67, 9, pp. 335-341, (2016).
160. Lazicki A., Y. Fei, R. J. Hemley: High-pressure differential thermal analysis measurements of the melting curve of lithium, *Solid State Communications*, 150, 13-14, pp. 625-627, (2010).
161. Krellner C.: Differenz-Thermoanalyse (DTA), Goethe Universität, Frankfurt, (2013)
162. Nishimura: Evaluation of Softening, Shrinking and Melting Reduction Behaviour of Raw Materials for Blast Furnace, (2011).
163. Potash mine, available at matrixlabourleasing.com. (accessed 18 January 2016).
169. Huffingtonpost: http://www.huffingtonpost.com/mike-roberts/will-robotics-breed-a-new-generation_b_6315812.html. (assessed 11 November 2016).

Appendix

A-1 Reduction curves of ferrous burden materials under different process conditions and alkali contents

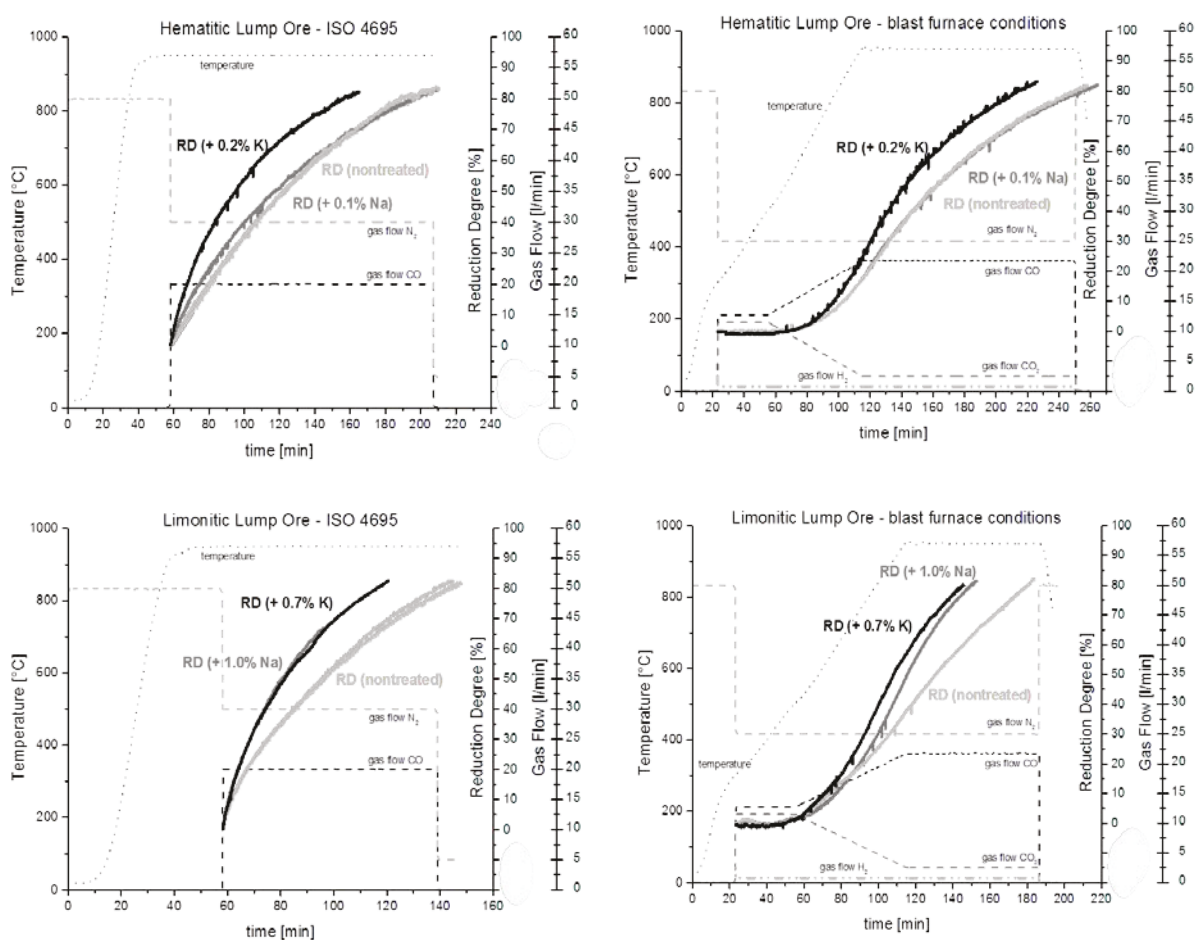


Figure A-1: Process data and curve of the reduction degree for lump iron ores

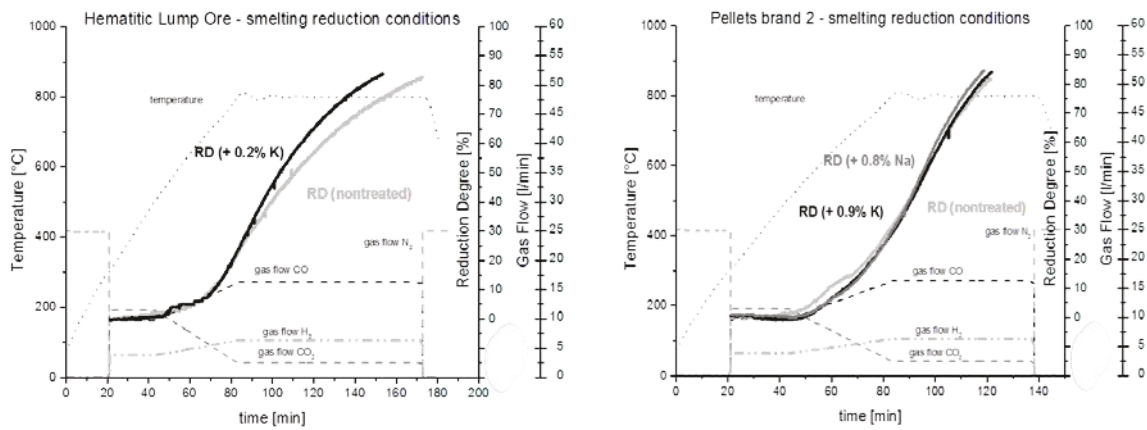


Figure A-2: Process data and curve of the reduction degree under SR conditions for hematite lump ore and pellets brand 2

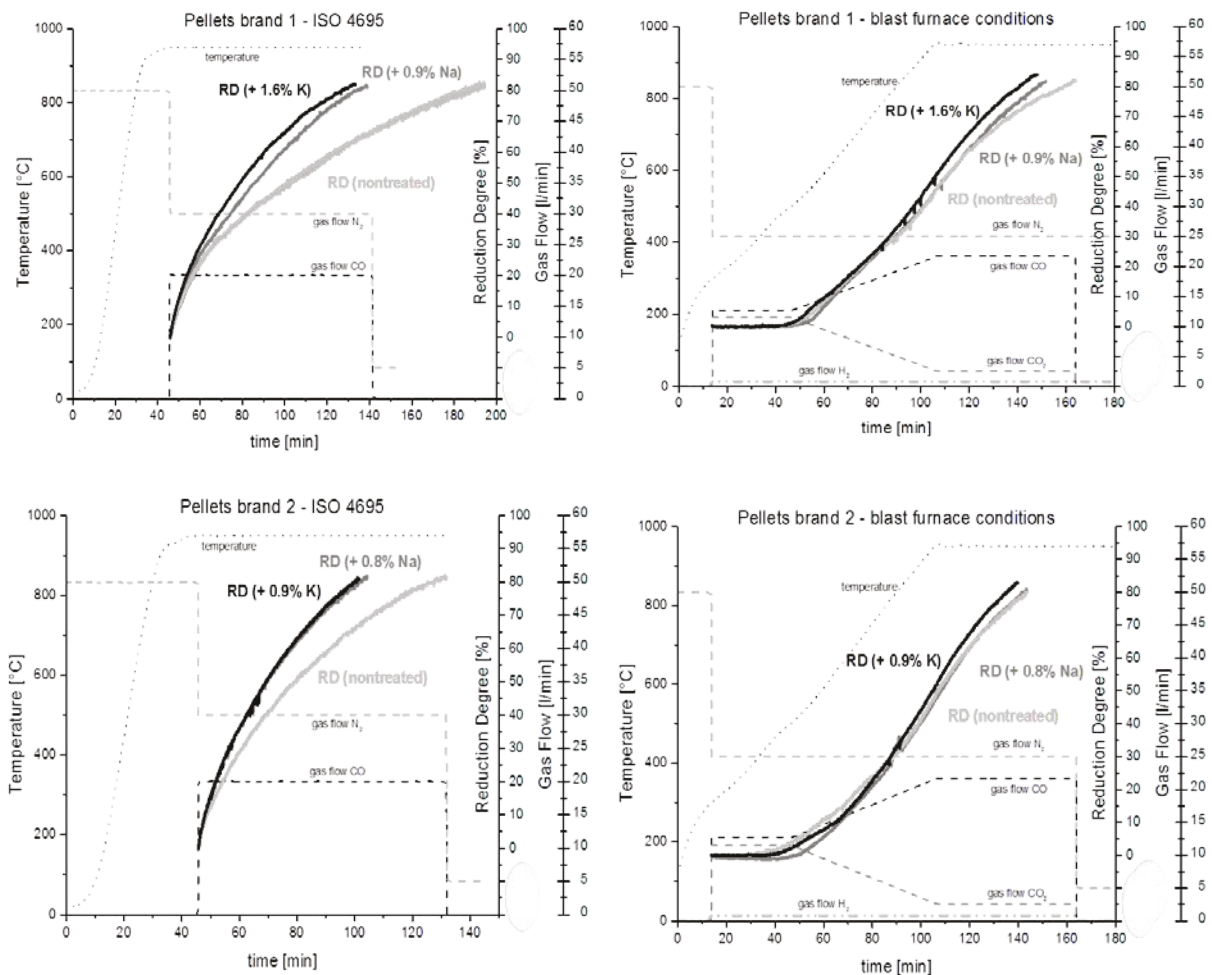


Figure A-3: Process data and curve of the reduction degree for pellets

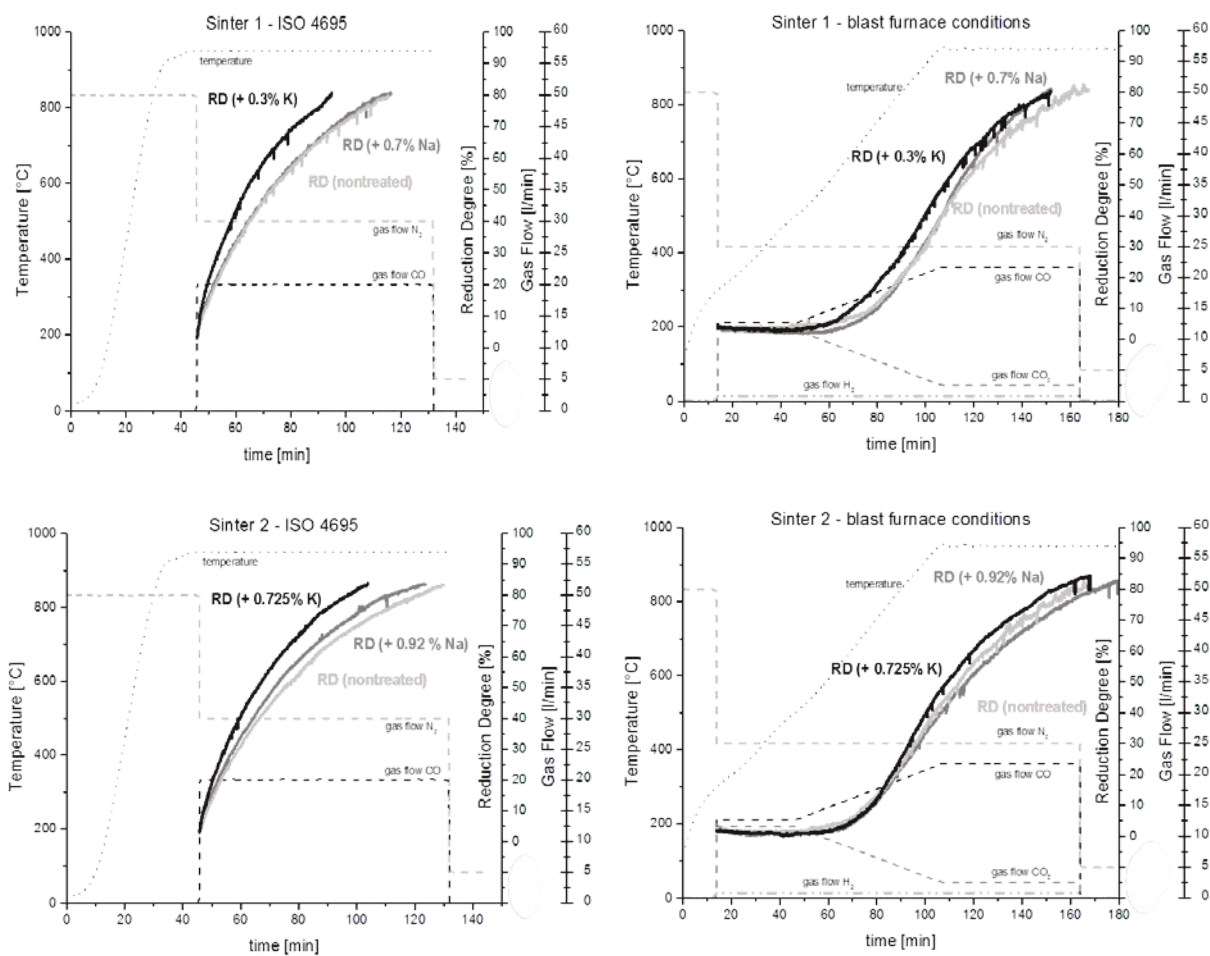


Figure A-4: Process data and curve of the reduction degree for sinter

A-2 Observations by HT-LSCM (partially reduced iron carrier)

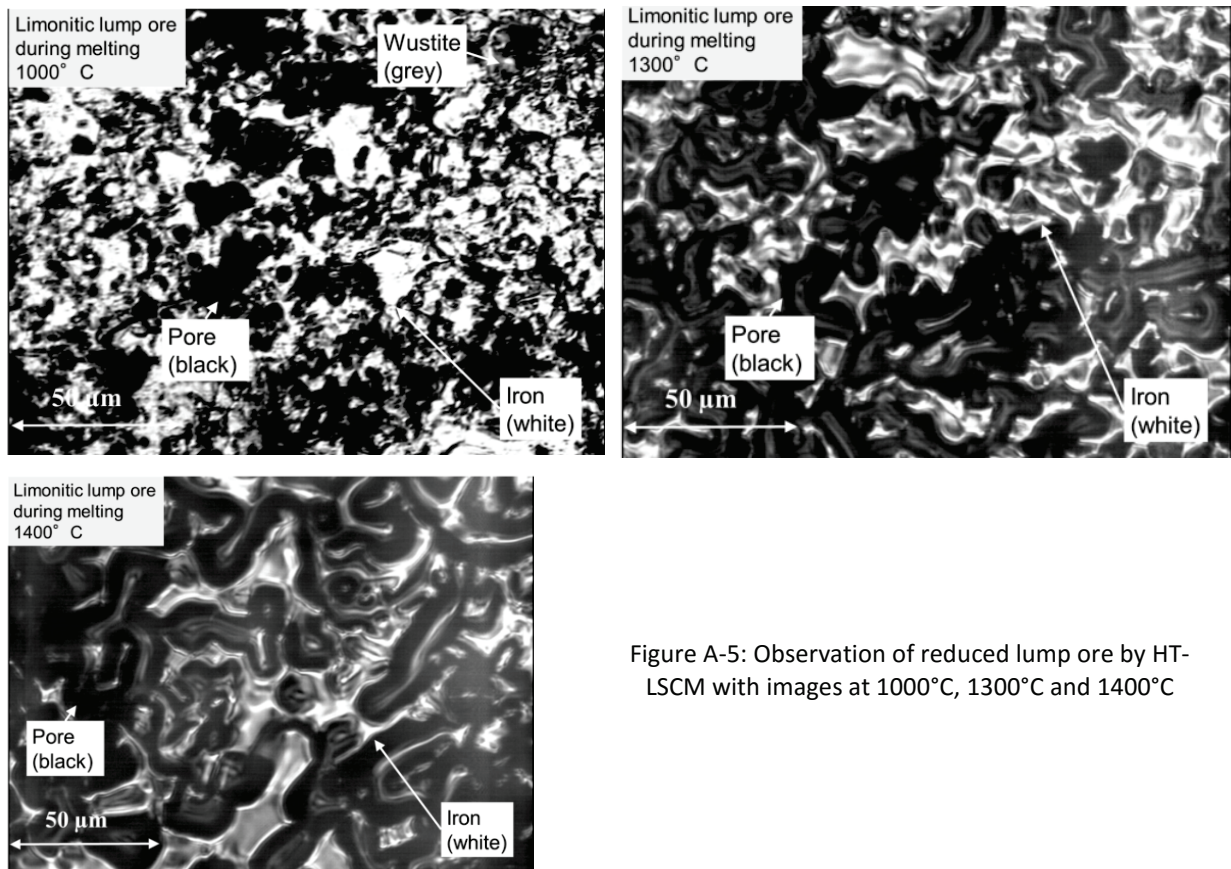


Figure A-5: Observation of reduced lump ore by HT-LSCM with images at 1000°C, 1300°C and 1400°C

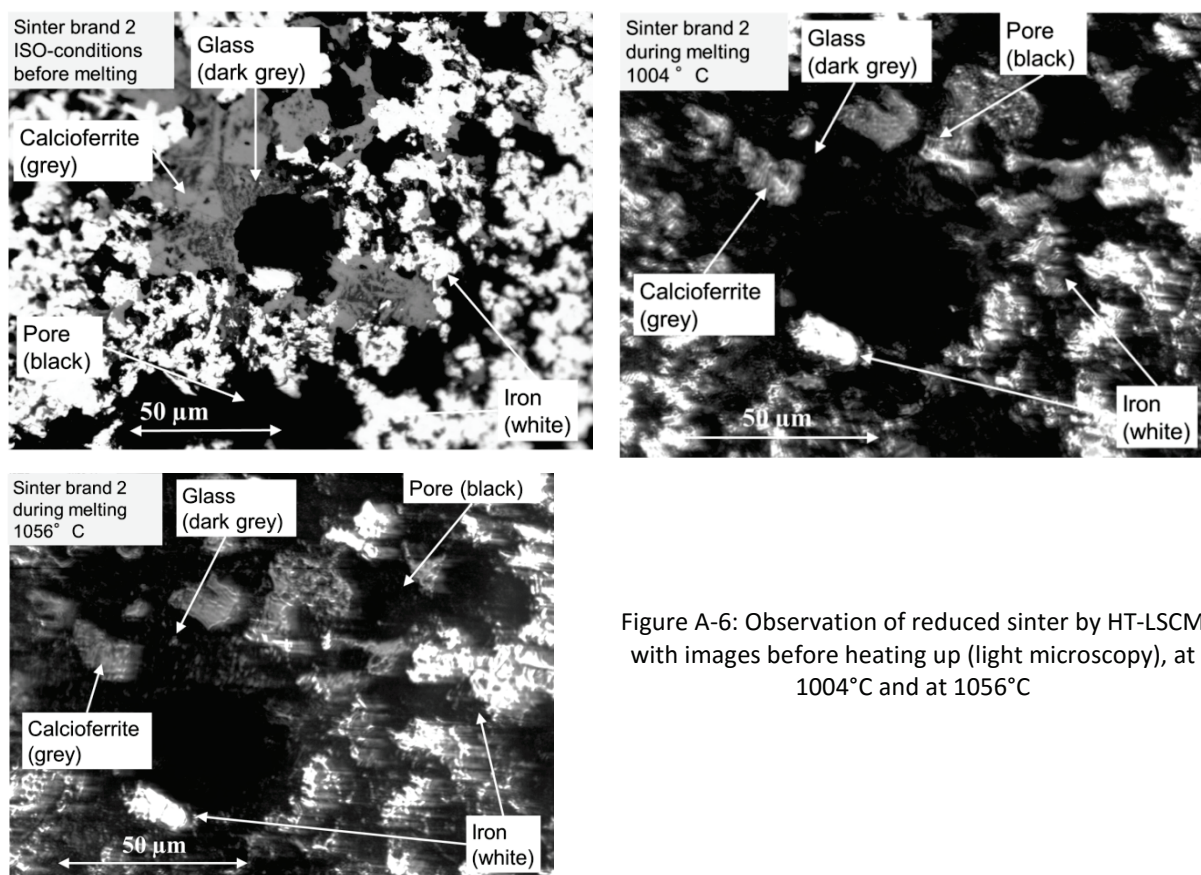


Figure A-6: Observation of reduced sinter by HT-LSCM with images before heating up (light microscopy), at 1004°C and at 1056°C

A-3 Ternary systems for the evaluation of alkali addition

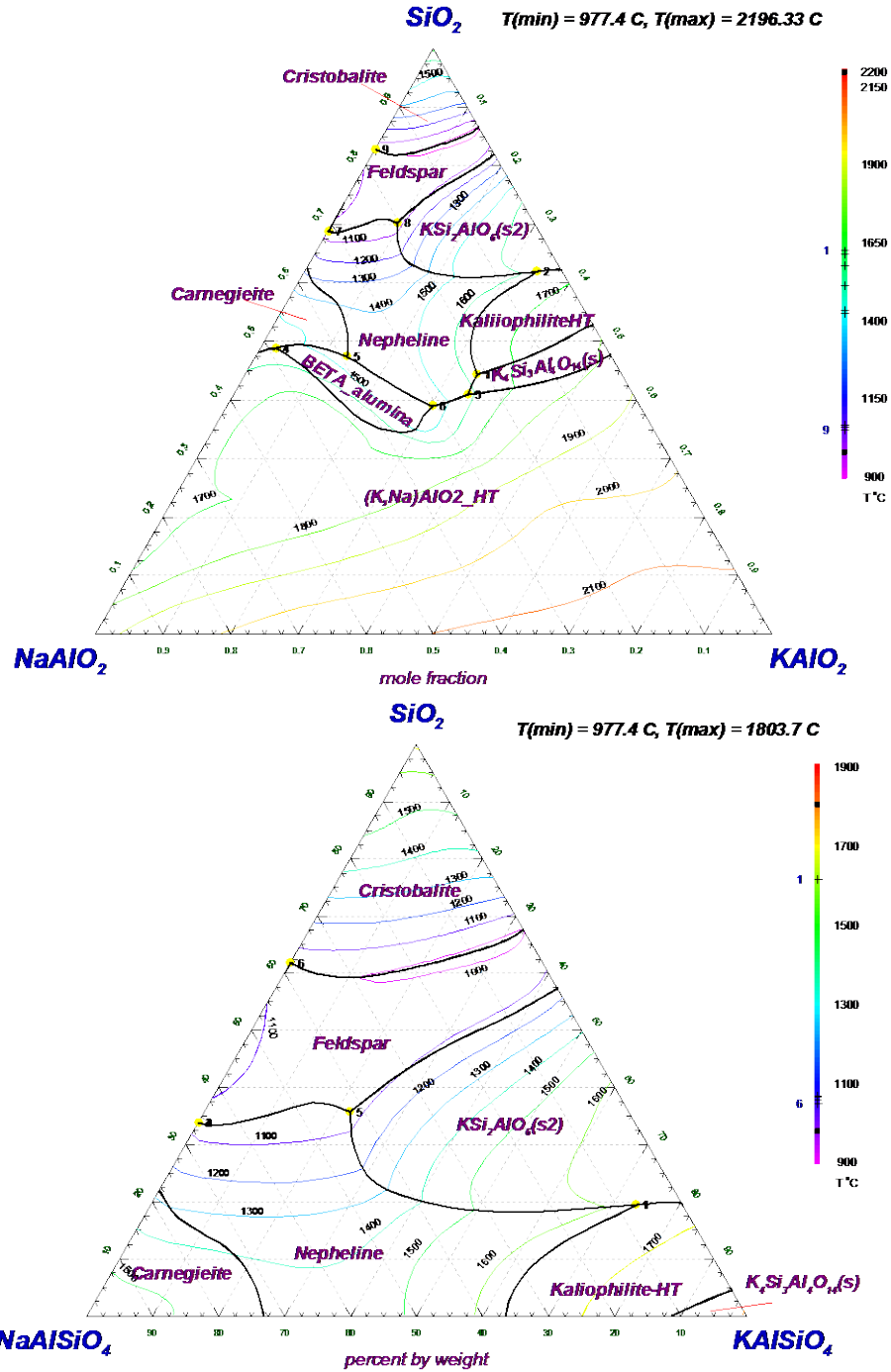


Figure A-7: Supporting ternary systems SiO_2 - NaAlO_2 - KAlO_2 (top) and SiO_2 - NaAlSiO_4 - KAlSiO_4 (bottom) for evaluation of the influence of alkalis on oxidic systems, including the liquidus lines⁹³

A-4 Profiles of elements in experimental blast furnace

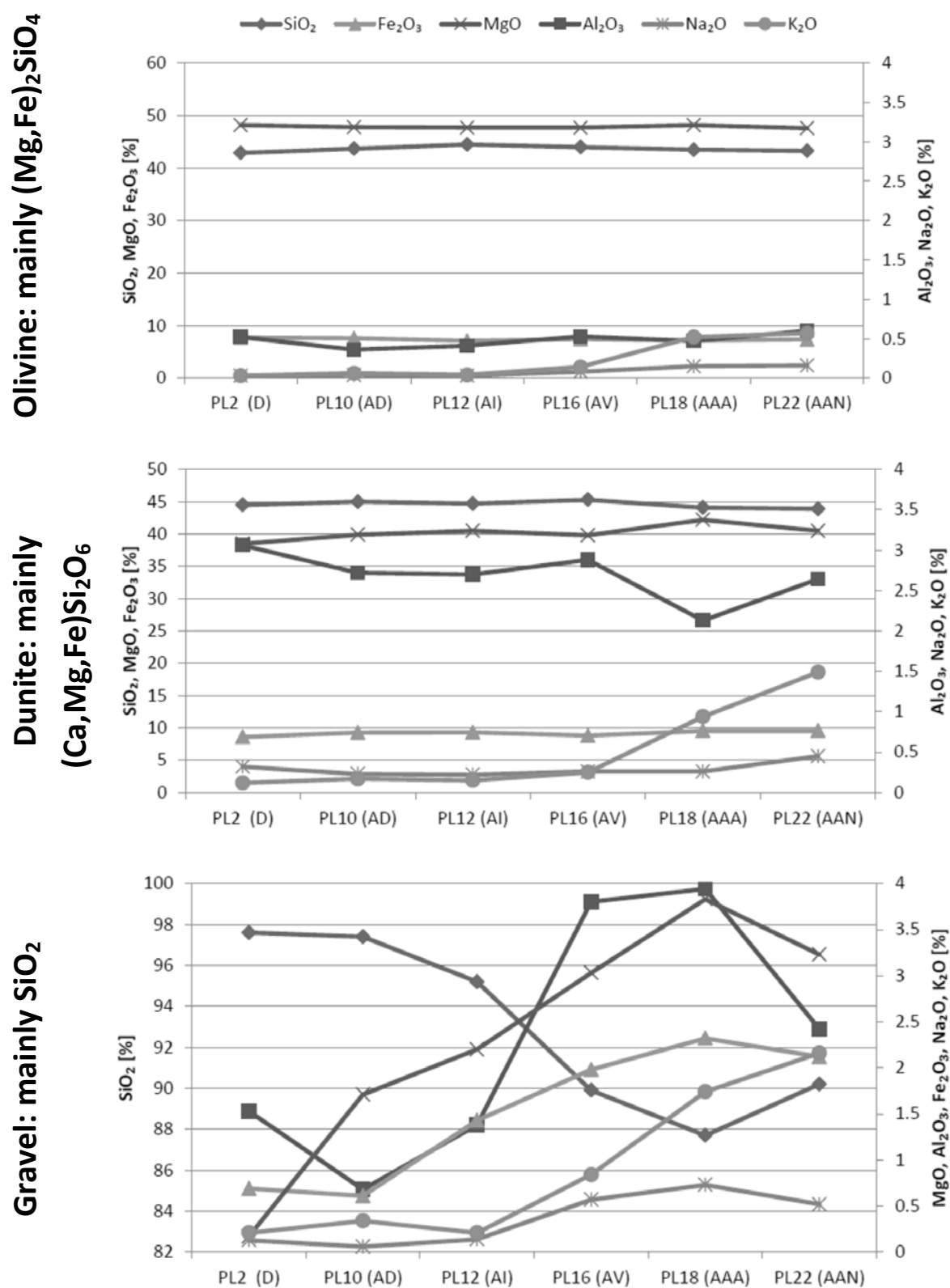


Figure A-8: Chemical composition of SiO_2 - MgO -bearing materials during the operation in an experimental blast furnace (testing layers from top-left to bottom-right)¹³⁸

B-1 List of Figures

Figure 1-1: Steel consumption in relation to the GDP/capita [US\$], including the population (circle size) ¹	2
Figure 1-2: Steel usage in modern civilizations	2
Figure 1-3: Ashby diagrams for strength-density and strength-service temperature ^{11,12}	3
Figure 2-1: Actual routes of steel production ³⁴	7
Figure 2-2: Layout of a modern blast furnace (top) ³⁵ and a schematic picture of the top gas treatment system (bottom) ^{36,37}	8
Figure 2-3: Multi-zone model of the blast furnace (top) ³⁷ and the gas, temperature, and pressure profile for an exemplary furnace derived from literature ^{28,35,43} (bottom).....	10
Figure 2-4: Flow sheet for direct and smelting reduction processes, including energy and iron ore sources ⁴⁸	12
Figure 2-5: Schematic pictures of the COREX [®] process (left) ⁹ and the FINEX [®] process (right) ...	14
Figure 2-6: Layout of the melter gasifier, including the chemical reactions (top) and process parameters like temperature, pressure and gas profile for each zone (bottom) ⁵⁵	15
Figure 2-7: Richardson-Ellingham diagram for the most important metals, oxides, and gases in ironmaking reactors (data from Factsage 7.0 ⁷⁵)	20
Figure 2-8: Phase diagram iron and oxygen ⁷⁶	21
Figure 2-9: Baur-Glaessner diagram for CO/CO ₂ and H ₂ /H ₂ O mixtures ⁸⁰	23
Figure 2-10: Mass loss for iron and iron oxides during reduction in relation to RD and MD ⁸¹	23
Figure 2-11: Kinetic mechanisms of iron ore reduction for porous particles ^{71,72}	25
Figure 2-12: Kinetic mechanisms of iron ore reduction for dense particles ⁸⁸	25
Figure 2-13: Exemplary pictures of a dense hematite particle, including the defined interface areas (left) and a comparison between dense and porous particles after reduction ^{80,84,89}	26
Figure 2-14: Kinetic models of progressive conversion (a) and shrinking core (b), including the concentration profiles of the solid reactant ^{80,91}	27
Figure 2-15: Schematic picture of the solid particles and the gas-concentration profiles for diffusion-limited processes for a dense (left) and a porous (right) particle ⁸⁰	28

Figure 2-16: Schematic representation of the solid particles and the gas-concentration profiles for reaction-limited processes for a dense (left) and a porous (right) particle ⁸⁰	28
Figure 2-17: Layout of the blast furnace, including the correlation between temperature/pressure profile and softening/melting areas in the cohesive zone ^{21,35,92}	29
Figure 2-18: Ternary system CaO-SiO ₂ -Al ₂ O ₃ (CSA) calculated by Factsage™ and compared with data from literature (isothermal section at 1600°C and 1 bar) ⁹³	31
Figure 2-19: Ternary system CaO-SiO ₂ -FeO (CSF) calculated by Factsage™ and compared with data from literature (liquidus lines for 1200, 1300, 1400, and 1650°C, and 1 bar) ⁹³	31
Figure 3-1: Interaction of alumina silicates with K, Na, and Ca in a ternary system, including minerals ⁹⁵	33
Figure 3-2: Geological structure of hematite iron ore from banded iron formations (left and middle: optical microscopy; right: SEM) ¹⁰²	34
Figure 3-3: Internal alkali cycles for potassium in a blast furnace ²¹	36
Figure 3-4: Richardson-Ellingham diagrams for alkali compounds (left: metals and oxides; right: cyanides), including the process conditions for BF and MG ^{75,106}	37
Figure 3-5: Exemplary amounts of the alkali output of European BFs ¹⁰⁹	39
Figure 3-6: Model of the formation of scaffolds in the blast furnace shaft ⁹⁶	41
Figure 3-7: Alkali infiltration into the refractory of the middle part of the shaft (including the consumption of material during operation) ¹¹⁰	41
Figure 3-8: Comparison of different BFs according to their alkali balance (left: input masses and the ratio of K or Na in the specific phase compared to the total K or Na load; centre: alkali load; right: output ratio of Na and K and masses)	43
Figure 3-9: Alkali handling of European BF operators: Correlation of alkali load [kg/tHM] and B ₂ -basicity ¹⁰¹	45
Figure 3-10: Alkali distribution in the dust over the BF height (left: total content of K/Na; right: compounds measured by XRF analysis); data derived from Lin ³⁶	46
Figure 3-11: Alkali flow for potassium in the COREX® and FINEX® process, including the stable phases and complex gas treatment system ^{120,121}	48
Figure 3-12: Increase in reaction rate of iron oxide in correlation with the ionic radius of alkali and earth alkali elements ²⁸	49
Figure 3-13: Ternary system for CaO-SiO ₂ and K ₂ O projection, including the isothermal lines for T _m for different compositions (pressure =1 atm) ⁹³	51
Figure 4-1: Connection between single elements of the model ¹³²	54

Figure 4-2: Simplified equilibrium conditions for the reduction and evaporation of alkalis in the slag phase	57
Figure 4-3: Evaporation rate for K (empirical) in connection with the optical basicity of blast furnace near-slag compositions and different temperatures (curves mathematically fitted to results and points from literature ^{109,122,134-136})	58
Figure 4-4: Simplified alkali flow in the reactor for the reaction model ⁴³	60
Figure 4-5: Reaction areas of the multi-stage model and the separation into cold and hot zones	60
Figure 4-6: Distribution of alkali compounds for the standard blast furnace over the furnace height ⁴³	62
Figure 4-7: Distribution of alkali compounds for the standard blast furnace ⁴³	63
Figure 4-8: Alkali flow of standard 50 tHM/h blast furnace	64
Figure 4-9: Comparison of calculated values (see values of single compounds in the table and the allocation to top gas fractions on the right) with analysis from industrial operation ⁴³	65
Figure 4-10: Alkali load (total potassium and sodium) for a basicity $B_2=1$ and a slag temperature of 1420°C (standard model), and comparison with the alkali distribution (middle: total K/Na in coke; right: sum of K/Na-oxidic in the coke ash) over the blast furnace height based on industrial investigations ^{36,109,119}	67
Figure 4-11: Comparison of alkali flows [kg K/tHM] between own alkali model (middle for standard blast furnace with high alkali input), prediction from other models (left), and from industrial data (right).....	67
Figure 4-12: Alkali distribution over the furnace height in kg/tHM (sum of cold and hot areas; values and black columns for BF-variation 1, grey columns for the standard BF)	69
Figure 4-13: Distribution of total K and selected K compounds in the different reaction areas of the blast furnace (variation 2) in kg/tHM (sum of cold and hot columns) ⁴³	70
Figure 4-14: Influence of slag temperature on the alkali content in the reactor with the alkali load in zone 5 (square points), and the alkali vapour (spotted points) from the slag phase (continuous lines) and the top gas (dotted lines) ⁴³	71
Figure 4-15: Alkali load for the standard melter gasifier	77
Figure 4-16: Alkali balance for the standard melter gasifier with input data and output masses from industrial data and calculated K/Na in the slag and dust.....	78
Figure 4-17: Alkali load (total potassium and sodium) for the blast furnace (left) and the melter gasifier (right)	80
Figure 4-18: Chlorine in the blast furnace, including the interaction with alkalis ¹¹³	82
Figure 5-1: Flow sheet for the evaluation of ferrous burden material affected by alkalis	85

Figure 5-2: Alkali content of the ferrous material in correlation with the molarity of the solution	86
Figure 5-3: Mineralogical structure (left) and K distribution after treatment (right) in hematite lump ore	87
Figure 5-4: Mineralogical structure (left) and K distribution after treatment (right) for limonitic lump ore	87
Figure 5-5: Mineralogical structure (left) and K distribution after treatment (right) for Sinter 188	
Figure 5-6: Testing device (retort) for the reduction of iron ores ¹³¹	89
Figure 5-7: Process route of the blast furnace process-near reduction test (BF) in the Baur-Glaessner diagram	90
Figure 5-8: Process route of the smelting reduction process-near reduction test (SR) in the Baur-Glaessner diagram	90
Figure 5-9: Schematic picture of the tumbling drum, including the dimensions ¹³¹	91
Figure 5-10: Process data and reduction curve for limonitic lump ore under ISO (left) and BF (right) conditions and the addition of K or Na	92
Figure 5-11: Process data and reduction curve for acid pellet 1 (left) and basic pellet 2 (right) under ISO condition (pure CO) and the addition of K or Na.....	92
Figure 5-12: Process data and reduction curve for sinter 2 under ISO (left) and BF (right) conditions, and the addition of K or Na.....	93
Figure 5-13: Process data and reduction curve for hematite lump ore (left) and basic pellet 2 (right) under smelting reduction near conditions and the addition of K or Na	93
Figure 5-14: Relative change in reducibility by the addition of alkalis for different materials	95
Figure 5-15: Summary of the disintegration tendency (mass ratio <6.3 mm) for ferrous burden material (untreated and alkali-treated).....	96
Figure 5-16: Summary of the abrasion tendency (mass ratio <0.5 mm) for ferrous burden material (untreated and alkali-treated).....	97
Figure 5-17: Summary of the sticking tendency (mass ratio >12.5 mm) for ferrous burden material (untreated and alkali-treated).....	98
Figure 5-18: Morphological comparison of untreated pellets with Na-treated pellets after reduction under ISO conditions.....	99
Figure 5-19: Morphological comparison of untreated sinter with K-treated sinter after reduction under ISO conditions	99

Figure 5-20: Effect of KCl addition on reduction degree under CO/CO ₂ atmosphere at 900°C ¹⁴⁹	101
Figure 5-21: Change in reduction rate by the addition of K ₂ O at 800°C at a reduction degree of 5 and 30% ¹²⁴	101
Figure 5-22: Reduction curves for doped iron oxide under CO, CO ₂ , H ₂ and N ₂ atmosphere at different temperatures ¹²⁶	101
Figure 5-23: Effect of different carbonates on the reduction degree at 1000°C and 5% additives after 150 minutes ¹⁵⁰	101
Figure 5-24: Reduction of lump ore with pure CO (left) and pure H ₂ (right) atmospheres (testing conditions derived from ISO 4695).....	102
Figure 5-25: Influence of alkali on the chemical mechanisms during reduction by CO	104
Figure 5-26: Exemplary result of the melting behaviour recorded by hot stage microscopy (left: ambient temperature, softening point at 1525°C, hemispherical point at 1527°C, and flowing point at 1531°C) ¹⁵⁸	106
Figure 5-27: Schematic picture of the HT-LSCM, including the sample holder (Al ₂ O ₃ crucible) ¹⁵⁹	106
Figure 5-28: Exemplary schemata of DTA curves for phase transformations (endothermic reaction for melting [left] and exothermic reaction for recrystallization [right]) ¹⁶⁰	107
Figure 5-29: Exemplary result of the melting behaviour recorded by hot stage microscopy (top: partially reduced limonite, Na-treated; bottom: partially reduced pellets, K-treated) ¹⁵⁸	108
Figure 5-30: Observation of reduced pellets by HT-LSCM before heating up (light microscopy) to 1023°C, 1090°C, 1158°C and 1183°C	109
Figure 5-31: Comparison of the recorded DTA curves for reduced ferrous materials (untreated and treated).....	111
Figure 5-32: Fe-O binary system including the phase transformations and temperatures ⁷⁵	115
Figure 5-33: Comparing the binary systems of FeO-SiO ₂ (black) and FeO-Na ₂ SiO ₃ (grey) ⁷⁵	116
Figure 5-34: Ternary system CSF with the liquidus lines for 1000–1600°C, and the modifications with 5 wt-% K ₂ O and Na ₂ O (chemical composition of the oxidic compounds of the investigated materials marked as points)	117
Figure 5-35: Ternary system CAF with the liquidus lines for 1000–1600°C, and the modifications with 5 wt-% K ₂ O and Na ₂ O (chemical composition of the oxidic compounds of the investigated materials marked as points)	118

Figure 5-36: Ternary system SAF with the liquidus lines for 1000–1600°C, and the modifications with 5 wt-% K ₂ O and Na ₂ O (chemical composition of the oxidic compounds of the investigated materials marked as points)	119
Figure 5-37: Pressure profile during a melting test for an acidic pellet grade (left) and a basic pellet grade (right) ¹⁶²	120
Figure 5-38: Pressure profile during a melting test for a sinter sample with B ₂ =2.1 (left), and comparison of different burden materials and pure substances by viscosity measurement (right) ¹⁶²	121
Figure 6-1: Exemplary illustration of the alkali distribution and the alkali compounds for a 50 tHM/h blast furnace and a load of 4.1 kg alkalis per tHM	124
Figure 6-2: open-bit mining for potash production ¹⁶³	127
Figure 6-3: evolution of industrial production towards industry 4.0 ¹⁶⁹	128
Figure A-1: Process data and curve of the reduction degree for lump iron ores.....	I
Figure A-2: Process data and curve of the reduction degree under SR conditions for hematite lump ore and pellets brand 2	II
Figure A-3: Process data and curve of the reduction degree for pellets	II
Figure A-4: Process data and curve of the reduction degree for sinter.....	III
Figure A-5: Observation of reduced lump ore by HT-LSCM with images at 1000°C, 1300°C and 1400°C	IV
Figure A-6: Observation of reduced sinter by HT-LSCM with images before heating up (light microscopy), at 1004°C and at 1056°C.....	V
Figure A-7: Supporting ternary systems SiO ₂ -NaAlO ₂ -KAlO ₂ (top) and SiO ₂ -NaAlSiO ₄ -KAlSiO ₄ (bottom) for evaluation of the influence of alkalis on oxidic systems, including the liquidus lines ⁹³	VI
Figure A-8: Chemical composition of SiO ₂ -MgO-bearing materials during the operation in an experimental blast furnace (testing layers from top-left to bottom-right) ¹³⁸	VII

B-2 List of Tables

Table 2-1: Typical process condition of the BF derived from literature: The basis for the standard BF model ^{35,40}	11
Table 2-2: Typical process condition of melter gasifier derived from literature: A basis for the standard melter gasifier model ^{53,59}	16
Table 3-1: Melting and boiling temperatures of alkali compounds (left value from Factsage TM 75 ,right from Gudenau ²¹)	33
Table 3-2: Summary of the alkali balances of different blast furnace operators (European Union [EU], Eastern Europe and Russia [EaEu], Japan [Jpn], North America [NA]).....	42
Table 3-3: Overview of the chemical analysis of dust or gas samples over the BF: A horizontal profile ³⁶	45
Table 4-1: Exemplary data of potassium and sodium in input and output materials derived from literature for standard BF model ^{19,36,115,133}	55
Table 4-2: Process parameters for the outline of the reactor profiles and the following thermochemical calculations for the standard blast furnace model	56
Table 4-3: Reaction zones of the standard blast furnace, including temperature, pressure (absolute), and gas composition derived from industrial data ^{21,28}	61
Table 4-4: Specific alkali load and ratios of the outer cold and inner hot zones (standard blast furnace for slag temperature 1420°C and $B_2=1$) ⁴³	63
Table 4-5: Process parameters of the blast furnace—variation 1 (including the parameters of the standard blast furnace)	70
Table 4-6: Effect of slag composition on K/Na content in top gas and in the lower stack region of a blast furnace (zone 3) ⁴³	72
Table 4-7: Exemplary data of potassium and sodium in input and output materials derived from industrial data ⁵⁵ for the melter gasifier model.....	74
Table 4-8: Process parameters for the outline of the profiles of the melter gasifier	75
Table 4-9: Reaction zones of the standard melter gasifier, including temperature, pressure (absolute), and gas composition derived from industrial data ^{21,28}	75
Table 4-10: Important differences in the process layouts of the standard reactors.....	79
Table 4-11: Comparison of the main findings by the alkali model for blast furnace and melter gasifier	81
Table 5-1: Chemical composition and specific surface area of the investigated raw materials....	84

Table 5-2: Chemical analysis of K/Na of untreated and treated raw materials	86
Table 5-3: Summary of the K/Na content in different iron carriers under the influence of alkalis	88
Table 5-4: Technical data and values ¹³¹	89
Table 5-5: Parameters of the standardized and process-near reduction tests.....	90
Table 5-6: Testing conditions of the tumbling tests and equations for the evaluation ¹³¹	91
Table 5-7: Summary of reduction times and reduction rates of the performed tests.....	94
Table 5-8: Summary of disintegration and abrasion tendencies under ISO and BF conditions	98
Table 5-9: Comparison of activation energy for iron oxide reduction	102
Table 5-10: Chemical analysis of partially reduced iron carriers for the softening and melting tests.....	105
Table 5-11: Process conditions for the softening and melting tests.....	107
Table 5-12: Comparison of transformation temperature influenced by alkalis ¹⁵⁸	113
Table 5-13: Analysis of melted material (based on partial reduced pellet brand 2, Na-treated) by SEM measurement ¹⁵⁸	114
Table 5-14: Comparison between the oxidic systems of the iron carriers (C-CaO, A-Al ₂ O ₃ , S-SiO ₂ , F-FeO)	116
Table 6-1: Summary of the investigations on the effect of alkali metals on ferrous burden material	125

B-3 Acronyms

A	Al ₂ O ₃	HT-LSCM	High-temperature laser scanning confocal microscope
AT	Abrasion tendency	IND	India
AT	Ambient temperature	ISO	International Organisation for Standardization
B	Basicity	JPN	Japan
B	Boiling temperature	KOR	Republic of South Korea
BF	Blast furnace	LOI	Loss on ignition
BET	Brunauer-Emmett-Teller	LTB	Low temperature breakdown
BOF	Basic oxygen furnace	M	MgO
C	CaO	M	Melting temperature
CN	People's Republic of China	m	Melting
DR	Direct reduction	MD	Metallization degree
DRI	Direct reduced iron	met	Metallic/metallized
DT	Disintegration tendency	MG	Melter gasifier
DTA	Differential thermal analysis	NA	North America
EaEu	Eastern Europe	PCI	Pulverized coal injection
EAF	Electric arc furnace	RSA	Republic of South Africa
EBF	Electric blast furnace	RD	Reduction degree
EU	European Union	S	SiO ₂
F	FeO	SAF	Submerged arc furnace
GG	Generator gas	SEM	Scanning electron microscope
GOD	Gas oxidation degree	SR	Smelting reduction
HBI	Hot briquetted iron	ST	Sticking tendency
HCI	Hot compacted iron	tot	Total
HGC	Hot gas cyclone	XRF	X-ray fluorescence
HM	Hot metal		
HSM	Hot stage microscope		

B-4 Publications

Contribution to journals, conferences and scientific boards

Pichler A., S. Feichtinger: Analyse- und Untersuchungsmethoden zur Charakterisierung der Eigenschaften von Hüttenkoks für moderne Hochöfen, Proceedings of the 18th International Student's Day of Metallurgy, Leoben, AUT, March (2011).

Skorianz M., H. Mali, J. Schenk, J.-F. Plaul, A. Pichler, M. Hanel: Mineralogical and structural evaluation of iron ore fines reduced in a lab scale fluidized bed reactor, Conference proceedings of the 6th international congress on the science and technology of ironmaking- ICSTI, Rio de Janeiro, BRA, Sept. (2012), pp. 2347-2359.

Pichler A., J. Schenk, M. Skorianz: Charakterisierung und Bewertung der morphologischen Veränderung von Feineisenerzen während der Reduktion in einer Wirbelschicht, ASMET-Forum für Metallurgie und Werkstofftechnik, Leoben, AUT, May (2013).

Pichler A., M. Skorianz, H. Mali, J. Schenk, J.-F. Plaul, B. Weiss: Process behaviour of fine iron ores during reduction in a fluidized bed reactor and characterization of the morphological evolution, Conference proceedings to the 1st ESTAD and 31st JSI, Paris, FRA, April (2014), pp. 100-102.

Kolb F., A. Pichler, H. Mali, J. Schenk: Standardized iron ore characterization methodology for metallurgy, Practical Metallography, 52, 1, Jan. (2015), pp. 5-20.

Pichler A., M. Hanel, H. Mali, F. Hauzenberger, H. Stocker, C. Thaler, J. Schenk: Influence of alkalis on mechanical properties of lumpy iron carriers during reduction, Conference proceedings to the 23rd international conference on metallurgy and materials, Brno, CZ, May (2014), pp. 2676-2682.

Skorianz M., H. Mali, J.Schenk, J.-F. Plaul, B. Weiss, A. Pichler: Reduction behaviour and structural evolution of iron ores in fluidized bed technologies. Part 1: Method for the determination, Steel research international, 87, 5, (2016), pp. 633-641.

Pichler A., M. Skorianz, H. Mali, J.Schenk, J.-F. Plaul, B. Weiss: Reduction behaviour and structural evolution of iron ores in fluidized bed technologies. Part 2: Characterization and evaluation of worldwide traded fine iron ore brands, Steel research international, 87, 5, (2016), pp. 642-652.

Pichler A., J. Schenk, F. Hauzenberger, H. Stocker, C. Thaler, Thermochemical modelling of the alkali balance in modern blast furnaces, AsiaSteel 2015, Yokohama, JAP, Oct. (2015), pp. 282-283.

Pichler A., J. Schenk, M. Zarl, J. Fellner, Iron-Balance Austria, K1-MET Scientific Exchange Day, Leoben, AUT, March (2016).

Pichler A., J. Schenk, F. Hauzenberger, C. Thaler, H. Stocker: Influence of slag properties on the alkali-cycle of a blast furnace, Proceedings to AISTech 2016, Pittsburgh, USA (2016), pp. 341-352.

Pichler A., J. Schenk, F. Hauzenberger, H. Stocker, C. Thaler, Analysis of the alkali-distribution in ironmaking reactors by thermochemical modelling, ECIC 2016, Linz, AUT (2016), pp. 534 ff.

Teaching and lectures

220.041: "Ferrous Metallurgy II Modul 1", Chair of Ferrous Metallurgy, Montanuniversitaet Leoben, SS 2015-2016.

220.046: "Lab in ferrous metallurgy-processes", Chair of Ferrous Metallurgy, Montanuniversitaet Leoben, SS 2013-2016.

220.053: "Seminar on steel process technology", Chair of Ferrous Metallurgy, Montanuniversitaet Leoben, WS 2012-2015.

220.058/220.060: "Excursion on ferrous metallurgy 1 & 2", Chair of Ferrous Metallurgy, Montanuniversitaet Leoben, WS 2013-2015.

220.087: "Metallurgical Project", Chair of Ferrous Metallurgy, Montanuniversitaet Leoben, WS 2014.

220.090: "Fundamentals of metallurgy", Department of Metallurgy, Montanuniversitaet Leoben, SS 2016.

601.005: "Process Management II: Logistics Process Design", Chair of Industrial Logistics, Montanuniversitaet Leoben, SS 2014-2016.

Guest lecture: "Alkalien: Mikro- und Makroskopische Einflüsse bei der Eisenherstellung", Institute of water quality, resources and waste management, Technische Universität Wien, WS 2014.

Supervised theses

Tauchner Cornelia: "Mineralogisch-petrographische Beschreibung von Eisenerzen, Gangart und Pellets, Bachelor Thesis, Montanuniversitaet Leoben, (2014).

Li Tong: "Untersuchung des Verhaltens verschiedener SiO₂-MgO-Träger in Abhängigkeit von der Absinktiefe in einem Versuchshochofen", Bachelor Thesis, Montanuniversitaet Leoben, (2016).

Kaltenböck Ilena: „Erweichungs- und Schmelzverhalten von reduzierten Eisenträgern unter Berücksichtigung des Einflusses von Alkalien“, Master Thesis, Technische Universität Graz, (2014).

Spreitzer Daniel: "Optimierung der Prozessparameter für die Reduktion von Feineisenerzen mittels Wirbelschichtverfahren", Master Thesis, Montanuniversitaet Leoben, (2016)

Leoben, November 14th, 2016**B-5 Curriculum Vitae**

Name Dipl.-Ing. Anton Pichler

Address Dölla 10, Weinberghof
A-3661 Artstetten

Phone 0043 (0) 664 8832 3194

E-Mail anton.pichler@unileoben.ac.at

Date and place of birth: August 1st, 1988, Melk

Nationality: Austria

**Education:**

-
- 2012-2017 **Doctoral Thesis**, Chair of Ferrous Metallurgy
“Influence of alkalis on the process behaviour of iron carriers in different ironmaking reactors” (Dec. 2016)
- 2007-2012 Academic studies at the Montanuniversitaet Leoben, Bachelor- and Master-Studies in Metallurgy; Master program: Specialization in Iron- and Steelmetallurgy, Industrial Economics
Master Thesis, Chair of Ferrous Metallurgy: *“ Development of a methodology to characterize the morphological evolution of iron ore fines during reduction in the fluidized bed process ”* (Oct. 2012)
2nd Bachelor Thesis, Chair of Ferrous Metallurgy: *“ Contribution to the development of a standardized methodology for evaluating the reduction of fine ores ”*) (Nov. 2011)
1st Bachelor Thesis, Chair of Ferrous Metallurgy: *“ Analysis and testing methods for the characterisation of furnace coke properties for modern blast furnaces ”* (Nov. 2010, Presented at the International Students’ Day of Metallurgy in Leoben in 2011
- June 2006 Higher School Certificate, passed with distinction
- 2002-2006 Grammar School, focus on science, Stiftsgymnasium Melk
- 1998-2002 Secondary Modern School, Pöggstall
- 1994-1998 Elementary School in Artstetten

Work Experience:

- Since 2016 **Engineer (R&D, Processes)**, voestalpine Stahl GmbH, Linz
Department Technical Processes (R&D) and Blast Furnace (Production)
- 2012-2016 **Research Assistant**, Montanuniversitaet Leoben, Chair of Ferrous Metallurgy,
Working group “Primary Metallurgy”; Doctoral Thesis within the K1-MET
metallurgical competence centre and in collaboration with the industrial partners
Primetals Technologies GmbH, voestalpine Stahl GmbH, voestalpine Stahl Donawitz
GmbH and Posco (KOR)
- 2010-2012 Student worker, Montanuniversitaet Leoben, Chair of Ferrous Metallurgy
- 2007 Military service (Engineering battalion No.3., Biragokaserne Melk-Austria)
- 2003-11 Internships in **timber industries** (Sonnenmöbel-Persenbeug/AUT, Stora Enso Timber-
Gruvön/SWE), **concrete industry** (Xella Porenbeton- Loosdorf/AUT), **metals**
industries (Neuman Aluminium-Lilienfeld/AUT, voestalpineStahl-Linz/AUT, HKM-
Duisburg/GER)

Additional Skills and Information:

Languages: German: Mother tongue

 English: Fluent

 Russian: Basic knowledge

IT-skills: MS Office, Origin, Factsage™, VBA programming,

Memberships: ASMET (Austrian Society for Metallurgy and Materials)

 VDEh (Verein Deutscher Eisenhütte)